

University of Windsor

Scholarship at UWindor

Electronic Theses and Dissertations

Theses, Dissertations, and Major Papers

2008

The Development of an Electrostatic Storage Ring for Low Energy Electrons

David Ronald Tessier
University of Windsor

Follow this and additional works at: <https://scholar.uwindsor.ca/etd>



Part of the [Physics Commons](#)

Recommended Citation

Tessier, David Ronald, "The Development of an Electrostatic Storage Ring for Low Energy Electrons" (2008). *Electronic Theses and Dissertations*. 8284.

<https://scholar.uwindsor.ca/etd/8284>

This online database contains the full-text of PhD dissertations and Masters' theses of University of Windsor students from 1954 forward. These documents are made available for personal study and research purposes only, in accordance with the Canadian Copyright Act and the Creative Commons license—CC BY-NC-ND (Attribution, Non-Commercial, No Derivative Works). Under this license, works must always be attributed to the copyright holder (original author), cannot be used for any commercial purposes, and may not be altered. Any other use would require the permission of the copyright holder. Students may inquire about withdrawing their dissertation and/or thesis from this database. For additional inquiries, please contact the repository administrator via email (scholarship@uwindsor.ca) or by telephone at 519-253-3000ext. 3208.

**THE DEVELOPMENT OF AN ELECTROSTATIC
STORAGE RING FOR LOW ENERGY ELECTRONS**

BY

DAVID R. TESSIER

**FACULTY OF GRADUATE STUDIES
UNIVERSITY OF WINDSOR
2008**

LEDDY LIBRARY
UNIVERSITY OF WINDSOR

THE DEVELOPMENT OF AN ELECTROSTATIC STORAGE RING FOR LOW
ENERGY ELECTRONS

By
David R. Tessier

A Dissertation
Submitted to the Faculty of Graduate Studies
through the Department of Physics
in Partial Fulfillment of the Requirements for
the degree of Doctor of Philosophy at the
University of Windsor

Windsor, Ontario, Canada
2008

© 2008 David R. Tessier

6 August 2008

THE DEVELOPMENT OF AN ELECTROSTATIC STORAGE RING FOR LOW ENERGY ELECTRONS

LEOL
THE
Thesis
2008
.T47

By
David R. Tesler

A Dissertation
Submitted to the Faculty of Graduate Studies
through the Department of Physics
in partial fulfillment of the requirements for
the degree of Doctor of Philosophy at the
University of Windsor

Windsor, Ontario, Canada
2008
© 2008 David R. Tesler

1229164

"The Development of an Electrostatic Storage Ring for Low Energy Electrons"

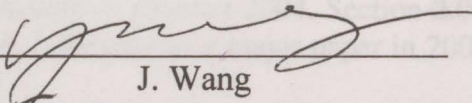
by

David Ronald Tessier

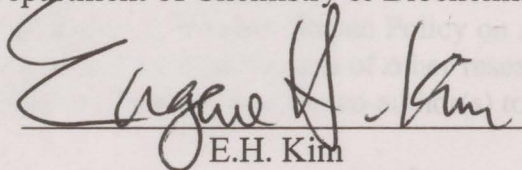
APPROVED BY:



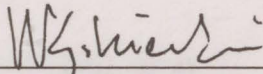
R.C. Schiell, External Examiner
Trent University



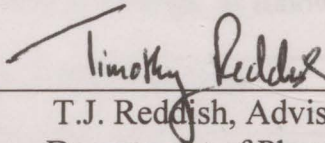
J. Wang
Department of Chemistry & Biochemistry



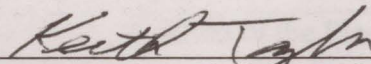
E.H. Kim
Department of Physics



W. Kedzierski
Department of Physics



T.J. Reddish, Advisor
Department of Physics



K. Taylor, Chair of Defense
Department of Chemistry & Biochemistry

6 August 2008

Declaration of Co-Authorship / Previous Publication

I. Co-Authorship Declaration

I hereby declare that this thesis incorporates material that is result of joint research, as follows:

The instrument that is unique in design and construction was made to function by the author through the designs and concepts presented in Chapters 4 and 5. The results and analysis of Chapters 5 and 6 were performed by the author. This thesis also incorporates the outcome of a joint research undertaken with Dr. Benjamin G. Birdsey and Aaron J. Alderman under the supervision of Dr. Peter Hammond and Dr. Frank H. Read. The collaboration is covered in Chapter 2 of the thesis. Section 3.2 was a collaborative project, and with the exception of section 3.3 of Chapter 2, the key ideas and primary contributions were performed by the author. The physical design of the instrument as presented in section 1.0 of chapter 3 was performed by Drs. Peter Hammond and Timothy J. Reddish prior to my start date of summer 2004. Section 2.0 of Chapter 3 was based on the research of Ying Niu as published as a major paper in 2006, and was re-designed and re-engineered by the author.

I am aware of the University of Windsor Senate Policy on Authorship and I certify that I have properly acknowledged the contribution of other researchers to my thesis, and have obtained written permission from each of the co-author(s) to include the above material(s) in my thesis.

I certify that, with the above qualification, this thesis, and the research to which it refers, is the product of my own work.

II. Declaration of Previous Publication

This thesis includes four original papers that have been previously published/submitted for publication in peer reviewed journals, as follows:

Thesis Chapter	Publication title/full citation	Publication status
Chapter 2	Stability Criteria for a Passive Electrostatic Non-Relativistic Charged Particle Storage Device	In preparation
Chapter 3	The Practical Realization of the Electron Recycling System	In Preparation
Chapter 4	D.R. Tessier <i>et.al.</i> , <u>The Development of an Electrostatic Charged – Particle orbit Recycling System</u> , Australian IOP Congress, Proceedings, 50 , WC0328, (2006), Editor(s): R Sang and J Dobson, Griffith University, Australian IOP, ISBN 0-9598064-7-4	Published

Chapter 5	D.R. Tessier <i>et.al.</i> , Passive Electrostatic Recycling Spectrometer of Desk-Top Size for Charged Particles of Low Kinetic Energy, <i>Phys Rev Lett</i> , 99 , 253201, (2007)	Published
-----------	---	-----------

I declare that, to the best of my knowledge, my thesis does not infringe upon anyone's copyright nor violate any proprietary rights and that any ideas, techniques, quotations, or any other material from the work of other people included in my thesis, published or otherwise, are fully acknowledged in accordance with the standard referencing practices. Furthermore, to the extent that I have included copyrighted material that surpasses the bounds of fair dealing within the meaning of the Canada Copyright Act, I certify that I have obtained a written permission from the copyright owner(s) to include such material(s) in my thesis.

I declare that this is a true copy of my thesis, including any final revisions, as approved by my thesis committee and the Graduate Studies office, and that this thesis has not been submitted for a higher degree to any other University of Institution.

ABSTRACT

A cyclical electrostatic device, referred to as an *Electron Recycling Spectrometer* (ERS) for charged particles is described and demonstrated. The system has been developed with storing electrons with typical kinetic energies of tens of eV. The orbital path for the electrons is 0.65 m long and defined through the application of design voltages to two series of cylindrical lenses inserted between two identical hemispherical deflector analyzers. The ERS design concept exploits the very low scattering cross sections in electron-molecule collisions, where the majority of electrons do not interact with the target. Unscattered electrons are collected and passed back through the ERS for another collision opportunity in the interaction region.

The design of the charged particle optics and the basic operating characteristics of the storage ring are discussed. An overall transfer matrix is formed for the ERS by individual transfer matrices of charged particle optics. The conditions of stability within the ERS are extracted from the fundamental inequality involving the trace of the total transfer matrix. The stability lies within a region in a resonant-like pattern, defined by the focal lengths of the electrostatic lenses.

Electron orbit spectra are displayed for a number of ERS operating conditions. Exponential decay rates, average orbit time, and mean electron energy are presented for each spectrum. Analysis was performed by fitting each orbit or "peak distribution" with a Gaussian curve. The noble gases helium and argon were used as the scattering target for electron detection. Ionization spectra provide long term storage times, as an electron beam must be present in the system to produce an ion species. The optimal ion storage exponential decay lifetime achieved is $\sim 55 \mu\text{s}$, which is target gas pressure limited and corresponds to ~ 200 orbits of the 0.65 m orbital circumference for a drop in particle yield of e^* . Studies of beam dynamics were performed, analyzing the width evolution of each peak as a function of orbit number. Separate modes were observed that are non-linear with respect to the orbit number.

* i.e. the base of the natural logarithm

ACKNOWLEDGEMENTS

I would like to thank Dr. Timothy J. Broderick for his supervision and support of this thesis. I would also like to thank Dr. Peter Hammond for his guidance and support of my work throughout my time on this project. In addition, I would like to thank Dr. Peter Hammond for his comments and suggestions regarding the development of the thesis. I would also like to express my thanks towards Dr. Hammond's mother, Dr. Mary Ann A. Alderson for their contributions. I would also like to thank Dr. Peter Hammond for his contribution to the matrix modeling of the optical system and his contribution to the design of the optical system in general.

I would also like to express my sincere gratitude to Dr. Peter Hammond for his contribution to my classification from the M.S. to the Ph.D.

I hereby dedicate this thesis to
my parents and whole Tessier and Broderick families

ACKNOWLEDGEMENTS

I am most grateful to Dr. Timothy J. Reddish for his supervision and support of this project, and for his scrutiny of this thesis. I would also like to thank Dr. Peter Hammond for his support and guidance of my work throughout my time on this project. In addition, Dr. Hammond's invaluable comments and suggestions toward the development of the storage ring. I would also like to express my thanks towards Dr. Hammond's students Dr. Benjamin G. Birdsey and Aaron A. Aldermen for their contributions. I greatly appreciate Dr. Frank H. Read, for not only his contribution to the matrix modeling of the storage ring, but also his invaluable contribution to electron optics in general.

I would like to take this opportunity to express my sincere gratitude to Drs. Reddish and Hammond for their recommendation for my reclassification from the MSc. to the PhD program.

Special thanks to Dr. Dominic Seccombe for his work on the storage ring in addition to his training and general laboratory techniques that he imparted on me. In addition to Ying "Mike" Niu who overlapped a year with me during his masters work on the storage ring, including initial assembly and electrical wiring, with modeling and construction of electron gun. I would also like to recognize all the undergraduate students that spent time in my lab during my graduate studies and provided me with assistance during their stay. In particular I would like to thank: Daniel Trojand, Michael Sullivan, Theresa Spanjers, Violeta Piasecka, and Brandon Disher.

I would like to thank Sabrina Ludmann for her translation of articles written in German to English. I would also like to thank Natalie Crumb for proof reading this manuscript and correcting Grammar and Spelling. Special thanks to Mr. Sinisa Jezdic for designing the necessary electronic instruments and advice on all electronic devices that were designed and build by the author. A special thanks to Mr. Louis Beaudry and Mr. Eric Clausen for all their work on the construction of elements and maintenance of vacuum pieces for the storage ring.

I would also like to extend my personal gratitude toward Arathi Padmanabhan and all my fellow graduate students and post-doctoral fellows of the physics department for their support and engaging conversation during my stay at the University of Windsor. I would also like to thank all my friends and family for moral support and encouragement throughout my eight years at the University of Windsor.

I would also like to recognize the copyrighted software used throughout this thesis. Namely, Microsoft Office for the generation of the thesis, and Mathcad as part of Mathsoft® to use for the analysis of the data presented in Chapters 4, 5, and 6 of this thesis.

1.1	TRAPPING	3
1.1.1	The Linear Paul Trap	3
1.1.2	The Linear Paul Trap	4
1.1.3	The Penning Trap	7
1.1.4	Linear Electrostatic Trap	9
1.1.5	Normal Particle Trap	11
1.2	POSITION ACCUMULATOR	13
1.3	STORAGE RINGS	15
1.3.1	The Ion Storage Ring (Paul Trap Design)	15
1.3.2	Synchrotron Ring	17
1.3.3	Microtron Rings	18
1.3.4	Storage Ring	19
1.4	ELISA	20
1.4.1	Pin	21
1.4.2	Device	22
1.5	SUMMARY	23
1.6	REFERENCES	24
2	OPTICAL - ELECTRON STORAGE FOR RACE TRACK	26
2.1	INTRODUCTION TO ELECTRON OPTICS	27
2.1.1	Paraxial Lenses and Focusing Conditions	28
2.1.2	Helmholtz - Lagrange Relation	33

TABLE OF CONTENTS

DECLARATION OF CO-AUTHORSHIP/ PREVIOUS PUBLICATION	iii
ABSTRACT	v
DEDICATION	vi
ACKNOWLEDGEMENTS	vii
LIST OF TABLES	xiii
LIST OF FIGURES	xiv
I. INTRODUCTION	1
1.1 AN OVERVIEW OF CHARGED PARTICLE TRAPS AND STORAGE RINGS	2
1.2 TRAPPING	3
1.2.1. The Localized Paul Trap	3
1.2.2. The Linear Paul Trap	4
1.2.3. The Penning Trap	7
1.2.4. Linear Electrostatic Trap	9
1.2.5. Neutral Particle Trap	11
1.3 POSITRON ACCUMULATOR	13
1.4 STORAGE RINGS	15
1.4.1. The Ion Storage Ring (Paul Trap Design)	15
1.4.2. Synchrotron Ring	17
1.4.3. Electrostatic Rings:	18
i. Brookhaven Storage Ring	19
ii. ELISA	20
iii. Flair	21
iv. Desiree	22
1.5 SUMMARY	23
REFERENCES	24
II. THEORETICAL – ELECTRON STORAGE FOR RACETRACK GEOMETRY	26
2.1 INTRODUCTION TO ELECTRON OPTICS	27
2.1.1 Electrostatic Lenses and Focusing Conditions	28
2.1.2 Helmholtz – Lagrange Relation	33

2.1.3 Hemispherical Deflector Analyzer (HDA)	34
2.2 THE TRANSFER MATRIX	36
2.2.1 Background	37
2.2.2 The Electron Recycling System (ERS)	39
2.3 STABILITY	41
2.3.1 Phase Space	42
2.3.2 Constraints Imposed on the Transfer Matrix	44
i. Unity Matrix	45
ii. Deviations from Unity Matrix	47
iii. Generalized Expression	49
iv. Asymmetric Lens Setup	53
v. Aberrations	57
2.3.3 Stability Modeling	59
4. SUMMARY	60
REFERENCES	61
III. EXPERIMENTAL I – SYSTEM DESIGN	63
3.1 THE ELECTRON RECYCLING SYSTEM	64
3.1.1 Overview	64
3.1.2 Cylindrical Lens	72
3.1.3 Vacuum Chamber	73
3.2 ELECTRON GUN	74
3.2.1 Gun Design	74
3.2.2 Pulsing Circuit	81
3.3 VOLTAGE POWER SUPPLY SCHEMATIC	85
3.4 SUMMARY	86
REFERENCES	87
IV. EXPERIMENTAL II – ELECTRON BEAM INJECTION	88
4.1 FIRST ATTEMPTS AT ELECTRON INJECTION AND STORAGE	89
4.1.1 Introduction	89
4.1.2 Scattering off Argon Gas	91

4.2 STORAGE ACHIEVED	94
4.2.1 Scattering off tungsten ring	95
4.2.2 Results: tungsten ring injection	101
i. Preliminary data	102
ii. Optimized data	104
4.3 GUN POSITIONED ON HDA	106
4.4 PULSING SCHEMES	110
4.5 SUMMARY	114
REFERENCES	115
V. RESULTS AND DISCUSSION – GUN POSITIONED ON HDA	116
5.1 SYMMETRIC SETUP	117
5.1.1 Introduction	117
5.1.2 Data of (15 15) Pass Energy Setup	119
5.1.3 Bunch Analysis	120
5.2 ASYMMETRIC SETUP	124
5.2.1 Introduction	124
5.2.2 Metastable Background	125
5.2.3 (4 18) Pass Energy	126
5.2.4 (4 15) Pass Energy	128
5.2.5 (7 15) Pass Energy	130
5.2.6 (9 18) Pass Energy	132
5.2.7 Comparison: Asymmetric Pass Energies	134
5.3 IONIZATION STUDIES	135
5.4 SUMMARY	138
REFERENCES	141
VI. ANOMALOUS BEHAVIOUR	142
6.1 NON – COHERENT EVALUATION	143
6.1.1 Preliminary Results	144
6.1.2 Peak Width Saturation for Symmetric Pass Energy	146

6.1.3	Peak Width Saturation for Asymmetric Pass Energy	148
6.1.4	Peak Width Saturation at Slightly Asymmetric Pass Energy	149
6.1.5	Summary	151
6.2	OSCILLATIONS ABOUT OPTIC AXIS	151
6.2.1	Symmetric Pass Energy	152
6.2.2	Asymmetric Pass Energy	153
6.2.3	Small Oscillations	155
6.3	SUMMARY	156
	REFERENCES	158
VII.	CONCLUSION	159
	APPENDICES	
1-A	M_{st} Matrix for Symmetric Setup	163
1-B	Eigenvalues of M_{st}	164
1-C	Solving M_{ST} for $M_{SS} = -I$	166
1-D	Components of M_{SS} (non - unity case)	167
1-E	Solving M_{st} (Asymmetric Setup)	169
2.	Photographs	171
3.	Gun Pulse Shapes	175
4.	Hemisphere Pulse Shapes	176
5.	Typical Voltages	177
6.	Additional Spectra	178
	VITA AUCTORIS	181
	PERMISSION OF REPRINT	182
	PUBLICATIONS	183

LIST OF FIGURES

	Page
1.1 Paul trap	4
1.2 Linear Paul trap	5
1.3 Penning trap	7
1.4 Penning trap with split ring electrodes	8
1.5 Penning trap with laser cooling, and utilizing both E and B fields	9
1.6 Linear electrostatic trap (Zajfman's group)	10
1.7 Sextupole field from hyperbolic magnets	12
1.8 Trajectory focusing in a sextupole field	13
1.9 Penning – Malmberg trap	13
1.10 Penning – Malmberg Trap with buffer gas cooling	14
1.11 Paul Type Racetrack Storage Ring	16
1.12 Synchrotron storage ring	18
1.13 ELISA storage ring	20
1.14 FLAIR storage ring	21
1.15 DESIREE	22
2.1 Basic schematic of Electron Recycling System (ERS)	27
2.2 Collimation	29
2.3 Thin lens	29
2.4 Thick lens	30
2.5 Triple Cylindrical Lens	32
2.6 Dispersion within an 180° electrostatic hemispherical deflector analyzer	35
2.7 Ray trace within a field free region	38
2.8 Phase Space ellipse	43
2.9 Schematic diagram of thick lens	46
2.10 Stability graphs	52
2.11 Computer simulation of electron trajectories within ERS	55
2.12 CPO3D computer simulation of electron beam cross sections within the ERS	60
3.1 Schematic of ERS	65

3.2	Schematic of source stack	65
3.3	Schematic of interaction stack	65
3.4	Channeltron Detector	67
3.5	Detailed schematic of ERS	69
3.6	Dimensions of inner and outer hemisphere	71
3.7	Dimensions of a lens for the ERS	72
3.8	Cylindrical lens showing ERS parameters	72
3.9	Deflector system	75
3.10	Deflector elements with dimensions	76
3.11	Deflector system	77
3.12	Schematic of grid and filament support system	77
3.13	Aperture dimensions of electron gun	78
3.14	The emission region of a filament tip	78
3.15	The accelerating region	79
3.16	Modified gun schematic	79
3.17	Filament cradle and grid dimensions	80
3.18	Electron Gun dimensions	80
3.19	Support base for aperture lens	80
3.20	Electron Gun Pulsing Circuit Schematic	82
3.21	Driving Pulse for Electron Filament	83
3.22	Fall-time of electron driving pulse	83
3.23	Pulse output with capacitor	84
3.24	Power supply circuit for the ERS storage ring	85
4.1	Venn diagram of phase space parameters	89
4.2	Differential Cross Section for electron - argon scattering	91
4.3	Energy distribution of electrons excited by electrons of copper	96
4.4	Secondary Electron Distribution for Inelastic scattered electrons	96
4.5	Injection schematic for wire ring setup	97
4.6	Pulsing sequence for filament contact potential and source region	98
4.7	Computer modeling of source region including field lines and electron trajectories	99

4.8	Effect of the Target wire on a parallel beam	99
4.9	Data of early wire ring setup	102
4.10	Data acquisition setup	103
4.11	Electron peak spectrum for preliminary data for wire ring setup	103
4.12	Linear plot of the data of figure 4.11	104
4.13	Electron peak spectrum for optimized data for wire ring setup	105
4.14	Linear plot of the data of figure 4.13	105
4.15	Peak width evolution of the data for the data of figure 4.13	106
4.16	Logarithmic plots of the peak height and area variation for the data of figure 4.13	106
4.17	General Schematic of an Operational amplifier	107
4.18	Schematic of updated ERS storage ring	108
4.19	Electrical schematic for the gun elements	109
4.20	Describing the energy of the electrons according to the effects of all the floating points	109
4.21	An analogue of the pulse ramp as a series of narrow – energy steps	112
4.22	Power supply layout for the first trial of optimizing injection	112
4.23	Selection points on the filament driving pulse for the energy of the stored electrons	112
4.24	Point matching of filament and hemisphere pulse, second trial of optimizing injection	113
5.1	Basic Schematic of ERS	118
5.2	Data of electron signal collected at the interaction region for a setup of 15.0 eV pass energy and 15.0 eV ERS energy	119
5.3	Linear plot of the data of figure 5.2	119
5.4	Variation in peak height and peak area for the data of figure 5.2	120
5.5	Beam width variation as a function of orbit number for the linear electrostatic trap	121
5.6	Peak width variation for the data of figure 5.2	123
5.7	Example, production of a metastable state	125
5.8	Logarithmic plot of an electron beam that has traveled three quarters around the ring followed by a metastable peak	126
5.9	Data of electron signal collected at the interaction region for a setup of 4 eV Top HDA and 18 eV bottom HDA pass energy, for an ERS energy	127

	of 40.0 eV	148
5.10	Linear plot of the data of figure 5.9	127
5.11	Variation in peak width for the data of figure 5.9	128
5.12	Data of electron signal collected at the interaction region for a setup of 4 eV Top HDA and 15.0 eV bottom HDA pass energy, for an ERS energy of 22.0 eV	128
5.13	Linear plot of the data of figure 5.12	129
5.14	Variation in peak width for the data of figure 5.12	129
5.15	Logarithmic plot of electron signal collected at the interaction region for a setup of 7 eV Top HDA and 15.0 eV bottom HDA pass energy, for an ERS energy of 25.0 eV	130
5.16	Linear plot of the data of figure 5.15	130
5.17	Peak width variation for the data of figure 5.15	131
5.18	Data of electron signal collected at the interaction region for a setup of 9 eV Top HDA and 18.0 eV bottom HDA pass energy, for an ERS energy of 50.0 eV	132
5.19	Linear plot of the data of figure 5.18	132
5.20	Peak width variation for the data of figure 5.18	133
5.21	Helium ionization spectra taken within the ERS operating in the recycling and non-recycling modes	135
5.22	Helium ion time-of-flight distributions	136
5.23	Plot of lifetimes as a function of pressure	137
6.1	Peak width spectra with the linear electrostatic trap by Zajfman's group	143
6.2	Peak width saturation with the linear electrostatic trap by Zajfman's group	144
6.3	Data of electron signal collected at the interaction region for a setup of 12.0 eV pass energy and 30.0 eV ERS energy, for preliminary results within the exotic features section	145
6.4	Linear plot of the data of figure 6.3	145
6.5	Electron peak spectrum, for the ERS operating in peak width saturation mode	146
6.6	Linear plot of the data of figure 6.5	146
6.7	Peak width variation of the data of figure 6.5	147
6.8	Data of electron signal collected at the interaction region for a setup of 9 eV Top HDA and 15.0 eV bottom HDA pass energy, for an ERS energy of 22.0 eV, for the ERS operating in peak width saturation mode	148

6.9	Linear plot of the data of figure 6.8	148
6.10	Peak width variation of the data of figure 6.8	149
6.11	Data of electron signal collected at the interaction region for a setup of 12 eV Top HDA and 15 eV bottom HDA pass energy, for an ERS energy of 30.0 eV, for the ERS operating in peak width saturation mode	150
6.12	Peak width variation of the data of figure 6.11	150
6.13	Data of electron signal collected at the interaction region for a setup of 15 eV Top HDA and 15 eV bottom HDA pass energy, for an ERS energy of 15.0 eV, for the ERS operating in 'oscillation about the optic axis mode'	152
6.14	The variation in the peak height for the data of figure 6.13	152
6.15	Linear plot of the data of figure 6.13	153
6.16	Data of electron signal collected at the interaction region for a setup of 8 eV Top HDA and 15 eV bottom HDA pass energy, for an ERS energy of 30.0 eV, for the ERS operating in 'oscillation about the optic axis mode'	153
6.17	Linear plot of the data of figure 6.16	154
6.18	Peak height variation of the data of figure 6.16	154
6.19	Data of electron signal collected at the interaction region for a setup of 18 eV Top HDA and 18.0 eV bottom HDA pass energy, for an ERS energy of 36.0 eV, for the ERS operating in 'oscillation about the optic axis mode'	155
6.20	Linear plot of the data of figure 6.19	155
6.21	Peak height variation of the data of figure 6.19	156
6.22	Peak area variation of the data of figure 6.19	156

CHAPTER 1: INTRODUCTION PARTICLE TRAPS AND STORAGE RINGS

1.1 AN OVERVIEW OF CHARGED PARTICLE TRAPS AND STORAGE RINGS	2
1.2 TRAPPING	3
1.2.1 The Localized Paul Trap	3
1.2.2 The Linear Paul Trap	4
1.2.3 The Penning Trap	7
1.2.4 Linear Electrostatic Trap	9
1.2.5 Neutral Particle Trap	11
1.3 POSITRON ACCUMULATOR	13
1.4 STORAGE RINGS	14
1.4.1 The Ion Storage Ring (Paul Trap Design)	15
1.4.2 Synchrotron Rings	17
1.4.3 Electrostatic Rings:	18
i. <u>Brookhaven Storage Ring</u>	19
ii. <u>ELISA</u>	19
iii. <u>Flair</u>	20
iv. <u>Desiree</u>	21
1.5 SUMMARY	22
REFERENCES	23

1.1 AN OVERVIEW OF CHARGED PARTICLE TRAPS AND STORAGE RINGS

A variety of instruments and methods have been developed over the last 50 to 60 years that are designed to trap and confine charged particles. An overview of these methods is presented in the chapter and will give the reader an appreciation of the types of rings and applied electric and magnetic fields used to store charged particles (or neutral particles in special traps). Storage of charged particles can be static or dynamic. In the static sense, the conglomerate will be centered at a point within the trap, whereas dynamic traps confine the particles in one or two dimensions while propagating along a single axis. The methods and practices presented here place this thesis in a historical context.

Storage and confinement experiments occur in the form of ion and atom traps, neutral polarized particle traps, magnetic storage rings, and electrostatic storage rings. The instruments in point can have the following effects on the particles: improve precision of knowing the particle's position and energy, or select its quantum state. A particle or beam that is confined will be labeled by a set of parameters i.e. $x \pm \delta x$, $p \pm \delta p$, $E \pm \delta E$ (position, momentum, and energy). The magnitude of δ is proportional to the uncertainty in the measurement, which is determined by the type and quality of the operations listed above. Thus, optimal confinement will minimize the uncertainty δ , and produce highly precise results in any particle collision or irradiation experiment (either trapping or stored orbits).

A static or "point trap" is designed to "hold" a number of charged particles (for example: Cs^+ , Ba^+ , In^+) in a region of typical size ~ 0.10 to 0.5 mm. Trapped ions are held at very low temperatures making an ideal target for collision studies (since they are relatively stationary and in a discernable quantum state). The traditional Paul and Penning trap (which will be the focus of the next two sections) center the trapped ions on a single position. The Paul trap design has been expanded to a dynamic sense to trap charged particles on an axis, while maintaining the same electric field arrangement. These axial traps are commonly referred to as linear traps and can be bent into a closed ring

formation. Moving from the static trap concept, accelerating and non-accelerating rings will send charged particles circulating a closed ring, and in some applications improve the energy resolution within the ring. Generally, charged particle rings store projectile charged particles to be aimed at a target, rather than the static trapping setup, where the target was held and a projectile beam was directed at it. Storing within a static trap allows for experiments of a different nature to be performed due to the low temperature and high density of the target. The chapter will conclude with the presentation of electrostatic charged particle storage rings due to its relevance to this thesis.

1.2 TRAPPING

The general form of Laplace's equation in free space is given in equation 1.1 [Jackson (1998)]:

$$\frac{\partial^2 \Phi}{\partial x^2} + \frac{\partial^2 \Phi}{\partial y^2} + \frac{\partial^2 \Phi}{\partial z^2} = 0. \quad (1.1)$$

A static electric field $\mathbf{E}(x, t) = \mathbf{E}(x)$ satisfies the Laplace equation. However, there are no maxima or minima, and therefore the \mathbf{E} field cannot contain charged particles within a fixed region. The problem of trapping was circumvented by the Paul and Penning trap designs. Wolfgang Paul created a trap by using both DC and AC electric fields.* On the other hand, the Penning model traps ions through a DC electric field with the addition of a static magnetic field \mathbf{B} [Paul (1990)].

1.2.1 The Localized Paul Trap

Suppose a system was set up with hyperbolic electrodes (as in figure 1.1), carrying an electric potential to generate an electric field \mathbf{E} . A time-invariant potential will give only unstable solutions (for example, an oscillation in one dimension and exponential escape in another). The general equation of motion is: $\ddot{x} \pm Ax = B$ (where A and B are constants, and B can be null). The general solution depends heavily on the \pm in the Ax term. Thus,

* DC are static fields with no time dependence, and AC fields contain a time dependence

by adding a time dependent term into the potential Φ will cause periodic focusing and present a stable setup [Paul (1990), Jefferts *et.al.* (1995)]. The applied potential now takes on the form of equation 1.2:

$$\Phi_0 = U - V \cos \omega t . \quad (1.2)$$

(see Paul (1990) for details). The particles are then confined in 3 or 2 dimensions depending on the setups given in the figure below. The picture on the left corresponds to the setup for trapping of charged particles centered at a point. The notion is also extended to confining particles in 2 dimensions[†] in the diagram on the right (being x and z in this case), leaving the y component free to oscillate.

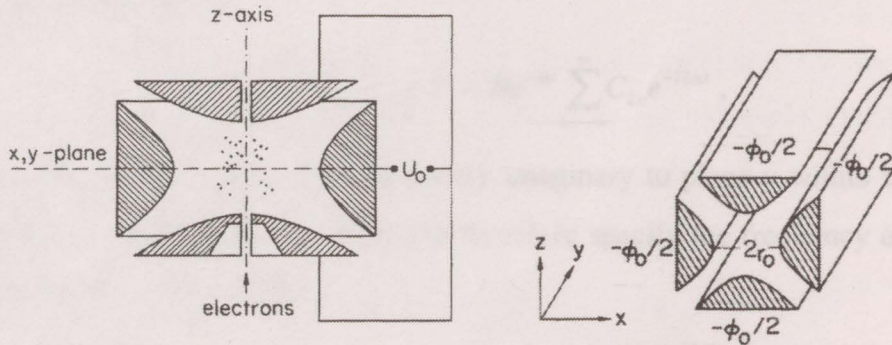


Figure 1.1: Schematic diagram showing the hyperbolic electrodes of the Paul Trap.

1.2.2 The Linear Paul Trap

An extension to the previous section is the linear Paul trap, which stores ions in a dynamic manner corresponding to the right picture in figure 1.1. Discussed below is an alteration in setup with identical physical concepts. In general, the equations of motion are:

$$\frac{d^2u}{d\tau^2} + (a_u - 2q_u \cos 2\tau)u = 0 \quad (1.3)$$

(which is of the form of Mathieu's Equation, and keeping the notation of that given in the setup of figure 1.1, $u = x, z$ leaving the storage axis as y). The solutions to Mathieu's

[†] which is stable, provided the charged particle beam is not injected on the y - axis

Equation give both a stable and unstable solution depending on the parameters a_u and q_u [Whittaker and Watson (2002)]. The equations of motion are parameterized by:

$$a_u = \frac{4eU}{mr_0^2\omega^2}, \quad q_u = \frac{2eV}{mr_0^2\omega^2}, \quad \tau = \frac{\omega t}{2}, \quad (1.4)$$

where r_0 is the distance from the hyperbolic electrode to the center of the trap. The stability conditions are dependant on the DC voltage U , the AC amplitude V , and the driving frequency ω . A stable trap can be set up by specifying the system to lie within the first region of stability: $0 < a_u, q_u < 1$ [Paul (1990), Whittaker and Watson (2002), Abramowitz and Stegun (1972)]. In general, the solutions to the Mathieu's Equation are a series solution of the form:

$$u = Ae^{\mu x} \sum_{n=-\infty}^{\infty} C_{2n} e^{i2nx} + Be^{-\mu x} \sum_{n=-\infty}^{\infty} C_{2n} e^{-i2nx}, \quad (1.5)$$

where it has been found that μ must be purely imaginary to place u within the stability region [Wukeker (1959)]. The solution will therefore specify the frequency ω to trap an ion of given e/m in a stable region.

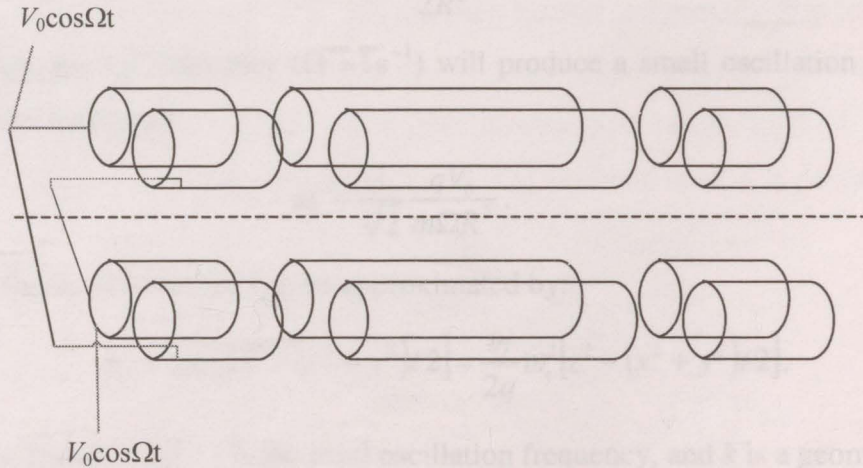


Figure 1.2: A side view of the linear Paul Trap, displaying cylindrical electrodes with time dependent and independent (not shown) voltages, dashed line represents storage axis [Paul (1990), Raizen (1992)].

An alternative design to figure 1.1 is the quadrupole linear trap, whereby the electrodes are arranged in a quadrupole manner and are laid out physically parallel to the trapping axis, with the addition of straight sections placed between the two endcap regions (see figure 1.2). The electrodes have the same function as above, i.e. preventing the escape of

the charged particles in the y direction (keeping in practice to the labeling of figure 1.1). The AC component of the potential is commonly radiofrequency (RF), which is transverse to the entire storage axis and gives the radial confinement. A static potential U is added to the end electrodes to hold the trapped beam over the axial range of y meters. However, there is an increase in the loss of the charged particles in this setup due to dispersion in the beam as it oscillates over the axis that guides some of the particles out of the storage region. This style of trapping provides a longer interaction region with a sacrifice in trap lifetime. To elaborate, the linear trap lifetime is a few seconds, whereas the Paul Trap may be a few hundred seconds [Thompson, Harmon and Ball (2002)].

The group of Raizens [Raizens *et.al.* (1992)] give an expression for the fields and frequencies of the particles within the trap seen in figure 1.2. The total electric potential (DC plus AC) can be rewritten as $\phi = U_0 - V_0 \cos \omega t$. The near axis AC potential component is approximated by:

$$V_{AC} = \frac{V_0(x^2 - y^2)}{2R^2} \cos \Omega t, \quad (1.6)$$

where a high driving frequency ($\Omega \gg 1 \text{ s}^{-1}$) will produce a small oscillation in the radial direction with frequency:

$$\omega_r = \frac{1}{\sqrt{2}} \frac{qV_0}{m\Omega R^2}. \quad (1.7)$$

Moreover, the static potential can be approximated by:

$$\phi_{DC} = kU_0[z^2 - (x^2 + y^2)/2] = \frac{m}{2q} \omega_z^2 [z^2 - (x^2 + y^2)/2], \quad (1.8)$$

where $\omega_z (= (2kqU_0/m)^{1/2})$ is the axial oscillation frequency, and k is a geometric factor.

As seen in equation 1.8 the fields are mass and charge dependant. The length of the rods can be extended to ~ 6 m to provide a long drift region that allows for time-of-flight measurements. In this configuration one can scan through the voltages U_0 and V_0 to make the trap function as a mass spectrometer [Paul (1990)].

1.2.3 The Penning Trap

Similar to the Paul Trap design with respect to the physical geometric setup of the apparatus, the Penning trap stores the charged particles in the center of two pairs of endcaps, as in figure 1.3. Incidentally, the electrodes are usually hyperbolic, although an extension can be made to a linear cylindrical containment region, similarly done in the linear Paul trap, without causing any considerable limitations to storage. The Penning trap chronologically precedes the Paul trap, which is expected, since the Penning trap contains less complex design features. To elaborate, the design includes a planar electric field that will confine the trapped particles in two dimensions (x and y by convention), leaving the third dimension (labeled z by convention) open which cannot be closed with an static electric field as indicated by the Laplace equation [equation 1.1] and as stated above under the general discussion for trapping. For trapping to occur, the z direction must be closed by some external force. In the field of electrodynamics, once the notion of a static electric field has been eliminated as an option, the next economical choice is a static magnetic field (Wolfgang Paul took this one step further and successfully implemented a time – dependant electric field in place of the static magnetic field) [Paul (1990), Rich and Wesley (1972)]. The presence of both electric and magnetic field, results in a spiraling motion on any charged particle that tries to extricate itself away from the center.

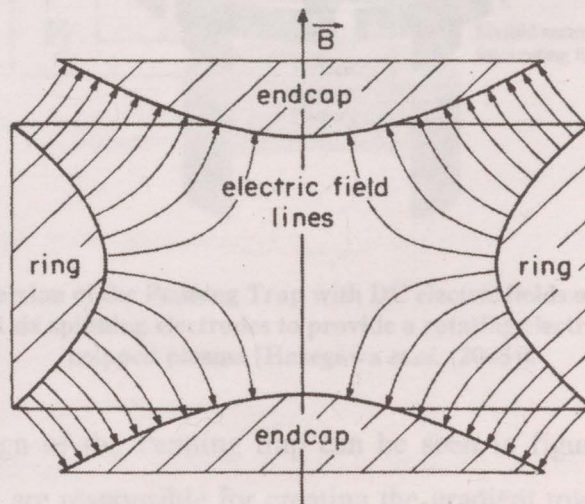


Figure 1.3: Schematic diagram displaying the Penning trap with two pairs of endcaps with the magnetic field directed top to bottom (typically produced by a pair of toroidal magnets) [Brown and Gabrielse (1986)].

Since the particles are moving with some finite (small) velocities they will precess within the $x - y$ plane at a cyclotron frequency given by:

$$v_c = \frac{qB}{m}, \quad (1.9)$$

and will oscillate in the z axis at the axial frequency:

$$v_z = \left(\frac{2qU_0}{mR_0^2} \right)^{1/2}, \quad (1.10)$$

where U_0 is the applied voltage (i.e. $\phi = U_0$). The center of the ion bunch rotates about the trap axis at a magnetron frequency of:

$$v_m = \frac{1}{2}v_c - \left(\frac{1}{4}v_c^2 - \frac{1}{2}v_z^2 \right)^{1/2}. \quad (1.11)$$

The magnetron motion is ultimately the trapping process, as it confines the charged particles to the center of the trap oscillating indefinitely [Brown and Gabrielse (1986)].

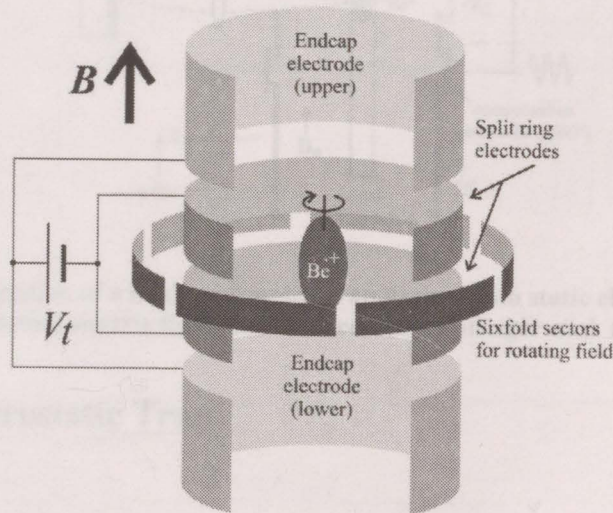


Figure 1.4: A modern version of the Penning Trap with DC electric fields on the inner electrodes, an axial magnetic field, and six spinning electrodes to provide a rotating electric field that influences the trapped plasma [Hasegawa *et.al.* (2005)].

A more modern design of the Penning trap can be seen in figures 1.4 and 1.5, which display the fields that are responsible for creating the gradient toward the center. Figure 1.4 shows an example of the Penning trap used to confine a plasma cloud, whereby the trapping fields remain as the static electric and magnetic field. The addition of the rotating electric field is to influence and help control the rotational rate of the plasma,

which will affect its shape and density [Hasegawa *et.al.* (2005)]. The presence of the laser in the next figure (figure 1.5) has the purpose of ‘cooling’ the ionic cluster (which is the process of reducing the kinetic energies of the individual particles, and hence lowering the effective temperature of the ion cloud). The cluster is free to rotate about the z axis; the rotational freedom that can lead to particle escape is controlled by the rotating electric field [Bollinger *et.al.* (2000)].

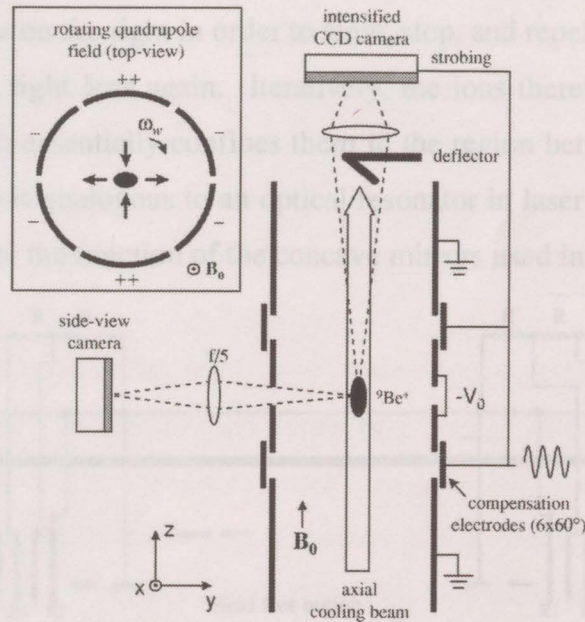


Figure 1.5: A representation of a modern Penning trap design, with static electric field, magnetic field, rotating electric field, and laser cooling [Bollinger *et.al.* (2000)].

1.2.4 Linear Electrostatic Trap

The linear electrostatic trap developed by Zajfman’s group [Pedersen *et.al.* (2001), Zajfman *et.al.* (1997), and Zajfman *et.al.* (2004)] is a modern instrument to contain ions dynamically within a desktop sized apparatus. Making use of electrostatic elements only, ions are contained on a linear storage axis between two multi-element lenses. The lens setup on the right (of figure 1.6) is held at fixed potentials; however they can be made to vary in order to optimize the storage efficiency of the trap.

The lens on the left in figure 1.6 will begin with grounded electrodes to allow for ion injection. Following injection, an electric switch that is connected to the lens elements changes the grounding to the elements to the applied voltages $\{V_s, Z_1\}$ that are identical to the right lens. Once the ions have entered through the left lens (grounded and field free) they continue to the right and get decelerated by the right lens, stop and get repelled in the opposite direction to which they entered. During the previous stage, the electric switch has been activated to change the voltages on the left lens from ground, such that they are set up equal to the lens on the right in order to slow, stop, and repel the ions back again on a heading toward the right lens again. Iteratively, the ions therefore ‘bounce’ from the right to the left, which essentially confines them in the region between the two lenses or “mirrors”. This setup is analogous to an optical resonator in laser optics, where the right and left lenses simulate the function of the concave mirrors used in those applications.

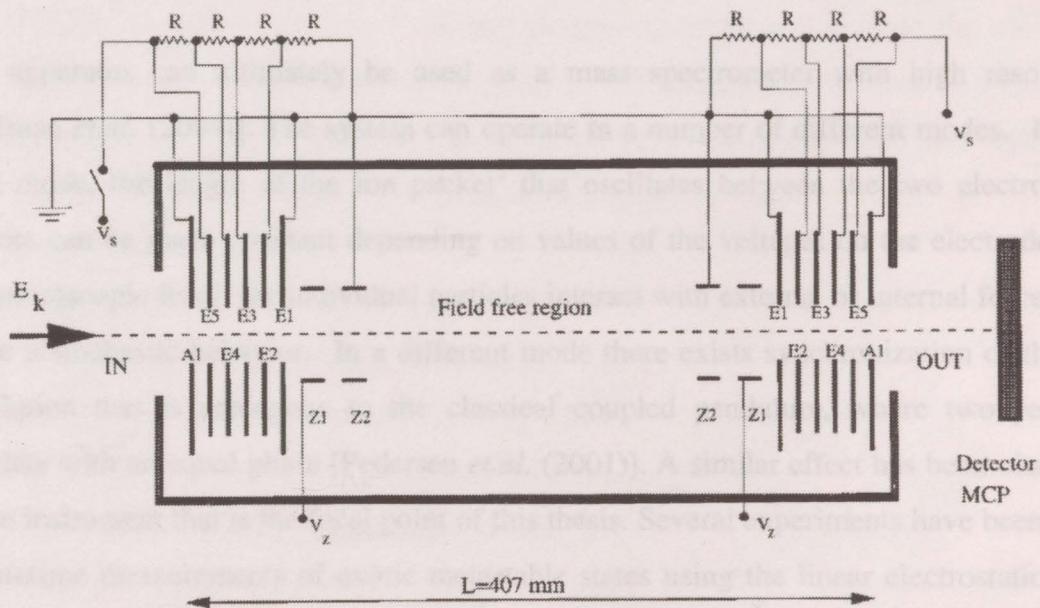


Figure 1.6: Diagram of the Zajfman ion trap. The ion beam is injected from the left, (the entrance electrodes are pulsed to ground). The other electrodes are used for focusing, slowing, and repelling the ions. Neutral particles are formed by electron capture of the ions, which escape the trap and are monitored by a microchannel plate detector downstream [Zajfman *et.al.* (1997)].

The ion source (not shown in the diagram) is produced by ionizing a gas, which is then accelerated and focused into a mass spectrometer, whereby an ion of a given charge to mass ratio is selected and then further accelerated and collimated before entering the

system. Following collimation, the ion beam is directed into the trap through the back of the lens element (left, in the figure).

Each lens consists of five cylindrical elements that are labeled E1 to E5 in the figure. In addition, a grounded lens element, A1, is placed at the end of the train and two electrodes (labeled Z1 and Z2) are placed at the entrance of the lens. The lens functions as both a barrier and a focusing element. Therefore, the electrode E5 is set to energy eV_s greater than that of the ion kinetic energy E_k . The elements E2 to E4 are voltage divided to set up the appropriate voltage ratios in order to focus the beam. The remaining elements (E1, Z2, and A1) are grounded. This serves as an Einzel lens setup (no net change in velocity) and aids in preventing field penetration into the desired field free regions. Moreover, the Z1 and Z2 elements act as an asymmetric Einzel lens setup (additional focusing).

The apparatus can ultimately be used as a mass spectrometer with high resolution [Zajfman *et.al.* (2004)]. The system can operate in a number of different modes. In one such mode, the length of the ion packet[‡] that oscillates between the two electrostatic mirrors can be made constant depending on values of the voltages on the electrodes. At the microscopic level, the individual particles interact with external or internal forces that cause a stochastic behavior. In a different mode there exists synchronization of the ion oscillation that is analogous to the classical coupled pendulum, where two pendula oscillate with an equal phase [Pedersen *et.al.* (2001)]. A similar effect has been observed in the instrument that is the focal point of this thesis. Several experiments have been done on lifetime measurements of exotic metastable states using the linear electrostatic trap; see for example [Wester *et.al.* (1999), Bhushan *et.al.* (2000), and Naaman *et.al.* (2000)].

1.2.5 The Neutral Particle Trap

Neutral particles encompass any sub-atomic particle, molecule, or conglomerate that has no net charge, i.e. any particle where the Lorentz force is zero in the presence of an electromagnetic field. Confinement of neutral particles can be accomplished within a

[‡] Full width at half maximum of the peak

region, provided that they possess a dipole moment. Moreover, a particle can only be trapped if they can be manipulated by electromagnetic fields. For example, an apparatus that can confine neutrons is referred to as a “Magnetic Bottle,” [Bennewitz and Paul (1954), Bennewitz, Paul and Schlier (1955)] which will be the focus of this sub-section. Suppose a particle with no net charge has a magnetic dipole moment of magnitude μ , then its energy will form a minimum in the presence of a magnetic field \mathbf{B} , given as $U = -\mu B$, where $B = |\mathbf{B}|$. For an inhomogeneous \mathbf{B} field, there will be a consequent force: $\mathbf{F} = \text{grad}(\mu B)$. A particle may therefore follow the gradient into a relatively small confined region, making trapping possible. Since a neutron has two spin states (i.e. up and down), an external magnetic field will cause the neutrons to be oriented either parallel or anti-parallel to the \mathbf{B} field. Whereby, the parallel or anti-parallel result will ultimately be the determining condition to whether the neutron is repelled from the field or attracted into it. The \mathbf{B} field that will satisfy the force and energy equations and provide the necessary gradient to trap neutrons is a sextupole field (A sextupole magnetic field is created by setting up three magnetic north and three magnetic south poles which are alternately arranged around an axis) [Paul (1990), and Suzuki *et.al.* (2003)].

The figure on the right of this paragraph (fig. 1.7) displays an ideal sextupole field. In practice, an experimenter will set up six current carrying wires to act as the \mathbf{B} field producers. Although the field lines are not identical to an arrangement of six hyperbolic magnetic elements than those of the setup for six current carrying wires, it will act as a sextupole lens for a good approximation; this is applied to experiments involving neutrons moving

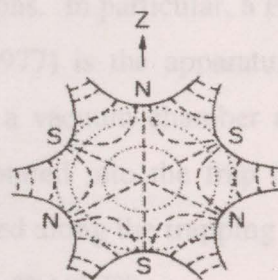
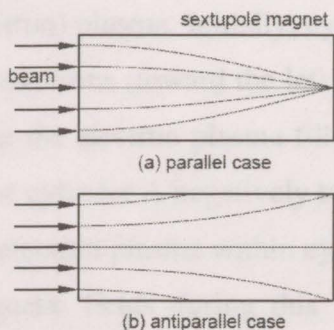


Figure 1.7: Schematic of a sextupole magnetic field produced by six hyperbolic magnets

along the focusing axis (axis coming in or out of the page) [Suzuki *et.al.* (2003)]. In this application, neutrons that are aligned parallel to \mathbf{B} will follow a gradient into the field (the beam will be focused toward the central axis). Alternatively, the anti-parallel aligned neutrons will diverge and leave the field as is displayed in figure 1.8 [Suzuki *et.al.*, (2003)]. The concept of trapping must now be addressed. This is achieved by creating a

closed loop (commonly spherical or toroidal) of the six current carrying wires. Moreover, the particles are driven toward a central axis with a finite momentum (i.e. not zero) component on that axis; hence, once the axis is closed on itself, the neutrons will travel along the axis in a storage ring sense, i.e. the neutrons will move on a circular orbit about



a torus. However, in the magnetic sphere, the neutrons are confined within the center of the sphere (after being laser cooled) while oscillating about the center until they escape the stable oscillating trajectory due to perturbations and collisions with background gasses [Paul (1990)].

Figure 1.8: A simulation showing that neutron trajectories converge or diverge depending on their spin orientation.

1.3 POSITRON ACCUMULATOR

The process of trapping positrons is identical to trapping electrons; thus, electron trapping techniques will be employed to accumulate or “trap” positrons. In particular, a Penning – Malmberg trap discussed in deGrassie and Malmberg (1977) is the apparatus to trap positrons, see figure 1.9. The apparatus is placed within a vacuum chamber at a base pressure[§] of $\sim 10^{-7}$ torr. Cylindrical symmetry is incorporated into the trap design to provide a radial barrier; an axial magnetic field B_0 is applied along the trapping axis of

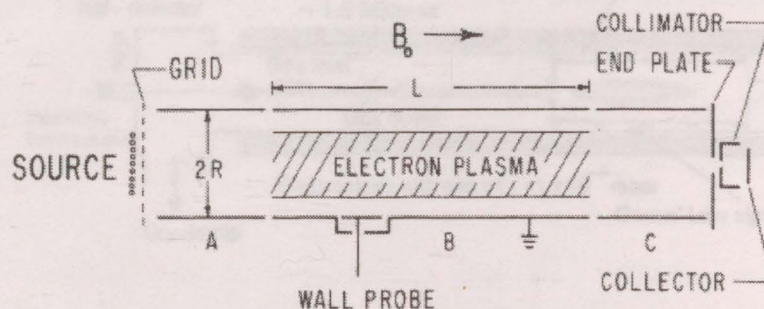


Figure 1.9: A diagram of the Penning – Malmberg Trap, this setup is divided into 3 cylinders A, B (the storage region), and C [deGrassie and Malmberg (1977)]

[§] lowest pressure attainable within the vacuum chamber by the vacuum pumps attached to the system

the cylinder (an example of this would be that of an ideal solenoid in electromagnetism). For example, working from the electron analog, an electron source injects electrons into the entrance of the cylinder as in figure 1.9. The entire cylinder is divided into three sections labeled A, B, and C that are pulsed in three stages to trap the electron (or positron) plasma. Initially, cylinder C is set to a high negative potential in order to reflect the electrons (toward the left in figure 1.9), and cylinder A is grounded. During this first stage the electron plasma fills the region of the cylinders A and B. The next phase is to pulse cylinder A negatively to repel the electrons from the source and simultaneously trap the electron plasma within cylinder B. The electron plasma is confined by the electric and magnetic fields during this “storing” stage. Finally, cylinder C is pulsed to ground, whereby the electron plasma is released and the electrons travel toward the right (in figure 1.9) along the B_0 field lines, and get collimated and exit the system.

Positrons produced by a radioactive source are high in energy, which is in contrast to most electron traps [Schultz and Lynn (1988)]. Several methods are used to collect and slow the positron beam; buffer gas cooling, field ionization**, and laser cooling are some of the popular approaches. The figure below (figure 1.10) displays the general idea of a buffer gas used to capture and cool positrons as an addition to the electron Penning – Malmberg trap explained above [Clarke *et.al.* (2006), Holzscheiter, Charlton and Nieto (2004)].

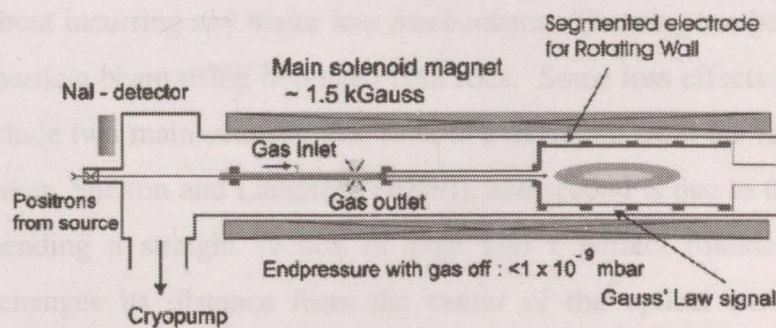


Figure 1.10: An illustration of a modified Penning – Malmberg Trap utilizing buffer gas cooling to slow the high energy plasma [Holzscheiter, Charlton and Nieto (2004)]

** A Rydberg positronium atom is formed, then field ionized, whereby either the electron or positron can be collected depending on the electrode voltages

1.4 STORAGE RINGS

A method to confine charged particles is presented in this section that allows for continuous motion of the particles on a closed path, which is the topic most relevant to this thesis. These closed structures use electric and magnetic fields (not necessarily both) as well as field free regions (usually straight lengths) to guide a myriad of charged particles on a trajectory that has the same beginning and ending. Thus, the charged particles are “stored” within the ring and will execute many of these “orbits” until vanishing within the ring due to unavoidable loss mechanisms. Ignoring perturbations, a storage ring could permit an infinite number of orbits. It is found however, that certain experimental circumstances will truncate the number of orbits to some finite value. Some of the significant effects that limit the number of orbits include: space charge effects, non-uniform electromagnetic fields, gravitational fields, second and higher order aberrations, radiation energy loss, mechanical misalignment, and collisions with residual gas.

1.4.1 The Ion Storage Ring (Paul Trap Design)

In principle, this takes a linear Paul trap and bends it into a closed loop form. The impetus behind the closed loop is to increase the storage lifetime. The traditional Paul Trap was based on charged hyperbolic electrodes, and the linear trap used straight rods as a substitution without incurring any major loss mechanisms. This ring has been designed to trap a charged particle beam using hollowed bent rods. Some loss effects from this style of geometry include two main sources. The first, is a deviation from the ideal hyperbolic geometry [Wuerker, Shelton and Langmuir (1959)], and second is due to the difficulty in mechanically bending a straight section of pipe into a perfect rounded surface. An electrode that changes its distance from the center of the optical axis will cause a variation in the field that is proportional to r_0/r ; thus, the greater the imperfections in the curved sections will ultimately lead to greater losses (where r_0 is the average radius and r is the distance from the optical axis to the electrode) [Church (1969)]. A schematic can be seen in figure 1.11 of an ion storage ring.

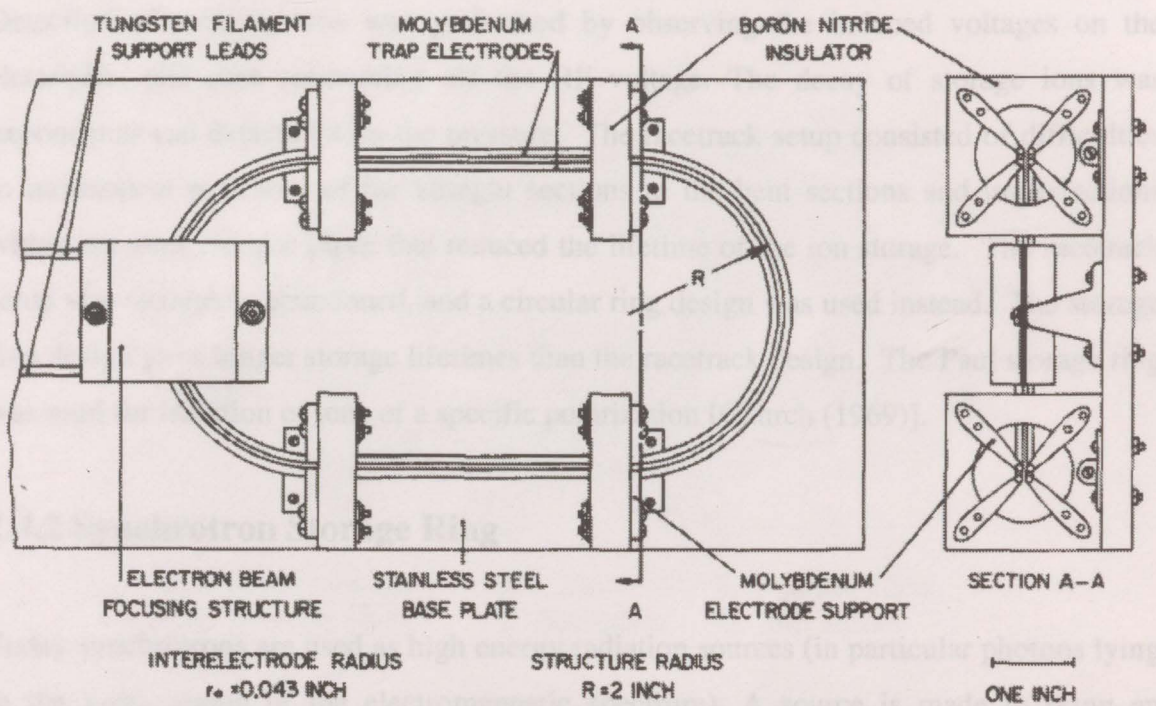


Figure 1.11: A schematic diagram of the Paul-Type Racetrack Storage Ring [Church (1969)].

Copper and molybdenum were used for most of the supports of the apparatus. Copper is often used due to its innate malleability and low surface absorption (which is most important for outgassing^{††}), and molybdenum is a very sturdy and durable metal. The electrodes were constructed from 316 stainless steel (very low magnetic properties, i.e. not a source of a magnetic field) that is coated in a thin layer of rhodium to act as a barrier against gas diffusion. The electronics for the system were placed directly on the chamber (on the air side). It is speculated that this mounting technique was done for the purpose of eliminating aerial pick-up that would deposit noise on the electrodes (which can occur in long cables extending from the electronics to the chamber). The DC inputs included low pass filters that were contained in separate shielded boxes to block radio-frequency signal from reaching the electrodes, causing interference with the stored charged particles. Injection is brought about by a basic filament that is heated by a 60 Hz voltage supply. The emission current of the filament was 5 – 10 mA, and was pulsed for a 5 to 10 second duration by a gate relay that would interrupt the heating current supply [Church (1969)].

^{††} A process that slowly releases gases trapped within surfaces of materials within vacuum

Detection of orbiting ions was performed by observing the induced voltages on the electrodes, and then subtracting off the RF voltage. The decay of storage ions was exponential and dependant on the pressure. The racetrack setup consisted of difficulties in mechanical matching of the straight sections to the bent sections and imperfections within the bent circular pipes that reduced the lifetime of the ion storage. The racetrack setup was ultimately abandoned, and a circular ring design was used instead. The storage ring design gave longer storage lifetimes than the racetrack design. The Paul storage ring was used for isolation of ions of a specific polarization [Church (1969)].

1.4.2 Synchrotron Storage Ring

Today synchrotrons are used as high energy radiation sources (in particular photons lying in the x-ray region of the electromagnetic spectrum). A source is made to bring an electron beam tangentially into the ring where a radially varying magnetic field is applied to drive the electrons around the synchrotron ring. Electrons (or positrons) are made to circulate at relativistic speeds within a circular ring; the acceleration due to the circular motion is responsible for the radiation. The beam is focused in the vertical direction which results in a lessening of the radial focus. In order for the trajectory of the circulating or “orbiting” electron beam to be stable, the strengths of both focii must be compromised. Moreover, the following inequality must be upheld: $0 < n < 1^{**}$. The preceding inequality places restrictions on the aperture sizes of the lens elements within the ring as well as the symmetry nature of the guiding and accelerating fields [Courant and Snyder (1958), Duke (2000)].

A schematic of a synchrotron is shown in figure 1.12. The synchrotron is not perfectly circular, but rather a polygonal geometry, whereby the electrons uniformly travel through the straight sections, which then become accelerated at the bending sections. A linear accelerator coupled with an electron gun provides the initial injected high energy electrons.

^{**} n is the field gradient index of the synchrotron, which is the defining parameter for the ring

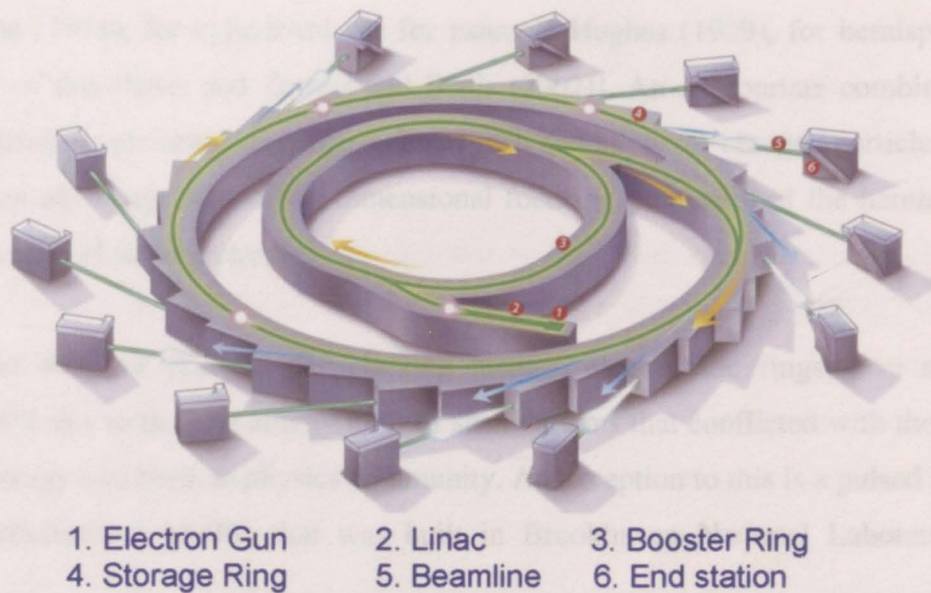


Figure 1.12: A representation of a synchrotron storage ring, showing the high energy electrons formed by a linear accelerator which then enter the booster ring and finally enter the storage ring along a tangential pathway; radiation comes from the acceleration of the electrons at the bending sections adjacent to each end station [www.sync.monash.edu.au/assets/images/synchrotron.jpg]

1.4.3 Electrostatic Rings^{§§}

In contrast to the high energy and particle physics field, these storage rings exclusively encompass electric fields as the bending and focusing operator for charged particle beams without the use of magnetic fields. Static electric fields permit electrons or ions to travel on trajectories independent of their mass. These setups avoid magnetic hysteresis, high power consumption, or water cooling that would arise with magnetic elements. This subsection will present a variety of apparatuses using static electric fields.

Time independent electric fields can be used to guide, focus, and bend charged particle beams. In general, cylindrical or planar elements will guide and focus the beam through the right combination of these elements. A charged particle beam can be deflected or “bent” by passing the beam through an electrostatic device that is naturally angled; such

^{§§} This sub-section is of most relevance to this dissertation, which involves the development of an electrostatic storage ring.

as hemispherical, cylindrical, or toroidal energy analyzers [for toroid see for example Roy and Carette (1971), for cylindrical see for example Hughes (1929), for hemisphere see Chapter 2 of this thesis and Zouros and Benis (2002)]. An appropriate combination of these electrostatic elements can form a closed path and allow for charged particle storage, which takes advantage of the two dimensional focusing properties of the hemispherical deflector analyzer, as an example.

Throughout most of charged particle ring history, electrostatic rings have not been implemented due to the low energy limit of such systems that conflicted with the aims of the high energy and particle physics community. An exception to this is a pulsed alternate gradient synchrotron (AGS) that was built in Brookhaven National Laboratory (see below).

i. Brookhaven Storage Ring

An electrostatic circular ring measuring 141.4 feet in circumference was built in 1954 [Green and Courant (1959)]. A 1.0 MeV Van de Graaff generator supplies the injection energy for the electrons emitted on a near tangent to the ring and brought on the azimuth by a pulsed field. The electrons begin to fill the ring for the duration of the inflection potential pulse. The electrons from the injected beam will begin the storage cycle and continue to circulate around the ring. Storage could be achieved by weak pulsed magnetic fields, however, their research group found a number of experimental difficulties with achieving very precise pulsed **B** fields. Thus, electric fields were implemented through the use of static electric potentials applied to stainless steel electrodes. The lens or “focusing section” consists of unit cells which contain a combination of a half – focusing lens and a half – defocusing lens. A total of *forty* of these unit cells have been incorporated into the synchrotron ring. The unit cells have been figured with lenses with an aperture of 0.8 inch in diameter. Electrons circulate within the ring with a revolution frequency of 7.0 MHz (or orbit period of 0.14 μ sec). The system has also incorporated “kicker” elements to alter effective gradients, which will boost the electron beam after

energy is lost to electromagnetic radiation. The AGS at Brookhaven was built to store electrons, and used for diagnostic tests only [Andersen, Heber and Zajfman (2004)].

ii. ELISA

A racetrack style heavy ion storage ring that encompasses electrostatic elements only, was built in Denmark in 1997 [Moller (1997), Moller and Pedersen (2001)]. The *ELISA* system or *electrostatic ion storage ring, Aarhus* consists of two 160 degree electrostatic deflectors, four 10 degree parallel plate deflectors, and four pairs of electrostatic quadrupoles, as is shown in figure 1.13. The system measures approximately 6.28 meters in circumference, with an injection energy of ~ 25 keV, and an orbit time of $2.9 \mu\text{sec}$ [protons] and $77 \mu\text{sec}$ [C-60 ions]. Initially the 160 degree deflectors were 180 degrees, which was found to give an over-focusing for their system. The 180° hemispherical deflectors were then changed to the 160° style, which resulted in a well-defined beam. The 160° (opposed to 180°) provides a clever setup that incorporates the 10° deflectors to inject the keV ion beam directly on the axis (see figure 1.13). In this setup there is no need to pulse any high voltage storing elements, which is advantageous as AC potentials will radiate and can induce small amplitude AC signals or “noise” on elements that can act as perturbations on the storage conditions. However, the injection system (not shown in diagram) does contain pulsing elements that, although separate from the main storage ring, results in noise “pick – up” on the elements of the main ring, which has not been discovered to be deleterious to the stored beam.

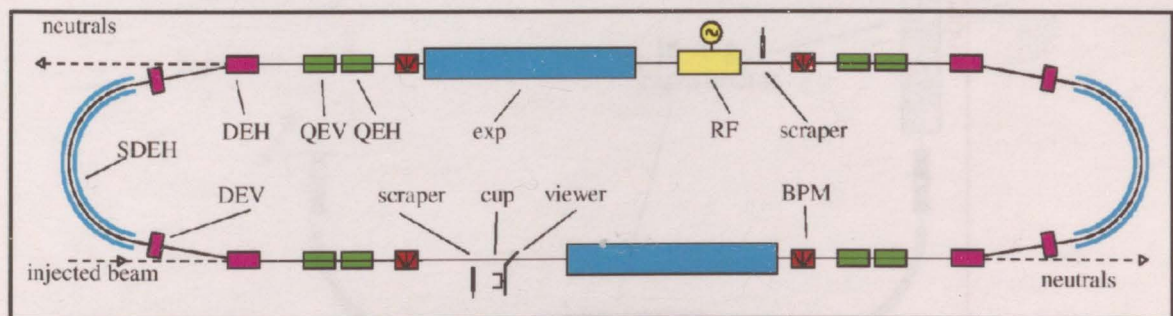


Figure 1.13: A schematic illustration of the ELISA storage ring. The system contains 160° spherical electrostatic deflectors (SDEH), 10° parallel plate deflectors (DEV and DEH), horizontally and vertically focusing quadrupoles (QEV and QEH), and RF frequency drift tube [Moller (1997)].

The *ELISA* design has been experimentally copied in Japan with the same racetrack ring style [Tanabea *et.al.* (2002)]. The group of Tanabea has created their ring with a larger circumference of 8.136 meters, and corresponding higher energy. Instead of protons or C-60 ions inside the ring, the Japanese experiment used O^+ ions at 30 keV.

iii. FLAIR

At the Facility for Low-energy Antiproton and Ion Research (FLAIR), Welsch's group have designed an electrostatic ring to store antiprotons [Welsch and Ullrich (2004), Welsch *et.al.* (2005)]. The storage ring design can be seen in the schematic shown in figure 1.14. The system can fit within a six meter square (an area of 36 m^2), and consists of four 90° electrostatic cylindrical deflectors, and quadrupole doublets. The energy of the antiprotons that will enter the 90° deflectors is $\sim 300\text{ keV}$ that is divided by two concentric electrodes with $\sim \pm 19\text{ keV}$ voltages. Quadrupole lenses are to be employed to provide transverse bunching to overcome the deficiency of focusing on the perpendicular

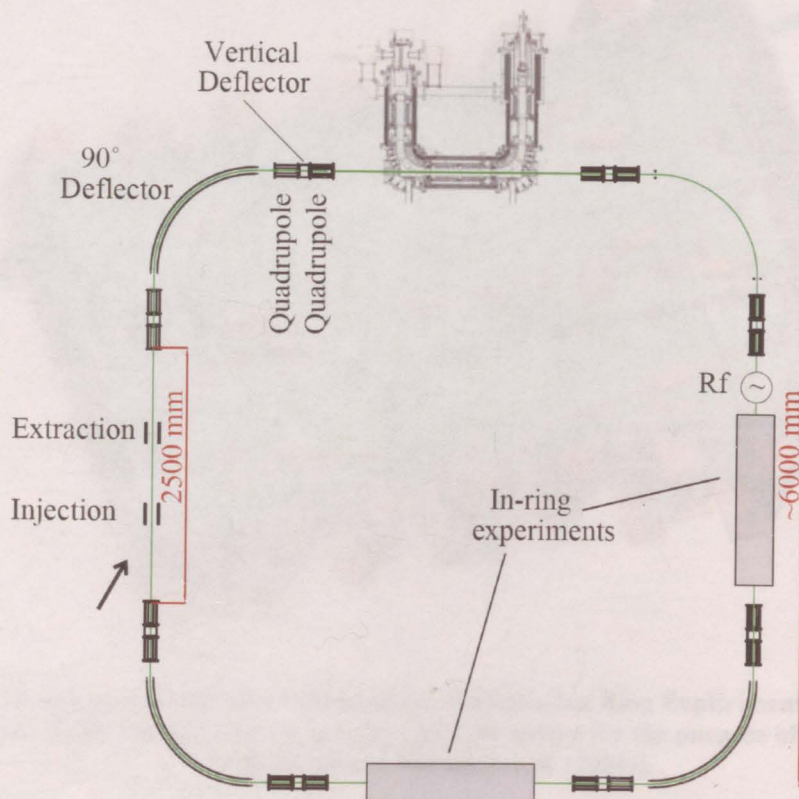


Figure 1.14: A schematic diagram of the FLAIR storage ring (see text for details) [Welsch *et.al.* (2005)].

direction from the 90° cylindrical deflectors. The system will implement a radiofrequency tube (with voltages < 100 V) that will counteract the innate longitudinal debunching effects (spreading of the beam width).

iv. DESIREE

The DESIREE apparatus is a double electrostatic storage ring that encompassed two electrostatic rings of the same style as the ELISA or Tanabea rings (discussed above) that was designed, and is under construction, at the Manne Siegbahn Laboratory and Stockholm University (see figure 1.15) [Rensfelt *et.al.* (2004)]. It consists of two 9.2 m rings^{***} with one common straight section. The common straight section is present for the purpose of ion – ion collision studies. The whole double ring instrument is placed in a vacuum chamber and cryogenically cooled to ~ 10 K. This provides the necessary environment to mimic ion interactions within interstellar plasma. The double ring layout

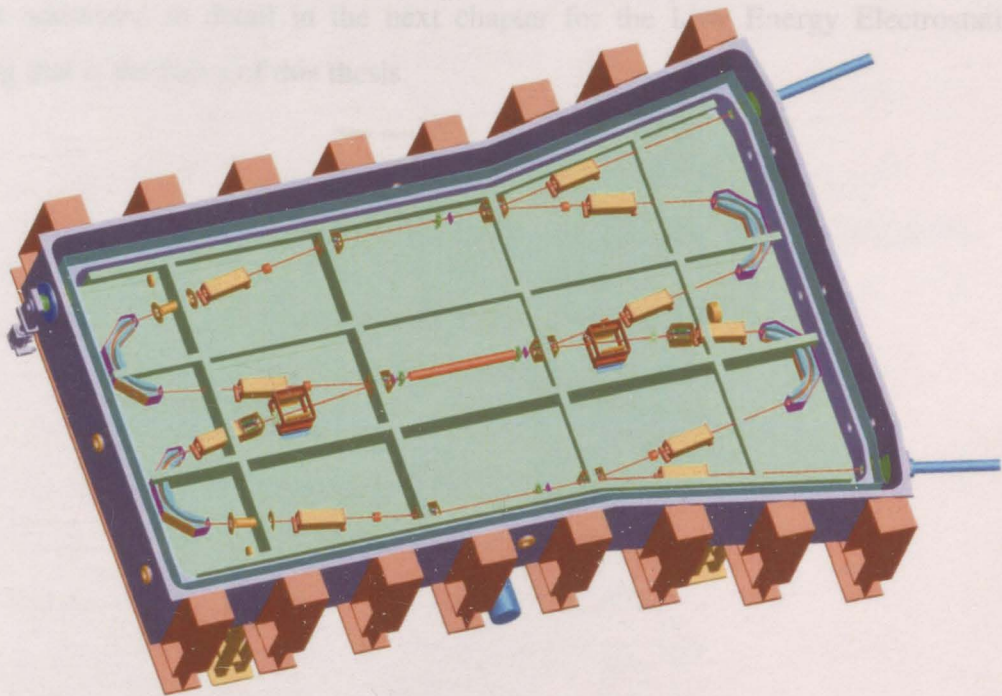


Figure 1.15: A diagram of DESIREE (Double ElectroStatic Ion Ring ExpERiment), two rings each similar to the ELISA design share a common straight section for the purpose of co-linear beam collision studies [Rensfelt *et.al.* (2004)].

^{***} A slightly larger circumference than the storage ring built by Tanabea's group in Japan

offers merged beam tests for both positive and negative ions. The cold environment of the system provides an ultrahigh vacuum that is ideal for longer lifetimes of the stored beam.

1.5 SUMMARY

Over the previous few decades research groups have addressed challenges in both design and experiment to maximize the efficiency of their traps. A number of techniques of trapping and storing of charged particles have been presented. The chapter introduced apparatuses that confine particles at a single point, which although not identical to this thesis, provides the concept of behaviors of charged particles within different electromagnetic field combinations. The point trap concept imparts the notion that trapping is related to both the type and magnitude of the fields that are present. Storage rings were also presented showing some of the innovations and theoretical constraints that will be addressed in detail in the next chapter for the Low Energy Electrostatic Storage Ring that is the focus of this thesis.

REFERENCES

- Abramowitz M., and Stegun I.A. Handbook of Mathematical Functions, Dover publications (1972)
- Andersen L.H., Heber O., and Zajfman D., *Jour. Phys. B: At. Mol. Opt. Phys.*, **37** (2004) R57–R88
- Bennewitz H.G., and Paul W, *Z. Phys.*, **139** (1954) 489
- Bennewitz H.G., Paul W., and Schlier C., *Z. Phys.*, **141** (1955) 6
- Bhushan K. G., Pedersen H. B., Altstein N., Heber O., Rappaport M. L., and Zajfman D., *Phys. Rev. A*, **62** (2000) 012504
- Bollinger J. J., Mitchell T. B., Huang X.P., Itano W. M., Tan J. N., Jelenkovic B. M., and Wineland D. J., *Phys. Plas.*, **7** (2000) 7
- Brown L.S., and Gabrielse G., *Rev. Mod. Phys.*, **58** (1986) 233
- Church D.A., *Jour. App. Phys.* **40** (1969) 3127
- Clarke J., van der Werf D. P., Griffiths B., Beddows D. C. S., Charlton M., Telle H. H., and Watkeys P. R., *Rev. Sci. Instrum.*, **77** (2006) 063302
- Courant E.D., and Snyder H.S., *Ann. Phys.* **3** (1958) 1 – 48
- deGrassie J. S., and Malmberg J. H., *Phys. Rev. Lett.*, **39** (1977) 1077
- Duke P., Synchrotron Radiation, Oxford University Press (2000)
- Green G.K. and Courant E.D., Handbuch der Physik, Band XLIV, (Berlin: Springer) p. 319 (1959)
- Hasegawa T., Jensen M.J., and Bollinger J. J., *Phys. Rev. A*, **71** (2005) 023406
- Holzscheiter M.H., Charlton M., and Nieto M.M., *Phys. Rep.* **402** (2004) 1–101
- Hughes A.L., *Phys. Rev.*, **34** (1929) 284
- Jackson, J.D. Classical Electrodynamics, Wiley & Sons Inc. 1998
- Jefferts S.R., Monroe C., Bell E.W., and Wineland D.J. *Phys. Rev. A* **51** 3112
- Moller S.P., *Nucl. Instrum. Methods A*, **394** (1997) 281 – 286.
- Moller S.P., and Pedersen U.V., *Phys. Scr.*, **T92** (2001) 105 – 109
- Naaman A., Bhushan K. G., Pedersen H. B., Altstein N., Heber O., Rappaport M. L., Moalem R., and Zajfman D., *J. Chem. Phys.*, **113** (2000) 4662
- Paul W., *Rev. Mod. Phys.*, **62** No. 3 (1990)
- Pedersen H. B., Strasser D., Ring S., Heber O., Rappaport M. L., Rudich Y., Sagi I., and Zajfman D., *Phys. Rev. Lett.* **87** (2001) Ar. Num. 055001
- Raizens M. G., Gilligan J. M., Bergquist J. C., Itano W. M., and Wineland D. J., *J. Mod.*

Opt. **39**, No. 2, (1992) 233-242

Rensfelt K.G., Andler G., Bagge L., Blom M., Danared H., Källberg A., Leontein S., Liljeby L., Löfgren P., Paál A., Simonsson A. and Skeppstedt Ö., *Proc. EPAC 2004*, (2004) 1425

Rich A., and Wesley J.C., *Rev. Mod. Phys.*, **44** (1972) 250

Roy D., and Carette J.D., *Jour. App. Phys.*, **42** (1971) 3601

Schultz J., and Lynn K.G., *Rev. Mod. Phys.*, **60** (1988) 701

Suzuki J.I., Oku T., Adachi T., Shimizu H.M., Hirimachi T., Tsuchihashi T., and Watanabe I., *J. Appl. Cryst.*, **36** (2003) 795 - 799

Tanabea T., Chidaa K., Nodab K., and Watanabe I., *Nucl. Instrum. Methods A*, **482** (2002) 595 – 605

Thompson R.I., Harmon T.J., and Ball M.G., *Can. Jour. Phys.* **80** (2002) 1433

Welsch C. P., and Ullrich J., *Phys. Rev. ST – Accel. Beams*, **7** (2004) 080101

Welsch C. P., Grieser M., Ullrich J., and Wolf A., *Nucl. Instrum. Methods A*, **546** (2005) 405 – 417

Wester R., Bhushan K. G., Altstein N., Zajfman D., Heber O., and Rappaport M. L., *J. Chem. Phys.*, **110** (1999) 11830

Whittaker E.T., and G.N. Watson, *A Course of Modern Analysis*, (2002) reprint from Original Forth Edition 1927

Wuerker R.F., Shelton H., and Langmuir R.V., *Jour. App. Phys.* **30** (1959) 342

Zajfman D., Heber O., Vejby-Christensen L., Ben-Itzhak I., Rappaport M., Fishman R., and Dahan.M., *Phys. Rev. A* **55** (1997) R1577 – R1580

Zajfman D., Strasser D., Heber O., Goldberg S., Diner A., Rappaport M.L., *Nucl. Instrum. Methods A*, **532** (2004) 196–202

Zouros T.J.M., and Benis E.P., *J. Elect. Spect. Rel. Phenom.* **125** (2002) 221–248

CHAPTER 2: THEORETICAL*

ELECTRON STORAGE FOR RACETRACK GEOMETRY

2.1 INTRODUCTION TO ELECTRON OPTICS	27
2.1.1 Electrostatic Lenses and Focusing Conditions	28
2.1.2 Helmholtz – Lagrange Relation	33
2.1.3 Hemispherical Deflector Analyzer (HDA)	34
2.2 THE TRANSFER MATRIX	36
2.2.1 Background	37
2.2.2 The Electron Recycling System (ERS)	39
2.3 STABILITY	41
2.3.1 Phase Space	42
2.3.2 Constraints Imposed on the Transfer Matrix	44
i. Unity Matrix	45
ii. Deviations from Unity Matrix	47
iii. Generalized Expression	49
iv. Asymmetric Lens Setup	53
v. Aberrations	57
2.3.3 Stability Modeling	59
2.4 SUMMARY	60
REFERENCES	61

* This chapter is the product of joint research

2.1 INTRODUCTION TO ELECTRON OPTICS

This chapter presents electron optics background along with the theory relating to the design and stability of the electron recycling system (ERS, see figure 2.1 for a general schematic). The general principles of electrostatic lenses, ray tracing, and hemispherical deflector analyzers (HDA), will be discussed first in this chapter, followed by stability theory within a general closed storage ring setup. The chapter will finish with the operation of the ERS ring, encompassing all the material discussed up to that point; i.e. a transfer matrix for the whole ERS is created from the combination of lenses and HDAs, and is related to stability theory. The ERS contains elements found in any electrostatic spectrometer; thus, the general operation of a spectrometer will begin the discussion.

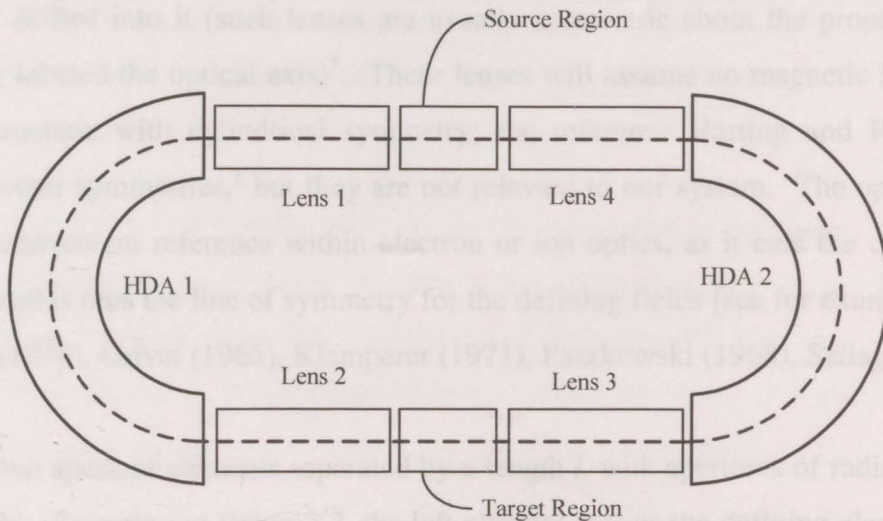


Figure 2.1: Basic schematic of Electron Recycling System (ERS), displaying 2 Hemispherical Deflector Analyzers (HDA), four lenses, and a source and target region.

An ideal electron source ejects electrons with the aim of forming a near parallel beam based on the field gradients present. The source used here utilizes a hairpin shaped filament to produce the electron beam that subsequently propagates through a series of collimating and focusing lenses (a series of individual electrodes comprises a 'lens'). An energy deflector analyzer is added in succession to the first lens to redirect and disperse the beam in a manner like that of a prism in light optics (the deflection angles are dependent on the geometry of the energy deflector that includes common values of 180° , 160° , 127° , or 90°). A second lens is added to the system in series to the energy deflector

analyzer to further collimate and focus the beam. The lens focuses the beam onto a target; for example, a gas target in order to perform ionization cross section studies. The scattered particles are focused a third time and are collected in an energy or momentum detector, see for example [Read *et.al.* (1974)].

2.1.1 Electrostatic Lenses and Focusing Conditions

The field of charged particle optics is analogous to light optics with respect to beam propagation, focusing, and ray tracing. Space charge and external field perturbations are some of the main differences between the two fields of study. An electrostatic lens is simply a sequence of electrically charged metallic elements with a physical hole or “aperture” drilled into it (such lenses are usually symmetric about the propagation axis commonly labeled the optical axis)[†]. These lenses will assume no magnetic \mathbf{B} fields and only electrostatic with cylindrical symmetry; the reference Harting and Read (1976) discusses other symmetries,[‡] but they are not relevant to our system. The optical axis is usually a convenient reference within electron or ion optics, as it cuts the center of the apertures and is thus the line of symmetry for the defining fields [see for example Harting and Read (1976), Grivet (1965), Klemperer (1971), Paszkowski (1968), Szilagyi (1988)][§].

Consider two aperture elements separated by a length l , with apertures of radius r_1 and r_2 , respectively. Referring to figure 2.2, the left element acts as the defining element for the radius of the beam, and consequently the object size (which could, be the ‘image’ of a previous lens). The first element can be considered an optical “window” for an incoming beam of straight trajectories. Suppose a beam enters the first aperture at position r_w (outer edge of beam, same as r_1), and at an angle θ_B (beam angle) to the beam axis. The right element acts as a “pupil” as it defines the solid angle for all points in the object that will be transported further through the optical system (for a field free region, see Figure 2.2).^{**}

[†] for example an electron beam that travels through circular apertures will take on a cylindrical shape, making it appropriate to use cylindrical symmetry, whereby the coordinates ρ , ϕ , and z would be employed. Thus, the optical axis is coincident with the z axis

[‡] Other symmetries include planar or rectangular

[§] These references were the main resource for this section

^{**} See Paszkowski (1968) for details

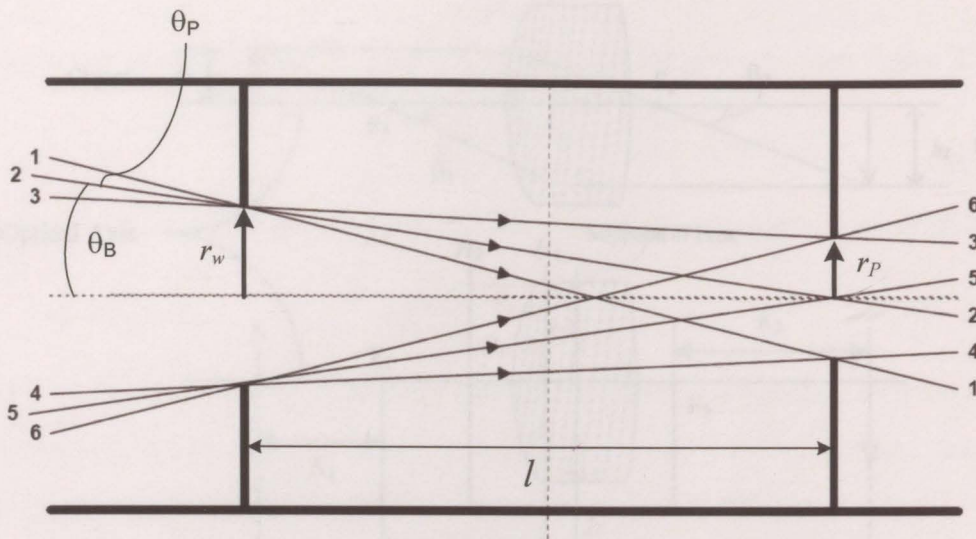


Figure 2.2: Straight line trajectories within a field free region containing 2 circular defining apertures showing the process of collimation, and illustrating the difference with θ_B and θ_p .

The lens parameters are related by the following relations (equation 2.1):

$$\theta_p \approx \frac{r_p}{l}; \quad \theta_B \approx \frac{r_w}{l}. \quad (2.1)$$

The pencil angle θ_p is the half – angle of the rays at a point in the object, and similarly, the beam angle is the half – angle between pencil cones at opposite edges of the object. Expanding on the ideas presented in figure 2.2, collimation will remove a number of the electrons from the beam. A minimum of two apertures are required to collimate a beam: defining the radial spread r_w and pencil angle θ_p of the object [Read *et.al.* (1974)].

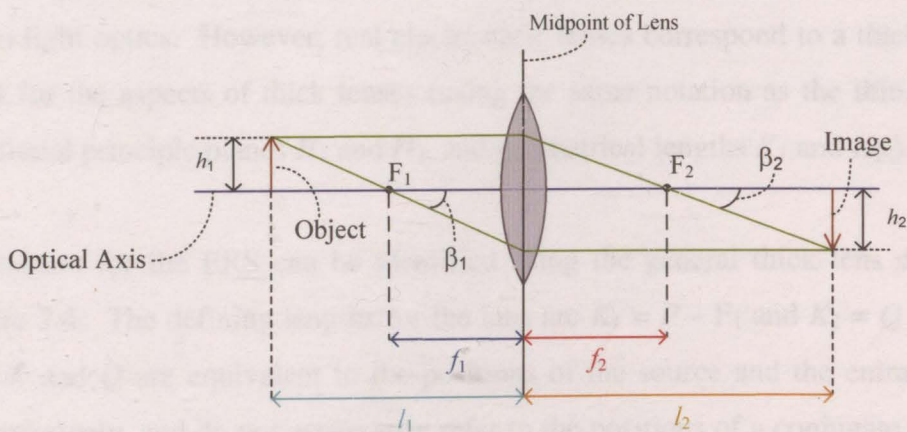


Figure 2.3: Showing a ray trace and refraction of trajectories of a lens, in this case a thin lens is presented (see text for definition of parameters).

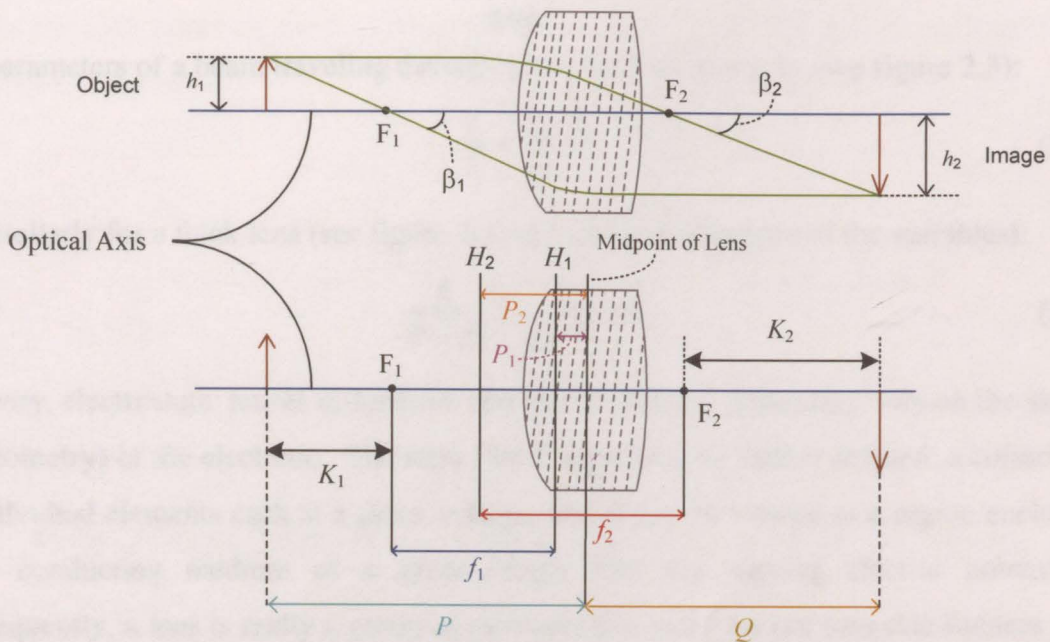


Figure 2.4: To properly describe the behaviour of trajectories within electrostatic cylindrical lenses, a thick lens is used in place of a thin lens. The characteristic parameters and cardinal points/planes are shown and mentioned in the text.

Similar to light optics, electron optical lenses are best defined by focal lengths and principle planes (such lenses retain the ‘thick’ or ‘thin’ lens classifications). In figure 2.3 a thin lens is displayed with focal points F_1 and F_2 , focal lengths f_1 and f_2 , angles β_1 and β_2 , and object and image heights h_1 and h_2 , respectively. The electron beam will bend or “refract” according to an index of refraction given by the lens. Electrostatic lenses have no distinct boundary surfaces, and thus have a continuously changing refractive index [Paszkowski (1968)]. A thin lens introduces the topic of lenses within electron optics in analogy to light optics. However, real electrostatic lenses correspond to a thick lens; see figure 2.4 for the aspects of thick lenses (using the same notation as the thin lens case, with additional principle planes H_1 and H_2 , and geometrical lengths K_1 and K_2).

The parameters for the ERS can be identified using the general thick lens dimensions from figure 2.4. The defining lengths for the lens are $K_1 = P - F_1$ and $K_2 = Q - F_2$. The distances P and Q are equivalent to the positions of the source and the entrance to the HDA, respectively, and do not necessarily refer to the positions of a conjugate object and image. Tables for the numerical values of P and Q , and aberration coefficients can be found in [Harting and Read (1976)].

The parameters of a beam traveling through a thin lens are given by (see figure 2.3):

$$\frac{f_1}{l_1} + \frac{f_2}{l_2} = 1, \quad (2.2)$$

and similarly for a thick lens (see figure 2.4 for a visual description of the variables):

$$\frac{f_1}{P - P_1} + \frac{f_2}{Q - P_2} = 1. \quad (2.3)$$

In theory, electrostatic lenses differ from one type to another depending only on the shape (or geometry) of the electrode. The term “lens” must now be further defined: a collection of individual elements each at a given voltage, which can be viewed as a region enclosed by a conducting medium of a given length that has varying electric potentials. Consequently, a lens is really a group of elements that make up one lens that focuses and collimates the beam. Generally, a lens can be classified according to the influence on the charged particle velocity from the object side (v_1) to the velocity on the image side (v_2), which is best summed up in table 1 below:

accelerating	$v_2 > v_1$
neutral	$v_2 = v_1$
decelerating	$v_2 < v_1$

Table 1

The cylindrical symmetry of the lens implies that electrons that travel near the optic axis will in general experience fewer deflections than those nearer to the outside of the beam. The near axis electrons, or “paraxial” electrons, are more likely to be conserved throughout the storage ring, as they will not collide with apertures and inner walls.

Apertures were defined above (in figure 2.2), where a through hole exists in a single plane metallic element and is separated by a distance to the next planar element. In that sample the apertures were set up as a field free region, this can be extended to the use of apertures as a lens. Another common type of electrostatic lens is the cylindrical lens, as shown in figure 2.5, whereby each element is simply a metallic cylinder with a hole of fixed diameter drilled through its center. Cylindrical lenses have been implemented

within the ERS based on the 3 element design and will be explained in more detail in the following paragraphs.

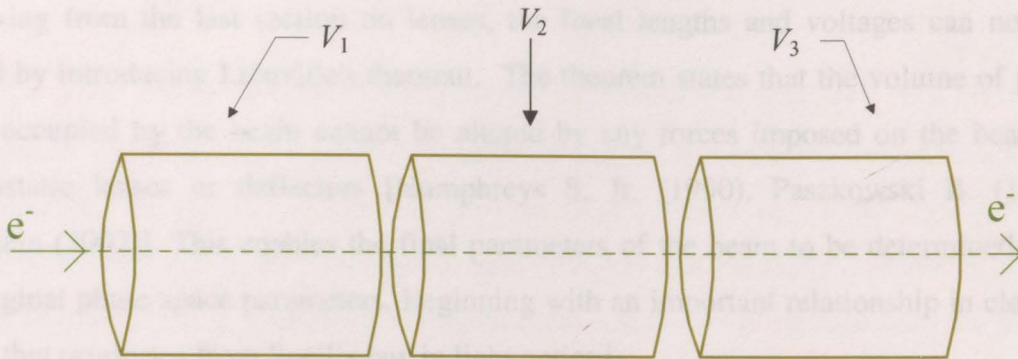


Figure 2.5: Triple Cylindrical Lens, consisting of 3 elements each at separate voltages.

Consider a lens that consists of two cylindrical lens elements with voltages V_1 and V_2 and radii of R_1 and R_2 . The condition that the radii of the two lenses are identical ($R_1 = R_2 = R$) will also be applied to this sample, and the key parameter to determine the effective focusing of a beam is $\sigma = V_2 / V_1$, which is the ratio of the electric potentials, regardless of the number of elements and the individual values of V_1 and V_2 themselves. The energy of the electrons through the first element and second element are eV_1 and eV_2 , respectively, which will lead to defining the refractive index of the lens (see below on Helmholtz – Lagrange equation).

An electron or ion traveling through a lens can have its energy raised or lowered depending on the value of σ (i.e. accelerated or decelerated when traversing a lens, see table 1 above). Given that $U(r, z)$ is the representation for the electron energy within the cylindrical coordinate system, then the axial potential is defined as $U(r = 0, z)$ at any point within the lens, these potentials are not linearly dependent on the electron optical variables and can take complicated forms. The field gradients determine the refraction of the trajectories. The large number of trajectories within the presence of non – linear field gradients causes the analysis and calculations of parameters to become complex. Thus, for a three-element or greater lens, the expressions for the parameters (f_1 and f_2 for example) are determined numerically rather than analytically.

2.1.2 Helmholtz – Lagrange Relation

Following from the last section on lenses, the focal lengths and voltages can now be related by introducing Liouville's theorem. The theorem states that the volume of phase space occupied by the beam cannot be altered by any forces imposed on the beam by electrostatic lenses or deflectors [Humphreys S. Jr. (1990), Paszkowski B. (1968), Goldstein (2002)]. This enables the final parameters of the beam to be determined from the original phase space parameters. Beginning with an important relationship in electron optics that originates from Snell's law in light optics is:

$$n_1 \sin \theta_1 = n_2 \sin \theta_2, \quad (2.4)$$

that relates the product of index of refraction in one medium and incident angle to the index of refraction in another medium with the angle of refraction, and that the components orthogonal to the normal of the plane are equal. Therefore, conserving the volume of phase space leads to the Helmholtz -Lagrange equation: the product of the parameters of a beam $\{p, r, r'\}$ will be a constant (where the values in the parenthesis are momentum, radius, and tangent of the angle).

Charged particles will behave in an identical manner to photons in light optics, provided the following conditions are met:

- The medium is non – absorbing, i.e. the number of particles remain constant (conservation of current)
- No space charge effects, electron rays can be considered as geometrical optics, i.e. non-interacting particles
- No aberrations
- No dispersion, i.e. no velocity dependant forces (prism effects)

Defining the lens potential with respect to the zero of the electron energy, rather than real ground or earth, gives the kinetic energy of the electrons to be equal to eV , where V is the voltage on a particular lens element. Media of a constant index of refraction is replaced by regions of constant voltages of V_1 and V_2 for the object and the image, respectively.

The Helmholtz – Lagrange equation can now be expressed mathematically for an electron beam:

$$\sqrt{eV_1} r_1 \tan \beta_1 = \sqrt{eV_2} r_2 \tan \beta_2, \quad (2.5)$$

where eV is the energy of the electrons (object or image), and note: $\sqrt{eV} \propto p$, r_1 and r_2 are the distances of the object and image from the optical axis (see Figure 2.4 with $r \equiv h$), and the angles in equation 2.5 are in fact the pencil angles [Sturrock (1955), Pierce (1954), and Banford (1966)]. One should note however that the tangent of the angle that appears in equation 2.5 is valid for Gaussian optics, in the more general case the sine of the angle is used in accordance with Abbe's sine theorem [Paszkowski (1968)]; in the small angle approximation $\sin\beta \approx \tan\beta \approx \beta$. The gradient of the electric potential V will cause the charged particle to bend toward the optic axis (analogue: converging lens), or diverge from the axis. Consequently, the Helmholtz – Lagrange equation is a constraint placed upon a charged particle beam under the influence of electrostatic forces, which relates the final energy to the initial energy by the angular spread of the beam [Klemperer (1971)].

2.1.3 Hemispherical Deflector Analyzer (HDA)

The energy spread of the electron beam can be narrowed by an energy filtering element. In analogy to light optics, it can be interpreted as an electrostatic prism (i.e. a device that breaks up the energy of the beam). An example of this is a velocity dependent field that will only pass any charged particle of a definitive energy and reject all other energies. An HDA consists of two hemispherical surfaces, a hemisphere is placed concentrically within a larger hemisphere at separate potentials, V_I (I = inner, and is positive for electrons) and V_O (O = outer, and is negative for electrons), see figure 2.6. The HDA functions like a prism in that it gives the image at the exit, whereby the electron beam disperses into bands of energy, which gives the HDA the label of energy analyzer. A charged particle beam is directed toward the midway point of the HDA entrance. The narrow band in the center of the gap within the concentric hemispheres has an effective electric potential V_0 , commonly referred to as the *passing voltage*, and eV_0 is the *pass energy*; this defines the

mean energy of the electrons that are focused at the exit. An HDA analyzer will focus in two directions due to spherical symmetry. However, electrons with energy greater than the pass energy will be focused in the same exit plane to a point closer to the outer hemisphere. Electrons with energies less than the pass energy will be focused in the exit plane closer to the inner hemisphere. Thus, there is an energy dispersed image in the exit plane of the HDA. Through the placement of an aperture at the entrance and exit, the hemisphere will behave like a prism with resolving power given by the energy resolution

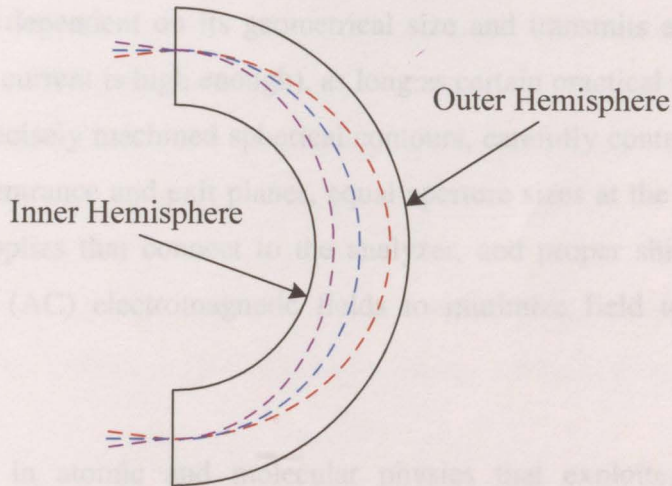


Figure 2.6: Electron trajectories within a 180 degree electrostatic HDA

<u>Properties</u>	<u>Hemispherical Analyzer</u>
Potential Equation	$V(r) = V_0 \left[\frac{2R_0}{r} - 1 \right]$
Potential Difference	$\Delta V = V_0 \left[\frac{R_2}{R_1} - \frac{R_1}{R_2} \right]$
Energy Resolution	$\frac{\Delta E_{FWHM}}{E_0} \approx \frac{r_s}{R_0} + 0.25\alpha^2$
Electric Field	$E \propto \frac{1}{r^2}$
Energy – Dispersive refocusing	After a deflection of π

Table 2: Summary of HDA properties as discussed in the text

of the analyzer, see Table 2 [for a good coverage on 180° analyzers see Purcell (1938), Imhof, Adams and King (1976), and Zouros and Benis (2002)]. The list of properties

found in table 2 give a summary of the relevant voltage and energy dispersion relations of HDAs. The quantity R_0 corresponds to the HDA mean radius, R_1 and R_2 are the radii of the inner and outer hemisphere, respectively, r_s is the radius of the aperture at the entrance and exit of the HDA, and α is the angle of the electron trajectory upon entering or exiting the HDA.

Hemispherical deflector analyzers can be summed up as “monochromators” whose resolving power is dependent on its geometrical size and transmits a workable current (provided the input current is high enough), as long as certain practical concerns are taken into effect: high precisely machined spherical contours, carefully controlled electric field termination in the entrance and exit planes, equal aperture sizes at the entrance and exit, precise voltage supplies that connect to the analyzer, and proper shielding of external alternating current (AC) electromagnetic fields to minimize field termination effects [Simpson (1964)].

Early applications in atomic and molecular physics that exploited the 180° HDA [Simpson (1964)] are the measurement of differential cross sections of neon, argon, krypton, and xenon for elastic scattering and optical transitions [Geiger (1964)]. HDAs are still widely used in atomic and molecular physics and in surface science for material characterization. These devices have a geometry that lend themselves to position sensitive detectors [Zouros (2006)], which improves the overall detection efficiency. Furthermore, advances in electron optics e.g. multi-element zoom lenses in software modeling allows one to obtain the best performance from HDAs and even compensate for aberrations [Dahl (2000), <http://www.electronoptics.com/>, Zouros, Benis and Chatzakis (2005)].

2.2 THE TRANSFER MATRIX

The electrons will travel on the total path within the ERS that is broken up into a number of sections or “cells” that contain elements such as lenses, HDAs or field free regions. Each cell will affect the propagating beam, and is best expressed mathematically by the use of transfer matrices. Any element will have its own transfer matrix, whereby a

collection of elements is expressed as a single transfer matrix that is a product of the transfer matrices for the elements that are present. Through this process the entire ERS will be represented as a single transfer matrix.

2.2.1 Background

Conventionally, the degrees of freedom of charged particles are given by its position (which is denoted r for the case of a cylindrical symmetric coordinate system) and angle relative to the optical axis (denoted by θ_B and $r' = \tan \theta_B$). The parameter r' is further defined by the ratio of velocities of the beam at points within the transfer cell:

$$r' = \frac{dr}{dz} \cong \frac{v_r}{v_z}. \quad (2.6)$$

The classification of an electron at the entrance and exit of an electrostatic optical element which could be a lens or HDA is given by the vectors \mathbf{x}_0 and \mathbf{x}_1 , respectively:

$$\mathbf{x}_0 = (r_0, r'_0) \quad (2.7)$$

$$\mathbf{x}_1 = (r_1, r'_1). \quad (2.8)$$

Since the HDAs operate with static linear electric fields, the vector components can be expressed as:

$$r_1 = a_{11}r_0 + a_{12}r'_0 \quad (2.9)$$

$$r'_1 = a_{21}r_0 + a_{22}r'_0 \quad (2.10)$$

or in matrix form:

$$\begin{bmatrix} r_1 \\ r'_1 \end{bmatrix} = \mathbf{A} \begin{bmatrix} r_0 \\ r'_0 \end{bmatrix} = \begin{bmatrix} a_{11} & a_{12} \\ a_{21} & a_{22} \end{bmatrix} \begin{bmatrix} r_0 \\ r'_0 \end{bmatrix}. \quad (2.11)$$

The values a_{mn} are dependent on the forces present.

A transfer matrix was introduced in equation 2.11 as a mathematical expression used to describe the beam dynamics over a region containing lenses or analyzers (or any element that operates on a charged particle beam). Mathematically, a beam goes from an initial

state $\{r_0, r_0'\}$ to a different state $\{r_1, r_1'\}$ at a later time by means of the transfer matrix. The operator \mathbf{A} ($= [a_{mn}]$) in the above equation is the general form of the transfer matrix.

Provided the acceleration over the transfer region is zero, then the determinant of the transfer matrix is equal to unity (see Section 1.2 on Helmholtz-Lagrange relation). Similar to light optics, if the electron passes through any number of linear transfer devices, there will be a single transfer matrix (which is a product of the transfer matrices of each device) to describe the transformation. For a good background on transfer matrices see, for example, [Humphreys (1990), Lawson (1977)].

A transfer matrix \mathbf{A} can be assigned to an individual linear lens element, or a set of linear lens elements. The formation of a transfer matrix in charged particle optics is similar to the cases that are dealt within light optics. Suppose, for example, the electron beam traverses a field free region (denoted by a given length K_1), defined by the drift – length matrix:

$$\begin{bmatrix} 1 & K_1 \\ 0 & 1 \end{bmatrix}, \quad (2.12)$$

where K_1 is the difference between the positions r_0 and r_1 , see figure 2.7. For the ERS, K_1 and K_2 correspond to the geometry of the system, see figure 2.4 of Section 1.1.

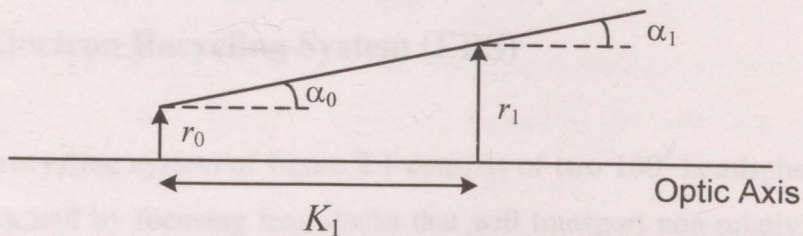


Figure 2.7: Ray trace of the trajectory of a beam within a field free region

Geometrically, the image radius is: $r_1 = r_0 + K_1 \tan \alpha$ or $r_1 = r_0 + K_1 r_1'$ and the angle remains the same: $\alpha_0 = \alpha_1$ (see figure 2.7). This simple example demonstrates the operation of the transfer matrix that relates the initial and final parameters of the beam:

$$\begin{bmatrix} r_1 \\ r_1' \end{bmatrix} = \begin{bmatrix} 1 & K_1 \\ 0 & 1 \end{bmatrix} \begin{bmatrix} r_0 \\ r_0' \end{bmatrix}. \quad (2.13)$$

A particle traversing a lens (a thick lens, for example see figure 2.4) has the following transfer matrix (again notice the similarities to light optics):

$$\begin{bmatrix} 0 & f_1 \\ -\frac{1}{f_2} & 0 \end{bmatrix}. \quad (2.14)$$

In a zeroth order approximation, the HDA acts simply as a deflector and not as a prism. From the general definition of an HDA, transfer matrix m_h (equation 2.16) is a first order approximation that ignores higher order effects such as spherical and chromatic aberrations (which are addressed later in this chapter), whereby the position r will increase by a Δr term [Wollnik (1987), Hammond *et.al.* (2008)]. Then the transfer matrix for an HDA will “reflect” the beam, which is the image – inversion function of the hemisphere, i.e. the HDA in this context will merely invert the beam angle and change its direction of propagation by 180 degrees:

$$\begin{bmatrix} r_1 \\ r'_1 \end{bmatrix} \rightarrow \begin{bmatrix} -r_1 \\ -r'_1 \end{bmatrix}; \quad (2.15)$$

therefore,

$$m_h = -I = -\begin{bmatrix} 1 & 0 \\ 0 & 1 \end{bmatrix}. \quad (2.16)$$

2.2.2 The Electron Recycling System (ERS)

The electron recycling system of figure 2.1 consists of two 180° hemispherical deflector analyzers separated by focusing lens stacks that will transport non-relativistic electrons. The focusing lens stacks include a source side (being the lens stack that transports the injected electron beam in addition to passing many recycled electron beams) and an interaction or “target” side (this includes a gas source that will be the region for electron gas collisions coupled with a detector that is non – disrupting to the storage beam). An elaborative description of the ERS is given in Chapter 3.

A full orbit begins at the source and returns back to the source. For an electron beam to execute such a path, a series of transitions must occur. The whole orbit can be broken up into separate pieces and studied individually. From the source to the entrance of the HDA, the electron beam is focused onto the entrance of the HDA through the lens – 1 transfer matrix m_1 , where the quantities a_{mn} for m_1 are determined by the position of the source and entrance of the HDA. Following m_1 , is the transfer matrix for the HDA m_h . Exiting the HDA, the beam will travel through lens – 2 or m_2 leading to the interaction region (not shown in figure 2.1). At this point the beam has traveled one half orbit, which is described by the source to target transfer matrix M_{ST} . To complete the full orbit the beam will then pass through a third lens, m_3 , another HDA and a final lens m_4 defined by a target to source transfer matrix M_{TS} , leading to a final source to source transfer matrix M_{SS} .

The lenses could be set up equivalently, which would provide an inherent symmetry in the system (symmetric setup, i.e. geometries and voltages are the same); alternatively, the system could be set up with lens 1 and 4 equal to each other and 2 and 3 equal to each other (refer to this arrangement as asymmetric). Assuming the symmetric setup, the electron beam will hence traverse m_2 with a time reversed transfer matrix of m_1 (to be further discussed in the cases given below).

For m_1 , a transfer matrix is used for the case of a general focusing system with foci f_1 and f_2 [Wollnik (1987)]. Thus, the path from the source to the entrance of the HDA is described by:

$$\begin{aligned}
 m_1 &= \begin{bmatrix} 1 & K_2 \\ 0 & 1 \end{bmatrix} \begin{bmatrix} 0 & f_1 \\ -\frac{1}{f_2} & 0 \end{bmatrix} \begin{bmatrix} 1 & K_1 \\ 0 & 1 \end{bmatrix} \\
 &= \begin{bmatrix} 1 & K_2 \\ 0 & 1 \end{bmatrix} \begin{bmatrix} 0 & f_1 \\ -\frac{1}{f_2} & -\frac{K_1}{f_2} \end{bmatrix} \\
 &= -\frac{1}{f_2} \begin{bmatrix} K_2 & K_1 K_2 - f_1 f_2 \\ 1 & K_1 \end{bmatrix}.
 \end{aligned} \tag{2.17}$$

The m_2 transition will be equivalent to the above transition (m_1) with the evident swap of foci and drift – length matrices: $f_1 \rightarrow f_2$ and $f_2 \rightarrow f_1$, $K_1 \rightarrow K_2$ and $K_2 \rightarrow K_1$ thus:

$$m_2 = -\frac{1}{f_1} \begin{bmatrix} K_1 & K_1 K_2 - f_1 f_2 \\ 1 & K_2 \end{bmatrix}. \quad (2.18)$$

Accordingly, the total transfer matrix for the source to interaction region is given by the following product (see Appendix 1-A for derivation):

$$\begin{aligned} M_{ST} &= m_2 m_h m_1 \\ &= \frac{1}{f_1 f_2} \begin{bmatrix} f_1 f_2 - 2K_1 K_2 & 2K_1 (f_1 f_2 - K_1 K_2) \\ -2K_2 & f_1 f_2 - 2K_1 K_2 \end{bmatrix}. \end{aligned} \quad (2.19)$$

For the symmetric setup (see above), the path of the electron beam from the target to the source is the same as from the source to the target:

$$M_{ST} = M_{TS}. \quad (2.20)$$

The total transfer matrix for a beam starting from the source, traveling a full orbit, back to the source is:

$$\begin{aligned} M_{SS} &= M_{TS} M_{ST} = M_{ST} M_{ST} \\ &= (m_2 m_h m_1)(m_2 m_h m_1) \\ &= m_2 m_1 m_2 m_1, \end{aligned} \quad (2.21)$$

due to the simple form of m_h .

2.3 STABILITY

This section will contain all the conditions on a system (an abstract view, yet directly applicable to this thesis project) that will allow for a beam to remain in the stability region (i.e. range of parameters). For the notion of a storage ring, these conditions can allow for an eternal number of orbits, without considering any loss mechanisms (for example, perturbations). In this application, the transfer matrix becomes an invaluable tool for ascertaining the stable trajectories.

2.3.1 Phase Space

In either a many body or single electron picture, the properties of electron behaviour within the ERS can be understood by making use of phase space, which consists of six dimensions $\{x, y, z, v_x, v_y, v_z\}$. Whereby, each electron has a position with a common velocity at a given time t . Simply, a particle could be labeled in the x direction by $\{x, v_x\}$. The beam cross section is formed by all the points that define the beam and the range of angles of each electron trajectory [Humphreys (1990)]. A variety of cross section geometries are possible, such as parallelogram, octagon, or ellipse; mathematically the equations of motion are most easily decided from an elliptical cross section, thus, it will be assumed that the phase space is elliptical. The beam enters a sequence of transfer matrices referred to as a cell. The beam at the exit of the cell is described by a phase space ellipse of area ϵ_x classified by Twiss parameters (where a whole storage ring may be classified by a number of unit cells) [Wollnik (1987)].

For a system with no net acceleration, the determinant of its transfer matrix, M , will be unity. According to linear algebra this physically implies that the differences in position and velocity between individual particles will be preserved from the entrance to exit of a cell that contains linear transformation forces, which relates to the conservation of phase space parameters within the Helmholtz – Lagrange relation. This is another constraint for the stability.

The phase space ellipse takes on the recognizable mathematical form:

$$\left(\frac{x}{l_a}\right)^2 + \left(\frac{a}{l_b}\right)^2 = 1, \quad (2.22)$$

and is parameterized with the Twiss parameters A_T , B_T , and C_T :

$$x^2 C_T + 2xaA_T + a^2 B_T = \epsilon_x, \quad (2.23)$$

where $\epsilon_x = l_a l_b$ (i.e. the area of the ellipse). Here the ellipse is defined in $\{x, a\}^{\dagger\dagger}$ space, which merely describes the lateral position x and the longitudinal position a . A particle

^{††} There is a direct analogy using x and y axes labels, and it defines the position of each trajectory.

that moves once around the ellipse has traveled the full length of a unit cell. A phase – space mapping can be done: $\{x, a\} \rightarrow \{u, v\}$ to represent the ellipse as a circle (a result of $\det M = 1$). As a particle moves from one position at time t_1 , to another position at a later time t_2 , it will move an angle σ around the circle (which is referred to as a ‘phase shift’, which measures the difference in the cell length to the actual travel length of a particle along the optic axis, see figure 2.8). Suppose the phase space ellipse at the entrance of the cell is equal to the ellipse at the exit of the cell, i.e. conservation of phase space, this gives the transfer matrix of the following form:

$$\begin{bmatrix} m_{11} & m_{12} \\ m_{21} & m_{22} \end{bmatrix} = \begin{bmatrix} \cos \sigma + A_T \sin \sigma & B_T \sin \sigma \\ -C_T \sin \sigma & \cos \sigma - A_T \sin \sigma \end{bmatrix}, \quad (2.24)$$

which expresses σ in relation of the Twiss parameters, and is a common form within storage rings [Courant and Snyder (1958), Wollnik (1987), and Tzenov (2004)]. Thus, the trace of transfer matrix will express σ independent of the Twiss parameters that will trivialize the expression for the phase shift, namely:

$$\text{Tr}(M) = m_{11} + m_{22} = 2 \cos \sigma \quad (2.25)$$

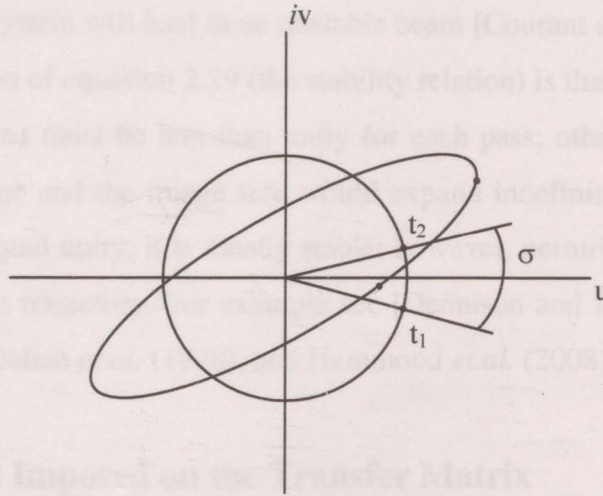


Figure 2.8: A particle exists on two points of a phase space ellipse at two different times. The ellipse is mapped into a circle, and the points that were on the ellipse become transformed to two new points on the circumference at times t_1 and t_2 separated by the phase shift σ .

The form of a circle in (u, v) space is [for example see, Mathews and Howell (2001)]:

$$w = u + iv = \sqrt{\epsilon_x} e^{i\sigma} \quad (2.26)$$

$$u^2 + v^2 = \varepsilon_x. \quad (2.27)$$

To retain the circular geometry, the angle σ must be real.

Considering the possibility of a complex angle (meaning an angle with an imaginary component: $\sigma = \alpha + i\beta$), will result in more solutions than for a completely real angle:

$$\exp[i(\alpha + i\beta)] = e^{-\beta} \exp(i\alpha). \quad (2.28)$$

Viewing equation 2.28 reveals that a complex angle will give an exponential deviation from the trajectory (coming from the $e^{-\beta}$ term) resulting in an unstable orbit (the phase space portrait is now hyperbolic) [José (1998)]. Therefore, for a purely real σ the particles will remain confined to the orbit trajectory ($|\cos \sigma| \leq 1$). Therefore the condition for stability comes from equations 2.25 and 2.28:

$$\frac{1}{2} |Tr(M)| \leq 1. \quad (2.29)$$

The condition of stability is ultimately related to the phase shift. For the result $|\cos \sigma| = 1$ the storage device will be stable for a perfect machine; however, a slight misalignment within the physical system will lead to an unstable beam [Courant and Snyder (1958)]. A physical interpretation of equation 2.29 (the stability relation) is that the overall radial and angular magnifications must be less than unity for each pass; otherwise, the trajectories would quickly diverge and the image size would expand indefinitely. For the case that the magnifications equal unity, it is ideally stable; however, perturbations may induce an escape from the orbit trajectory. For example see [Dennison and Berlin (1946), Courant and Snyder (1958), Dahan *et.al.* (1998), and Hammond *et.al.* (2008)].

2.3.2 Constraints Imposed on the Transfer Matrix

The physical degree of freedom that causes the system to operate in a given mode is the voltage on each lens element, namely: V_1 , V_2 , and V_3 of the three cylindrical elements, making up each of the lenses. It has already been mentioned that the K term in the transfer matrices correspond to geometric lengths, which are accordingly applied to cylindrical lenses as well. A stable working system is dictated by equation 2.29 (the stability

relation), thus, the transfer matrix will reveal the physical voltages capable of producing a stable working system. The net effect of a beam transported within the ERS will also be revealed through the analysis of the setup conditions.

i. Unity Matrix

A proposal for the transfer matrix M_{SS} is:

$$M_{SS} = \begin{bmatrix} 1 & 0 \\ 0 & 1 \end{bmatrix}. \quad (2.30)$$

Here, all final configurations are identical to the initial; i.e. trajectories are precisely repeated on each orbit (positions and angles):

$$\begin{bmatrix} r_1 \\ r'_1 \end{bmatrix} = \begin{bmatrix} 1 & 0 \\ 0 & 1 \end{bmatrix} \begin{bmatrix} r_0 \\ r'_0 \end{bmatrix} = \begin{bmatrix} r_0 \\ r'_0 \end{bmatrix}. \quad (2.31)$$

Note that equation 2.30 satisfies both the determinant and trace relations: $\det M_{SS} = 1$, $|Tr M_{SS}| = 2$ (recall, the system is unstable for $Tr(M_{SS}) > 2$). Furthermore, because:

$$M_{SS} = M_{ST} M_{ST}, \quad I^2 = (-I)^2 = I \quad (2.32)$$

then,

$$M_{ST} = \begin{bmatrix} 1 & 0 \\ 0 & 1 \end{bmatrix}, \begin{bmatrix} -1 & 0 \\ 0 & -1 \end{bmatrix} \quad (2.33)$$

are the possibilities for the source to target transfer matrix. $M_{ST} = I$ can be implemented by setting $K_1 = K_2 = 0$ in equation 2.19 (causing the off diagonal elements of the M_{ST} matrix to vanish). See figure 2.4 for a geometrical interpretation of K_1 and K_2 . Here, the position of the source is at the first principle focus, and the entrance of the HDA 1 is at the second principle focus. Although a unity transfer matrix is only stable for a perfect system, it is an acceptable solution.

For the second case, $M_{ST} = -I$ would once again require the off diagonal elements to vanish. A more novel approach is to rewrite the matrix M_{ST} (equation 2.19) in a diagonal

form prior to equating it to the inverse matrix (i.e. $-I$). The conclusion is found to be non-trivial (see Appendix I-B):

$$f_1 f_2 = K_1 K_2. \tag{2.34}$$

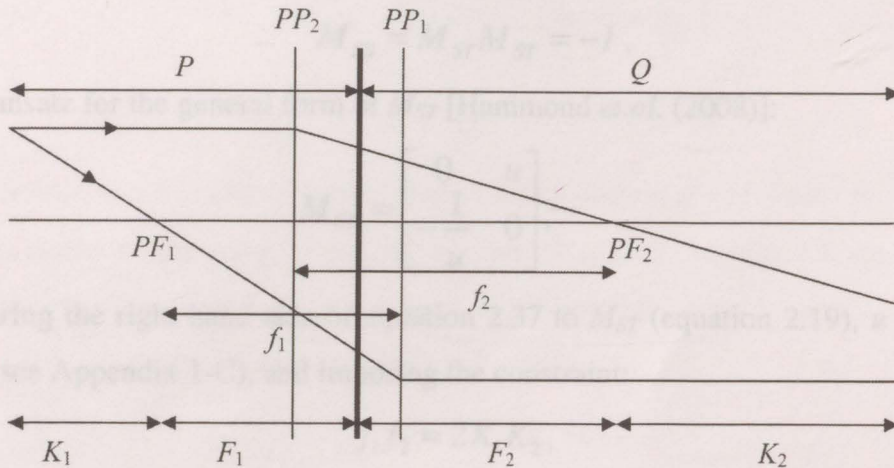


Figure 2.9: Schematic diagram showing the positions of the principal planes PP_1 and PP_2 and the principal foci PF_1 and PF_2 of a lens, together with the focal lengths f_1 and f_2 , the mid-focal lengths F_1 and F_2 and the lengths K_1 and K_2 defined in the text. The thick vertical line is the reference plane. The distances P and Q refer here to the positions of the source and the entrance to HDA 1 and do not refer to the positions of a conjugate object and image [Hammond *et.al.* (2008)]

This implies that the lengths will have to “match - up” at some point, implying that either the object or the image length would be extended from their assumed positions. This result does not satisfy the formation of an image from an object in terms of the cardinal points and the principles of electron optics [Harting and Read (1976)]. As seen in figure 2.9 the two focal lengths will always extend beyond the lengths of K_1 and K_2 ; thus, the product of the two focal lengths will never match the product of the object and image position from the principle foci. Hence $M_{ST} = -I$ is not considered a possible solution.

To achieve an overall transfer matrix of $M_{SS} = I$, the source to target transfer matrix must also be unity.

Following the same logic as above, consider a setup that has the trajectory return to the original position after two orbits, and still obey the trace and determinant conditions. The form of the source to source transfer matrix is:

$$M_{SS} = \begin{bmatrix} -1 & 0 \\ 0 & -1 \end{bmatrix} = -I. \quad (2.35)$$

The image after one orbit is then ‘inverted’, i.e. $(r, r') \rightarrow (-r, -r')$. An investigation of the relationship for M_{ST} will determine its possible forms:

$$M_{SS} = M_{ST}M_{ST} = -I. \quad (2.36)$$

Make an ansatz for the general form of M_{ST} [Hammond *et.al.* (2008)]:

$$M_{ST} = \begin{bmatrix} 0 & u \\ -\frac{1}{u} & 0 \end{bmatrix}, \quad (2.37)$$

by comparing the right hand side of equation 2.37 to M_{ST} (equation 2.19), u is found to equal K_1 (see Appendix 1-C), and imposing the constraint:

$$f_1 f_2 = 2K_1 K_2, \quad (2.38)$$

in order to cause the diagonal components of M_{ST} to vanish. As explicitly seen in Appendix 1-C is the solution for u in this setup:

$$u = K_1. \quad (2.39)$$

This is a physical solution, and will be discussed in more detail below.

ii. Deviation from the unity Matrix

In real experiments, achieving the unity matrix is very difficult. Aberrations and misalignments will cause a deviation from the unit matrix. Suppose the electron trajectories are measured at a fixed point (for example the position of the source), then in this operation they return to the initial phase space parameters every N full orbits; whereby, a deviation from the ideal transfer matrices given above will occur. The trajectories may retrace themselves with an inherent “shift” in the position. For example a re-trace occurs every $4/3 \pi$, which requires three full orbits to have $(r, r') \rightarrow (r, r')$ measured at the same position.

The source to source transfer matrix can best be amended in a similar manner to section (i) of this chapter employing the Twiss parameters [Courant and Snyder (1958), Hammond *et.al.* (2008)]:

$$M_{SS} = \cos \theta \begin{bmatrix} 1 & 0 \\ 0 & 1 \end{bmatrix} + \sin \theta \begin{bmatrix} b_{11} & b_{12} \\ b_{21} & -b_{11} \end{bmatrix} \quad (2.40)$$

$$\text{where, } \cos \theta = \frac{1}{2} \text{Tr}(M_{SS}) = \frac{1}{2} ((M_{SS})_{11} + (M_{SS})_{22})$$

($M_{SS} = M_{TS} M_{ST}$, and M_{ST} comes from equation 2.19), and $\sin \theta = (1 - \cos^2 \theta)^{1/2}$. From the above expression of the transfer matrix, M_{SS} and M_{ST} from section 2.1 are matched to solve for the physical conditions. To achieve such a setup it is concluded that $b_{11} = 0$ (see appendix I-D). Thus, the transfer matrix is reduced to:

$$M_{SS} = \begin{bmatrix} \cos \theta & b_{12} \sin \theta \\ b_{21} \sin \theta & \cos \theta \end{bmatrix}, \quad (2.41)$$

which is further simplified through the condition that the Helmholtz – Lagrange equation demands conservation of phase space, i.e. the determinant of the transfer matrix must equal unity. The transfer matrix is then trivialized to an expression dependent only on θ and b_{12} (see appendix I-D):

$$M_{SS} = \begin{bmatrix} \cos \theta & b_{12} \sin \theta \\ -\frac{1}{b_{12}} \sin \theta & \cos \theta \end{bmatrix}. \quad (2.42)$$

Incidentally, this form of M_{SS} is analogous to the rotation matrix, whereby the angle θ corresponds to the phase shift in the phase space ellipse after traversing one orbit (or cell). It should also be noted mathematically that if $|M_{SS}| \equiv 1$ then M_{SS}^N will always be unity, thus satisfying the conservation of phase space for multiple orbits. In general, the transfer matrix takes on the form (provided a unitary determinant):

$$M_{SS}^N = \cos(N\theta) \begin{bmatrix} 1 & 0 \\ 0 & 1 \end{bmatrix} + \sin(N\theta) \begin{bmatrix} b_{11} & b_{12} \\ b_{21} & -b_{11} \end{bmatrix}. \quad (2.43)$$

The system still has a stable mode of operation (provided θ is real), however, the constraints are more limiting [Courant and Snyder (1958), Brown (1981), Hammond *et.al.* (2008)].

iii. Generalized Expression

From the last section, the electron beam will re-trace^{‡‡} itself over a number of orbits. The proposals presented above for the source to source transfer matrix^{§§} can be re – written and re – analyzed from the generalized formalism of equation 2.43 as given in the following matrix:

$$M_{ST} = \begin{pmatrix} \cos(\theta/2) & L\sin(\theta/2) \\ -\frac{\sin(\theta/2)}{L} & \cos(\theta/2) \end{pmatrix}, \quad (2.44)$$

where L is an arbitrary length, θ is a parameter in phase space and is real, and corresponds to the phase space shift after a complete orbit, then $\theta/2$ is the shift after a half orbit for the symmetric condition. A comparison of the above general expression for M_{ST} with that given in equation 2.19, will provide the physical constraints for the system. Compare the M_{11} elements:

$$(M_{ST})_{11} = \frac{1}{f_1 f_2} (f_1 f_2 - 2K_1 K_2) = 1 - \frac{2K_1 K_2}{f_1 f_2} = \cos(\theta/2). \quad (2.45)$$

This relation implies that for $\cos \theta/2$ to equal ± 1 , then once again leads to the solution $M_{ST} = \pm I$. In addition, comparing the M_{21} elements (for example):

$$(M_{ST})_{21} = -\frac{2K_2}{f_1 f_2} = -\frac{1}{L} \sin(\theta/2), \quad (2.46)$$

and noting that *both* off diagonal elements must vanish when $M_{ST} = \pm I$, will lead to the conclusion that $L \rightarrow \infty$ or 0, or $\sin(\theta/2) = 0$. Since one can show L is defined as:

$$L^2 = \frac{K_1}{K_2} (f_1 f_2 - K_1 K_2), \quad (2.47)$$

for the case that L is not finite leads to an unstable operation, and thus $\sin(\theta/2) = 0$ (for finite L) will provide a both physical and stable solution [Hammond *et.al.* (2008)].

Continuing with the general formalism, the electron trajectories require a number of passes through the M_{ST} matrix before returning to unity. Suppose the electrons require an

^{‡‡} (i.e. return to its original phase space parameters at the same measured point)

^{§§} namely $M_{SS} = \pm I$

H number of executions of the M_{ST} matrix to retrace its path or invert its path ($\pm I$); then in terms of “half passes” of the total ring, M_{11} takes on the form:

$$\cos(\theta/H) = 1 - \frac{2K_1K_2}{f_1f_2} = 1 - 2\sin^2(\theta/2H), \quad (2.48)$$

which leads to the condition:

$$K_1K_2 = f_1f_2 \sin^2\left(\frac{m\pi}{2H}\right), \quad (2.49)$$

where θ is set to $m\pi$, m is in the range $0 < m < H$, which avoids the unstable resonance conditions when $m = 0$ (i.e. $K_1K_2 = 0$) and $m = H$, (i.e. $K_1K_2 = f_1f_2$).

There arise special solutions for the cases where m happens to be an exact integer:

1. An even integer will return to the unity matrix, i.e. H number of half orbits gives $M_{ST} = I$.
2. An odd integer of m will return M_{ST} to the form of the inverse matrix, namely $-I$.

Consider the case that $H = 2$ and $m = 1$, then the M_{11} element becomes:

$$K_1K_2 = f_1f_2 \sin^2\left(\frac{\pi}{4}\right) = \frac{f_1f_2}{2}. \quad (2.50)$$

Here the electron trajectories re-trace themselves after two full orbits, as $M_{ST} = -I$ after 2 half orbits, and the same condition is found from above, namely, $2K_1K_2 = f_1f_2$.

Now consider another case: $H = 3$; there are two possible integer m values ($m = 1, 2$) giving the following focusing conditions:

$$m = 1 \quad \Rightarrow \quad K_1K_2 = f_1f_2 \sin^2\left(\frac{\pi}{6}\right) = \frac{f_1f_2}{4} \quad (2.51)$$

$$m = 2 \quad \Rightarrow \quad K_1K_2 = f_1f_2 \sin^2\left(\frac{2\pi}{6}\right) = \frac{3f_1f_2}{4}. \quad (2.52)$$

Therefore, for $m = 2$ the electrons return to the original parameters for a travel length of one and half orbits:

$$M_{ST} = \begin{pmatrix} \cos(2\pi/3) & L\sin(2\pi/3) \\ -\frac{\sin(2\pi/3)}{L} & \cos(2\pi/3) \end{pmatrix} \quad (2.53)$$

$$\Rightarrow M_{ST}^3 = \begin{pmatrix} 1 & 0 \\ 0 & 1 \end{pmatrix}. \quad (2.54)$$

Therefore, for $m = 1$, the electrons will experience an inversion of their original parameters for a travel length of $1\frac{1}{2}$ orbits:

$$M_{ST} = \begin{pmatrix} \cos(\pi/3) & L\sin(\pi/3) \\ -\frac{\sin(\pi/3)}{L} & \cos(\pi/3) \end{pmatrix} \quad (2.55)$$

$$\Rightarrow M_{ST}^3 = \begin{pmatrix} -1 & 0 \\ 0 & -1 \end{pmatrix}, \quad (2.56)$$

thus, requiring three complete orbits (or six half passes) to return to the original trajectory. The odd solutions of m are theorized to be stable as long as $L \neq 0$ or ∞ , implying that the storage ring prefers a setup that has the electron beam invert rather than a precise retrace over any number of orbits, i.e. a solution of $+I$ is an unstable resonant condition.

In figure 2.10 are two graphs experimentally obtained showing the resonant profiles of the above generalized forms of the transfer matrix. Referring to figure 2.10 *each* horizontal green line represents a peak orbit spectrum of 90° scattered electrons collected within the target region (a sample spectrum that was recorded at the V_2 value of 130 V is shown in grey at the top of figure 2.10). For simplicity, the ERS was set up in a symmetric fashion, referring to equal pass energies of the HDAs at a value of 18 eV. The accelerating ratio of the lenses was held at 2.0 and 1.0 for the top and bottom graphs of figure 2.10, respectively. The middle element voltages of the lenses (which is the V_2 element) were varied in increments of two volts over the ranges indicated in the plots. The magnitude of the trace of the source to source transfer matrix M_{SS} must also be addressed in explaining the stability at a given ERS setup (see equation 2.29 of Section 3.1). The constraint of the trace inequality (equation 2.29) must be compared to the ratio K_1K_2/f_1f_2 , as predicted by the above generalized form of the M_{ST} matrix. Thus, when $Tr(M_{SS})$ is equal to “negative 2” and the ratio K_1K_2/f_1f_2 is equal to 0.5, the [$H = 2$ and $m = 1$] mode is being executed. This precise “match-up” occurs twice and is

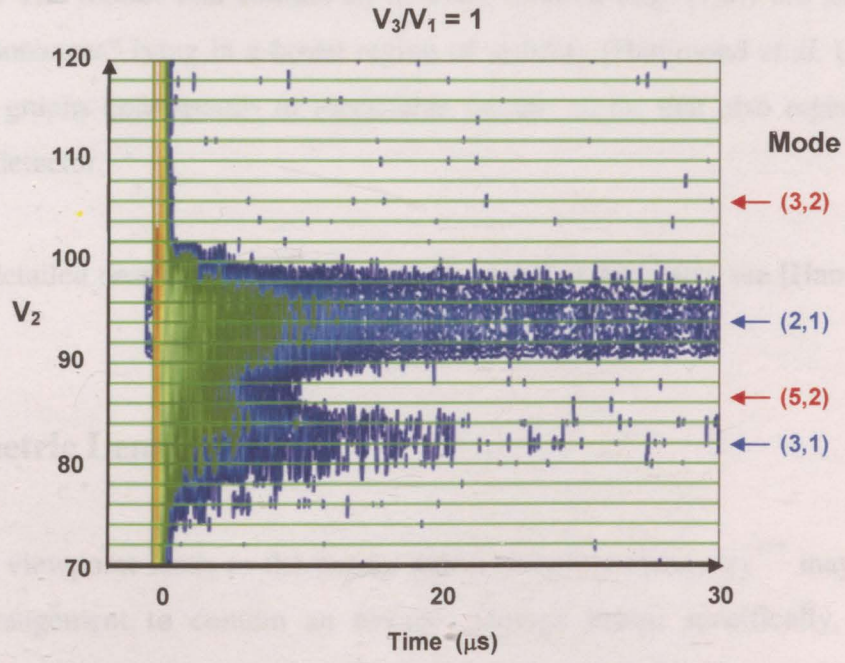
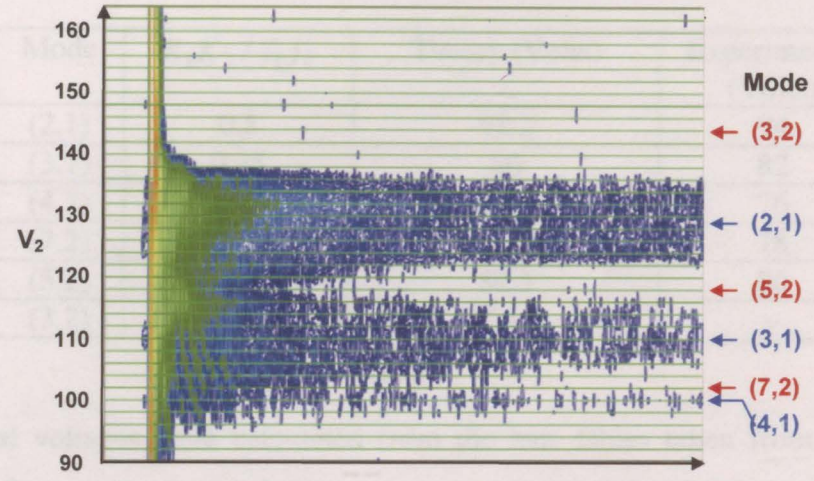
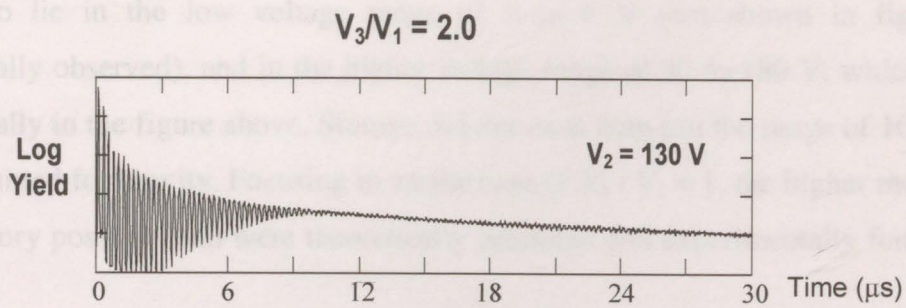


Figure 2.10: Stability graphs, displaying the resonant patterns of the unstable modes as a function of the V_3/V_1 lens voltage ratio. Each graph contains a series of spectra obtained over a broad range of V_2 values in 2 V intervals (green horizontal lines). The graph shows logarithm of the electron yield in a topographical colour contoured format: where white regions represent no storage, blue represents the adequate storage, and the green region is the significant yield. (Note that the data has been lightly “smoothed” to enhance the signal to noise ratio). Each graph includes the theoretical predicted positions of the resonant modes as obtained by Harting and Read (1976).

predicted to lie in the low voltage range of 0 to 6 V (not shown in figure, but experimentally observed), and in the higher voltage range of 90 to 180 V, which is seen experimentally in the figure above. Storage did not exist between the range of 10 to 90 V and was omitted for brevity. Focusing in on the case of $V_3 / V_1 = 1$, the higher modes $H > 2$ are in theory possible, and were theoretically predicted and experimentally found to lie at:

Mode	$K_1 K_2 / f_1 f_2$	Theory (Volts)	Experimental (Volts)
(2,1)	0.5	92.2	94
(3,1)	0.25	80	82
(4,1)	0.147	74.3	76
(7,2)	0.188	76.8	78
(5,2)	0.345	84.3	86
(3,2)	0.75	103.8	–

Table 3

The theoretical voltages were calculated from the lens tables taken from Harting and Read (1976). The modes that contain an m -even solution (e.g. (7,2)) are interpreted as “unstable resonances” lying in a broad region of stability [Hammond *et.al.* (2008)]. The noise in the graphs corresponds to metastable helium atoms that also registered at the channeltron detector.

For a more detailed description on deviations from the unity matrix see [Hammond *et.al.* (2008)].

iv. Asymmetric Lens Setup

A pragmatic viewpoint leads to the notion that a complete symmetry^{***} may not be the optimum arrangement to contain an electron storage beam; specifically, the source voltage V_s does not equal the target V_t (ultimately referring to the energy of the electrons within the source or target region, respectively). Thus, the m_2 transfer matrix is no longer the time reversal of m_1 . Assume that a left / right symmetry lies within the system

*** referring to figure 2.1, the asymmetric setup retains symmetry between lenses 1 and 4 and also between Lenses 2 and 3

(referring to figure 2.1), meaning that the lenses 1 and 4 are equal and lenses 2 and 3 are equal. In this setup, the condition $f_1 f_2 = 2K_1 K_2$ will still hold; lens 1 remains the same as in the symmetric case, and lens 2 will change to accommodate this new asymmetric setup. The lens transfer matrices m_1 and m_2 will take on the form:

$$m_1 = -\frac{1}{f_2} \begin{bmatrix} K_2 & -K_1 K_2 \\ 1 & K_1 \end{bmatrix}, \quad (2.57)$$

$$m_2 = -\frac{1}{f'_2} \begin{bmatrix} K'_2 & K'_1 K'_2 - f'_1 f'_2 \\ 1 & K'_1 \end{bmatrix}, \quad (2.58)$$

where the condition $f_1 f_2 = 2K_1 K_2$ has been substituted in the m_1 matrix. Figure 2.11 displays the behavior of the ERS as a transfer cell rather than an object and image electron optics system, which necessitates a transfer matrix.

An ansatz can be made for the form of the source to target transfer matrix in a similar manner as was done for the symmetric setup (see above):

$$M_{ST} = \begin{bmatrix} 0 & ru \\ -u^{-1} & 0 \end{bmatrix}, \quad (2.59)$$

[Hammond *et.al.* (2008)], where r is the ratio of f_1 to f'_2 (see equation 2.65 below). In this scenario the acceleration for each half orbit is non-unity, and for a single lens is:

$$\frac{f_1}{f'_2} = \left(\frac{V_S}{V_T} \right)^{1/2}. \quad (2.60)$$

see [Szilagyi (1988)].

The constraints for this setup are found from the following relation:

$$m_2 m_h m_1 = -\left(\frac{1}{f_2} \right) \left(\frac{1}{f'_2} \right) \begin{bmatrix} K_2 K'_2 + K'_1 K'_2 - f'_1 f'_2 & -K_1 K_2 K'_2 + K_1 (K'_1 K'_2 - f'_1 f'_2) \\ K_2 + K'_1 & -K_1 K_2 + K_1 K'_1 \end{bmatrix}, \quad (2.61)$$

where the following conditions (on the geometry and voltages) are required to cause the diagonal elements of M_{ST} to vanish:

$$K_2 = K'_1 \quad (2.62)$$

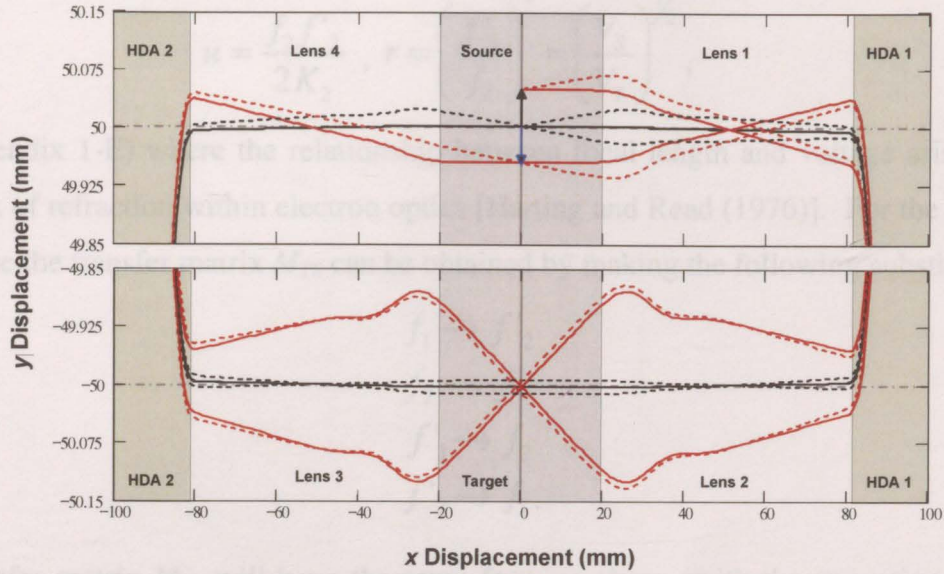


Figure 2.11: Showing the electron trajectories within the ERS. The electron trajectories pass through the interaction region and do not form an image at that point.

$$f'_1 f'_2 = 2K'_1 K'_2. \quad (2.63)$$

From the first constraint (which is purely geometrical) the distance from the entrance of the hemisphere to the second principle focus of lens one is equal to the distance of the exit of the hemisphere to the first principle focus of lens two. The final constraint is non-trivial and applies only to lens two (as the primes indicate). It is satisfied through changing one of the lens potentials and a lens position, or by varying two lens potentials. The physical arrangement of lenses of the system setup is specified by: $K_2 = K'_1$ and $K'_2 = K_1$. The distance from the target to the second principle focus of lens two is equal to the distance of the source to the first principle focus of lens one.

The individual lens potentials (V_1, V_2, V_3) and (V'_1, V'_2, V'_3) describe the fields in lens one and lens two, respectively. It is more appropriate to consider the following ratios:

$$\frac{V_2}{V_1}, \frac{V_3}{V_1}, \frac{V'_2}{V'_1}, \frac{V'_3}{V'_1}. \quad (2.64)$$

Moreover, the focal length f_1 and mid-focal lengths F_1 and F_2 are dependant on the above ratios. The four potential ratios (from above) are free to vary, provided that: $V_2/V_1 \neq V'_2/V'_1$ and $V_3/V_1 \neq V'_3/V'_1$; therefore, $f_1 \neq f_2 \neq f'_1 \neq f'_2$. Henceforth, the form of M_{ST} (equation 2.19) is achieved by having

$$u = \frac{f_2 f'_2}{2K_2}, \quad r = \left(\frac{f'_1}{f_2} \right)^2 = \left(\frac{V_S}{V_T} \right)^{1/2}, \quad (2.65)$$

(see appendix 1-E) where the relationship between focal length and voltage arises from the index of refraction within electron optics [Harting and Read (1976)]. For the target to the source the transfer matrix M_{TS} can be obtained by making the following substitutions

$$\begin{aligned} f_1 &\rightarrow f'_2 \\ f_2 &\rightarrow f'_1 \\ f'_1 &\rightarrow f_2 \\ f'_2 &\rightarrow f_1. \end{aligned} \quad (2.68)$$

The transfer matrix M_{TS} will have the same form as above, with the exception that the determinant will give a value r_{ts} (physically it represents a deceleration). There is geometrical symmetry in the system; thus, for M_{TS} , the K_i values remain unaltered throughout the equations, and reappear identically as for M_{ST} . Therefore, the transfer matrix is:

$$M_{TS} = \begin{bmatrix} 0 & r_{ts} u_{ts} \\ -u_{ts}^{-1} & 0 \end{bmatrix}. \quad (2.66)$$

From the above substitutions, the variables that define M_{TS} are:

$$u_{ts} = \frac{f_1 f'_1}{2K_2}, \quad r_{ts} = \left(\frac{f'_2}{f_1} \right)^2 = r^{-1}. \quad (2.67)$$

By imposing the condition of no overall acceleration, and if the first half of the orbit is given by equation 2.59, which is accelerating the electrons by a factor r , then the second half of the orbit must decelerate the electrons by $1/r$, which imposes the second half of the orbit to be the time reverse of the top, i.e. m_1 is time reverse of m_2 with an acceleration of r . Then $f'_1 = f_1$ and $f'_2 = f_2$, and $u = f_2^2/2K_2$, $u_{ts} = f_1^2/2K_2$. Therefore, the source to source transfer matrix is:

$$M_{SS} = \begin{bmatrix} 0 & r_{ts} u_{ts} \\ -u_{ts}^{-1} & 0 \end{bmatrix} \begin{bmatrix} 0 & ru \\ -u^{-1} & 0 \end{bmatrix}$$

$$\begin{aligned}
&= \begin{bmatrix} 0 & r^{-1}u_{ts} \\ -u_{ts}^{-1} & 0 \end{bmatrix} \begin{bmatrix} 0 & ru \\ -u^{-1} & 0 \end{bmatrix} \\
&= \begin{bmatrix} -r^{-1}u_{ts}u^{-1} & 0 \\ 0 & -u_{ts}^{-1}ru \end{bmatrix} \\
&= \begin{bmatrix} -\frac{f'_1 f'_2}{f_1 f_2} & 0 \\ 0 & -\frac{f_1 f_2}{f'_1 f'_2} \end{bmatrix} \\
&= \begin{bmatrix} -1 & 0 \\ 0 & -1 \end{bmatrix}. \tag{2.68}
\end{aligned}$$

The result leads to the inverse matrix in a corresponding style to the symmetric setup, and implies that the asymmetric setup has a stable solution.

v. Aberrations

The higher order effects of the hemispherical deflector analyzer will add loss effects that were not addressed in the above analysis. The zeroth order effect of the HDA was given in the m_h transfer matrix, which merely inverts the beam parameters (mirror effect). The first and second order effects are the chromatic and angular aberrations, respectively, that are a result of the dispersion of electron trajectories within the HDA. A third order effect is the spherical aberration that arises from the fundamental spread in the beam trajectories in the lenses [Lawson (1977), Harting and Read (1976)]. The details for aberration effects within the ERS can be found in [Hammond *et.al.* (2008)], and the results will be presented here.

Assume a mean energy of the electrons of E_0 and a total energy of $E = E_0 + \Delta E$, where $\Delta E \ll E_0$, the radial position at the exit of an HDA increases by $\Delta r = 2r_0 \Delta E_0 / E_0$. Therefore, one full orbit will have the effect of two Δr aberrations, and every succeeding orbit will be an $N - 1$ multiple of the chromatic aberrations of one full pass (where N is the number of full orbits). For $M_{SS} = -I$, the energy resolution is determined by one full orbit (not

cumulative for multiple orbits), and thus this mode is appropriate for energy analysis. For the case of $M_{SS} = I$, the position and angle of the beam at the N^{th} orbit transform as:

$$\begin{pmatrix} r_f^{(N)} \\ r_f'^{(N)} \end{pmatrix} = \begin{pmatrix} r_i \\ r_i' - \frac{4NR_0}{f_1} \frac{\Delta E}{E} \end{pmatrix}, \quad (2.69)$$

where, i and f subscripts stand for initial and final, respectively, and R_0 is the mean radius of the hemisphere (50.0 mm for the ERS). It is seen in the above equation that the angular spread is proportional to N , which implies that the apertures will ultimately limit the angular spread. In theory, the energy resolution will improve upon each orbit. However, it was stated in section (i) of this chapter on page 45 that this $M_{SS} = I$ mode is inherently unstable for a real recycling system (due to lens aberrations and mechanical alignment). Considering the special case of the generalized form of M_{ST} , the case of ($H = 2, m = 1$) have the same chromatic aberration effects as $M_{SS} = -I$, namely:

$$\begin{pmatrix} r_f^{(N)} \\ r_f'^{(N)} \end{pmatrix} = \begin{pmatrix} -r_i - \frac{4K_1 r_0}{f_1} \frac{\Delta E}{E} \\ -r_i' \end{pmatrix} \quad (2.70)$$

For the other case of ($H = 3, m = 1$, or 2), it was found that ($H = 3, m = 1$) gives the same energy resolution as the ($H = 2, m = 1$) or $M_{SS} = -I$ setups, which is equation 2.70. For the ($H = 3, m = 2$) mode there is no overall change in beam parameters, and the energy resolution is not predicted to narrow in this operation. For the general m values in an arbitrary H mode, the conclusions discussed above are very likely to repeat, namely that these modes are stable under chromatic aberrations.

Spherical aberrations are third order effects from the lenses. Thus, the aberrations are dominated by the second order effects of the HDAs, where the translation of the beam trajectories is related to the initial angle:

$$\begin{pmatrix} r_f \\ r_f' \end{pmatrix} = m_h \begin{pmatrix} r_i \\ r_i' \end{pmatrix} + \begin{pmatrix} -2R_0(r_i')^2 \\ 0 \end{pmatrix}. \quad (2.71)$$

Although, this aberration term is dependent on the square of the initial slope r' , it has a similar form to the chromatic aberration above. Under consideration of aberrations within the HDAs, the parameters of the beam remain bounded and are not cumulative.

2.3.3 Stability Modeling

The matrix analysis performed above gives a good indication that stable trajectories are obtainable for our system. Thus, the software program Charged Particle Optics 3D (CPO3D) simulator [CPO Ltd.] was used to reveal the conditions for stability of the ERS system in terms of lens voltages and pass energies specified for the ERS (i.e. parameters that the experimenter can immediately address).

The CPO3D program uses the surface charge method (or boundary element method) to give numerical solutions to Laplace's equation. CPO3D is capable of performing direct ray tracing, whereby an electrode is viewed as a continuous potential (meaning that each point "affects" the ray trace), which is more involved and thus slower to perform each simulation. An alternate method is by employing a 'mesh' instead of a continuous electrode. The 'mesh' method involves open spaces where the ray tracing integrals vanish (i.e. fewer computations. Symmetry is incorporated into the program (such as cylindrical or spherical) to allow for faster modeling. Accuracy can be sacrificed in such circumstances of complex geometries, such as a hemispherical analyzer. Moreover, a computer program will break a curved line down into a series of straight line segments, and many straight line segments will be more involved for the programmer and may not match correctly when rotated about a line of symmetry [Harvey (2000)]. Thus, care must

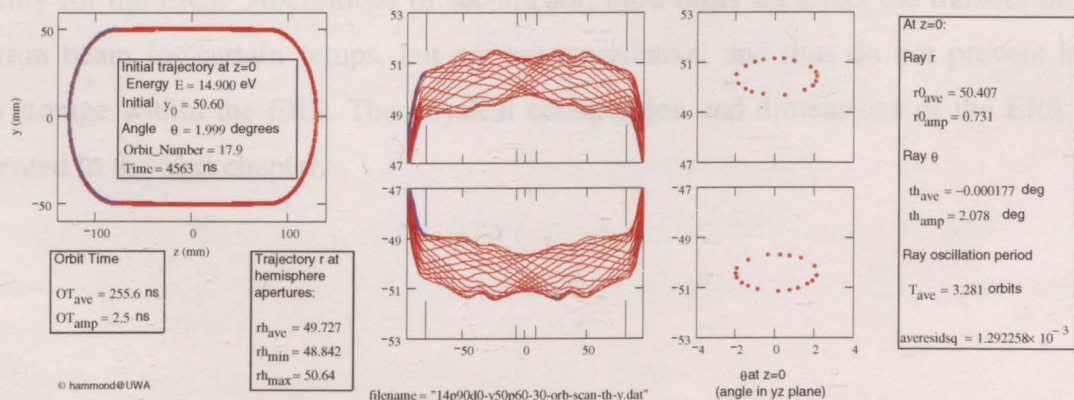


Figure 2.12: A more detailed view of the beam, *left* displays the beam orbiting throughout the ERS storage ring in the CPO program. *Middle*, possible trajectories the beam can undergo without diverging and being lost from the storage region. *Right*, displays the beam cross section, noting that any electron that lies outside the ellipse will diverge and be lost.

be taken by the user to minimize these effects. The CPO program was used with Dr. Hammond's research group in Australia [Hammond website] to simulate the storage conditions, matching the system in Windsor [Reddish website]. The diagram above shows a sample simulation performed with CPO3D. The trajectories are shown on the left and center throughout the whole ERS ring. On the right is a view of the cross section of the beam at the source (top) and target (bottom) region, showing that all electrons with parameters that lie in that ellipse will be stored, and that losses do not occur in those regions.

2.4 SUMMARY

The general background of charged particle optics has been presented, including electrostatic lenses and hemispherical deflector analyzers. The lenses and energy analyzers were further defined and specified for the ERS ring. Although there is a cylindrical symmetry for the straight lenses and spherical symmetry within the energy analyzers, due to the two dimensional focusing of the HDAs, the two systems come together in well matched form. The analogy to light optics continued through the expression of transfer matrices for every element that acts on the electron beam within the ERS. An overall transfer matrix was formed for a full orbit within the ERS, which by applying general conditions for storage within a closed ring, provided the conditions of stability for the ERS. Aberrations of second and third order do affect the transfer of the electron beam for certain setups, but are not cumulative, and thus do not prevent long term storage within the ERS. The physical construction and dimensions of the ERS are presented in the next chapter.

REFERENCES

- Banford A.P., The Transport of Charged Particle Beams, Spon: London (1966)
- Brown K.L., *Nucl. Instrum. Methods*, **187** (1981) 51
- Brunt J.H.M., Read F.H., and King G.C., *J. Phys. E: Sci. Instrum.* **10** (1977) 134 – 139
- Courant E.D., and Snyder H.S., *Ann. Phys.* **3** (1958) 1 – 48
- CPO Programs, <http://www.electronoptics.com/>, **CPO Ltd.**
- Dahan M., Fishman R., Heber O., Rappaport M., Altstein N., Zajfman D., and van der Zande W.J., *Rev. Sci. Instrum.*, **69** Issue 1 (1998) 76 – 83
- Dahl D., SIMION 3D Version 7.0 User's Manual, Bechtel BWXT IDAHO, LLC (2000)
- Dennison D.M., and Berlin T.H., *Phys. Rev.*, **70** (1946) 58
- Dietrich W., *Z. Phys.*, **152** (1958) 87
- Geiger J., *Z. Phys.*, **177** (1964) 138
- Goldstein H., Classical Mechanics, Addison Wesley, 2002
- Grivet P., Electron Optics, Pergamon Press, 1965
- Hammond P., Read F., Harvey P., Tessier D.R., and Reddish T., In Progress, 2008
- Hammond P., website: <http://internal.physics.uwa.edu.au/~hammond/>
- Harting E., and Read F., Electrostatic Lenses, Elsevier Scientific Publishing Ltd. 1976
- Harvey P., Computer Simulation of a Novel Electron Recycling Spectrometer, Thesis (2000) Victoria University of Manchester
- Humphreys S. Jr., Charged Particle Beams, John Wiley and Sons, 1990
- Imhof R. E., Adams A., and King G. C., *J. Phys. E*, **9** (1976) 138
- José J.V., and Saletan E.J., Classical Dynamics: A Contemporary Approach, Cambridge University Press 1998
- Klemperer O., Electron Optics 3ed edition, Cambridge University Press, 1971
- Lawson J.D., The Physics of Charged Particle Beams, Clarendon Press – Oxford (1977)
- Mathews J.H., and Howell R.W., Complex Analysis for Mathematics and Engineering 4th edition, Jones and Bartlett Publishers Inc. 2001.
- Paszkowski B., Electron Optics, Iliffe Books Ltd., 1968
- Pierce J.R., Theory and Design of Electron Beams, Van Nostrand Reinhold (1954)
- Purcell E.M., *Phys. Rev.*, **54** (1938) 818
- Read F.H., Comer J., Imhof R.E., Brunt J.N.H., and Harting E., *J. Electr. Spectr. Rel. Phenom.*, **4** (1974) 293 - 312

Reddish T.J., website: <http://web2.uwindsor.ca/courses/physics/reddish/TJR-HomePage.htm>

Simpson J.A., *Rev. Sci. Instrum.*, **35** (1964) 1698

Sturrock P.A., Static and Dynamic Electron Optics: An Account of Focusing in Lens, Deflector and Accelerator, Cambridge University (1955)

Szilagyi M., Electron and Ion Optics, Plenum Press, 1988

Tzenov S.I., Contemporary Accelerator Physics, World Science Publishing Company (2004)

Wollnik H., Optics of Charged Particles, Academic Press Inc. 1987

Zouros T.J.M., and Benis E.P., *J. Electr. Spectr. Rel. Phenom.*, **125** (2002) 221–248

Zouros T.J.M., Benis E.P., and Chatzakis I., *Nuc. Instrum. Meth. B*, **235** (2005) 535–539

Zouros T.J.M., *J. Elect. Spect. Rel. Phenom.*, **152** (2006) 67 – 77

34 SUMMARY

REFERENCES

CHAPTER 3: EXPERIMENTAL I* (ERS) SYSTEM DESIGN

3.1 THE ELECTRON RECYCLING SYSTEM (ERS)	64
3.1.1 Overview	64
3.1.2 Cylindrical Lens	72
3.1.3 Vacuum Chamber	73
3.2 ELECTRON GUN	74
3.2.1 Gun Design	74
3.2.2 Pulsing Circuit	81
3.3 VOLTAGE POWER SUPPLY SCHEMATIC	85
3.4 SUMMARY	86
REFERENCES	87

3.1.1 Overview

The general schematic for the ERS storage ring is displayed in figure 3.1 (below). As introduced in Chapter 2, the ERS consists of two hemispherical deflector analyzers, four focusing and collimating lens stacks (labeled 1 to 4), a source and target region, an electron gun (see below), a Parafly cup, and five channel electron multipliers (C.E.M., only three are shown in figure 3.1). Referring to figure 3.1, the lens stack in line with the electron gun contains the 'source region' and will henceforth be labeled as the source stack, and similarly the lens stack that contains the gas source (not shown in figure 3.1 see figure 3.3) will be labeled as the interaction stack (this labeling will reduce any confusion that is independent of the orientation of the ERS storage ring). Due to the three dimensional aspect of the ERS instrument, figures 3.2 and 3.3 (given below) are provided to display the source and interaction stacks with a rotation of 90 degrees about the optic axis to reveal the other two C.E.M. detectors that were not visible in figure 3.1.

* This Chapter is the product of joint research

3.1 THE ELECTRON RECYCLING SYSTEM (ERS)

The previous two chapters introduced the background and theory for the instrument that will be presented in this chapter. The system was introduced in Chapter 2 as being a confinement ring for charged particles (electrons being the only tested species on this apparatus). From the transfer matrices and conditions for stability that were presented in the last chapter, it can be concluded that the “small” size of the ERS limits the energy of the charged particles that can be stored. This chapter will cover the detailed parameters and geometry of the ERS. The cylindrical lenses and hemispherical deflector analyzers (HDAs) that were discussed in chapter 2 will be shown in proportion displaying all dimensions. The electron gun is the source of the electron beam and will be presented in this chapter as a prelude to chapter 4 that covers the styles of injection within the ERS. Finally, a layout of all the voltage supplies will be given, including reference grounds.

3.1.1 Overview

The general schematic for the ERS storage ring is displayed in figure 3.1 (below). As introduced in Chapter 2, the ERS consists of two hemispherical deflector analyzers, four focusing and collimating lens trains (labeled 1 to 4), a source and target region, an electron gun (see below), a Faraday cup, and five channel electron multipliers (C.E.M., only three are shown in figure 3.1). Referring to figure 3.1, the lens stack in line with the electron gun contains the ‘source region’ and will henceforth be labeled as the *source stack*, and similarly the lens stack that contains the gas source (not shown in figure 3.1 see figure 3.3) will be labeled as the *interaction stack* (this labeling will reduce any confusion that is independent of the orientation of the ERS storage ring). Due to the three dimensional aspect of the ERS instrument, figures 3.2 and 3.3 (given below) are provided to display the source and interaction stacks with a rotation of 90 degrees about the optic axis to reveal the other two C.E.M. detectors that were not visible in figure 3.1.

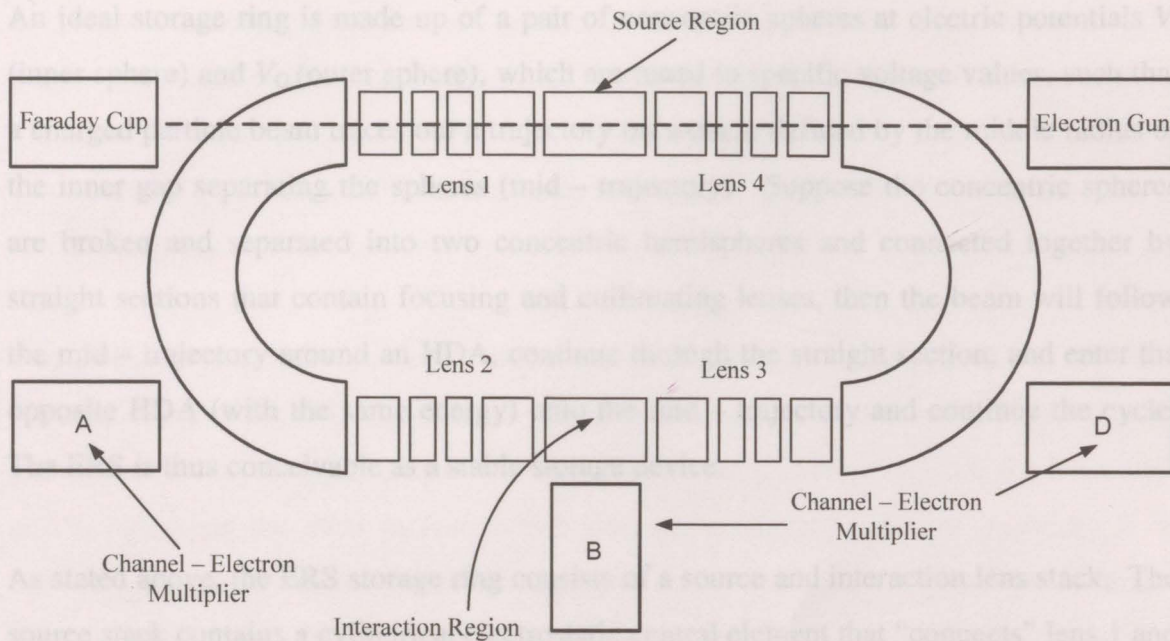


Figure 3.1: Schematic of ERS storage ring displaying detectors, HDAs, and lens stacks.

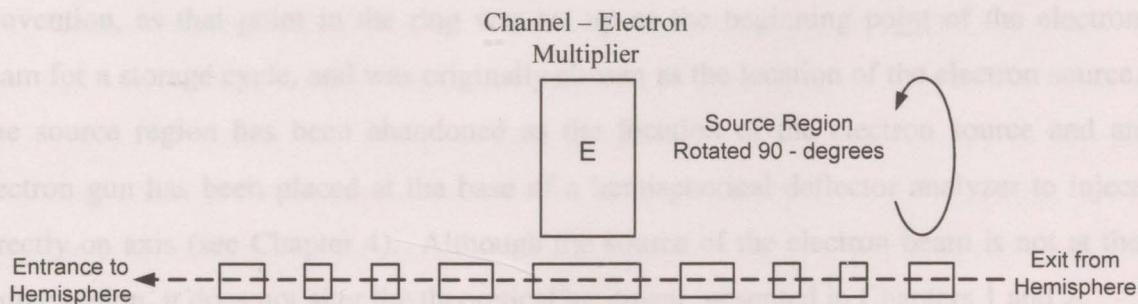


Figure 3.2: Schematic of source stack.

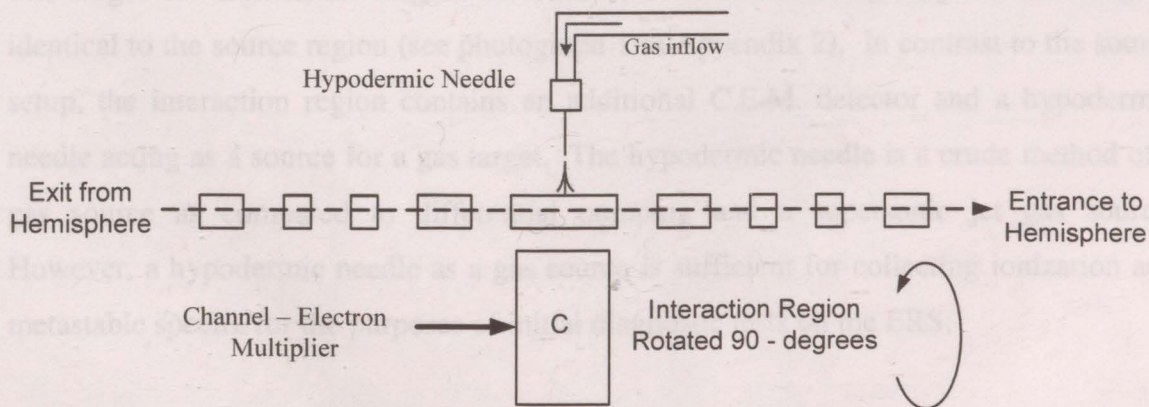


Figure 3.3: Schematic of interaction stack.

An ideal storage ring is made up of a pair of concentric spheres at electric potentials V_I (inner sphere) and V_O (outer sphere), which are tuned to specific voltage values, such that a charged particle beam traces out a trajectory on a circle defined by the middle radius of the inner gap separating the spheres (mid – trajectory). Suppose the concentric spheres are broken and separated into two concentric hemispheres and connected together by straight sections that contain focusing and collimating lenses, then the beam will follow the mid – trajectory around an HDA, continue through the straight section, and enter the opposite HDA (with the same energy) onto the mid – trajectory and continue the cycle. The ERS is thus conceivable as a stable storage device.

As stated above, the ERS storage ring consists of a source and interaction lens stack. The source stack contains a cylindrical electrostatic central element that “connects” lens 1 and lens 4, referred to as the source region. The labeling “source region” is done for convention, as that point in the ring was set up as the beginning point of the electron beam for a storage cycle, and was originally chosen as the location of the electron source. The source region has been abandoned as the location of the electron source and an electron gun has been placed at the base of a hemispherical deflector analyzer to inject directly on axis (see Chapter 4). Although the source of the electron beam is not at the source region, it does not alter the theoretical treatment presented in Chapters 1 and 2.

The target or “interaction” region in essence, consists of a single cylindrical element identical to the source region (see photograph 1 in Appendix 2). In contrast to the source setup, the interaction region contains an additional C.E.M. detector and a hypodermic needle acting as a source for a gas target. The hypodermic needle is a crude method of a gas source as compared to differential pumping and a supersonic jet gas source. However, a hypodermic needle as a gas source is sufficient for collecting ionization and metastable spectra for the purposes of initial diagnostic tests on the ERS.

The hypodermic needle is located in the interaction stack opposite detector C (see figure 3.3). Thus, an emerging gas jet will move at thermal energies with momentum directed toward detector C (low energy ions $\sim kT$ that will slowly drift toward the detector), which

is designed to collect ions that are produced by each pass of the electron beam. The needle is metallic copper that measures 0.51 mm in outer diameter and 0.17 mm in inner diameter. The needle is cradled by a stainless steel plate measuring 30 by 40 mm, and is connected by a 1/8th inch stainless steel pipe to allow for gas transfer from the 'air' side to the 'vacuum' side of the chamber.

The ERS system includes five "Single Channel Electron Multipliers" (or Channel Electron Multiplier: C.E.M. same as above, see Photonis Reference). These C.E.M. detectors work on a similar idea to a photomultiplier tube. Electrons enter the front cone and impact upon the inner surface, which liberates secondary electrons (typically 3 for each incident electron) that get accelerated and collide with a surface at a point further down the spiral and liberate more secondary electrons. The process continues until the electrons reach the end of the C.E.M. detector. The electron current is applied through a 50 Ω resistor, which results in a 500 μ V to 500 mV pulse being generated (giving rise to a time structure within the electron signal). The front cone is raised to a potential of ~ 50 V (relative to real ground) to help give the impact electrons sufficient energy to liberate secondary electrons from the surface, as the surface usually consists of a high work function in order to reduce the number of thermal electrons that would result in electrical noise (see figure 3.4 for details) [Moore (1989)].

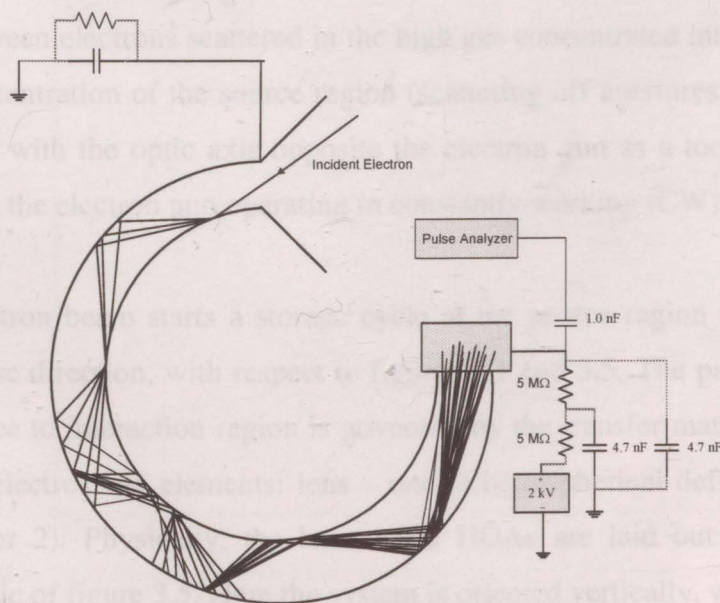


Figure 3.4: Channeltron detector showing electron pulse cascade.

Channeltron A is positioned off the optic axis at the back of the hemisphere behind an exit through-hole. Ions are collected at detector – A from electron-atom collisions from the gas that has dispersed throughout the first half of the interaction stack and the HDA. Signal collected from the detector A can be compared to the ions collected from a higher gas concentration in the interaction region at the center of the interaction stack, setting up time-of-flight type system. Detector B is located at the interaction cylinder (centered at the interaction region) 90° from the optic axis and 90° from the gas jet (hypodermic needle), which is designed to collect electrons scattered 90° from the gas jet. Electrons travel a short distance relative to the circumference of the ERS; therefore, detector B is used to display each pass of the electron beam. Channeltron C is placed directly in the path of the gas jet beam so as to take advantage of the inertia toward the detector, since metastable atoms or molecules are neutral and are therefore not affected by DC electromagnetic fields. Thus, detector C is used as a metastable detector. Channeltron D is placed behind the bottom HDA beneath the interaction stack, which could in principle be utilized for “beam dump” tests to aid in determining the current density of the electron beam (on the optic axis) as a function of beam orbit cycle (as a relative measurement). Finally, channeltron E is placed at the source region 90° from the optic axis. This detector is designed for two purposes: (1) to analyze the initial injected beam profile, (2) comparison between electrons scattered in the high gas concentrated interaction region to the low gas concentration of the source region (scattering off apertures). A Faraday cup is placed in line with the optic axis opposite the electron gun as a tool for initial beam diagnostics from the electron gun operating in constantly working (CW) mode.

Suppose an electron beam starts a storage cycle at the source region and travels in the counter-clockwise direction, with respect to figures 3.1 and 3.5. The path of the electron beam from source to interaction region is governed by the transfer matrices of a specific permutation of electrostatic elements: lens – one, a hemispherical deflector, and lens – two (see Chapter 2). Physically, the lenses and HDAs are laid out according to the detailed schematic of figure 3.5. Here the system is oriented vertically, which mimics the

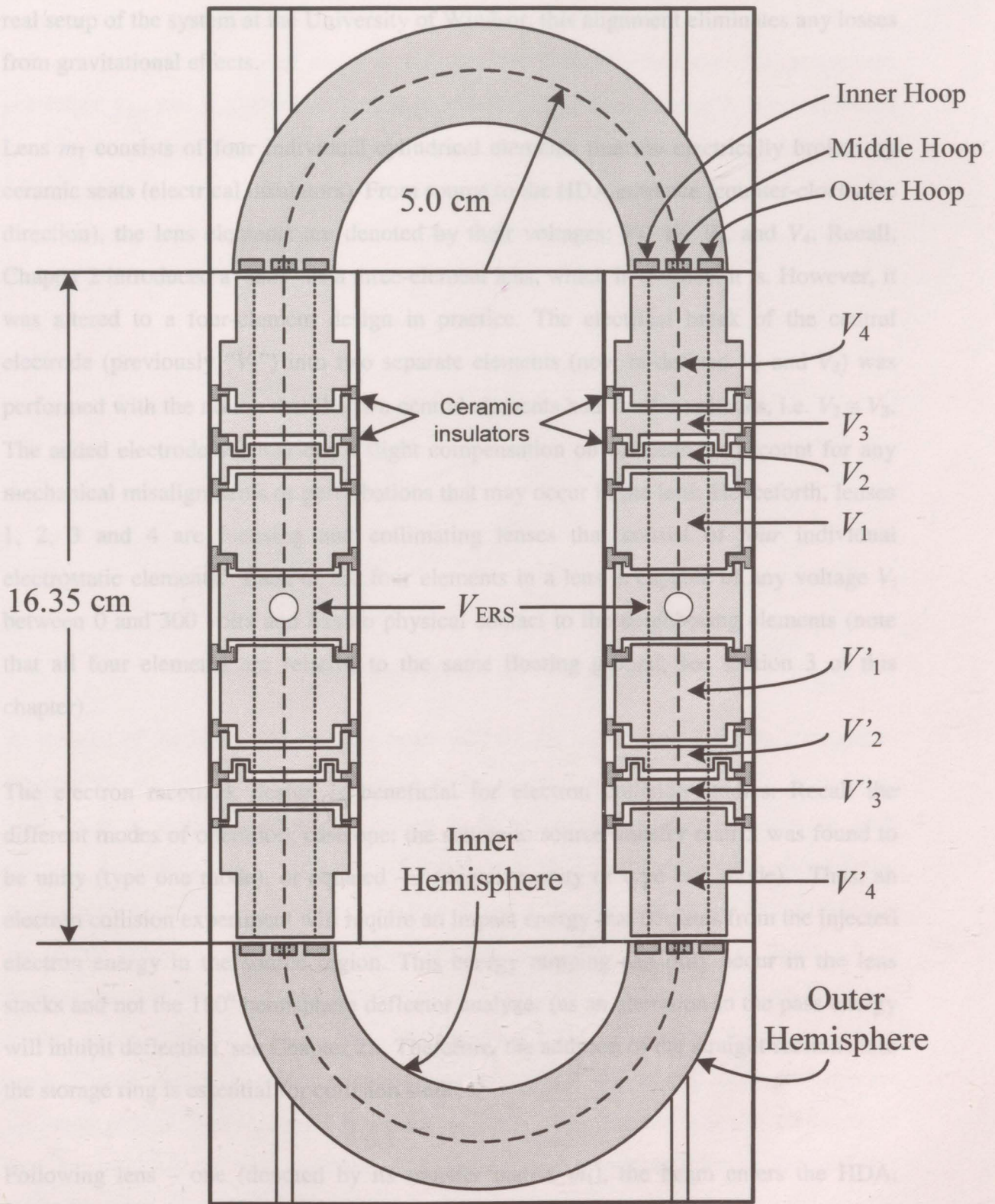


Figure 3.5: Electron Recycling System showing the break down of the lens m_1 into each electrode, HDAs, and the details of the lens geometries.

real setup of the system at the University of Windsor, this alignment eliminates any losses from gravitational effects.

Lens m_1 consists of four individual cylindrical elements that are electrically broken by ceramic seats (electrical insulators). From source to the HDA entrance (counter-clockwise direction), the lens elements are denoted by their voltages: V_1 , V_2 , V_3 , and V_4 . Recall, Chapter 2 introduced a “lens” as a three-element lens, which in essence, it is. However, it was altered to a four-element design in practice. The electrical break of the central electrode (previously “ V_2 ”) into two separate elements (now re-defined V_2 and V_3) was performed with the notion that the two central elements had similar voltages, i.e. $V_2 \cong V_3$. The added electrode V_3 provides a slight compensation on the beam to account for any mechanical misalignments or perturbations that may occur in the lens. Henceforth, lenses 1, 2, 3 and 4 are focusing and collimating lenses that consist of *four* individual electrostatic elements. Each of the four elements in a lens is capable of any voltage V_i between 0 and 300 volts and has no physical contact to the neighboring elements (note that all four elements are relative to the same floating ground, see section 3 of this chapter).

The electron racetrack design is beneficial for electron collision studies. Recall the different modes of operation; case one: the source to source transfer matrix was found to be unity (type one mode), or equaled $-I$ (negative unity or type two mode). Thus, an electron collision experiment will require an impact energy that deviates from the injected electron energy in the source region. This energy ramping can only occur in the lens stacks and not the 180° hemisphere deflector analyzer (as an alteration in the pass energy will inhibit deflection, see Chapter 2). Therefore, the addition of the straight sections into the storage ring is essential for collision studies.

Following lens – one (denoted by its transfer matrix m_1), the beam enters the HDA. Three hoops have been inserted at the hemisphere entrance and exit; classified as inner, middle, and outer, with potentials V_{IH} , V_0 , and V_{OH} , respectfully (eV_0 is the pass energy). Inner and Outer hoops are inserted at the entrance and exit of the hemisphere to

compensate for the edge effects of the electric field within the HDA. The hemispherical deflector analyzer consists of an inner and outer hemisphere (see figure 3.6) at separate potentials: V_{inn} and V_{out} . The hemisphere potentials are given in chapter 2. Typical values for the voltages for a setup of 10 eV pass energy are: $V_{\text{inn}} = 6.667$ V, $V_{\text{out}} = -4.0$ V, $V_{\text{IH}} = 3.81$ V, and $V_{\text{OH}} = -2.76$ V. The quantity R_0 is the mean radius for the concentric hemispheres. Suppose the radii of the inner and outer hemisphere are R_{inn} and R_{out} , respectively, then $R_0 = \frac{1}{2} (R_{\text{inn}} + R_{\text{out}})$.

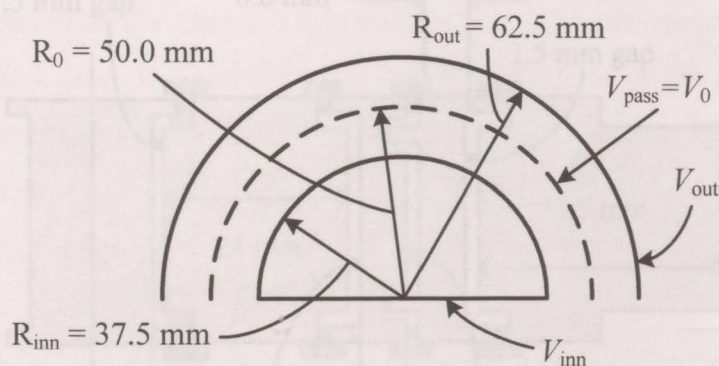


Figure 3.6: Dimensions of inner and outer hemisphere

At the exit of the HDA, the electron beam will see the hoop setup and then continue to traverse the m_2 lens (equivalent in setup to the m_1 lens, seen in figure 3.2). In order to give freedom during tuning, the voltage supplies are separately connected to each element. Following m_2 is the target region, which is a single cylindrical element that supports detectors and a gas jet nozzle (see figure 3.3). Succeeding the target region is the mirror image of the top half of the source stack as described above in figure 3.5. In order to simplify the operation of the ERS the lens stacks have certain common elements. In the source stack V_1 and V'_1 are wired together, which is repeated in the interaction stack. Finally, the top V_2 elements are the “same” voltage, and the bottom V_2 elements are the same voltage. The V_4 elements are set up in the same manner as the V_2 elements, in that they hold left and right symmetry in figure 3.5. The exception is the V_3 elements (i.e. each element is set at an individual voltage).

3.1.2 Cylindrical lens

The source and interaction lens stacks contain cylindrical electrodes to focus and collimate the electron beam. The lenses are positioned within the storage ring according to the above figures (their properties were described in Chapter 2). Shown in photograph 2 in appendix 2 is an example of a lens stack used in experiment; photograph 3 shows all of the electrodes that comprise a lens.

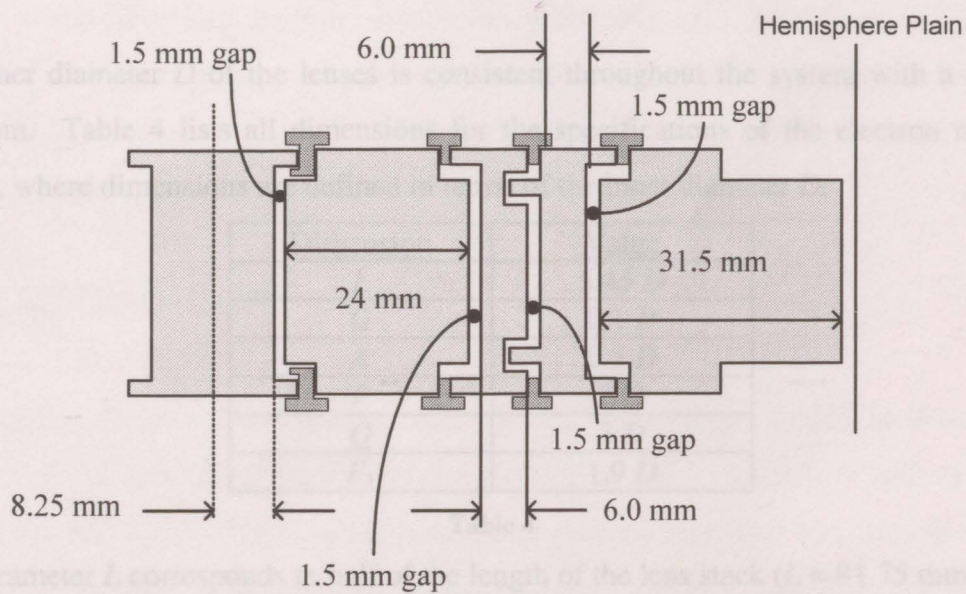


Figure 3.7: Cylindrical lens train with dimensions, and showing individual electrodes.

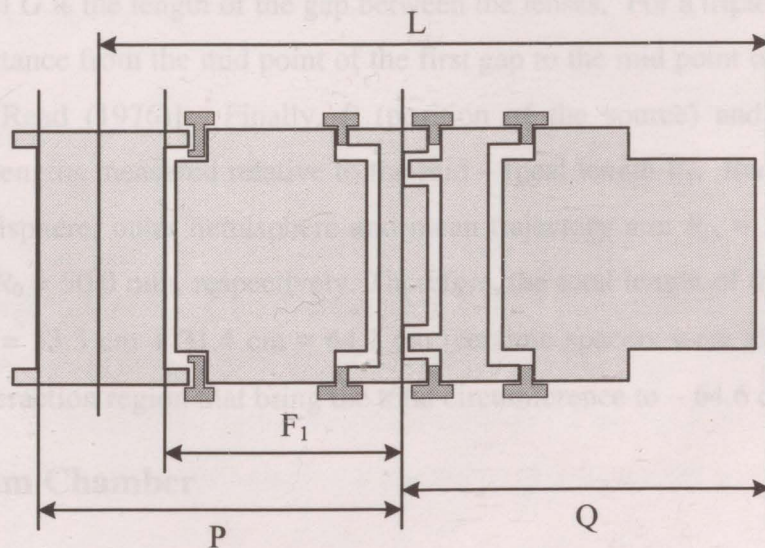


Figure 3.8: A cylindrical lens with parameters using notations from conventional electron optics.

The cylindrical electrodes in the ERS system at the University of Windsor are made of oxygen free copper and are gold plated to reduce patch fields and tarnishing that would otherwise distort the electric fields. The characters within the transfer matrices of Chapter 2 can be further classified with figure 3.7 and 3.8 (shown above), $K_1 = P - F_1$ and $K_2 = Q - F_2$. The quantity L corresponds to the length from the entrance of the HDA to the center of the source, or interaction region, which is half the distance from the entrance of a hemisphere to the exit of the other HDA.

The inner diameter D of the lenses is consistent throughout the system with a value of 15.0 mm. Table 4 lists all dimensions for the specifications of the electron recycling system, where dimensions are defined in terms of the inner diameter D .

<u>Dimension</u>	<u>Value</u>
L	$5.45 D$
G	$0.1 D$
A	$0.5 D$
P	$3 D$
Q	$3 D$
F_1	$1.9 D$

Table 4

The parameter L corresponds to half of the length of the lens stack ($L = 81.75$ mm), which is the length from the source center (or the target) to the end of the V_4 lens (see figure 3.8). The label G is the length of the gap between the lenses. For a triple lens system 'A' defines the distance from the mid point of the first gap to the mid point of the second gap [Harting and Read (1976)]. Finally, P (position of the source) and Q (hemisphere entrance) are lengths measured relative to the mid - focal length F_1 . Recall, the radii for the inner hemisphere, outer hemisphere and mean trajectory are: $R_{in} = 37.5$ mm, $R_{out} = 62.5$ mm and $R_0 = 50.0$ mm, respectively. Therefore, the total length of the optic axis is $S = 4L + 2\pi R_0 = 33.3$ cm + 31.4 cm \approx 64.1 cm (ceramic spacers were also placed in the source and interaction region that bring the total circumference to \sim 64.6 cm).

3.1.3 Vacuum Chamber

The vacuum chamber was manufactured by Torrovap Ind. Inc. and designed by Dr. Reddish (University of Windsor, Windsor, Ontario, Canada), which is of cylindrical

geometry with a height of 28.011 inches or 711.48 mm, 14 inch diameter or 355.6 mm, with wall thickness of 0.188 inch or ~ 0.5 mm. The chamber is fabricated of non – magnetic 304 grade stainless steel, and has a base weight of 315.31 pounds. The interior is lined with double layer coaxial Mu – metal magnetic shielding[†] to cancel or mitigate external alternating current (AC) and direct current (DC) magnetic fields. The chamber is placed within the center of square Helmholtz coils (oriented along three directions: North / South, East / West, and Up / Down or x , y , and z). Each element is wired by ultrahigh vacuum compatible Kaptain wire. Electrodes with voltages < 300 V are connected by solid core silver coated copper cable, and elements with electric potentials > 1.0 kV are connected by multi – core coaxial cable. All wires are transferred to the outside of the vacuum chamber by multi way electric feedthroughs.

3.2 ELECTRON GUN

Introduced in Chapter 2, the source of an electron beam for the system at Windsor is a simple electron gun. The function of the electron gun is to produce a well collimated parallel electron beam. The aim is to produce an electron beam that will enter through the back of the hemisphere and remain coincident with the optic axis at a low degree of divergence (preventing electrons to be lost to collisions with the walls and apertures within the spectrometer).

3.2.1 Gun Design

The electrons are boiled off a hot hairpin filament and the emerging electron beam, although focused, will have a broad energy spread of ΔE (of a Maxwell Distribution, with a Full Width at Half Maximum or FWHM of $\sim 2.45kT$)[‡] [Klemperer (1971)]. The tip of the filament protrudes through a truncated cone centered on the optic axis with walls at an angle of 60 degrees to the optic axis, and a top radius of 1.0 mm and bottom radius of 5.0

[†] Mu metal shielding is a metal of high permeability that has a reduced skin depth that aids in canceling out low frequency magnetic field, and certain static magnetic fields

[‡] k being the Boltzmann constant: 1.38066×10^{-23} JK⁻¹, and T being the temperature of the filament.

mm, which is biased negative with respect to the filament tip (electron energy) and “pushes” the electrons toward the back of the HDA. This truncated cone provides the “grid” within the gun. Next in line with the grid is an anode with a 1.0 mm aperture biased positive with respect to the electron energy. Following the anode are four electrodes arranged in a square layout (figure 3.9 or 3.10), with two sets of two positioned opposite from each other and are wired such that each set acts as a capacitor to produce an electric field to deflect the beam in both an ‘x’ and ‘y’ direction (referred to as deflectors in electron optics) [Klemperer (1971)], see figure 3.9:

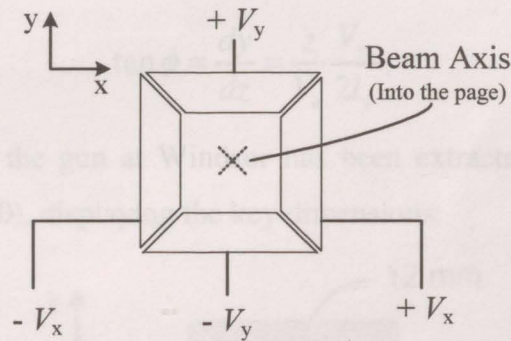


Figure 3.9: A diagram showing the deflector system, where an opposite pair of charged electrodes creates an electric field to deflect the electron beam.

Supposing the distances between each set of parallel plates are $2l_y$ and $2l_x$, then the electric field strengths for an electron beam that travels along the z axis are:

$$E_x = -\frac{V_x}{l_x}, \quad E_y = -\frac{V_y}{l_y}, \quad (3.1)$$

where V_x and V_y are the voltages on the deflectors (see figure 3.9), and the equations of motion are ($f = ma$):

$$m \frac{d^2 y}{dt^2} = (-e) E_y \quad (3.2)$$

$$m \frac{d^2 x}{dt^2} = (-e) E_x \quad (3.3)$$

$$m \frac{d^2 z}{dt^2} = 0. \quad (3.4)$$

The deflection angle ϕ_y is obtained by solving the above equations for a single deflection axis (and the beam axis), which can be applied in a similar fashion to the second deflecting axis through symmetry.[§] This leads to an equation for the y position:

$$y = \frac{z^2}{V_e} \frac{V_y}{4l_y}, \quad (3.5)$$

where E_e is the energy of the electrons at the point prior to entering the deflecting field region: $E_e = eV_e$. Finally, the deflection of a given set of deflector plates is properly defined by [Klemperer (1971)]:

$$\tan \phi = \frac{dy}{dz} = \frac{z}{V_e} \frac{V_y}{2l_y}. \quad (3.6)$$

The deflector setup for the gun at Windsor has been extracted from figure 3.9 and is shown below (figure 3.10), displaying the key dimensions:

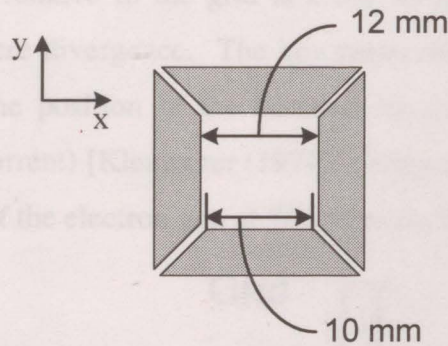


Figure 3.10: Basic schematic of deflector elements with dimensions.

For an experiment that employs an electron gun with a deflector system, the user does not rely on equation 3.6; alternatively, the voltages $\pm V_x$ and $\pm V_y$ are chosen by the user to optimize the beam current at a detector on the beam axis. Shown in figure 3.11 is a demonstration of the function of a deflector system (ignoring the x – direction).

The electrons are produced by thermal emission, i.e. electrons are boiled off a filament in an electric circuit that applies an electric current of ~ 2.2 amperes through the filament, which acts as the negative electrode or ‘cathode’. The filament heats up according to the

[§] Integrating the equations of motion twice, and applying initial conditions $y'|_0 = 0$, $y|_0 = 0$, $z'|_0 = v_z$ and $z|_0 = 0$, will give the z and y (note: x could also apply) positions as a function of time t . Hence, the y position can be written as a function of the z position through eliminating t between the z and y position relations.

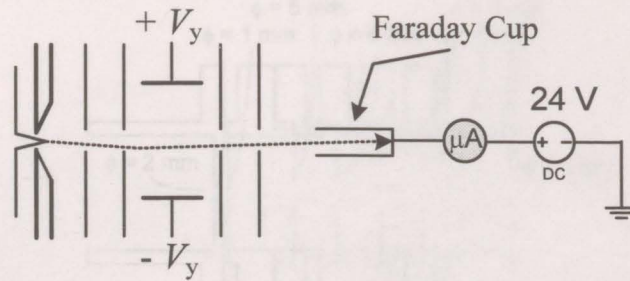


Figure 3.11: An example of the function of the deflector system is to bend the beam trajectory on axis.

power equation: $P = i^2 R$ from a tungsten hairpin style filament** (see figure 3.12 below). A hairpin style filament was chosen for the electron gun as the electrons are produced primarily from the tip, which produces electrons with an emission current in the μA range with small local magnetic fields. The filament tip has a small cross section with a diameter of $\sim 100 \mu\text{m}$ to produce a beam with current density $\sim 10^5 \text{ Am}^{-2}$. The location of the tip of the filament relative to the grid is a crucial quantity in producing a well defined beam without severe divergence. The key parameters for beam production are: dimensions of the grid, the position of the filament tip to the grid, and the filament temperature (or filament current) [Klemperer (1971)]. Shown below is a schematic of the grid and filament portion of the electron gun at Windsor (figure 3.12).

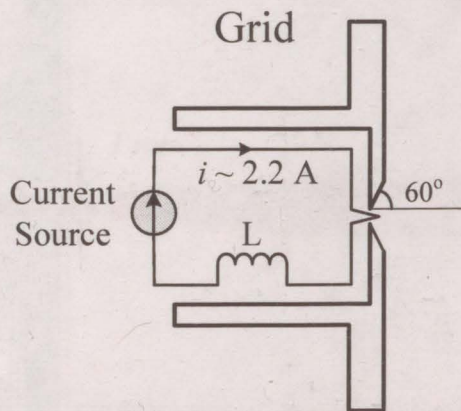


Figure 3.12: An illustration of the Grid and filament support showing the electric circuit for the filament (where the filament cradle was not shown for clarity).

The remainder of the electron gun setup consists of apertures (see figure 3.13) and deflectors to focus and collimate the outputting electron beam. The deflector system given in figure 3.9 and 3.10 are placed in the space between the anode (labeled A in the

** Resistance of about 0.8Ω at room temperature

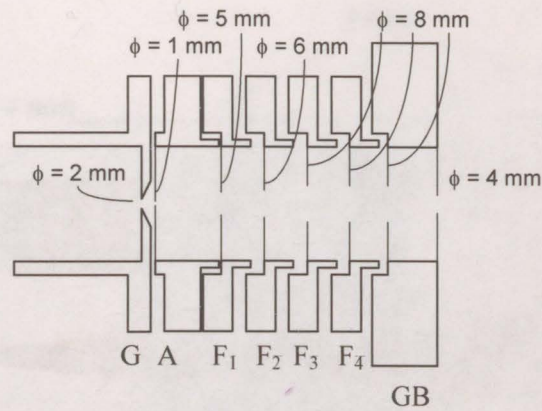


Figure 3.13: A transverse cross section of previous electron gun showing aperture sizes, dimensions, and electrode labeling specific to the ERS.

figure) and the first focusing element (labeled F_1 in the figure) and are not shown in figure 3.13. Each aperture element in figure 3.13 is given an additional label ϕ , which is the aperture size (i.e. the diameter of the aperture). These aperture sizes correspond to the electron gun employed prior to the new injection system, but were more or less retained with the new gun. A SIMION [Dahl (2000)] simulation of the beam trajectories within the gun are:

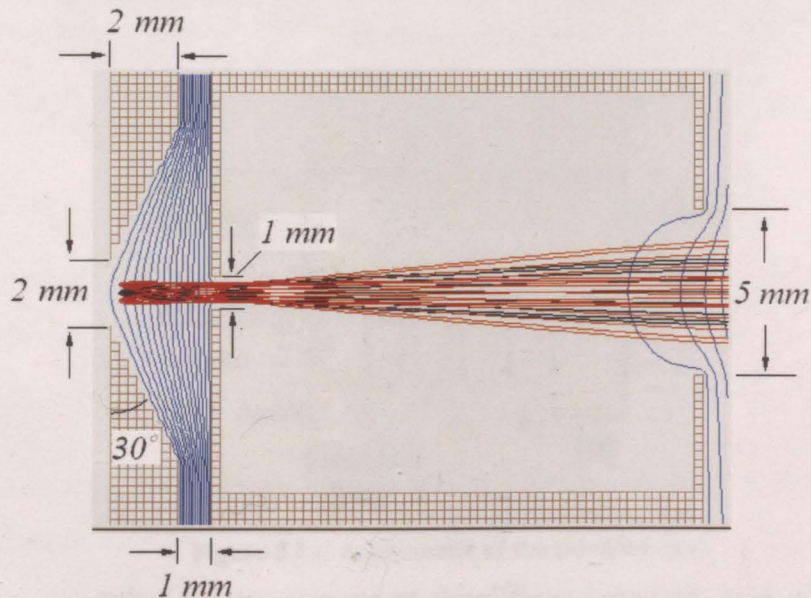


Figure 3.14: The emission region of a filament tip, grid and anode (deflectors are omitted within SIMION simulations) [Niu (2006)].

as shown in figures 3.14 and 3.15 [Niu (2006)]. The gun employs a focusing lens with four elements F_1 through F_4 ; initially, each element was electrically separated, giving

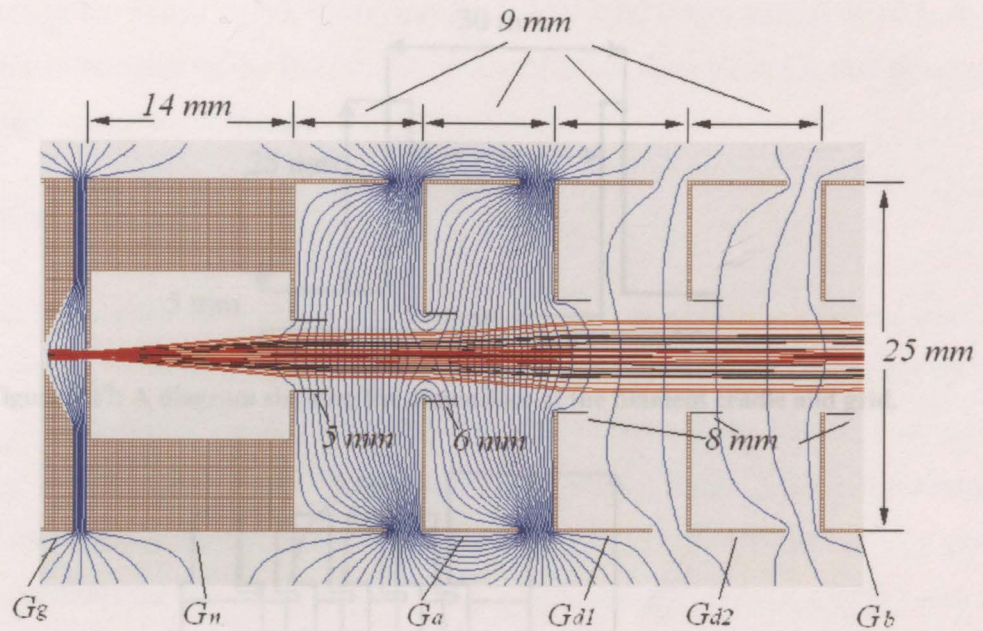


Figure 3.15 : The accelerating region within the electron gun [Niu (2006)].

each its own voltage. However, the recent gun setup (injection directly on axis through bottom hemisphere in figure 3.5) has made the following connection: $F_1 = \text{Anode}$ and $F_2 = F_3$ (electrically shorted together), which is displayed in figure 3.16:

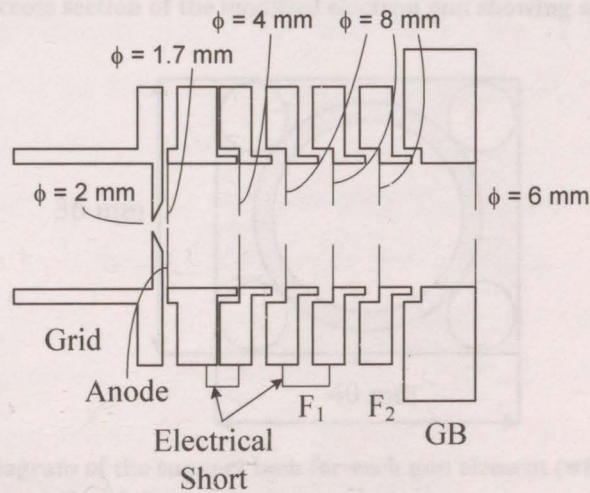


Figure 3.16: A schematic of the modified gun.

The gun was modified for the purpose of simplifying injection, as it was found through experiment that the freedom of a grid, anode, four deflectors, a four element lens and a final gun base voltage complicated the injection tuning.

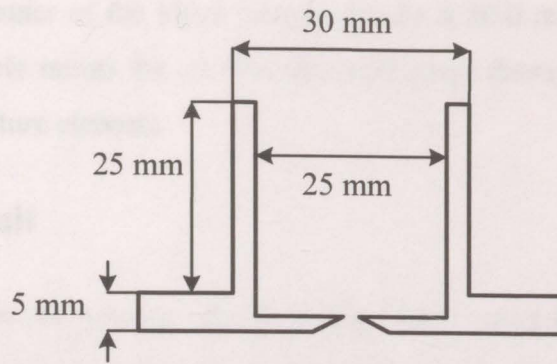


Figure 3.17: A diagram showing the dimensions of the filament cradle and grid.

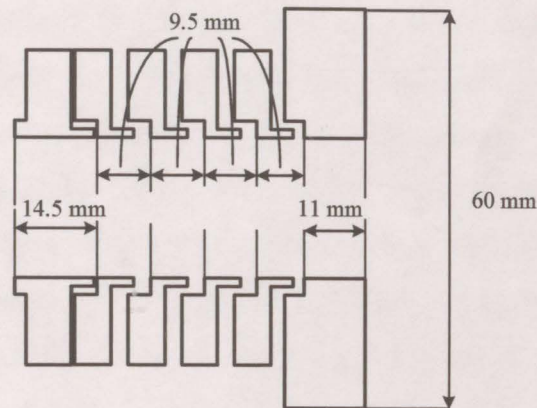


Figure 3.18: A cross section of the modified electron gun showing all dimensions.

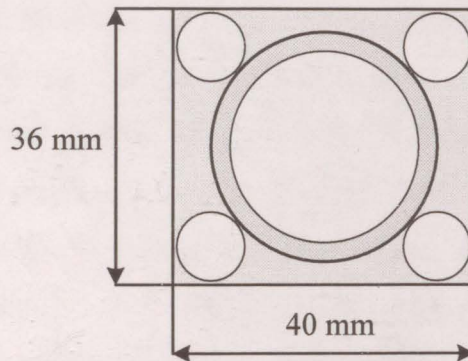


Figure 3.19: A diagram of the support base for each gun element (with dimensions).

Shown in figures 3.17, 3.18, and 3.19 are detailed dimensions of the gun composites, including the grid / filament support, lens train, and an individual support for an aperture element. Figure 3.17 shows the support for the filament, which is a well machined stainless steel cylinder that must be located precisely to position the filament tip ~ 1 mm protruding through the grid. An example of the F_i elements in figure 3.18 are shown with dimensions in figure 3.19, where a stainless steel block with a through hole of diameter

25.0 mm lies in the center of the block surrounded by a 30.0 mm partial blind hole (30 mm diameter blind hole minus the 25 mm diameter inner through hole) that provides a seat to support an aperture element.

3.2.2 Pulsing Circuit

This section introduces the pulsing voltage supply that is used on the electron gun and HDA. The results presented the section were extracted from the pulsing unit set up in a simulated mode, and do not reflect the actual setup parameters on the pulsing unit used in practice, e.g. driving pulse length. The electron filament of figure 3.12 is continuously boiling off electrons; however, not shown in that diagram is the electron energy power supply that provides the emitting electron with a kinetic energy. This energy is tuned to a specific value according to the voltages on the grid, anode, F_i elements, and gun base, to allow for the electron beam to fly through the lens train and exit the gun base and enter the system. Thus, a variation of 1 to 2 eV in the kinetic energy of the emission electrons will prevent them from exiting the gun and entering the system. Recall, the ERS stores a beam of electrons without further input of electrons^{††}; therefore, a pulse of 0 V is placed on the negative of the filament supply that lasts for a time T_0 and then switches to negative thirteen volts for the remainder of the storage cycle $\tau^{\dagger\dagger}$. Moreover, the power supply that defines the emission energy of the electrons is set to allow for continual injection into the system, the pulsing unit will then ‘shut the beam off’ by adding this additional ~ 13.6 volts to its energy, which lasts for a time of $\tau - T_0$. Figure 3.20 displays the schematic for the electron gun pulsing circuit. The circuit is designed with the following specifications: $C_1 = C_2 = 47.0 \mu\text{F}$, $C_3 = 1.0 \mu\text{F}$, $C_4 = 370 \text{ pF}$, $R_1 = R_2 = 680 \Omega$, $R_3 = 220 \Omega$, $R_4 = R_G = 330 \Omega$. The Opto – Isolator 7721 chip is a High Speed CMOS Optocoupler, and the AD811 is an inverting operational amplifier wired in the non – inverting setup (no parity inversion). For this example, the incoming pulse is a 350 nanosecond TTL pulse, which drives the optocoupler that emits a pulse that floats on the

^{††} Meaning, that an electron enters the system for a time T_0 , which implies that the electron injection is completely off after time T_0 until the storage cycle is complete.

^{††} A storage cycle (labeled τ and usually expressed in units of microseconds) is defined to be: the time one pulse of electrons is allowed to enter the system whence detection commences, and the cycle is complete when the user terminates the detection of orbits.

0 volt line (the chassis or “real ground” in this case). The V_{out} from the optocoupler is sent to the operational amplifier (AD811), and the V_{out} that leaves the Operational amplifier is the potential across electron filament (filament tip).

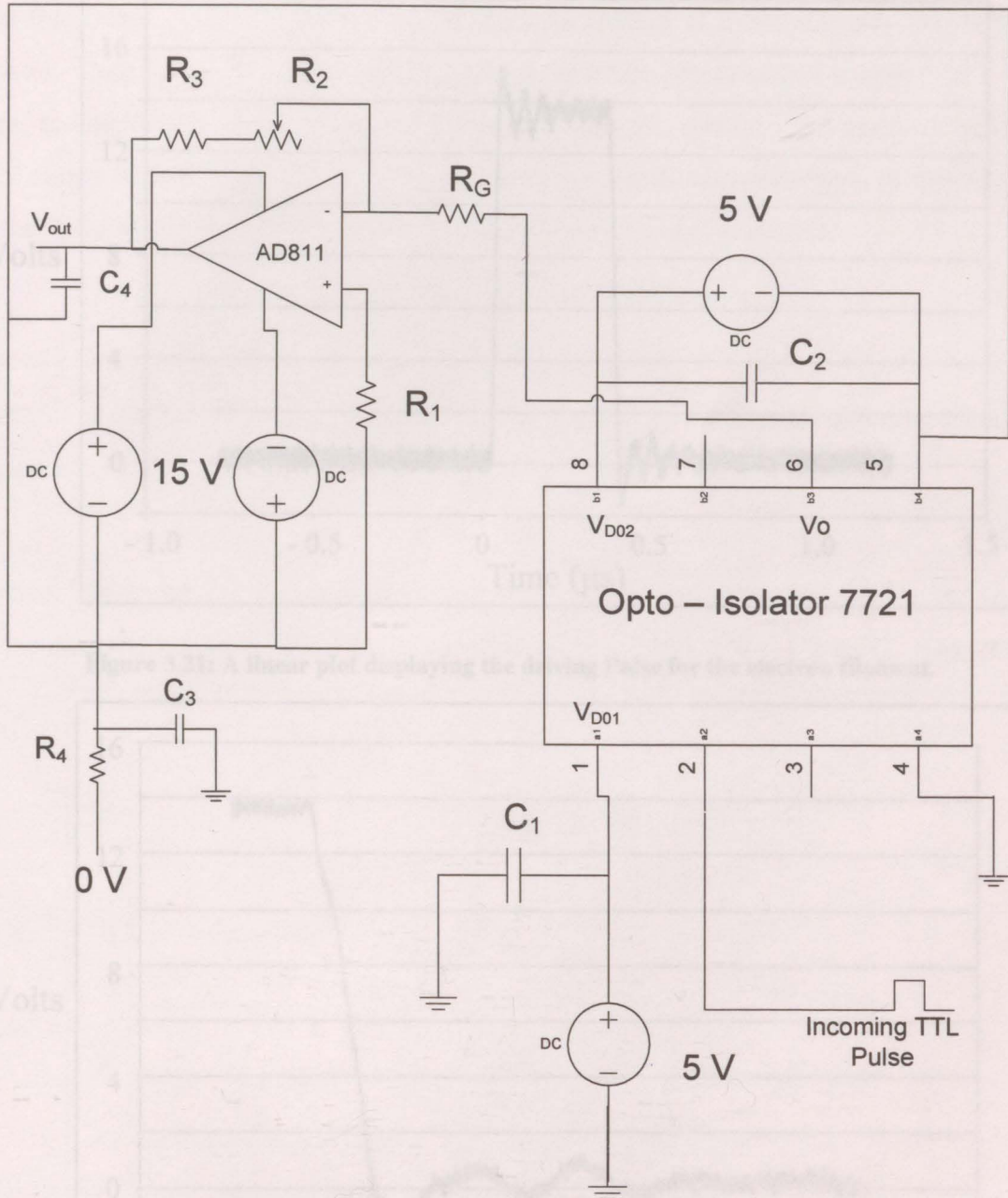


Figure 3.20: The generic pulsing circuit schematic, an incoming TTL pulse becomes amplified and referenced to virtual ground.

The previous circuit did not include a capacitor at the output of the operational amplifier. Consequently, the circuit was producing the pulse in figure 3.21. The pulse does not have a sharp turn-off fall time, rather a forty nanosecond decline (see figure 3.22) followed by

a one volt noise ripple. The noise ripple is damped and vanishes about 175 nanoseconds after the forty nanosecond falloff.

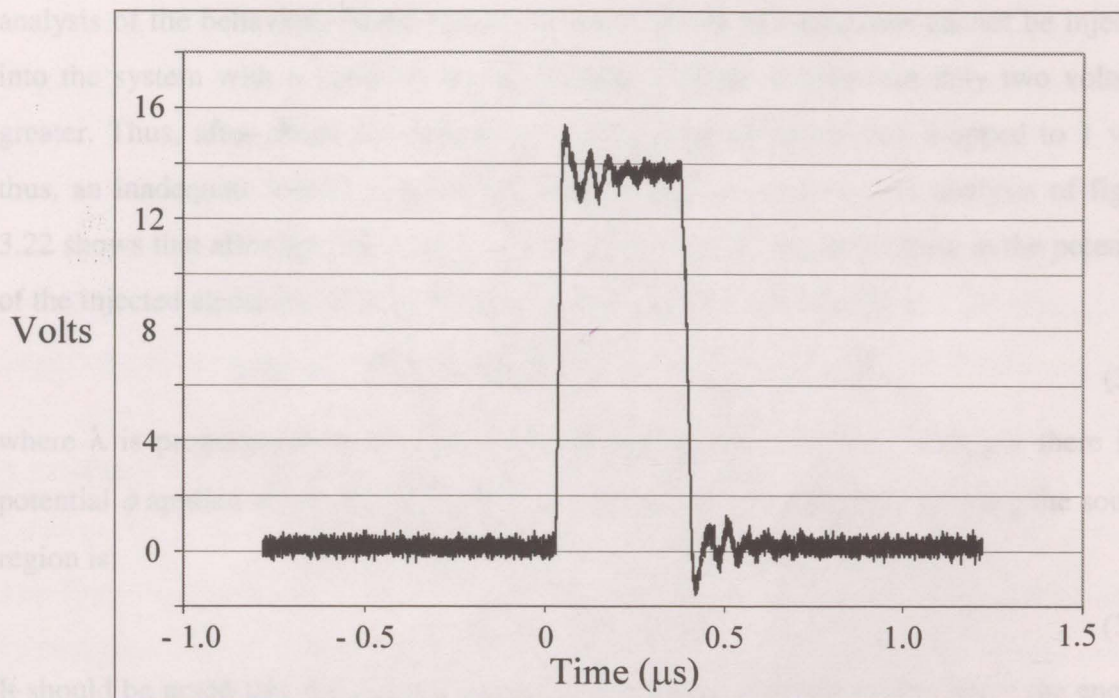


Figure 3.21: A linear plot displaying the driving Pulse for the electron filament.

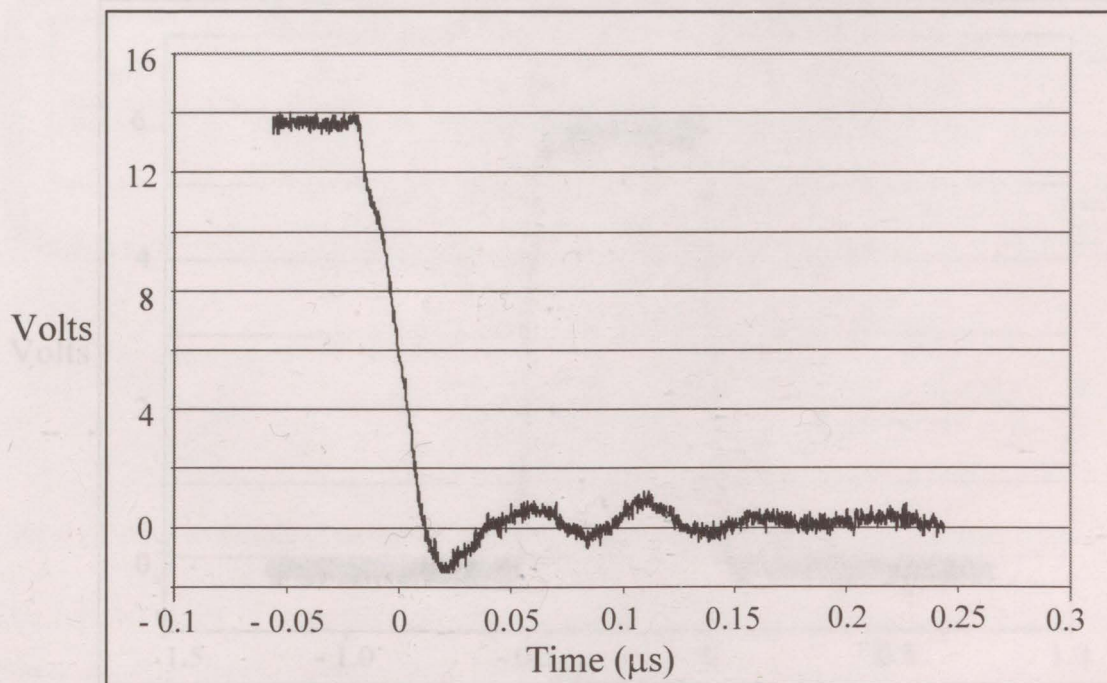


Figure 3.22: A graph showing fall-off time for the electron pulse (approximately 40 nsec). The fall-off includes an after ripple which remains for $(175 + 40 =) 215$ nsec after the pulse turns off.

The “ripple” or electric noise does not give any significant perturbations in the system. However, electric noise can be a concern for future setups and even for high detailed analysis of the behaviour of the beam. As stated above, the electrons cannot be injected into the system with a variation in the filament voltage of approximately two volts or greater. Thus, after about 5.7 nanoseconds the contact potential has dropped to 1 volt; thus, an inadequate kinetic energy for injection into the system. An analysis of figure 3.22 shows that after the pulse ‘turn – on’ there is an underdamped ripple in the potential of the injected electrons. The potential along the ripple is [Zill (2001)]:

$$V(t) = e^{-\lambda t} \left(C_1 \cos \sqrt{\omega^2 + \lambda^2} t + C_2 \sin \sqrt{\omega^2 + \lambda^2} t \right), \quad (3.7)$$

where λ is proportional to the damping coefficient, and $\omega = 2\pi f$. Suppose there is a potential ϕ applied across the filament, then the energy of an electron entering the source region is:

$$E = q_e [\phi + V(t)]. \quad (3.8)$$

It should be noted that the above equation is not the categorical answer, since the energy of the electron lies in the thermal energy distribution of ΔE (see Chapter 2). The above

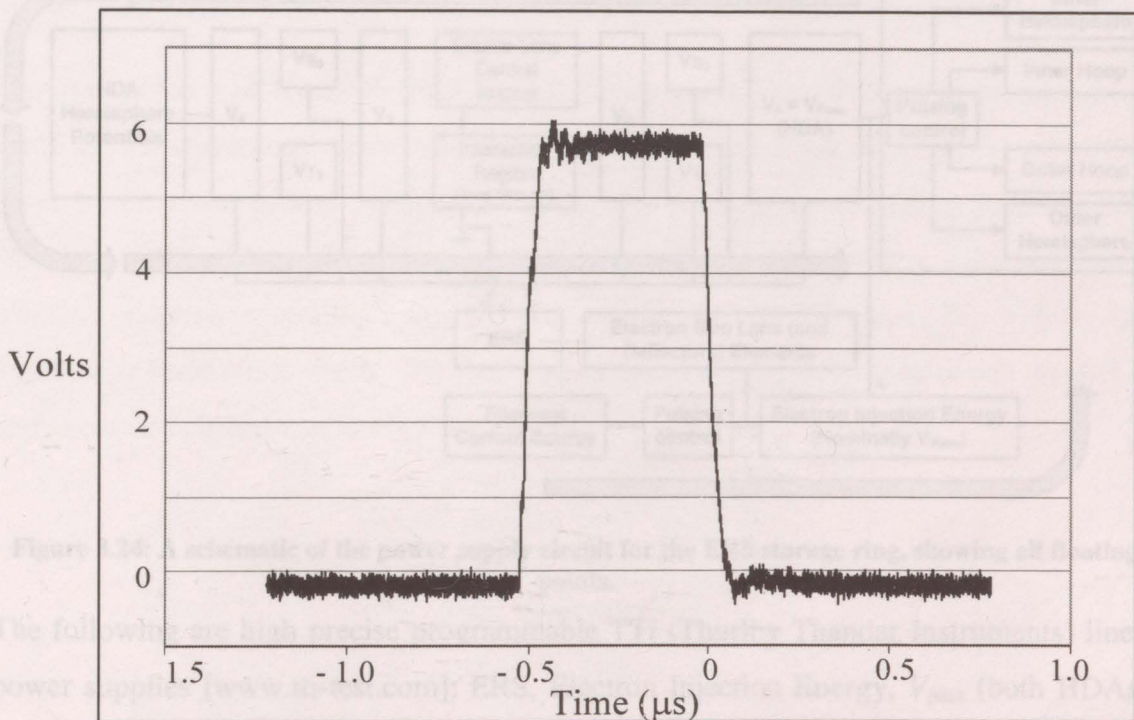


Figure 3.23: A graph depicting the pulse output with capacitor $C_4 \sim 100$ pF resulting in a lessening of ringing.

aberration may be caused from an inductance within the circuit, as it is known that an LRC circuit contains oscillations, which can be underdamped for a given set of L, R, and C [Nilsson (2001)]. The capacitor C_4 was added at the output in the pulsing circuit (figure 3.20) to mitigate these oscillations on the peak of the outgoing pulse (see figure 3.23).

The fine tuning of the electrical setup for the pulsing circuit lies in minimizing both the rise and fall times as well as noise or “ringing” of the signal. The electrical ringing if large enough can cause an external interaction on the electrons within the beam.

3.3 VOLTAGE POWER SUPPLY SCHEMATIC

The Electron Recycling System is a passive electrostatic instrument that uses constant voltage (low current output) power supplies. The power supplies that electrically charge each element are arranged according to the following schematic:

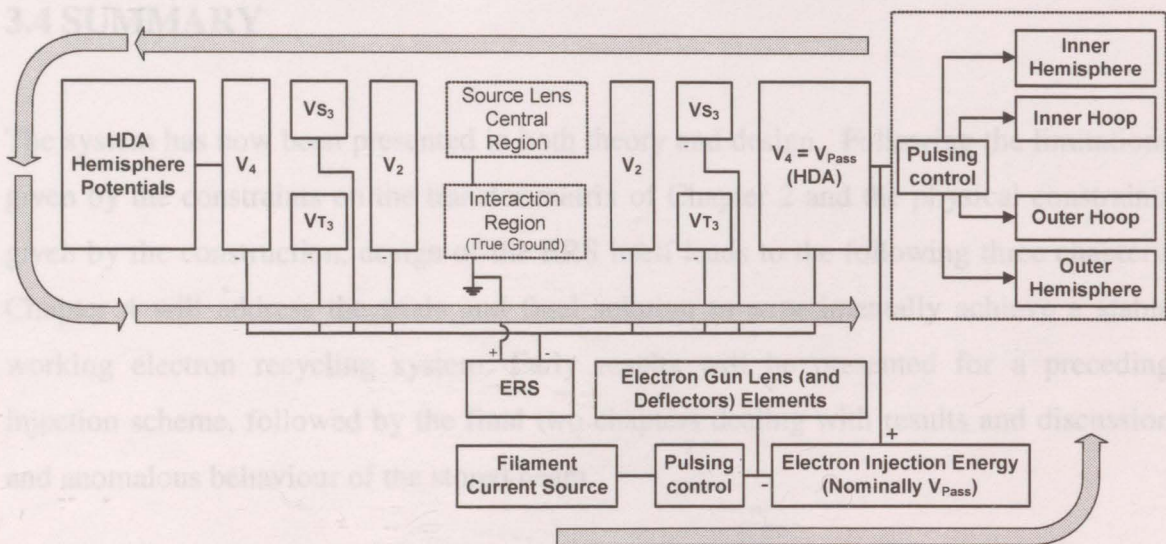


Figure 3.24: A schematic of the power supply circuit for the ERS storage ring, showing all floating points.

The following are high precise programmable TTi (Thurlby Thandar Instruments) linear power supplies [www.tti-test.com]: ERS, Electron Injection Energy, V_{pass} (both HDAs), inner and outer hemisphere (HDA on the left of 3.24, i.e. non – pulsed). The V_2 and V_3 elements and the grid (within the electron gun) are wired to Acopian narrow profile

switching power supplies [www.acopian.com]. All power supplies ultimately float on a single power supply labeled the ERS supply. This ERS energy causes the energy around the ring to be more like a “rollercoaster”; thus, the collision energy can be varied while still maintaining storage. In a similar notion the electron gun lens elements, grid, and deflectors all float on the electron energy, allowing for a change in the energy of the electrons while maintaining beam injection. The electron injection energy floats atop the pass energy of the pulsed hemisphere, that being the bottom hemisphere of figure 3.5. This power supply setup will facilitate electron injection by matching the electron energy to the energy of the storage system (i.e. the ERS energy). The current setup of the storage ring has the electron gun positioned at the bottom HDA of figure 3.5, meaning that the electrons that leave the gun will enter through the bottom hemisphere and travel through the column and through the gap between the inner and outer hemisphere to reach the V_4 cylindrical element, while maintaining near parallel beam trajectory. Thus, the energy of the electrons must be properly specified to prevent beam divergence.

3.4 SUMMARY

The system has now been presented in both theory and design. Following the limitations given by the constraints on the transfer matrix of Chapter 2 and the physical constraints given by the construction, design of the ERS itself leads to the following three chapters. Chapter 4 will address the trials and final solution to experimentally achieve a stable working electron recycling system. Early results will be presented for a preceding injection scheme, followed by the final two chapters dealing with results and discussion and anomalous behaviour of the stored beam.

REFERENCES

- Dahl D., SIMION 3D Version 7.0 User's Manual, Bechtel BWXT IDAHO, LLC (2000)
- Harting E., and Read F.H., Electrostatic Lenses, Elsevier Scientific Publishing Ltd. 1976
- Klemperer O., Electron Optics 3ed edition, Cambridge University Press 1971
- Moore J.H., Building Scientific Apparatus 2nd Edition, Perseus Books 1989
- Niu Y. The Development of an Electron Recycling Spectrometer, Major Paper
University of Windsor (2006)
- Nilsson J.W., and Riedel S.A., Electric Circuits 6th edition, Prentice Hall 2001
- Photonis, website: <http://www.photonis.com>
- Zill D.G., Differential Equations: With Modeling Applications, Brooks / Cole 2001

ii. Optimized Data	104
4.3 GUN POSITIONED ON HDA	106
4.4 PULSING SCHEMES	110
4.5 SUMMARY	114
REFERENCES	115

CHAPTER 4: EXPERIMENTAL II INJECTION AND STORAGE

ELECTRON BEAM INJECTION

4.1 FIRST ATTEMPTS AT ELECTRON INJECTION AND STORAGE	89
4.1.1 Introduction	89
4.1.2 Scattering off Argon Gas	91
4.2 STORAGE ACHIEVED	94
4.2.1 Scattering off Tungsten Ring	95
4.2.2 Results: Tungsten Ring Injection	101
i. Preliminary Data	102
ii. Optimized Data	104
4.3 GUN POSITIONED ON HDA	106
4.4 PULSING SCHEMES	110
4.5 SUMMARY	114
REFERENCES	115

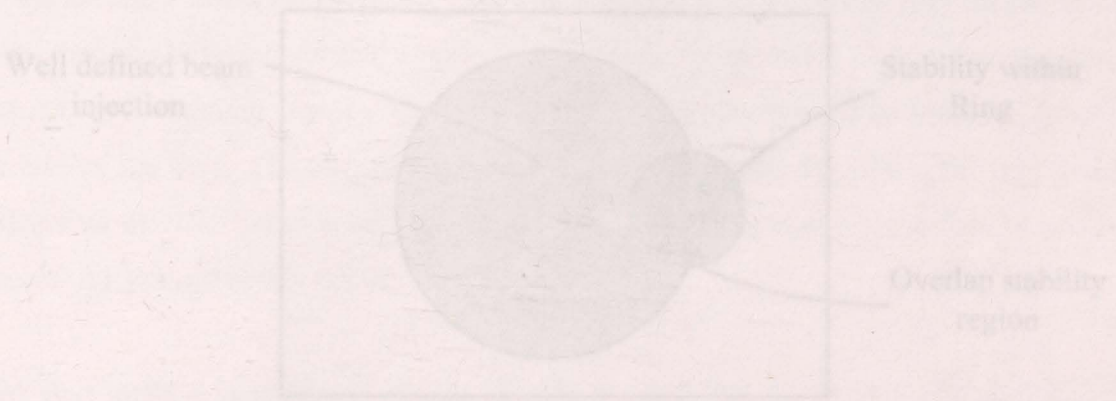


Figure 4.1: Venn diagram of the set of phase space parameters for the injection and storage processes within the ERS ring

4.1 FIRST ATTEMPTS AT ELECTRON INJECTION AND STORAGE

4.1.1 Introduction

A stored beam requires confining voltages around the entire closed path within the ERS ring. Therefore, to bring an electron beam into the ERS requires a method to temporarily interrupt a fixed voltage at some point within the storage ring. In addition to a “fast” break in a voltage, the phase space parameters of the initial electron beam $\{p, r, r'\}$ with regard to a common optical axis must be adequately matched to the acceptable phase space parameters of the ERS. Therefore, creating a stored beam in practice requires two crucial stages: injection and stable confinement in the ring. Consequently, the defining parameters $\{p, r, r'\}$ of the electrons from the injection stage to the storing stage must match up with each other to enable a stored beam. Since the two stages are inherently independent, it is realistic to assume that the two sets of parameters will only overlap, forming a union of parameters, referred to as *overlap stability region* in figure 4.1. Evidently, the better the “overlap” of the phase space parameters the more efficient the storage (a higher range of accepted trajectories within the ERS ring). The phase space parameters are determined by the electric potentials and geometry of the ERS elements, as well as the kinetic energy of the electrons at a given point within the ring. The difference in size of the stability regions in figure 4.1 originate from the small range of “accepted” trajectories and beam angles (with respect to the optic axis), as well as voltage ratios of the ERS lens elements (see Chapter 2).

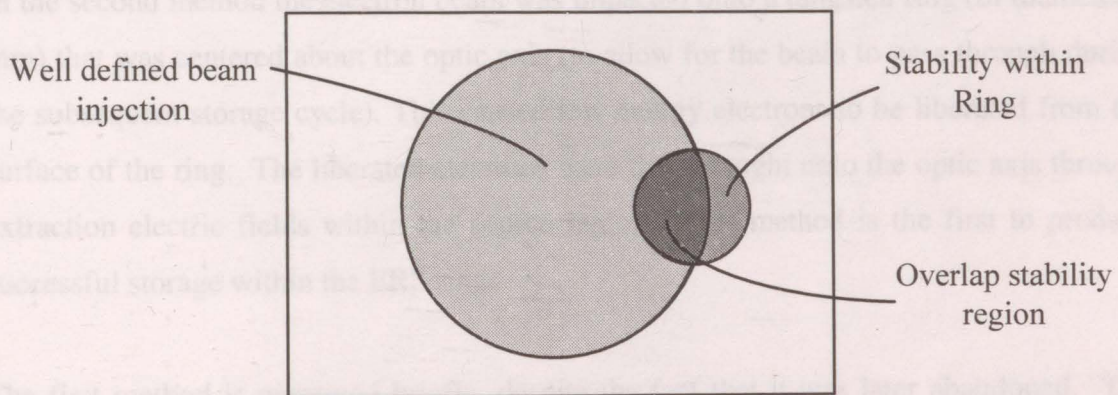


Figure 4.1: Venn diagram of the set of phase space parameters for the injection and storage processes within the ERS ring

In this chapter, three different forms of injection will be presented. The electron source must be transferred into a storage ring that is designed for electron beam storage at recycling voltages. Two methods will be presented over the next two sections:

- Argon Gas Scattering
- Tungsten Ring Scattering

The two methods are related by the location of the electron gun and the use of scattering an electron beam directed orthogonal to the optic axis.

In the first scheme a hypodermic needle was placed in the source region as a source of argon gas. A high gas concentration was built up in that region creating a gas cloud. An electron beam was directed at a Faraday cup opposite the gun that injected electrons on a straight path through the argon gas cloud. Prior to introduction of argon gas in the source region, the electron gun performance was optimized by maximizing the current in the Faraday cup. Argon gas was then introduced into the source region, and electrons with energy E_0 traveled through the gas cloud on a path to the Faraday cup. A number of electrons would not interact with the gas and would instead register at the Faraday cup.* Electrons that were interrupted by the gas would interact by elastic or inelastic collisions over a range of angles. The ERS ring was then tuned to focus on the 90° elastically scattered electrons that were directed onto the optical axis.

In the second method the electron beam was impacted onto a tungsten ring (of diameter 4 mm) that was centered about the optic axis (to allow for the beam to pass through during the subsequent storage cycle). This caused low energy electrons to be liberated from the surface of the ring. The liberated electrons were then brought onto the optic axis through extraction electric fields within the source region. This method is the first to produce successful storage within the ERS ring.

The first method is presented briefly, despite the fact that it was later abandoned. The argon gas scattering method outlined a more general problem with the ERS; namely,

* Typical E_0 values were ~ 90 to 100 eV.

scattering of electrons off background targets in the chamber. This, in addition to low axis currents, made difficult tuning conditions.

4.1.2 Scattering off Argon Gas

In this setup, the source region (center of the right lens stack in figure 3.5 or 4.18) is the location of the electron gun, a Faraday cup, and a hypodermic needle. The electron gun is a standard design that includes a hairpin filament and a focusing lens (see Chapter 3). The Faraday cup is placed opposite to the gun exit and acts as a tool to optimize gun

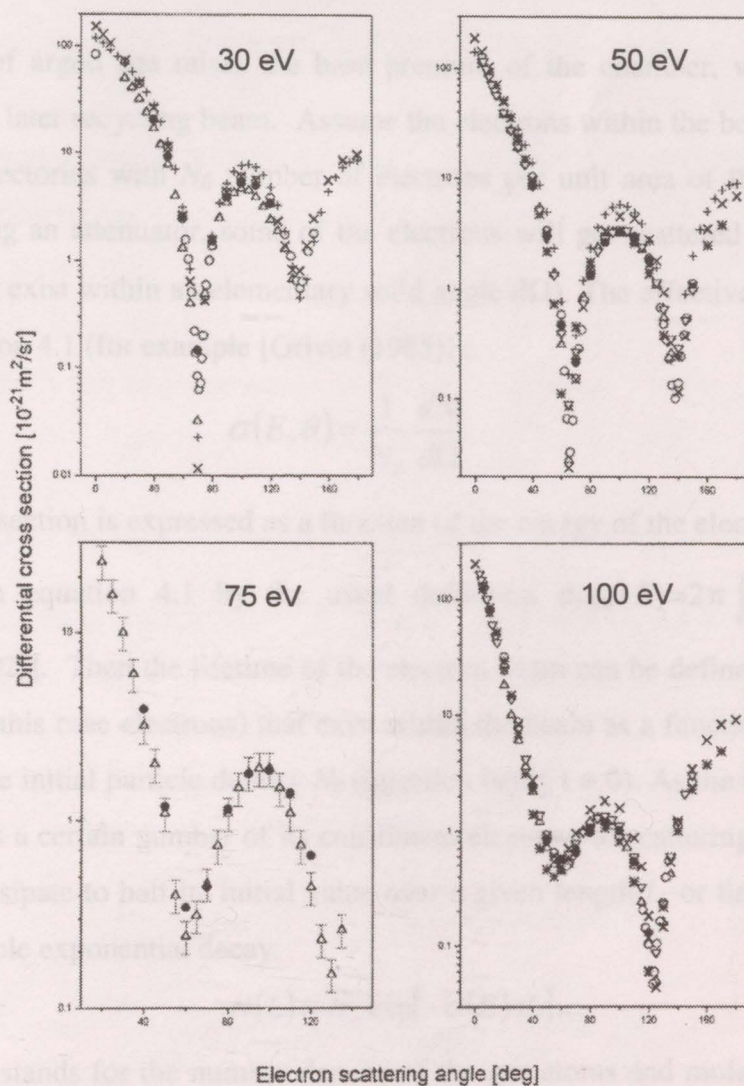


Figure 4.2: Differential Cross Section for electron - argon scattering for a variety of incident electron energies showing the excellent agreement between the data of various experimental groups; see Cvejanović and Crowe (1997) for details.

emission (by maximizing beam collection). The hypodermic needle is placed at 90° from the gun and acts as a crude gas jet nozzle, (see for example [King and Head (1978)]). Argon gas was chosen for the scattering target due to its high differential cross section for 90° elastic scattering at low incident electron energies (as compared to helium for example). Figure 4.2 [from Cvejanović and Crowe (1997)] shows the differential cross sections versus scattering angle, for a variety of incident electron energies. The “double dip” feature of the graphs in figure 4.2 is entirely due to dominance in the d -partial wave, which gets overshadowed at low incident energies by the s and p waves [Fon *et al.* (1983), McEachran and Stauffer (1983)].

The presence of argon gas raises the base pressure of the chamber, which acts as an attenuator for a later recycling beam. Assume the electrons within the beam are traveling on parallel trajectories with N_0 number of electrons per unit area of the cross section. While traversing an attenuator, some of the electrons will get scattered through a mean angle of θ (that exist within an elementary solid angle $d\Omega$). The effective cross section is given by equation 4.1 (for example [Grivet (1965)]):

$$\sigma(E, \theta) = \frac{1}{N_0} \frac{dN}{d\Omega}. \quad (4.1)$$

The total cross section is expressed as a function of the energy of the electrons, which can be found from equation 4.1 by the usual definition $\sigma_{\text{total}}(E) = 2\pi \int_0^\pi \sigma(E, \theta) \sin\theta d\theta$ [Goldstein (2002)]. Then the lifetime of the electron beam can be defined as the number of particles (in this case electrons) that exist within the beam as a function of time: $N(t)$, in relation to the initial particle density N_0 (injection being $t = 0$). As the beam traverses a medium it loses a certain number of its constituent electrons to scattering; thus, the beam density will dissipate to half its initial value over a given length L , or time of travel, and results in a simple exponential decay:

$$N(L) = N_0 \exp[-\sigma(E)nL]. \quad (4.2)$$

The quantity n stands for the number density of the gas atoms and molecules within the chamber (for this application argon would dominate) and is proportional to the pressure.

The lifetime τ of the electron beam can be defined as the time required for the beam density to drop by a factor of e , and is expressed as a function of time (see equation 4.3).

$$N(t) = N_0 e^{-\sigma_0 n v t} = N_0 e^{-t/\tau}, \quad (4.3)$$

For equation 4.3 the following is defined: σ_0 is the total cross section at the storage energy, and the length L has been substituted with $\bar{v}t$, where \bar{v} is the mean velocity of the electrons defined by:

$$\bar{v} = \frac{1}{N} \int_0^{\infty} v N(v) dv. \quad (4.4)$$

For example see [Andersen, Heber and Zajfman (2004), Tanabe *et.al.* (2002)].

Suppose an electron travels through a medium of scatterers of total cross section $\sigma(E)$, then from collision theory the mean free path is given by:

$$\lambda = \frac{1}{n\sigma}. \quad (4.5)$$

The number density can be expressed from the ideal gas law:

$$PV = NkT, \quad (4.6)$$

or can alternatively be expressed as: $n = \frac{P}{kT}$, where, $n \rightarrow N/V$, and kT is the thermal energy. Assume $\sigma_{total} \approx 18.9 \times 10^{-20} \text{ m}^2$ [Ferch *et.al.* (1985)] for an electron – argon collision for impact energy 10 eV, within a base pressure of 1×10^{-9} torr, then the mean free path is:

$$\lambda = \frac{1}{(P/kT)\sigma} \quad (4.7)$$

$$P = 1.33 \times 10^{-7} \text{ Pa}, \quad kT = 4.14 \times 10^{-21} \text{ J} \quad (4.8)$$

$$\lambda \approx \frac{1}{(3.212 \times 10^{13} \text{ m}^{-3})(18.9 \times 10^{-20} \text{ m}^2)} \\ = 164726.2 \text{ m} \approx 165 \text{ km} \quad (4.9)$$

The mean free path is inversely proportional to the pressure of the system, therefore the addition of argon increases the background gas pressure and number of residual gas collisions causing a considerable drop in the mean free path.

In order to achieve a sufficient current from scattering on injection, the argon level must be raised to a pressure of around 1×10^{-5} torr. Provided the electron beam travels once around, it must pass through the argon gas jet before continuing onto the second orbit, and thus become greatly attenuated during each pass. To elaborate, the mean free path of the electron beam within the presence of argon at a pressure of 1×10^{-5} Torr is ≈ 16.4 m (ignoring interaction with the high density gas jet). In addition to attenuation, argon gas will disperse throughout the system and mix with any sample gases within the interaction region during electron collision studies, causing a distortion in the results. The mean free path gives an approximation to the exponential decay in equations 3.2 and 3.3. The local gas pressure surrounding the hypodermic needle (causing the interaction region to be at a higher pressure than the background pressure of the chamber) was not factored into the above analysis, which would further reduce the mean free path.

This method of injection produced no successful results. No electron orbits were observed for this method, which is most likely due to the low current density scattered onto the optic axis. This method seems plausible in theory, however, to create a high flux of 90° scattered electrons requires a high number density of argon; this is counterproductive as it will cause attenuation of the stored electron beam. The only way to circumvent this setback is to create an electron source that does not depend on a gas target. Ideally, an electron injection scheme would consist of a high number density of electrons and low "gas" pressure. This can be achieved in practice by causing an electron beam to collide with a metal surface, whereby low energy electrons are liberated about the optic axis.

4.2 STORAGE ACHIEVED

Storage was first achieved with the electron source placed at the source region. A tungsten ring was placed at the center of the source region. Electrons can be brought onto the optic axis by:

- Elastic scattering
- Inelastic scattering,

with large number densities, which can enter the system and begin the storage cycle (with a low gas pressure). The next injection scheme was to have the gun positioned on the optic axis, by locating it on the back of the bottom HDA in figure 3.5. The need for a “fast” break of the HDA voltage must be addressed prior to implementing an injection technique. The pulsing circuit that drives the HDA was altered to produce pulses with fall / rise times of about forty nanoseconds.

The gun positioned at the back of the bottom HDA, gave a highly reliable injection setup. Several pulsing arrangements were tested to shorten the length of the pulses in the time and energy domain, and give an overall optimization of the injection. Moreover, the pulse of the HDA and filament contact potential has a significant impact on the phase space parameters: $\{p, r, r'\}$. It was found that the storage efficiency was optimized in shortening of the HDA pulse (~ 40 ns) while maintaining a longer contact potential width (~ 100 ns).

4.2.1 Scattering off Tungsten Ring

The physical bombardment of electrons on metal surfaces is used to introduce an electron beam onto the storage axis without introducing gas or pulsing of the HDAs. A primary electron beam of energy E_0 collides with a metal surface and produces secondary electrons by two processes. The incoming electrons collide with the conduction and valance band electrons bound to the metal. These electrons can be raised from the valance band and exit the metallic surface (secondary electrons of high energy). A second possibility is that the secondary electrons undergo a number of collisions with internal electrons, whereby the incident beam sacrifices some of its energy as new electrons are released. These electrons can reach the surface and exit with low kinetic energies. A generic example of the two metal scattering processes described above is an electron beam incident upon a copper surface [Koshikawa and Shimizu (1974)]. The low energy electrons form a wide distribution (typically 7 – 10 eV) and peak around 1.5 to 3.0

eV. For example, in figure 4.3 displaying both the low energy secondary peak and the elastic scattered peak in copper (E primary is 58 eV), and in figure 4.4 the low energy distribution of inelastically scattered electrons for $E_0 = 1.0$ keV.

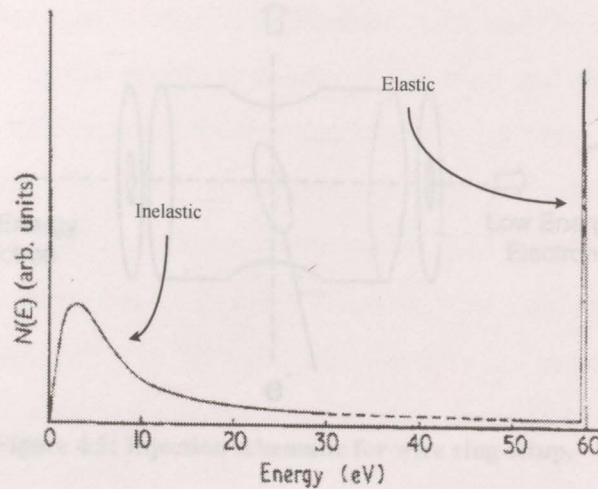


Figure 4.3: Energy distribution of electrons excited by electrons of copper (primary energy of 58 eV, [Koshikawa and Shimizu (1974)]).

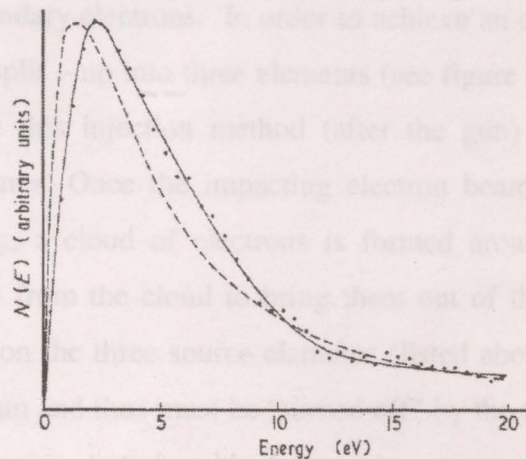


Figure 4.4: Low energy secondary electron distribution for inelastic scattered electrons (primary energy of 1 keV, [Koshikawa and Shimizu (1974)]).

Ninety degree scattering in the source region was well presented in the previous section of this chapter, where the hindrances lied in the presence of argon gas. Using the source region as the electron beam source will greatly improve the target to noise ratio (without adding extensive amounts of metal shielding around source and detectors).[†] An electron beam of energy E_0 is directed toward a fixed tungsten wire ring with the notion that a number of electrons will impact upon the ring and produce low energy secondary

[†] Here the target refers to the electrons that are collected after a number of orbits.

electrons in the manner described above and shown in figures 4.3, and 4.4. Figure 4.5 gives a diagram of the wire ring injection method, displaying the ring centered about the optic axis to allow for an open path for recycled electrons.

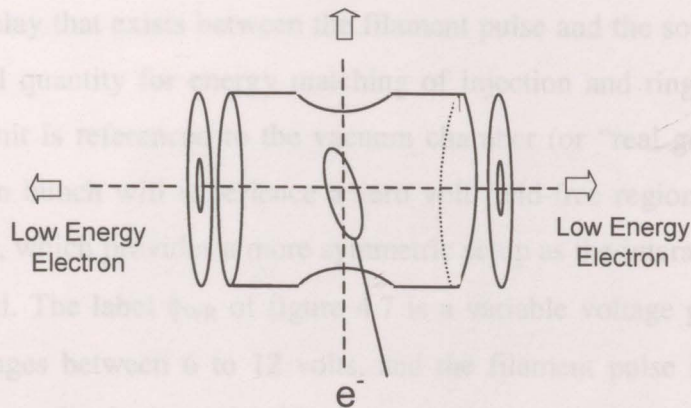


Figure 4.5: Injection schematic for wire ring setup.

It was found through the tuning trials that storage was most easily obtained by focusing on the low energy secondary electrons. In order to achieve an on axis propagating beam the source region was split – up into three elements (see figure 4.5). Explicitly, the three elements that compose this injection method (after the gun) are: target wire, source cylinder, and V_1 apertures. Once the impacting electron beam liberates the secondary electrons from the ring, a cloud of electrons is formed around the ring. In order to accelerate the electrons from the cloud to bring them out of the source region, electric potentials were placed on the three source elements (listed above). These voltages will influence the stored beam and thus must be “turned off” by the time the first stored pulse returned to the source region; therefore, the target wire, source cylinder, and V_1 apertures were driven by pulsing circuits similar to that of figure 3.20 (consisting of an operational amplifier and driving TTL pulse). Specifically, the target wire and source cylinder were set to a negative electric potential to force the electrons away from the ring and toward the optic axis, respectively, and the V_1 apertures were set positive to extract the electron cloud toward the apertures.

The energy of the electrons that exit the filament tip is about 100 eV with respect to ground. However, a 1 to 2 volt variation in the electric potential at the filament tip with respect to the neighboring grid electrode will cause a mismatch in electron kinetic energy

preventing electrons from leaving the gun, (technically the grid region itself). Efficient injection requires a specific pulsing sequence for the filament tip and the source region, which can be seen in figure 4.6 below, while maintaining a narrower pulse width of 150 ns. The 60 ns delay that exists between the filament pulse and the source region driving pulse is a critical quantity for energy matching of injection and ring confinement. The source pulsing unit is referenced to the vacuum chamber (or “real ground”) so that the recycling electron bunch will experience a zero volt field-free region upon returning to the source region, which provides a more symmetric setup as the interaction region is also set to real ground. The label ϕ_{WR} of figure 4.7 is a variable voltage given to the source elements that ranges between 6 to 12 volts, and the filament pulse is produced by the pulsing unit with amplitude determined by the gain of the operation amplifier, ~ 13.6 V in this case due to its ± 15 V voltage supplies.

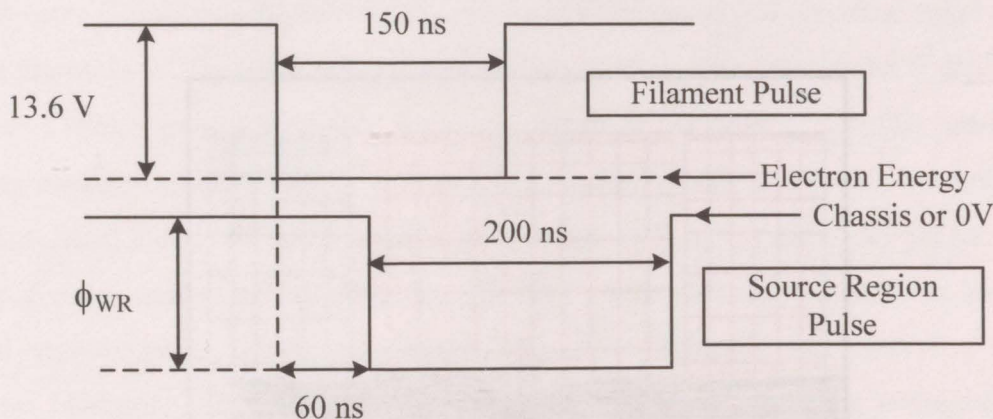


Figure 4.6: An illustration of the pulsing sequence for filament tip and source region.

Following injection, the electrons must orbit the ERS including both HDAs, lenses, interaction region, and the source region containing the tungsten wire loop. Suppose a 100 eV electron beam propagated through the source region to collide with a tungsten wire loop, those that were scattered by $\sim 90^\circ$ enter the m_1 lens and continue through the system. The tungsten wire loop target (diameter of 4.0 mm) is placed at a tilt of about 5° , the effect of the tilt is to increase the collision surface area for the incident beam; see the computer rendered diagram in figure 4.7). The storing electrons were approximated to have energy of ~ 13.1 eV while it propagated through the source region. The effect of the target wire loop on a 13.1 eV parallel beam (radius = 2.0 mm) is demonstrated in figure

4.8[‡]. Injection is then brought about by directing a 100 eV electron beam toward the tungsten ring to liberate low energy electrons. Modeling of the recycling beam gave a very good concept of the behavior of beam in the modified source region. It was found that the electron beam will indeed thread itself through the wire loop.

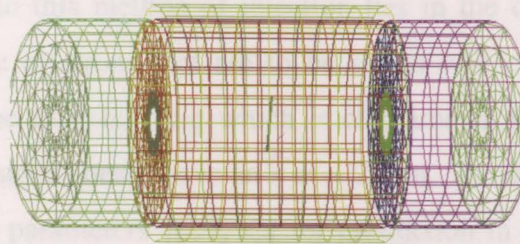


Figure 4.7: Source region modeling with wire ring at center, showing the separate components: center cylinder, top and bottom V_1 , and wire ring.

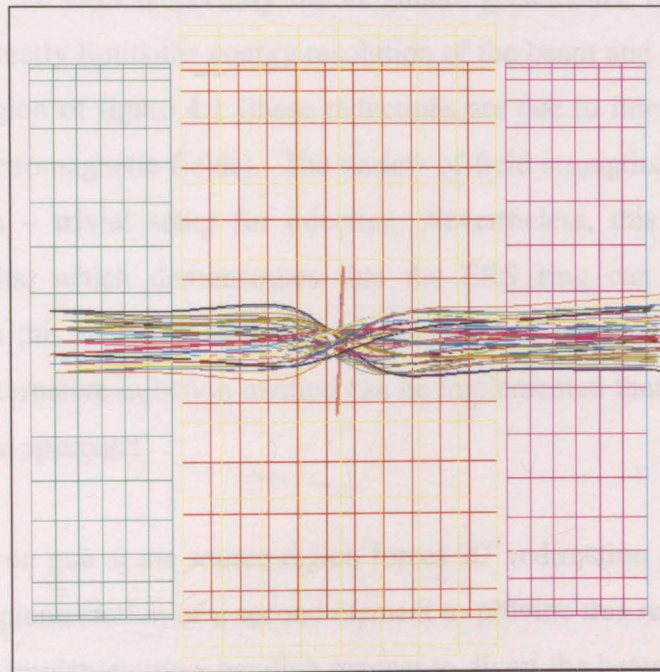


Figure 4.8: Effect of the Target wire on a parallel beam of electrons.

[‡] This modeling was performed by Dr. P. Hammond [Hammond P, website] using CPO3D simulator (see Chapter 2)

Injection of this type provides two separate propagating beams in opposite directions. Although two beams were produced from a single source, they did not have an equal current density due to the location of the wire ring and incoming primary electron beam. As it happens, the system favored a counter-clockwise directed beam.

A significant drawback to this method of injection lies in the off – axis production of electrons. Recall that the electrons that are to be stored will originate from the metal scattered electrons off the tungsten ring which is of diameter 4 mm; implying that the initial parameters of the stored beam have an r of ~ 2 mm. The difficulty is the matching of all of the phase space parameters $\{p, r, r'\}$ for production in the source region to the storage conditions of the ERS ring. There were inherent fluctuations in the system that caused drift in the electron beam stability into a region of instability similar to figure 4.1. Pulsing three elements within the source region is a high source of electrical noise deposit on the elements of the ERS (especially the neighboring elements, in particular the V_2 cylinders), which greatly limits the energy resolution of the beam and further reduces the stability overlap region of figure 4.1 (these reductions are due to interactions with these time dependant electromagnetic fields). The variety of field strengths[§] within the source region gives a non – trivial setup for injection. Nevertheless, this method produced several stored orbits, which demonstrates that the ERS ring can store low energy electrons. Although this injection method was successful in producing storage [Tessier *et.al.* (2006)], an alternative injection method can be implemented that is an overall more efficient and reliable approach.

Mounting the electron gun at the source region forces 90° redirection onto the optic axis, this requires the implementation of a second element to provide this redirecting effect. A possible solution is implementing a bending magnet to divert the beam on axis, similar to those in linear electron accelerators [Kahn (2003)]. However, a bending magnet would require a major mechanical alteration, as the magnetic fields cannot be allowed to interfere with the stored electron beam. Moreover, the addition of a magnetic field will

[§] Being Ewire, Ecylinder, and E_{V_1} as well as the energy of the primary electron beam and the ring defining energy, or 'ERS energy' see figure 3.24.

cause perturbations to the charged particle dynamics that will impede the stored beam. A solution to all of these issues is positioning of the gun directly on the optic axis, which will be better suited for the matching of the phase space parameters for the injection and storage within the ERS.

4.2.2 Results: Tungsten Ring Injection

The data recorded for the wire ring setup are presented in this section. These data sets (shown below) were recorded on detector B located at the interaction region (see figure 3.3). The data of the first graph (figure 4.9) was recorded with an Ortec MCS – PCI data acquisition card [Ortec (1998)], with specification of data acquisition of 100 ns / channel. In each of the graphs, the first peak on the left (at the zero marker) indicates the initial pass of the beam by detector B, which is a half orbit travel of the clockwise and counter-clockwise beam. The first peak will reach the half-way point (interaction region) without perfect matching of the phase space parameters. In order for the electron beam to reach the interaction region it must consist of trajectories that will thread their way through the apertures and HDAs. Stored electrons will not be detected when there are not many electrons with $\{p, r, r'\}$ to adequately match to the ERS conditions. The second peak (reading left to right) corresponds to one full orbit. Similarly, each subsequent orbit is n number of orbits that have passed through the interaction region, with the losses of the beam measured at the detector (electrons that are lost from the recycling beam by scattering will enter the detector).

Figure 4.9 provides the first results for long-time electron storage within the ERS ring on a logarithmic plot for storage cycle period of 5 μ s. Here, the Initial driving TTL pulse has been shortened down to \sim 150 ns. The data in figure 4.9 was obtained for the condition of \sim 10.5 eV pass energy (both top and bottom HDAs); also, the bottom hemisphere assembly (including inner and outer hemisphere and both hoops) was set to a slightly alternative voltage from its theoretical values for the inner and outer hemisphere. The lens and HDA potentials were tuned experimentally to maximize stored orbits.

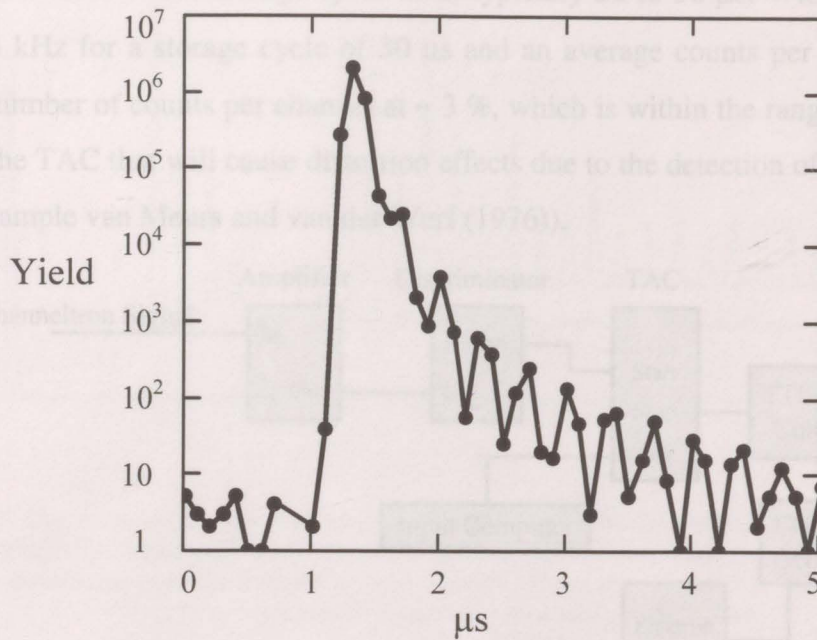


Figure 4.9: Data is plotted on a Logarithmic scale (y - axis) over a 5 μs period. The peak that lies between 1 and 1.5 μs time window is the initial injected peak, which has traveled half way around the ring, i.e. source to interaction region. Also shown are 10 subsequent storage peaks, each being a derived from the previous peak.

i. Preliminary Data

The data presented in this subsection corresponds to the first set of tuning parameters of the ERS ring for this injection mode (wire loop scattering). The ‘electron yield versus time’ plots (given below, and for the remainder of the thesis) are an accumulation of a multiple set of runs with electron injection every 30 μs (in the case of figure 4.13). The data presented in this section and throughout the remainder of this thesis was obtained with an Ortec Maestro-32 Package [Ortec (2001)], utilizing a MCA (multichannel analyzer) emulator that divides the storage cycle time by 2048 channels, i.e. a storage cycle of 10 μs will result in 5 ns / channel, which is a considerable improvement over the data acquisition tool of the previous section. The electron gun injects a beam of electrons at time zero, which marks the beginning of the acquisition time window, as dictated by the TTL pulsing unit. From time zero to the next injection pulse the channeltron signal enters the time to amplitude converter (TAC), see figure 4.10. Thus, the frequency of the

TAC is the inverse of the storage cycle time, typically 20 to 50 μs . With frequencies of about 33.3 kHz for a storage cycle of 30 μs and an average counts per second of 1000 gives the number of counts per channel at $\sim 3\%$, which is within the range before pile-up occurs in the TAC that will cause distortion effects due to the detection of multiple events (see for example van Meurs and van der Werf (1976)).

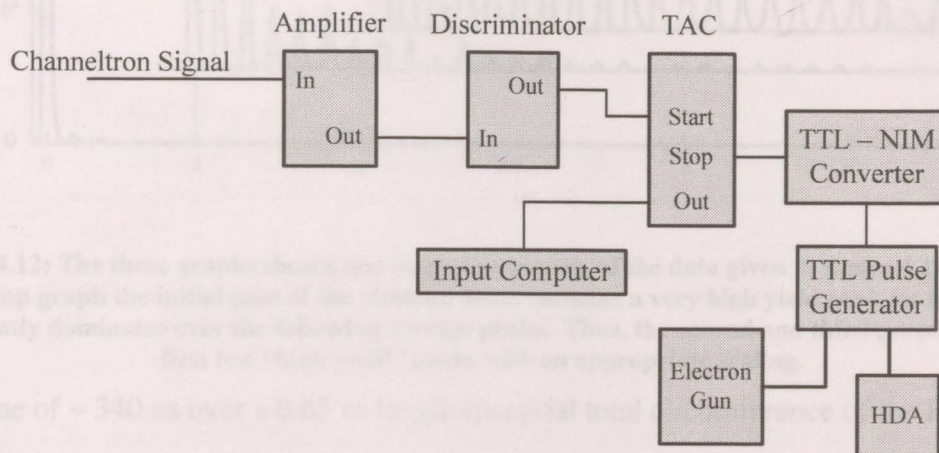


Figure 4.10: Data acquisition setup of NIM electronics driven by TTL generator (see text for details).

Figure 4.11 displays a spectrum of electron scattering from the gas jet and defining apertures in the interaction region as a function of elapsed time from the injection pulse, which demonstrates the achievement of passive electron storage. Subsequent peaks are separated by one full orbit that extends out to greater than 18 μs flight time, corresponding to $\sim 38\text{ m}$ flight distance and ~ 52 orbits. Analysis of the spectrum in figure 4.11 reveals that between the interval 6 to 12 μs the electron peak heights have an exponential decay of $\sim 11.6\ \mu\text{s}$ (with an uncertainty of $\sim 0.1\ \mu\text{s}$). The analysis reveals an

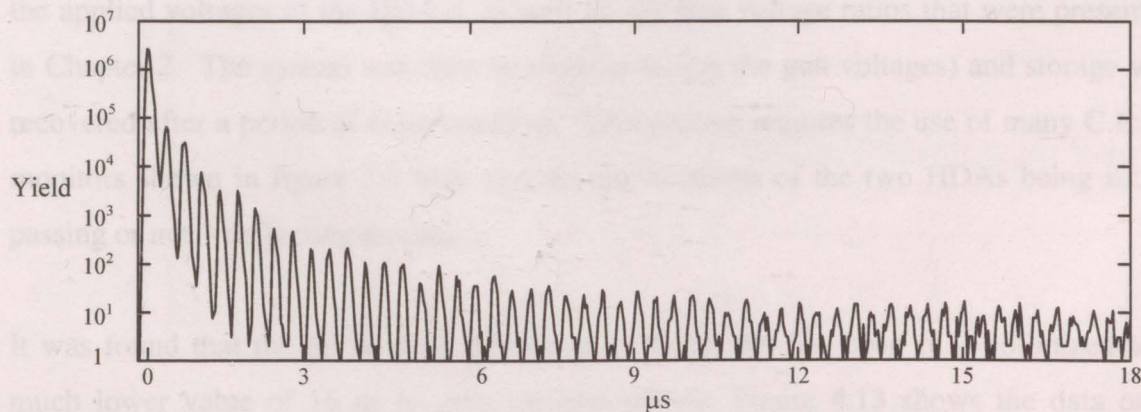


Figure 4.11: Logarithmic plot for a storage cycle period of 20 μs .

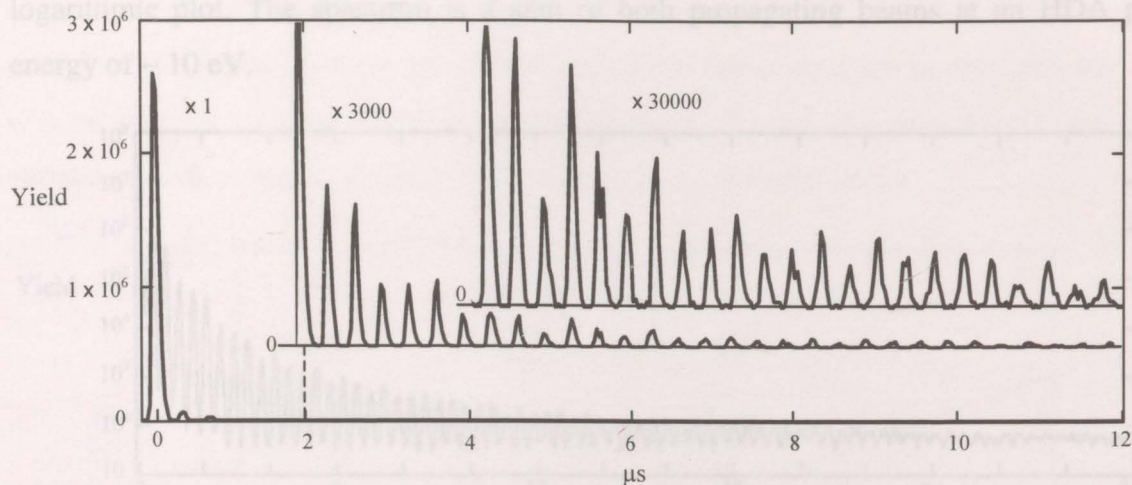


Figure 4.12: The three graphs shown above are linear plots of the data given in figure 4.11. As seen in the top graph the initial pass of the electron beam contains a very high yield peak (at time zero) that greatly dominates over the following storage peaks. Thus, the second and third graphs omit the first few “high yield” peaks with an appropriate scaling.

orbit time of ~ 340 ns over a 0.65 m length (paraxial total circumference of the ERS ring).

The peak height variation does not have a simple exponential decay; therefore, the system was retuned. Experimenting in this mode involved changes in voltage ratios, hemisphere potentials, and pulsing sequences.

ii. Optimized Wire Ring Data

Tuning the spectrometer into storage is a complex and challenging process that involves precise matching of the actual pass energies of the two HDAs (rather than the matching of the applied voltages of the HDAs), as well as, the lens voltage ratios that were presented in Chapter 2. The system was then retuned (including the gun voltages) and storage was recovered after a period of experimenting. This process requires the use of many C.E.M. monitors shown in figure 3.1 with various combinations of the two HDAs being set to passing or not – deflecting modes.

It was found that the 60 ns delay presented in figure 4.6 has been re – optimized to a much lower value of 16 ns to give optimal storage. Figure 4.13 shows the data on a

logarithmic plot. The spectrum is a sum of both propagating beams at an HDA pass energy of ~ 10 eV.

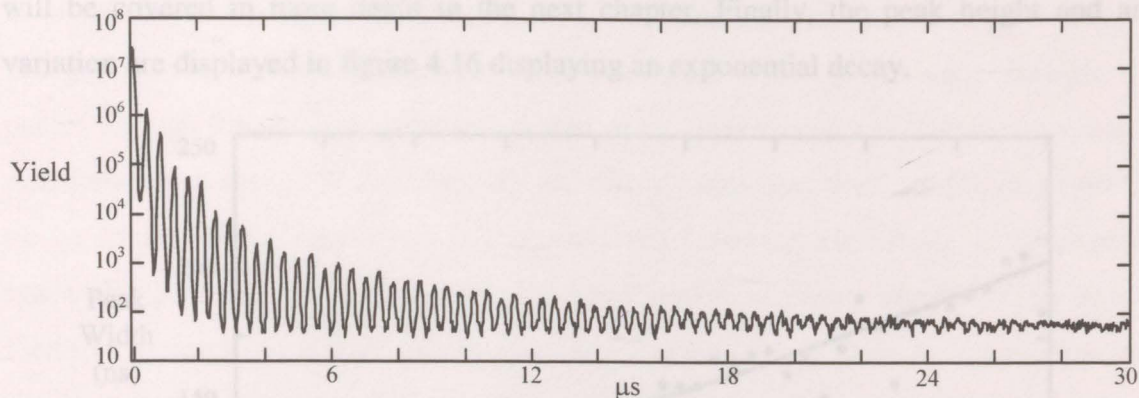


Figure 4.13: Displaying the first 30 μs of a 40 μs storage cycle on a Logarithmic plot, for setup 10 eV pass energy and ERS energy.

Analysis of the spectrum in figure 4.13 reveals that between the interval 9 μs to 30 μs the electron peak heights have an exponential decay of $\sim 9.9 \mu\text{s}$. The analysis reveals a mean orbit time of 326 ± 3 ns over a 0.65 m length and electron energy of ~ 11.1 eV throughout the storage ring, where the kinetic energy reported here was calculated from basic kinematic equations for a single electron traveling a distance of the mean circumference over a time span equivalent to the mean orbit time. Thus, the uncertainty in the mean energy is proportional to the uncertainty in the orbit time.

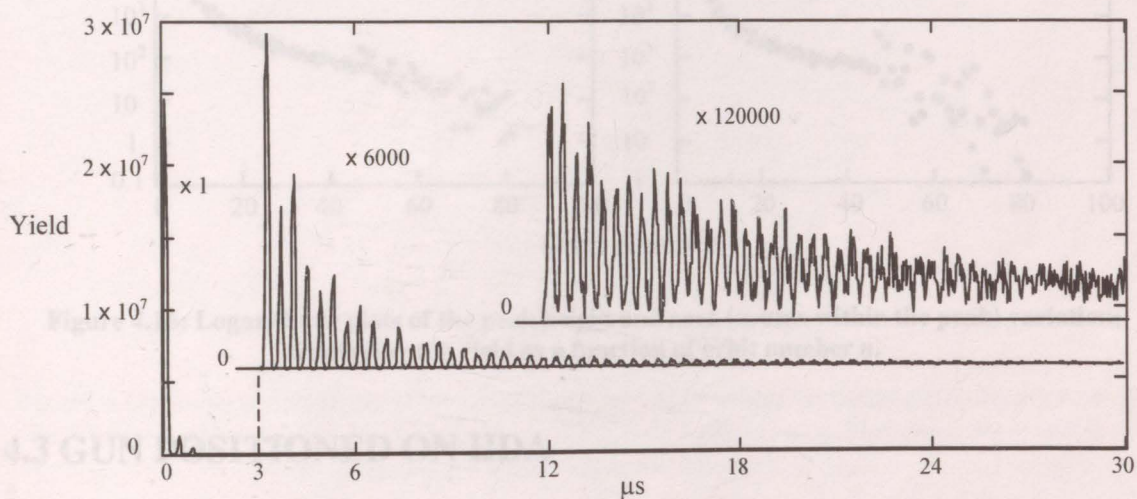


Figure 4.14: Displaying three Linear plots of the data given in figure 4.13.

In this later mode of wire ring storage, a dispersion in the peak widths is observed. The solid line in figure 4.16 corresponds to a fit to a non-linear equation in orbit number that will be covered in more detail in the next chapter. Finally, the peak height and area variation are displayed in figure 4.16 displaying an exponential decay.

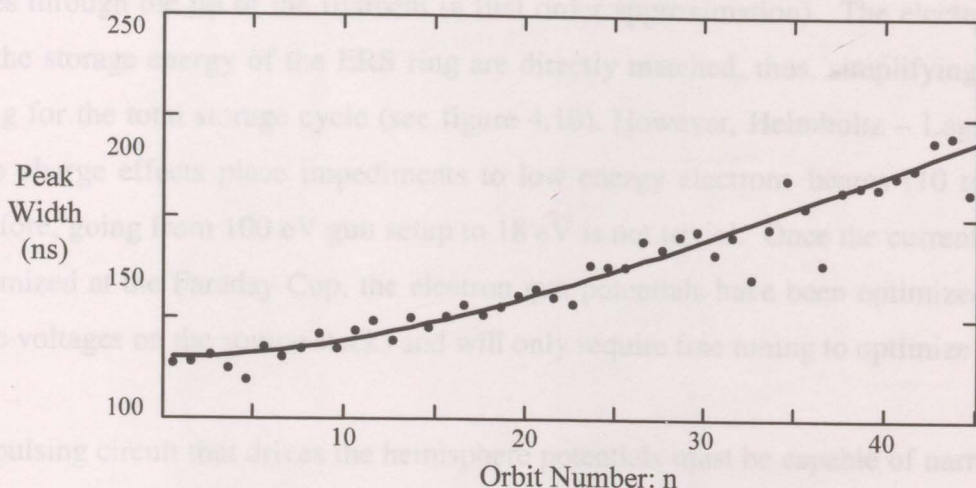


Figure 4.15: Time width of the stored electron bunches as a function of orbit number n for the peaks in figure 4.13. The solid line corresponds to a least square fit to describe the bunch width evolution.

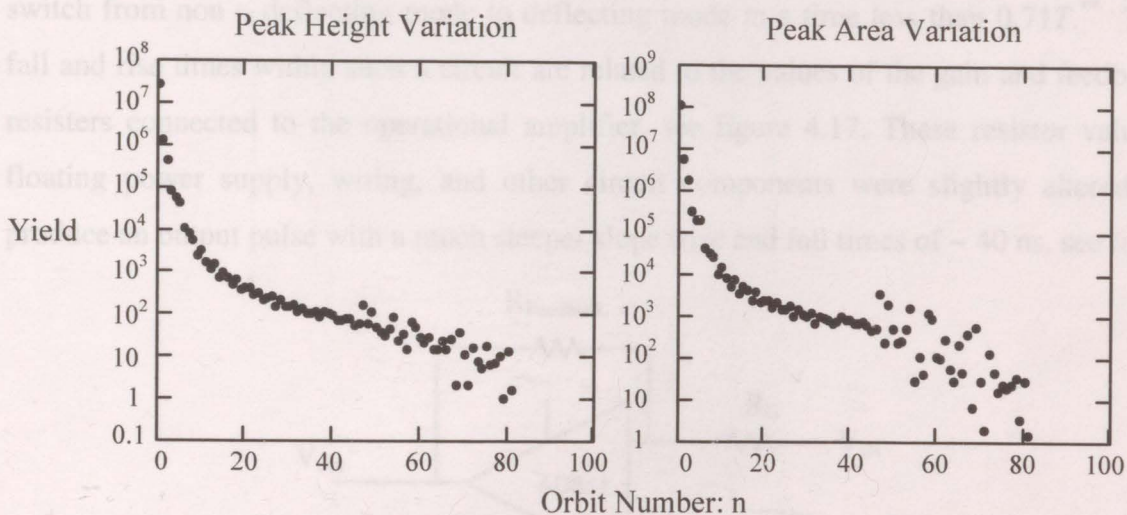


Figure 4.16: Logarithmic plots of the peak height and area (counts within the peak) variation; displaying the yield as a function of orbit number n .

4.3 GUN POSITIONED ON HDA

The following points will help to overcome the energy mismatching difficulties from the previous injection method:

- On axis beam injection, i.e. better matched phase space parameters
- High frequency pulsing circuit for the HDA
- Entire source region is now grounded, eliminating the non-trivial setup

The gun was re-positioned behind the HDA (see figure 4.18). In this setup the optic axis passes through the tip of the filament (a first order approximation). The electron energy and the storage energy of the ERS ring are directly matched, thus, simplifying injection tuning for the total storage cycle (see figure 4.10). However, Helmholtz – Lagrange and space charge effects place impediments to low energy electrons beams (10 to 20 eV); therefore, going from 100 eV gun setup to 18 eV is not trivial. Once the current has been maximized at the Faraday Cup, the electron gun potentials have been optimized (as well as the voltages on the source stack) and will only require fine tuning to optimize storage.

The pulsing circuit that drives the hemisphere potentials must be capable of narrow width pulses and steep fall and rise times. Due to the magnitude of the orbital period T of the stored beam (in the range of 250 to 350 ns), the electronics must be “fast” enough to switch from non – deflecting mode to deflecting mode in a time less than $0.71T$.^{**} The fall and rise times within such a circuit are related to the values of the gain and feedback resistors connected to the operational amplifier, see figure 4.17. These resistor values, floating power supply, wiring, and other circuit components were slightly altered to produce an output pulse with a much steeper slope (rise and fall times of ~ 40 ns, see for

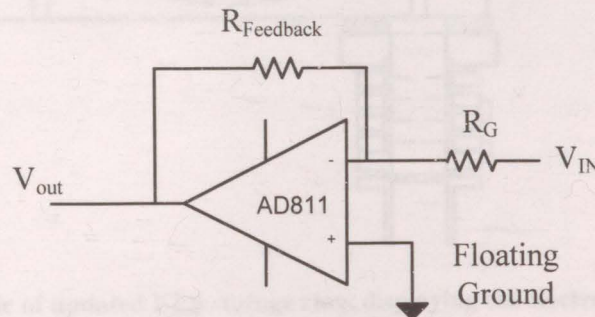


Figure 4.17: General Schematic of an Operational amplifier within the pulsing circuits presented in this Chapter, where the V_{IN} is a TTL pulse, and V_{out} is an inverted amplified pulse. $R_G = 680 \Omega$ and $R_{Feedback}$ is a variable resistor for a range 1 to 2 k Ω .

^{**} This value was taken as the length for the electrons to exit the hemisphere on injection, pass through the length of the remainder of the storage ring back to the bottom hemisphere entrance for the average energy of the electron beam.

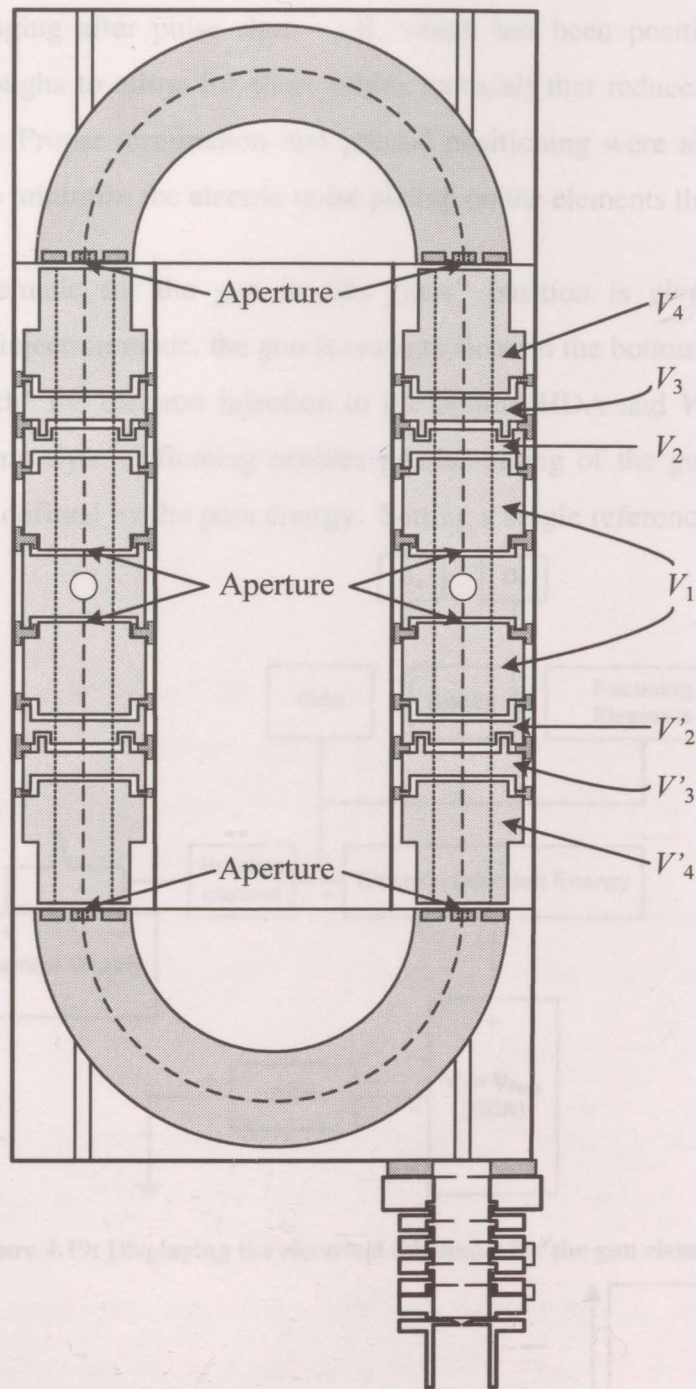


Figure 4.18: Schematic of updated ERS storage ring, displaying the electron gun positioned on the bottom hemisphere.

more detail Appendix 3 and 4). The pulsing circuit given in figure 3.20 remains as the model for the hemisphere pulsing circuit. Lower resistor values will pull a higher current from the power supplies, which have been replaced to accommodate a higher power output. The circuit has been optimized to produce an analogue variable output voltage

with minimal ringing after pulse shut – off, which has been positioned close to the chamber feedthroughs to allow for short cables (coaxial) that reduce aerial pickup (i.e. antenna effects). Proper termination and ground positioning were altered on all pulse carrying cables to minimize the electric noise pickup on the elements themselves.

The electric schematic for the gun in this “new” position is given in figure 4.19. Operating in this injection mode, the gun is made to float on the bottom HDA pass energy in order to “match” the electron injection to the bottom HDA and V_4 element (bottom pass energy). This style of floating enables precise tuning of the gun, since the mean “axial” energy is defined by the pass energy. Setting a single reference energy (bottom

4.4 PULSING SCHEMES

Injecting with the electron gun behind the HDA. The standard approach involves both the filament and an electron beam. The electrons are collected at a low orbit in the HDA, producing a series of peaks separated by a time interval. Each peak is proportional to both the inherent time spreading of the ERS and the energy resolution ΔE of the beam. Faster electrons lose the most energy and will reach the detector at a different time than slower electrons. The energy spread is given in table 4.10.

The electrons are collected at a low orbit in the HDA, producing a series of peaks separated by a time interval. Each peak is proportional to both the inherent time spreading of the ERS and the energy resolution ΔE of the beam. Faster electrons lose the most energy and will reach the detector at a different time than slower electrons. The energy spread is given in table 4.10.

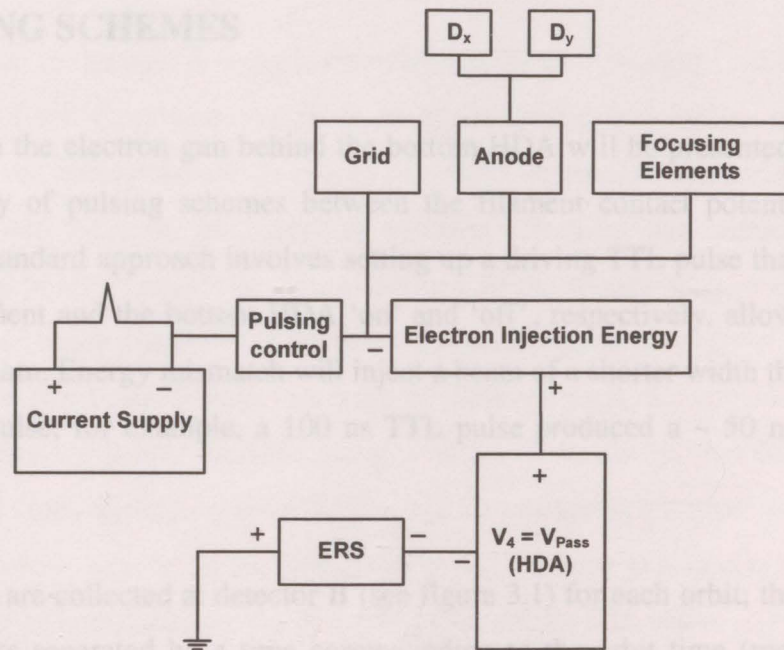


Figure 4.19: Displaying the electrical schematic for the gun elements

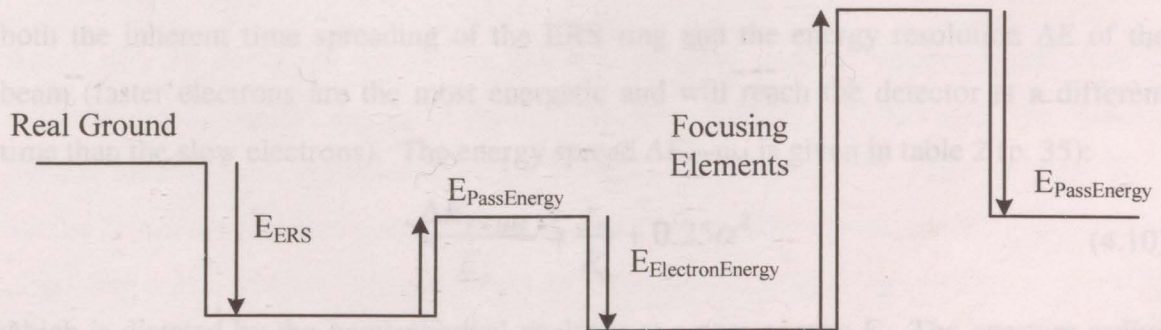


Figure 4.20: Describing the energy of the electrons according to the effects of all the floating points

pass energy) will create a uniformity in the energy of the electrons from injection to storage (crucial for injecting low energy electrons through the long length of the hemispherical analyzer / bottom V_4 and continuing to the Faraday cup, distance of ~ 30 cm).

Figure 4.20 shows the effect of all the different reference points that were imposed in figure 4.21. The energy of the electrons rise and fall in a similar manner to a “rollercoaster” kinematics problem, where, the energy of the electrons while traversing the HDA to the bottom of the source lens stack is negative with respect to real ground.

4.4 PULSING SCHEMES

Injecting with the electron gun behind the bottom HDA will be presented in this section with a variety of pulsing schemes between the filament contact potential and bottom HDA. The standard approach involves setting up a driving TTL pulse that would trigger both the filament and the bottom HDA ‘on’ and ‘off’, respectively, allowing passage of an electron beam. Energy mismatch will inject a beam of a shorter width than the duration of the TTL pulse; for example, a 100 ns TTL pulse produced a ~ 50 ns FWHM wide electron peak.

The electrons are collected at detector B (see figure 3.1) for each orbit; thus, producing a series of peaks separated by a time corresponding to the orbit time (measured peak to peak). Each peak will have a time – width associated with it; this width is proportional to both the inherent time spreading of the ERS ring and the energy resolution ΔE of the beam (faster electrons are the most energetic and will reach the detector at a different time than the slow electrons). The energy spread ΔE_{FWHM} is given in table 2 (p. 35):

$$\frac{\Delta E_{FWHM}}{E_p} \approx \frac{r_s}{R_0} + 0.25\alpha^2 \quad (4.10)$$

which is dictated by the hemispherical analyzer at a pass energy E_p . The aperture radius for the ERS ring is 1.5 mm and R_0 is 50.0 mm (see Chapter 3), where r_s is equal to 1.5

mm; therefore, by setting α equal to zero (assuming small angle of entrance of the electron beam, which becomes vanishingly small upon squaring) gives:

$$\frac{\Delta E_{FWHM}}{E_p} \approx 3\% \quad (4.11)$$

which is the FWHM of the electron beam that will be passed by the HDA. Therefore, if the electron beam has an energy resolution of $\Delta E_{GUN} > \Delta E_{HDA}$ (where ΔE_{HDA} is identical to ΔE_{FWHM}), the effect of the HDA will narrow the energy resolution of the beam, causing $\Delta E_{GUN} \rightarrow \Delta E_{HDA}$, and similarly, if $\Delta E_{GUN} < \Delta E_{HDA}$ then the energy resolution remains the same after passing through the HDA.

The peak width in the time domain is correlated to the energy width^{††}; thus, the measured time spread of the electron beam gives an upper limit to the energy resolution of the beam. Observed narrowing due to energy mismatch inspired re-evaluation of the pulsing setup that would focus on the “properly matched” electrons and eliminate the “waste” electron at the point of injection. The efficiency of the storage may be compromised by the presence of waste electrons in the beam by hindering the properly matched electrons during the first few orbits (clean – up stage of the ERS ring). By considering the energy spread of a directly heated cathode being a Maxwellian distribution of a few hundred milli-electron volts, will cause great difficulties for producing a narrow pulse [Klemperer (1971)]. Therefore, exploiting the selectivity of the electron gun injection onto the optic axis, the electric potential at the tip of the filament can be matched to a point on the pulse of the HDA; thus, producing a very narrow time spread of properly matched electrons.

Recall that the energy of the system that will properly store an electron beam must be matched to the injection energy of the electron beam for long term storage. The standard pulsing scheme for a system was shown in figure 4.6, where a TTL pulse of width 80 to 120 ns drives the filament contact potential and bottom HDA (see figure 4.19 for location of pulsing unit). The two driving pulses are separated by a 20 to 50 ns delay to allow for flight times and energy selection (the driving pulses are not perfectly square and will

^{††} Electrons of different energies will have different flight times; thus, producing a time distribution due to the velocity spread of the beam.

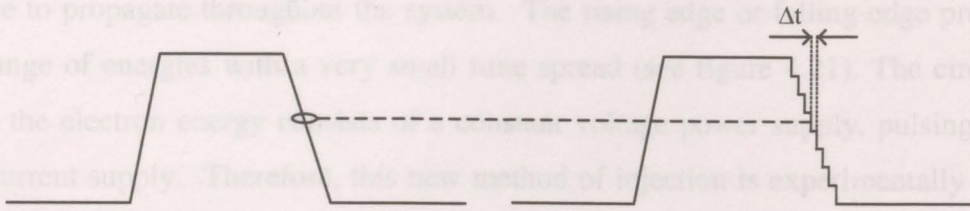


Figure 4.21: An analogue of the pulse ramp as a series of narrow – energy steps.

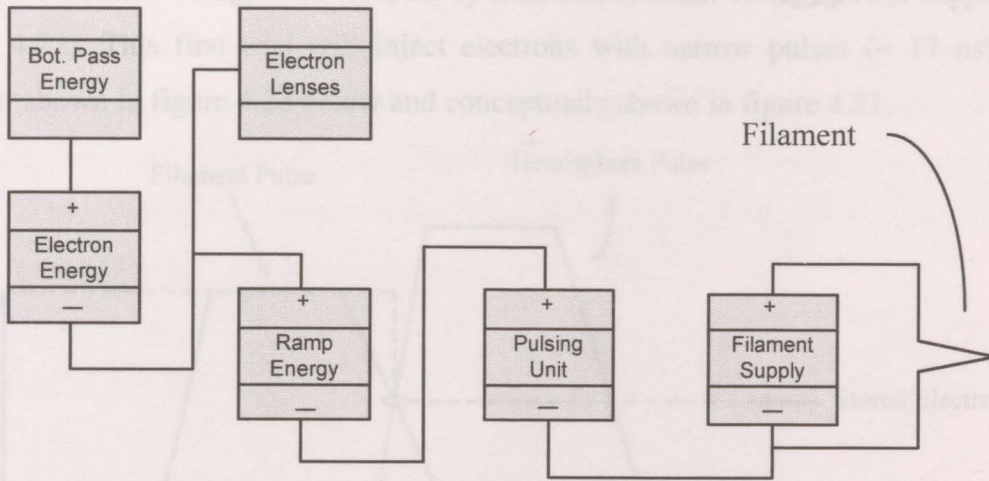


Figure 4.22: Power supply layout for the first trial of optimizing injection.

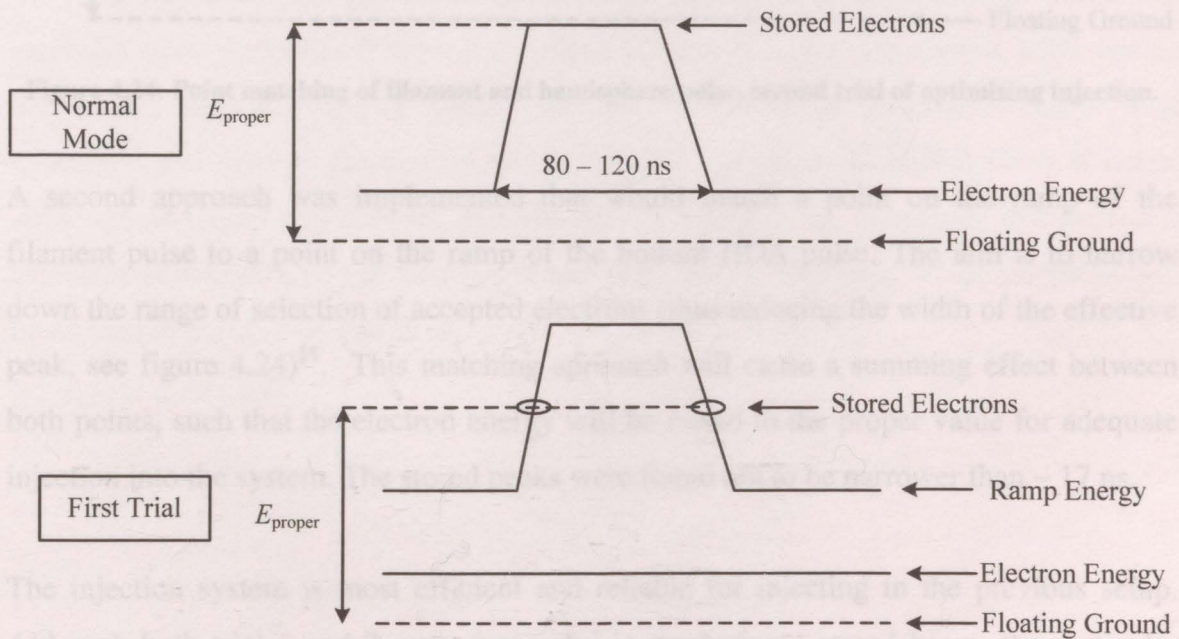


Figure 4.23: Selection points on the filament driving pulse for the energy of the stored electrons, where E_{proper} is the electron energy for adequate injection into the system.

provide a range of energies that are innately chosen by the storage ring). Thus, if a range of energetic electrons enter the system, only the electrons with the proper energy will

continue to propagate throughout the system. The rising edge or falling edge provides a large range of energies with a very small time spread (see figure 4.21). The circuit that defines the electron energy consists of a constant voltage power supply, pulsing circuit, and a current supply. Therefore, this new method of injection is experimentally reached by re – defining the energy between the pulsing circuit and the constant voltage supply; hence, the electron energy is interrupted by a second constant voltage power supply^{‡‡} (see figure 4.22). This first trial will inject electrons with narrow pulses (~ 17 ns) in the manner shown in figure 4.23 below and conceptually shown in figure 4.21.

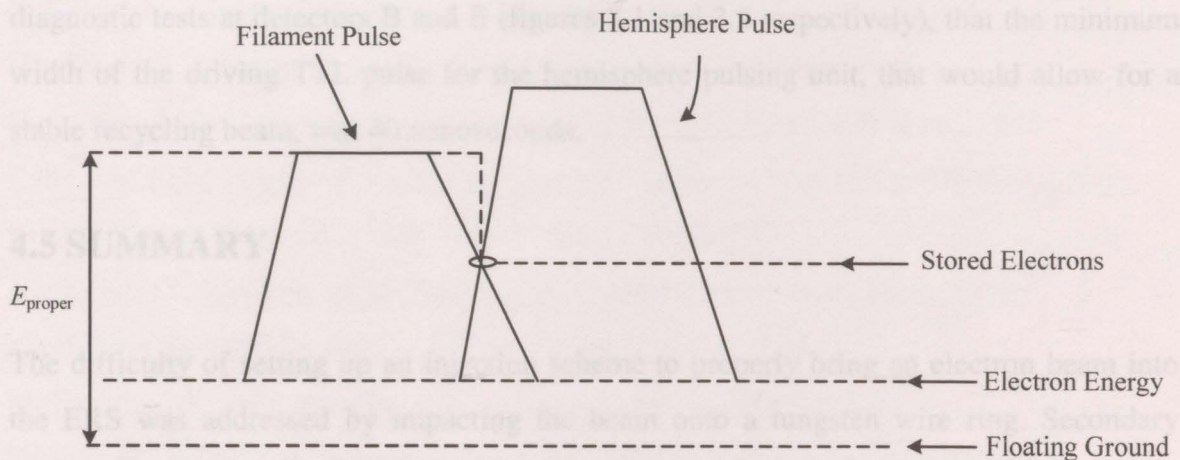


Figure 4.24: Point matching of filament and hemisphere pulse, second trial of optimizing injection.

A second approach was implemented that would match a point on the ramp of the filament pulse to a point on the ramp of the bottom HDA pulse. The aim is to narrow down the range of selection of accepted electrons (thus reducing the width of the effective peak, see figure 4.24)^{§§}. This matching approach will cause a summing effect between both points, such that the electron energy will be raised to the proper value for adequate injection into the system. The stored peaks were found not to be narrower than ~ 17 ns.

The injection system is most efficient and reliable for injecting in the previous setup. Although both trial 1 and 2 were successful in producing a stored beam, the particular energy selection in choosing the electron energy creates a very small range of phase space parameters that must be matched to the ERS parameters for efficient storage. Thus,

^{‡‡} This new power supply is referred to as the *ramp energy*

^{§§} In this second trial, the ramp energy power supply of figure 4.22 was removed

reducing the injection stability region of figure 4.1 creates a less manageable setup for efficient storage.

The HDA selects certain electron energies (and rejects the remainders), and will perform that operation within the system to narrow the energy spread of the beam. The bottom HDA allows the electron beam to enter the ERS ring by an “off” pulse. The width of this pulse will have a defining factor on the width of the injected beam. The electrical schematic for the ERS ring was returned to that of figure 3.24. It was determined through diagnostic tests at detectors B and E (figures 3.1 and 3.2 respectively), that the minimum width of the driving TTL pulse for the hemisphere pulsing unit, that would allow for a stable recycling beam, was 40 nanoseconds.

4.5 SUMMARY

The difficulty of setting up an injection scheme to properly bring an electron beam into the ERS was addressed by impacting the beam onto a tungsten wire ring. Secondary electrons were produced off the metal surface. A more efficient method was implemented that placed the electron gun directly on axis. A number of injection schemes were conceived and tried in practice to reduce the time spread of the stored electron beam. Although no pulsed was detected that was narrower than 17 ns, the energy distribution in this setup is unknown and needs to be further explored. A number of setup conditions will be addressed along with results in the next chapter.

REFERENCES

- Andersen L.H., Heber O., and Zajfman D., *J. Phys. B*, **vol. 37**, (2004) R57 – R88
- C&D Technologies website: www.cd4power.com
- Cvejanović D. and Crowe A., *J. Phys. B*, **30** (1997), 2873
- Ferch J., Granitza B., Masche C., and Raith W., *J. Phys. B*, **vol. 18** (1985) 967
- Fon W.C., Berrington K.A., Burke P.G., and Hibbert A., *J. Phys. B*, **vol. 16** (1983) 307
- Grivet P., Electron Optics, Pergamon Press, 1965
- Goldstein H., Classical Mechanics, Addison Wesley, 2002
- Hammond P., website: <http://internal.physics.uwa.edu.au/~hammond/>
- Horenstein M.N., Microelectronic Circuits and Devices, Prentice Hall Inc. 1996
- Kahn F.M., The Physics of Radiation Therapy, Lippincott Williams and Wilkins, 2003
- King D.B., and Head C.E., *Phys. Rev. A*, **vol. 17** (1978) 243
- Klemperer O., Electron Optics 3ed edition, Cambridge University Press, 1971
- Koshikawa T., and Shimizu R., *J. Phys. D*, **vol. 7** (1974) 1303
- McEachran R.P., and Stauffer A.D., *J. Phys. B*, **vol. 16** (1983) 4023
- Ortec®, MCS-PCI “www.ortec-online.com”, PLX Technology Inc. (1998)
- Ortec®, Maestro -32 “www.ortec-online.com”, PerkinElmer (2001)
- Tanabe T., Chida K., Noda K., and Watanabe I., *Nucl. Instrum. Methods A*, **vol. 482** (2002) 595
- Tessier D.R., Niu Y., Seccombe D.P., Reddish T.J., Alderman A.A., Birdsey B., Hammond P. and Read F.H., *Australian IOP Congress, Proceedings*, **vol. 50**, WC0328, (2006), Editor(s): R Sang and J Dobson, Griffith University, Australian IOP, ISBN 0-9598064-7-4.
- van Meurs B., and van der Werf R., *J. Phys. E*, vol. 9 (1976) 437
- Zajfman D., Strasser D., Heber O., Goldberg S., Diner A., Rappaport M.L., *Nucl. Instrum. Methods A*, **532** (2004) 196–202

CHAPTER 5: RESULTS AND DISCUSSION

GUN POSITIONED ON HDA

5.1 SYMMETRIC SETUP	117
5.1.1 Introduction	117
5.1.2 Data of (15 15) Pass Energy Setup	119
5.1.3 Bunch Analysis	120
5.2 ASYMMETRIC SETUP	124
5.2.1 Introduction	124
5.2.2 Metastable Background	125
5.2.3 (4 18) Pass Energy	126
5.2.4 (4 15) Pass Energy	128
5.2.5 (7 15) Pass Energy	130
5.2.6 (9 18) Pass Energy	132
5.2.7 Comparison: Asymmetric Pass Energies	134
5.3 IONIZATION STUDIES	135
5.4 SUMMARY	138
REFERENCES	141

5.1 SYMMETRIC SETUP

5.1.1 Introduction

The data presented in this section was gathered with the ERS set up with the electron gun positioned on the bottom hemispherical deflector analyzer (HDA), injecting an electron beam directly on axis (see Chapter 4). All storage peak spectra (raw data) are due to an electron signal collected on detector B of figure 3.1 of Chapter 3. The electron beam propagates throughout the system on or near the optic axis with the exception of the travel path within the HDA due to dispersion. As the beam traverses the interaction region, two main effects will cause electron losses from the stored beam:

- Collisions with the gas jet
- Metal scattering at the apertures of the V_1 elements.

Lost electrons in the storing beam account for the signal collected at detector B. Detection being a crucial component of this experiment requires losses in the beam in order to achieve the 90 degree scattering and collection within the detector; however, optimizing storage involves minimizing beam losses. Therefore, a target gas in the interaction region will scatter electrons into the detector according to the differential cross section, and will however attenuate the stored beam in proportion to the total cross section. The metal scattered electrons originate from an elastic and inelastic scattering process for $E_0 \sim 30$ eV (see Chapter 4), the elastic peak, being very sharp in reference to the inelastic peak, will not contribute as much particle yield as the wider inelastic peak. Due to the low energy of the inelastic electrons in comparison to the elastic scattered electrons (both gas and metal), a repeller plate was inserted between the interaction region and the detector to discriminate these “noise” electrons.

Recall, the ERS consists of four lenses each consisting of four elements, labeled V_1 through V_4 and two 180° HDAs. The system is positioned vertically to prevent any gravitational effects on the beam. Therefore, the two HDAs may be best classified by their vertical position, i.e. top and bottom (or upper and lower; the lower HDA being the mounting point of the electron gun). Electrons of kinetic energy of E_U will pass through

the upper HDA, and similarly those with energy E_L will pass through the lower HDA (which is also the pass energy or eV_0 of each HDA, mid-point voltage between the inner and outer hemisphere of each HDA: V_U or V_L of the HDA, see figure 5.1). The V_1 elements lie closest to the central cylinder (source or interaction region) and the V_4 element lies adjacent to the hemisphere entrance or exit. In order to well define the phase space parameters $\{p, r, r'\}$ near the apertures within the ERS, the V_1 element has been set to the voltage of the center cylinder V_{ERS} (typically ~ 30 V), and V_4 has been set to the HDA pass energy voltage V_0 .

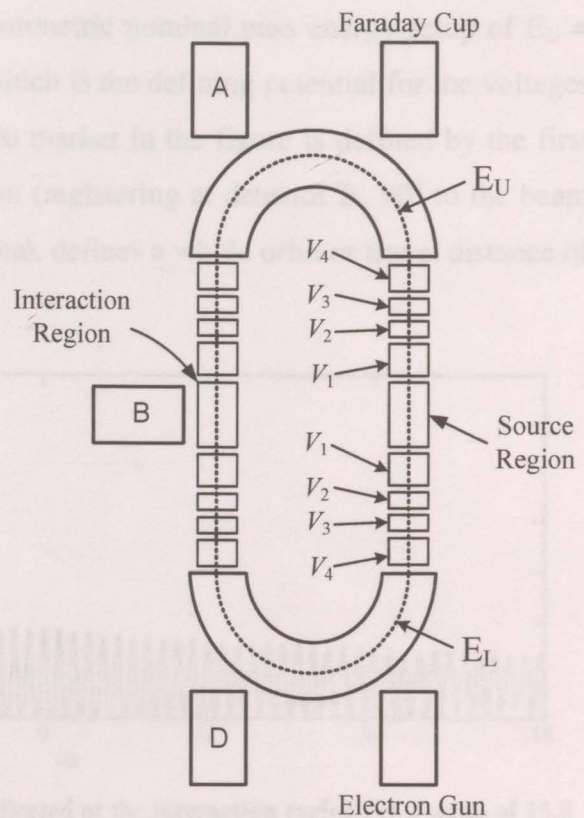


Figure 5.1: Basic Schematic of ERS, showing the pass energy for the upper and lower HDA, E_U and E_L , respectively.

There are two possible modes of operation:

- $E_U = E_L$ (Symmetric)
- $E_U \neq E_L$ (Asymmetric)

Both the symmetric and asymmetric modes allow for an efficient storage within the ring. From an experimental standpoint the symmetric mode is easier to operate, since the two HDAs are closely matched in energy (trajectories and phase space parameters are shared equally between each HDA and each pass of the beam through an HDA). The stability modes achieved are also predicted to be different for the symmetric case than the asymmetric case; the principles have been established, but the detailed voltages need to be found.

5.1.2 Data of (15 | 15) Pass Energy Setup

The following figure was recorded at the symmetric nominal pass energy setup of $E_U = E_L = 15.0$ eV and ERS energy of 15.0 eV (which is the defining potential for the voltages within the system see figure 3.24). The zero marker in the figure is defined by the first three quarter pass of the initial injected beam (registering at detector B, 90° to the beam axis given in figure 3.1). Each subsequent peak defines a whole orbit or travel distance of ~ 0.65 m.

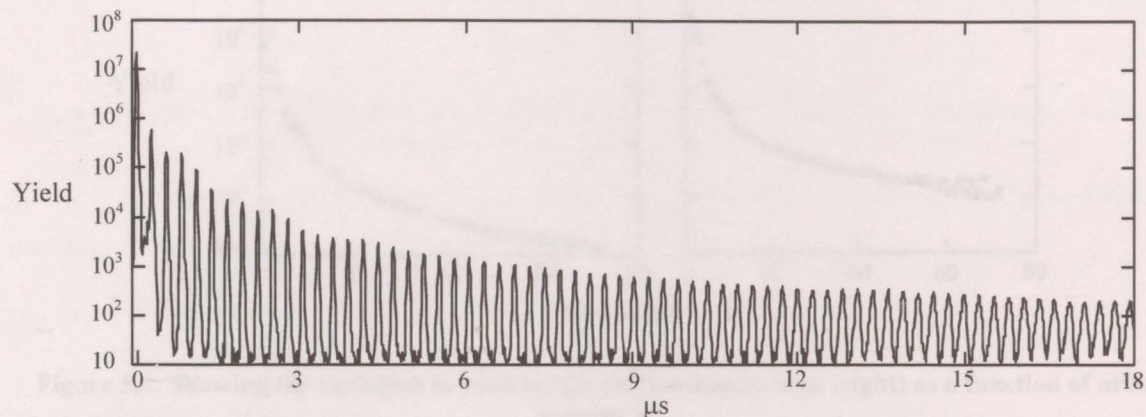


Figure 5.2: Logarithmic plot of electron signal collected at the interaction region for a setup of 15.0 eV pass energy and 15.0 eV ERS energy, storage-cycle period of 20 μs . Helium background pressure of 6.0×10^{-7} torr.

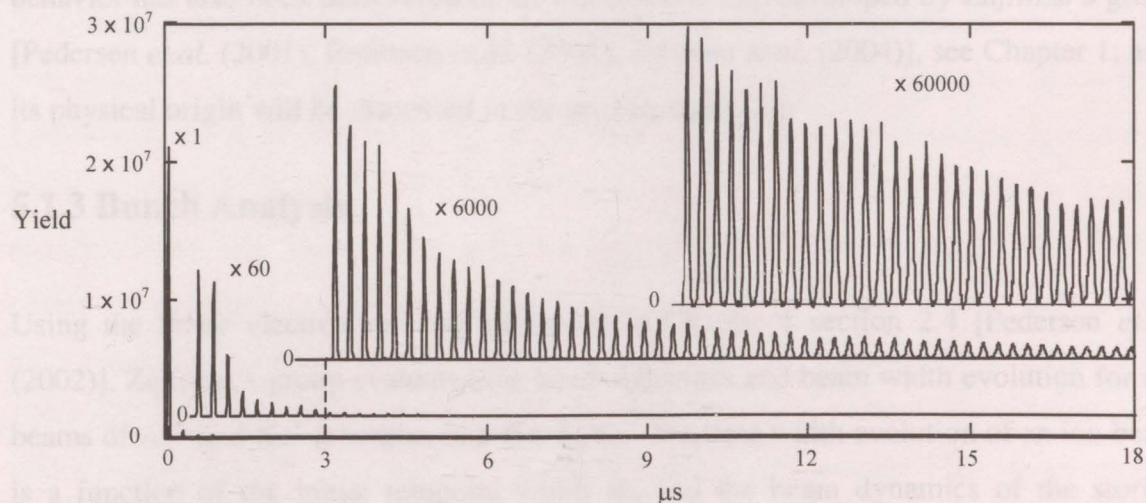


Figure 5.3: Displaying four linear plots of the data given in figure 5.2. The top plot is a cut-away section (between 10 and 18 μs) with a factor of a 60000 to bring out the peak features. Similarly, the graph between the x 60 and x 60000 has been expanded by a factor of 6000 to make the peaks between 3 and 18 μs more visible; beneath lies a linear plot expanded by a factor of 60 which is followed by the unaltered plot (x 1).

Analysis of the spectrum in figure 5.2 reveals that between the interval 5 to 18 μs the electron peak heights have an exponential decay of 5.8 μs , and the area within each peak (a better comparative measure) in that same interval has a decay of 8.1 μs (see figure 5.4). The analysis reveals an orbit time of 271 ± 2 ns over a 0.65 m length (paraxial total circumference of the ERS ring), corresponding to a mean energy of ~ 16 eV.

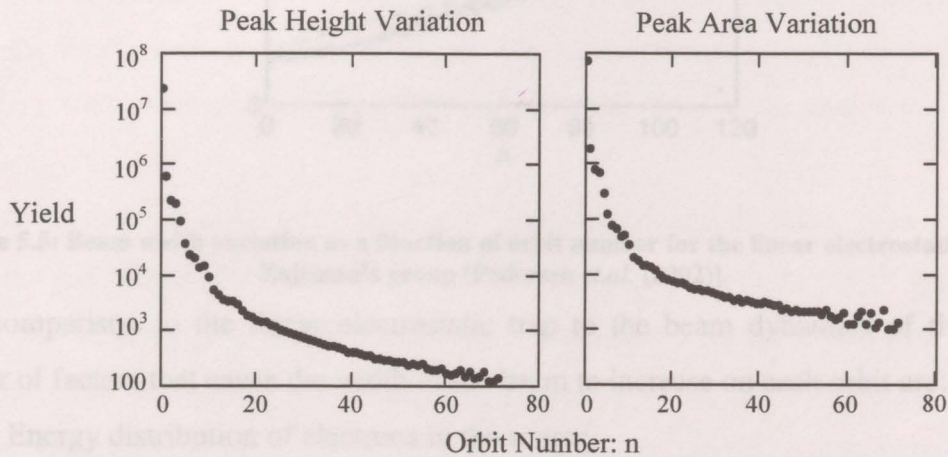


Figure 5.4: Showing the variation in peak height (left) and peak area (right) as a function of orbit number n.

The observed peak width variation is due to the beam dynamics within the ERS. This behavior has also been discovered in the electrostatic trap developed by Zajfman's group [Pedersen *et.al.* (2001), Pedersen *et.al.* (2002), Zajfman *et.al.* (2004)], see Chapter 1; also its physical origin will be discussed in the next section (1.3).

5.1.3 Bunch Analysis

Using the linear electrostatic trap presented in Chapter 1 section 2.4 [Pedersen *et.al.* (2002)], Zajfman's group evaluated the beam dynamics and beam width evolution for ion beams of Ar^+ and Xe^+ (energies of a few keV). The time width evolution of an ion beam is a function of the initial temporal width W_0 and the beam dynamics of the storing system. The beam width spreading of the beam is shown for the linear electrostatic trap for the experimental results (dots) and theoretical fit (solid* and dashed line) in figure 5.5.

* Ignoring external perturbations, such as scattering off residual gas and noise on the electrodes

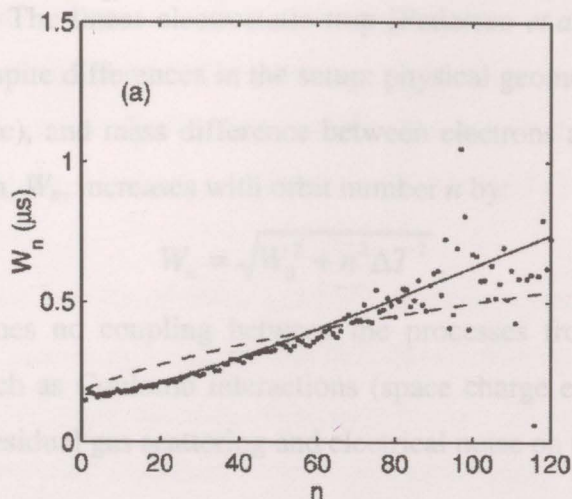


Figure 5.5: Beam width variation as a function of orbit number for the linear electrostatic trap by Zajfman's group [Pedersen *et.al.* (2002)].

As a comparison to the linear electrostatic trap to the beam dynamics of the ERS, a number of factors that cause the width of the beam to increase on each orbit are:

1. Energy distribution of electrons in the source
2. Range of acceptable trajectories within the storage ring
3. External perturbations
4. Internal perturbations
5. Initial time spread of injection pulse

First, there is an initial energy spread of the beam given by a thermal distribution that will give an inherent time spread of the beam (giving rise to a velocity spread). Second, the ERS allows for a number of stable trajectories that would produce a time spread of a beam of electrons that include a collection of positions and angles $\{r, r'\}$ for a given energy. Third and fourth considerations are interactions with external and internal perturbations. Two common examples of external effects could be electrical noise on the electrostatic elements, or collisions with background gas. Internal effects may be the Coulomb interaction between the electrons within the beam (commonly referred to as *space charge effects*). In both the linear electrostatic trap and the ERS, space charge effects are assumed to be negligible when operating with low current densities in the stored beam (electron beam currents in the pA range will result in energy spreading [Gopalan *et.al.* (2003)]). Fifth, injection is not a delta function in time, rather it has a finite width; therefore, there is a finite time spread of the beam by the TTL driving pulse

(typically ~ 50 ns). The linear electrostatic trap [Pedersen *et.al.* (2002)] observed very similar behaviors despite differences in the setup: physical geometry, a factor of ~ 1000 in time scale (orbit time), and mass difference between electrons and ions. They show the recycling pulse width, W_n , increases with orbit number n by:

$$W_n = \sqrt{W_0^2 + n^2 \Delta T^2} . \quad (5.1)$$

This equation assumes no coupling between the processes from internal mechanisms within the beam, such as Coulomb interactions (space charge effects), or from external perturbers, such as residual gas scattering and electrical noise on the electrodes.

The time spread per orbit, ΔT , consists of two components: (i) ΔT_{ERS} , the time spread within the ERS for an electron of given energy due to the possible ranges of positions and angles, $\{r, r'\}$, giving rise to a range of orbit times. These different trajectories depend on the geometrical configuration and operating potentials of the ERS; (ii) ΔT_S is due to the inherent spread in the electron energies at $t = 0$ and is usually a sole property of the source. In the present experiment, where $\Delta E_S > \Delta E_{ERS}$, it is sensible to define this ‘‘initial’’ time spread as that after the post-injection ‘‘clean up’’ of the first \sim few orbits. After the first few orbits, the bunch width increases with orbit number n . Taking ΔT_{ERS} and ΔT_S to be independent, the total time for each orbit bunch in the ERS is given by:

$$\Delta T^2 = \Delta T_{ERS}^2 + \Delta T_S^2 . \quad (5.2)$$

Ignoring external perturbations and internal coupling effects will cause ΔT to remain constant for all orbits as each electron moves independently of the others, preserving its initial orbital period.

Another behaviour of the beam spreading is a ‘non – coherent’ width evolution, whereby the electrons within the beam are treated in a stochastic sense. Here the width per orbit is re – defined by:

$$W_n = \sqrt{W_0^2 + n \Delta T^2} . \quad (5.3)$$

Assuming that the external and internal interactions cannot be ignored, a de – phase of the electrons within the beam will occur, implying that the electrons within the beam behave

stochastically (individual motion of the particles) [Pedersen *et.al.* (2002), Pedersen *et.al.* (2001)]. According to the central limit theorem (approximation for a large number of independent quantities), the distribution function for the electron beam will take on a Gaussian shape under these conditions [Khinchin (1949), Reif (1965)].

The spectra of this chapter (for example (15 | 15) symmetric pass energy) will display the bunch width as a decreasing trend in the first few orbits because $\Delta E_S > \Delta E_{ERS}$, and consequently the HDA's and apertures eliminate trajectories with inappropriate energy, radial distance and angle for sustained recycling (source energy spread is greater than that accepted by the ERS causing a "cleaning - up" of the beam).

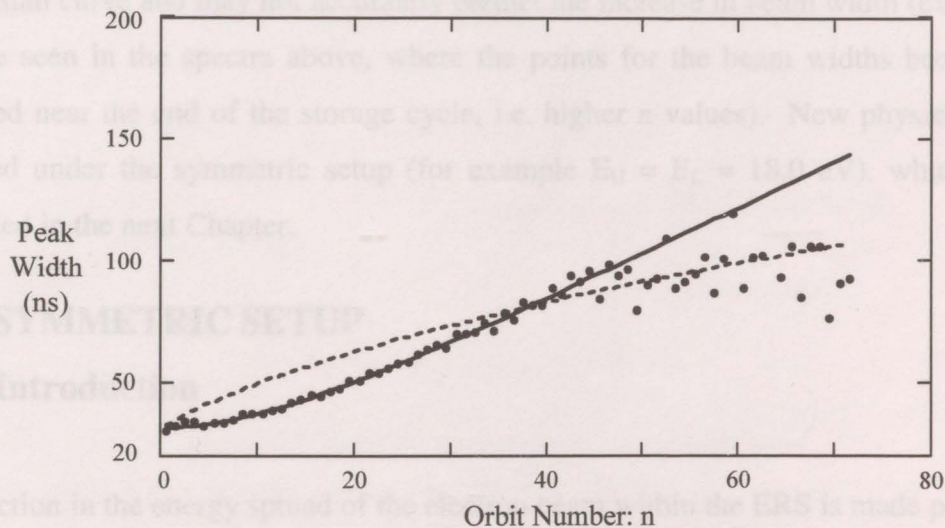


Figure 5.6: Displaying the peak width as a function of orbit number for the first 73 peaks of the data in figure 5.2. The results from the analysis (dot) are fit to coherent (solid) and non - coherent (dashed) formulas: Equations 5.1 and 5.3 (above).

In figure 5.6 the peak widths are presented as a function of peak number. It is seen that the widths increase consistently over the whole range of analysis. Omitting the first 2 peaks, the analysis was performed over the range of peak 3 (~ 1 μ s) out to peak 73 (~ 18 μ s); for widths beginning at ~ 32 ns to a value of ~ 98 ns. The solid line in figure 5.6 corresponds to a least square fit to equation 5.1; the fit reveals $W_0 = 33.36 \pm 0.05$ ns and $\Delta T = 1.5 \pm 0.1$ ns, and the dashed line is a fit to equation 5.3 with parameters $W_0 = 33.36 \pm 0.05$ ns and $\Delta T = 12.1 \pm 0.1$ ns. The points conform closely to the solid line fit; the peaks near the end (orbit number ~ 48) seem to deviate and scatter about both the solid

and dashed line, which may be due to a separation of the beam into two components (i.e. coherent and non – coherent or stochastic bunches).

Measurements were analyzed through fitting a Gaussian curve to each peak (each orbit). The peaks nearer the initial injected beam contained the best statistics of the peaks on the whole spectrum. Peak fitting analysis is most accurate for peaks that contain many points which naturally form a pattern similar to Gaussian curve. Although, the smaller peaks are better defined (i.e. more points per number of counts), the peaks with more counts will fit better than the smaller peaks near the end of the tail end that contained a lot of noise. Due to the lower statistics of orbits that lie on the latter half of the spectrum will not fit well to a Gaussian curve and may not accurately predict the increase in beam width (examples of this are seen in the spectra above, where the points for the beam widths become very scattered near the end of the storage cycle, i.e. higher n values). New physics has also emerged under the symmetric setup (for example $E_U = E_L = 18.0$ eV), which will be presented in the next Chapter.

5.2 ASYMMETRIC SETUP

5.2.1 Introduction

A reduction in the energy spread of the electron beam within the ERS is made possible by lowering the pass energy of the HDA. The bottom HDA has a lower limit on its pass energy value in comparison to the upper HDA, due to the difficulties of initial injection of the electron beam. Therefore, “good” resolution of the ERS ring requires *breaking* the *symmetry* of the top and bottom HDAs (i.e. the top HDA pass energy will be lowered from the bottom HDA pass energy, dissimilar from the previous section).

The pass energy setups given below are identified by ($V_U | V_L$). To simplify injection optimization, the bottom HDA was set up for only three incremental values of 12, 15, and 18 eV.

5.2.2 Metastable Background

Another process that takes place during electron storage is production of metastable atoms. Electrons traverse the interaction region with energy E , which, due to the presence of gas in the interaction region, leads to electron – atom collisions resulting in elastic collisions together with excitation and ionization of the target. For these measurements the gas will be either argon or helium having ionization thresholds of 15.76 and 24.5 eV, respectively [Brunt, King, and Read (1976)]. In general, a metastable state is formed when an atom is in a long – lived excited state as shown schematically in figure 5.7. Such states can be excited directly via electron collisions or indirectly by inelastic collisions that result in higher states that decay, for example, via fluorescence to the metastable state.

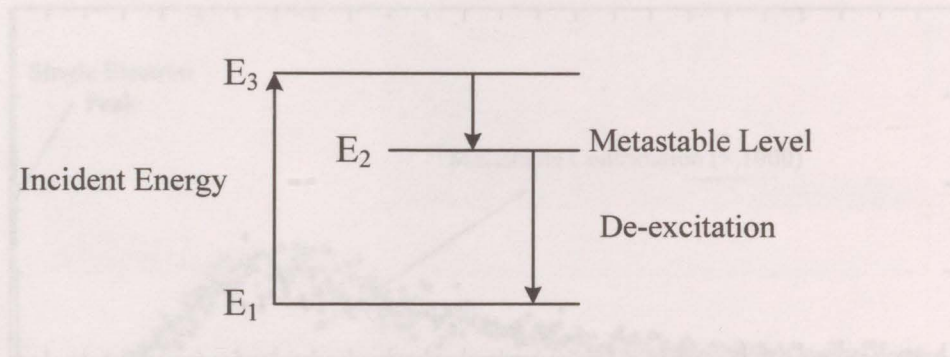


Figure 5.7: Example, production of a metastable state.

The metastable states present are the $(3p^5,4s) \ ^3P_2$ and $\ ^3P_0$ (argon) and $(1s,2s) \ ^3S_1$ and $\ ^1S_0$ (helium), whereby, the metastables will not decay down to the ground state $\ ^1S_0$ via electric dipole radiation. The lifetime for the $(1s,2s) \ ^1S_0$ to the ground state transition is ~ 19 ms [Baldwin (2005)], for the doubly forbidden transition $\ ^3S_1$ to $\ ^1S_0$ is predicted to be ~ 8000 seconds [Drake (1971)] and experimentally found to be ~ 5000 s within an experimental factor of three [Moos and Woodworth (1973)]. The argon metastable lifetimes are on a similar time scale of milliseconds (see for example [Phelps and Molnar (1953)]). The helium metastable travel time from the target region to the detector is ~ 6 μ s, which is well within the time span prior to decay [Tessier *et.al.* (2007)].

Metastables are therefore neutral particles that move at thermal velocities (for the ERS experiment), much slower than the “fast” moving electrons. The slow moving metastable

atoms will still register at the C.E.M. detector. The electrons within the neutral metastable atom will undergo an electron – electron collision with the electrons in the surface and liberate an electron, by de-exciting the metastable back to the ground state. The metastable peak formed by a passing electron beam will be very broad (thermal energy spread of heavy particles will result in a wide distribution in the time domain) and will have an onset at a later time ($\sim 6 \mu\text{s}$ in the case of helium) than that of the electron beam that caused the formation of the metastable state. The figure below (5.8) shows a single electron peak followed by a metastable peak for the ERS operating in non – recycling mode at the pass energy setup of (7 | 15). Since these metastable particles are neutral their temporal widths are independent of the potentials and only depend on the geometrical dimensions of the target region.

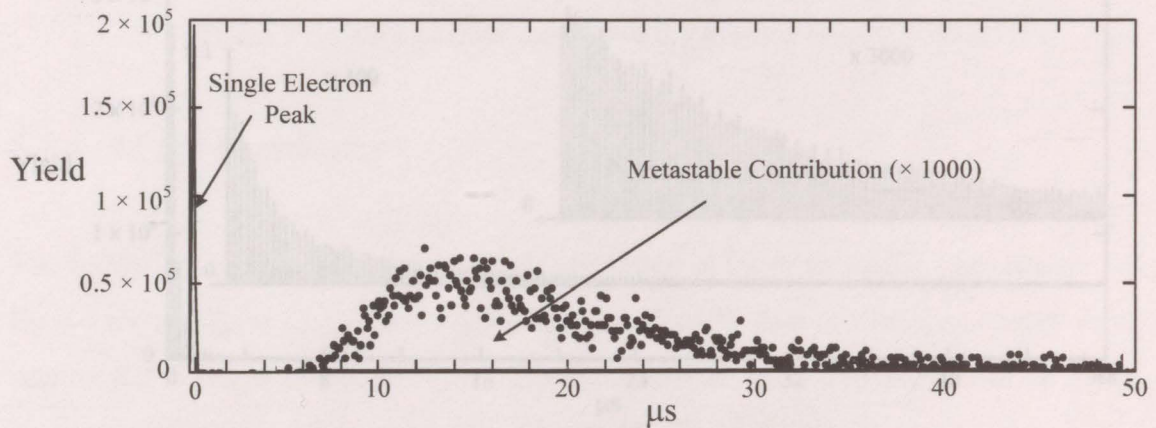


Figure 5.8: Logarithmic Plot of an electron beam that has traveled three quarters around the ring followed by a broad metastable helium peak.

5.2.3 (4 | 18) Pass Energy

The following figure is a logarithmic plot recorded at the asymmetric pass energy setup; $E_U = 4 \text{ eV}$ and $E_L = 18 \text{ eV}$, and ERS energy of 40.0 eV . Analysis of the spectrum in figure 5.9 reveals that between the interval 12 to $48 \mu\text{s}$ the electron peak heights have an exponential decay of $13.6 \mu\text{s}$, and the area within each peak in that interval has a decay of $19.4 \mu\text{s}$ [Tessier *et.al.* (2007)]. The analysis reveals an orbit time of $329.8 \pm 2 \text{ ns}$ over a 0.65 m length corresponding to a mean energy throughout the ring of $\sim 10.8 \text{ eV}$.

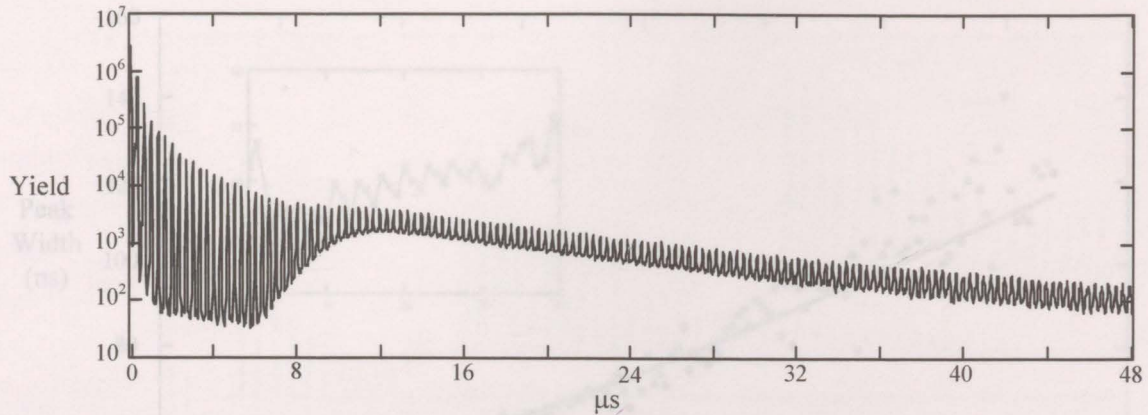


Figure 5.9: Logarithmic plot of electron signal collected at the interaction region for a setup of 4 eV Top HDA and 18 eV bottom HDA pass energy, for an ERS energy of 40.0 eV, storage-cycle period of 50 μ s. Helium background pressure of 7.0×10^{-7} torr [Tessier *et.al.* (2007)].

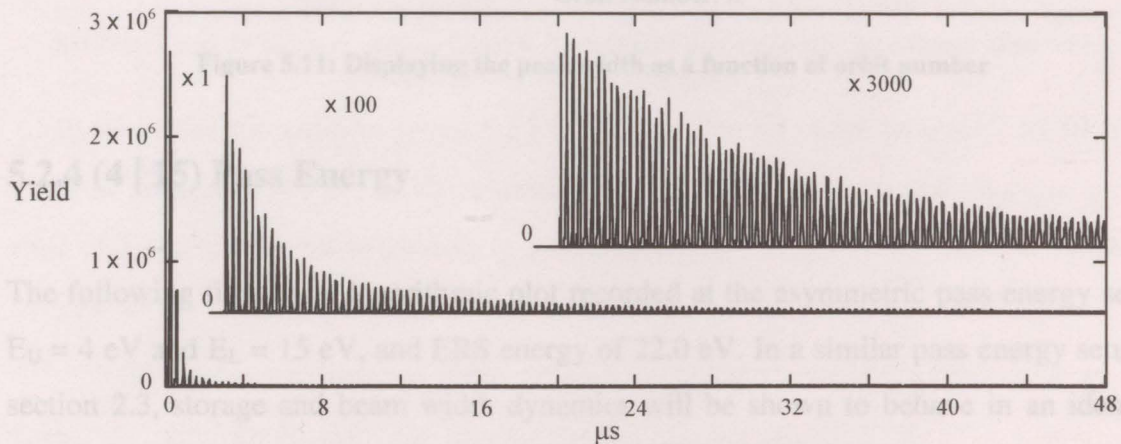


Figure 5.10 Displaying three linear plots of the data given in figure 5.9. The top plot is a cut-away section (between 20 and 48 μ s) with a factor of a 3000 to bring out the peak features. Similarly, the graph between the x 1 and x 3000 has been expanded by a factor of 100 to make the peaks between 3 and 48 μ s more visible.

In figure 5.11 the peak widths are presented as a function of peak number. From the insert, it is seen that there is an oscillation in the peak widths, whereby each oscillation peak is comprised of 4 points (orbits), it is speculated that the beam oscillates about the optic axis over a number of orbits (in this case 4 orbits). The widths begin at a value ~ 46.5 ns and increase to a value of ~ 120 ns. The solid line in figure 5.11 corresponds to a least square fit to equation 5.1; the fit reveals $W_0 = 46.5 \pm 0.1$ ns and $\Delta T = 0.74 \pm 0.05$ ns. There are no signs of a non-coherent beam width spreading.

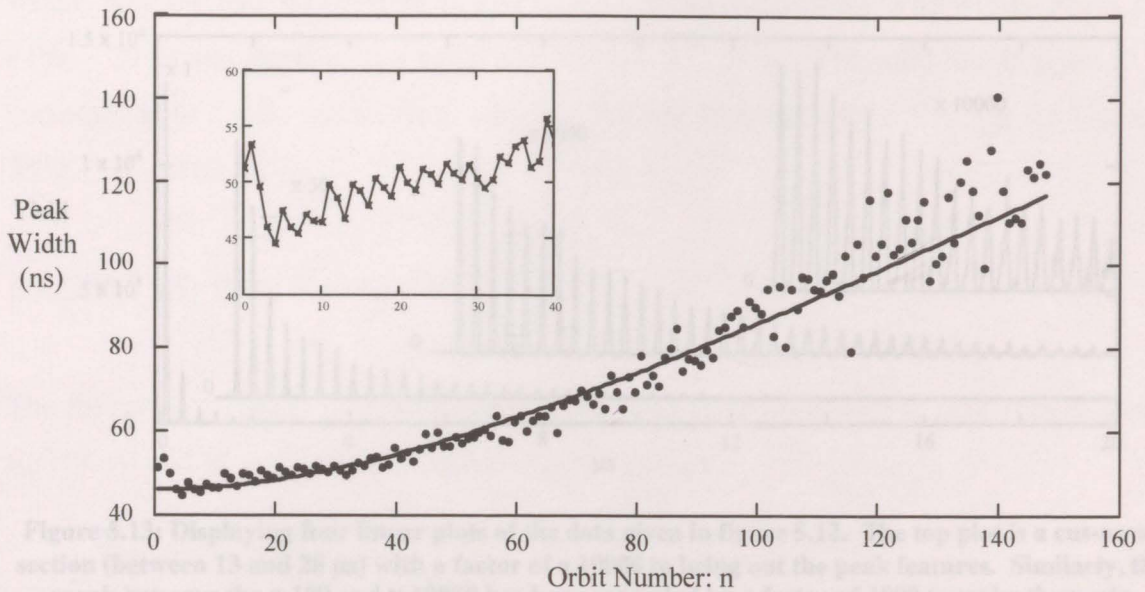


Figure 5.11: Displaying the peak width as a function of orbit number

5.2.4 (4 | 15) Pass Energy

The following figure is a logarithmic plot recorded at the asymmetric pass energy setup; $E_U = 4$ eV and $E_L = 15$ eV, and ERS energy of 22.0 eV. In a similar pass energy setup to section 2.3, storage and beam width dynamics will be shown to behave in an identical manner to the above spectra for a V_3 to V_1 ratio of nearly double.

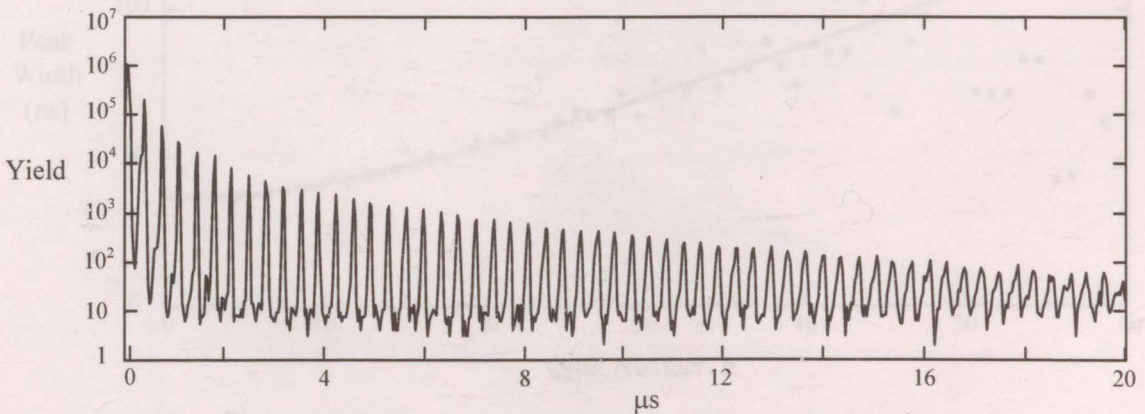


Figure 5.12: Logarithmic plot of electron signal collected at the interaction region for a setup of 4 eV Top HDA and 15.0 eV bottom HDA pass energy, for an ERS energy of 22.0 eV, storage-cycle period of 30 μ s displayed on a 20 μ s window. Helium background pressure of 6.2×10^{-7} torr.

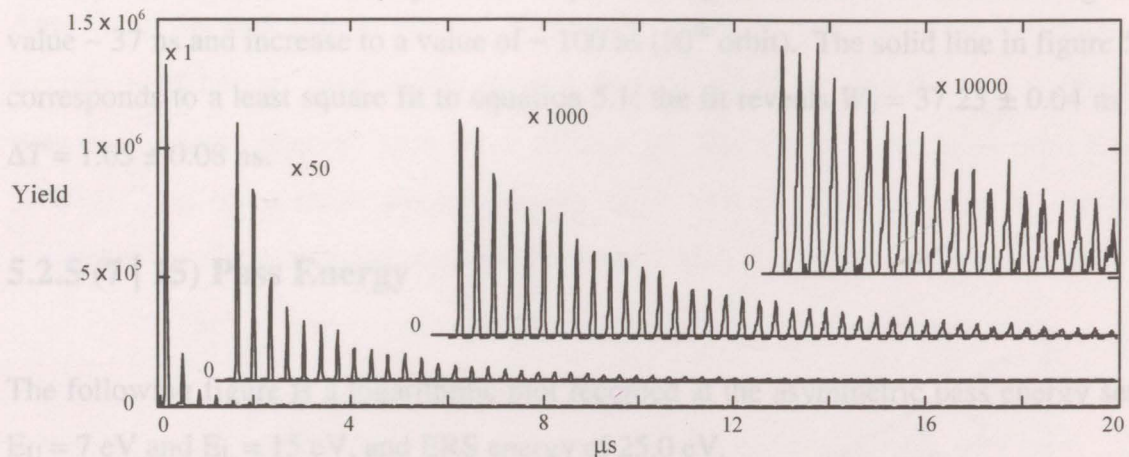


Figure 5.13: Displaying four linear plots of the data given in figure 5.12. The top plot is a cut-away section (between 13 and 28 μs) with a factor of a 10000 to bring out the peak features. Similarly, the graph between the $\times 100$ and $\times 10000$ has been expanded by a factor of 1000 to make the peaks between 6 and 28 μs more visible, beneath lies a linear plot expanded by a factor of 50 which is followed by the unaltered plot ($\times 1$).

Analysis of the spectrum in figure 5.12 reveals that between the interval 7 to 19 μs the electron peak heights have an exponential decay of 3.9 μs . The analysis reveals an orbit time of 349.6 ± 2 ns corresponding to a mean electron energy throughout the entire ring of ~ 9.0 eV.

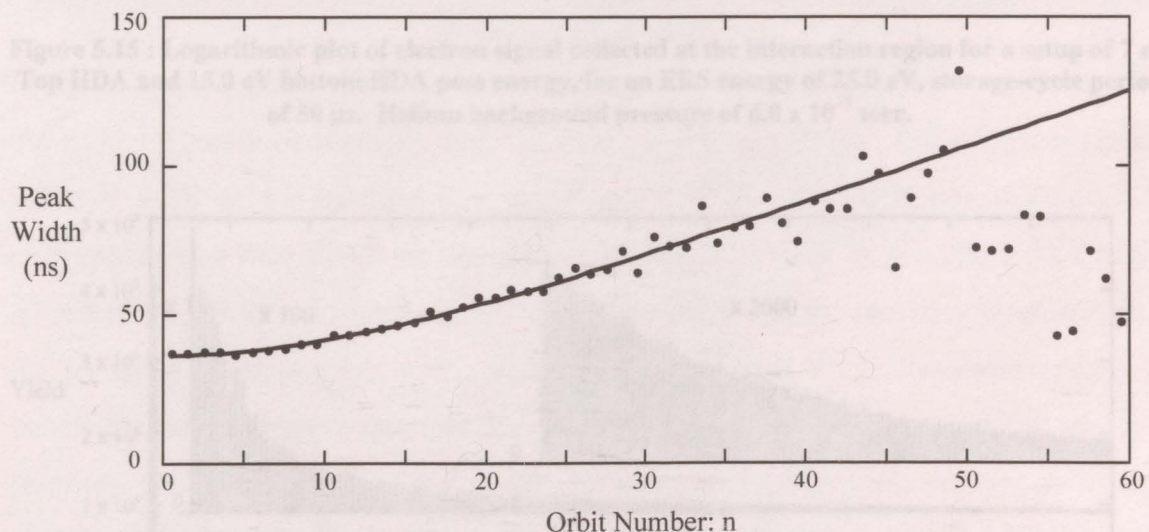


Figure 5.14: Displaying the peak width as a function of orbit number for the first 60 peaks

In figure 5.14 the peak widths are presented as a function of peak number. It is seen that the widths increase consistently over the range of 0 to the 50th orbit, with a scatter of peak

widths near the end, which may be due to peak fitting difficulties. The widths begin at a value ~ 37 ns and increase to a value of ~ 100 ns (50^{th} orbit). The solid line in figure 5.14 corresponds to a least square fit to equation 5.1; the fit reveals $W_0 = 37.23 \pm 0.04$ ns and $\Delta T = 1.65 \pm 0.08$ ns.

5.2.5 (7 | 15) Pass Energy

The following figure is a logarithmic plot recorded at the asymmetric pass energy setup; $E_U = 7$ eV and $E_L = 15$ eV, and ERS energy of 25.0 eV.

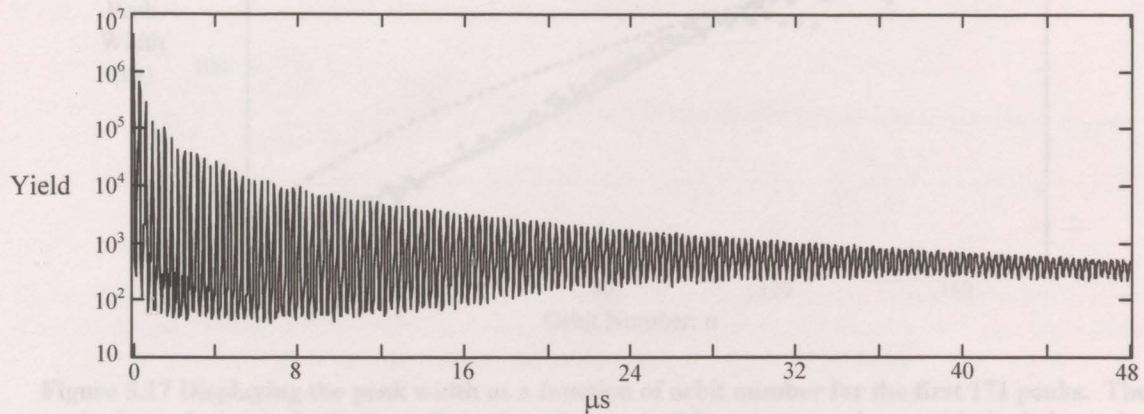


Figure 5.15 : Logarithmic plot of electron signal collected at the interaction region for a setup of 7 eV Top HDA and 15.0 eV bottom HDA pass energy, for an ERS energy of 25.0 eV, storage-cycle period of 50 μ s. Helium background pressure of 6.0×10^{-7} torr.

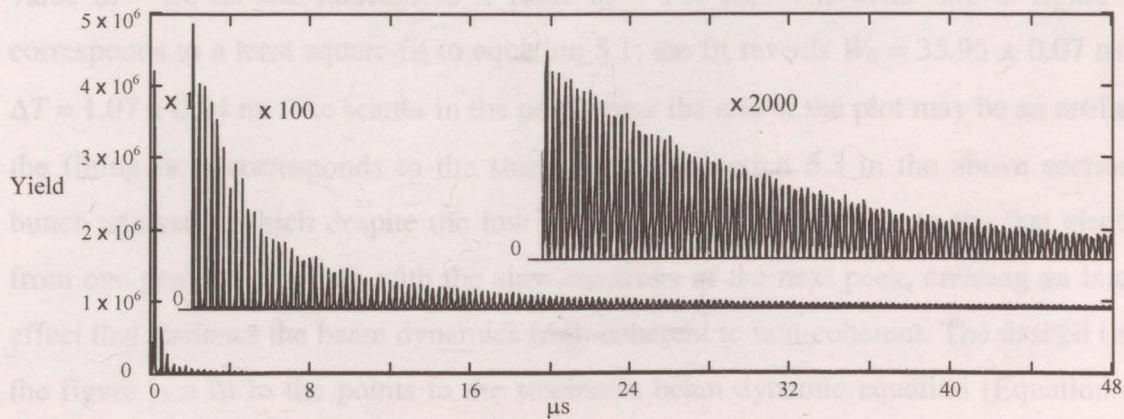


Figure 5.16: Displaying three linear plots of the data given in figure 5.15. The top plot is a cut-away section (between 20 and 48 μ s) with a factor of a 2000 to bring out the peak features. Similarly, the graph between the x 1 and x 2000 has been expanded by a factor of 100 to make the peaks between 2 and 48 μ s more visible.

5.2.6 (9) 18) Pass Energy

Analysis of the spectrum in figure 5.15 reveals that between the interval 5 to 48 μs the electron peak heights have an exponential decay of 10.08 μs , and the area within each peak in that same interval has a decay of 14.4 μs . The analysis reveals an orbit time of 300.9 ± 2 ns for a mean electron energy of ~ 13.0 eV. The merging of the peaks dominates the metastable signal, making the underlying continuum seem negligible.

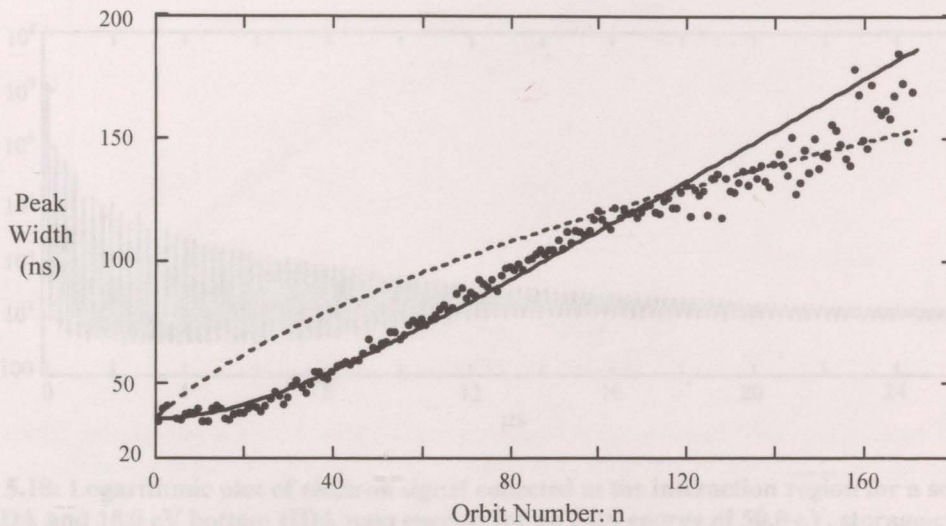


Figure 5.17 Displaying the peak width as a function of orbit number for the first 171 peaks. The results from the analysis (dot) are fit to the coherent (solid) and non - coherent (dashed) formulas: Equations 5.1 and 5.3 (above)

In figure 5.17 the peak widths are presented as a function of peak number. It is seen that the widths increase consistently over the range of 0 to the 48 μs . The widths begin at a value of ~ 36 ns and increase to a value of ~ 186 ns. The solid line in figure 5.17 corresponds to a least square fit to equation 5.1; the fit reveals $W_0 = 35.95 \pm 0.07$ ns and $\Delta T = 1.07 \pm 0.04$ ns. The scatter in the points near the end of the plot may be an artifact in the fitting or it corresponds to the stochastic fit (equation 5.3 in the above section on bunch analysis), which despite the low current density may be due to the fast electrons from one peak catching up with the slow electrons of the next peak, creating an internal effect that switches the beam dynamics from coherent to non-coherent. The dashed line in the figure is a fit to the points to the stochastic beam dynamic equation (Equation 5.3), with $\Delta T = 11.41 \pm 0.24$ ns. The peaks that are fitted to the equation 5.3 contain the lowest signal to noise ratio (as well as beam merging effects) that results in large error bars, which may account for the deviation in points about the dashed line.

5.2.6 (9 | 18) Pass Energy

The following figure is a logarithmic plot recorded at the asymmetric pass energy setup; $E_U = 9$ eV and $E_L = 18$ eV, and ERS energy of 50.0 eV. This setup will display the best example of a switch in modes from coherent to non-coherent in the beam width analysis.

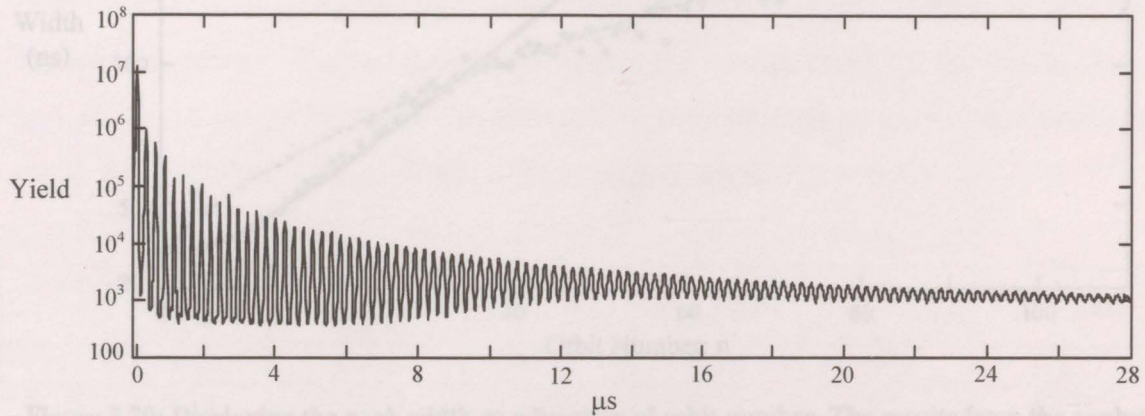


Figure 5.18: Logarithmic plot of electron signal collected at the interaction region for a setup of 9 eV Top HDA and 18.0 eV bottom HDA pass energy, for an ERS energy of 50.0 eV, storage-cycle period of 30 μ s. Argon background pressure of 7.0×10^{-7} torr.

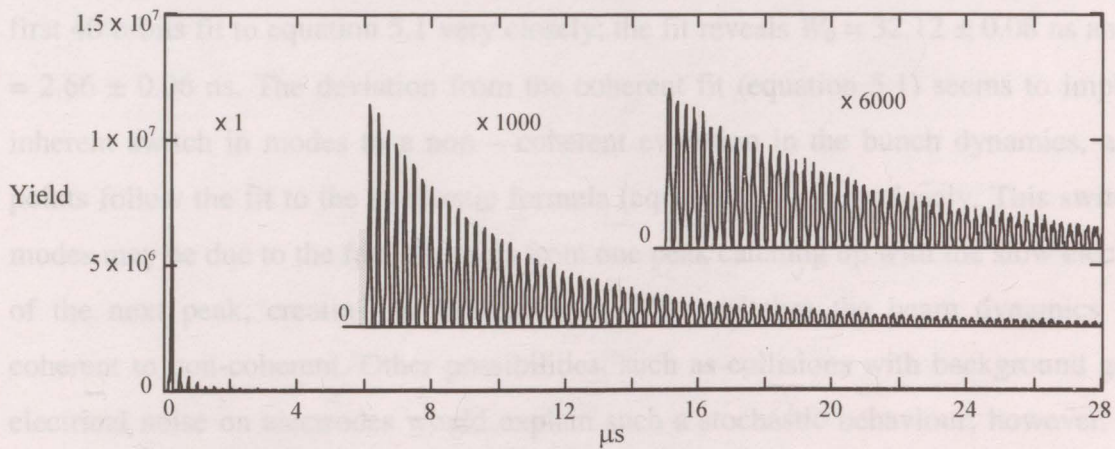


Figure 5.19: Displaying three linear plots of the data given in figure 5.18. The top plot is a cut-away section (between 15 and 28 μ s) with a factor of a 6000 to bring out the peak features. Similarly, the graph between the x 1 and x 6000 has been expanded by a factor of 1000 to make the peaks between 6 and 28 μ s more visible

Analysis of the spectrum in figure 5.18 reveals that between the interval 6 μ s to 28 μ s the electron peak heights have an exponential decay of 7.0 μ s, and the area within each peak

has a decay of $9.0 \mu\text{s}$. The analysis reveals an orbit time of $260.0 \text{ ns} \pm 3 \text{ ns}$ and mean electron energy of $\sim 17.5 \text{ eV}$.

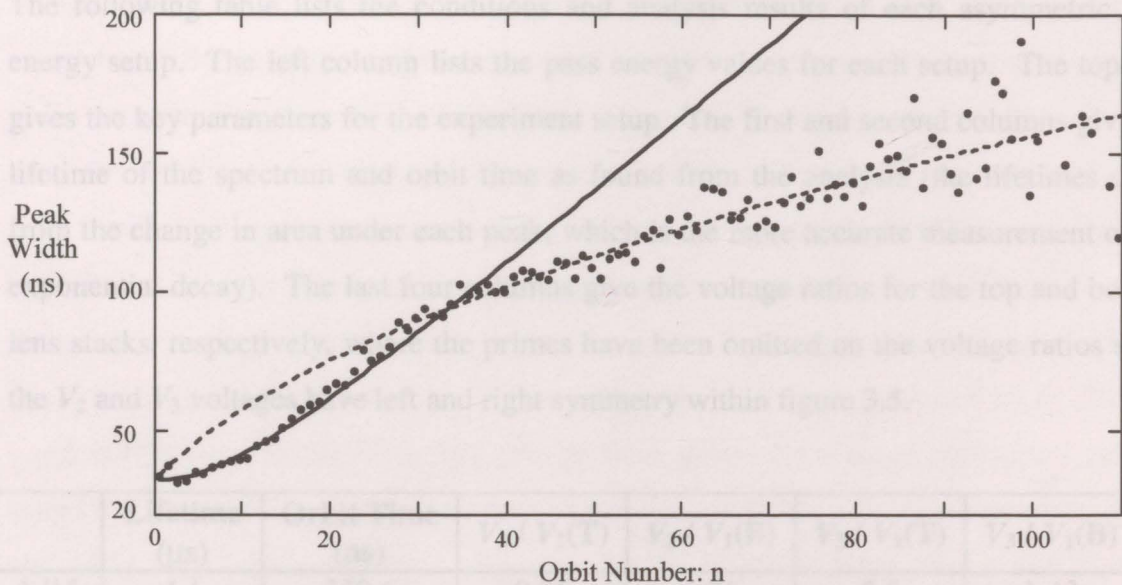


Figure 5.20: Displaying the peak width as a function of orbit number. The results from the analysis (dot) are fit to the coherent (solid) and non - coherent (dashed) formulas: Equations 5.1 and 5.3.

In figure 5.20 the peak widths are presented as a function of peak number. It is seen that the widths increase consistently over the whole range of analysis. The peak widths of the first 40 orbits fit to equation 5.1 very closely; the fit reveals $W_0 = 32.12 \pm 0.08 \text{ ns}$ and $\Delta T = 2.66 \pm 0.06 \text{ ns}$. The deviation from the coherent fit (equation 5.1) seems to imply an inherent switch in modes to a non - coherent evolution in the bunch dynamics, as the points follow the fit to the stochastic formula (equation 5.3) very closely. This switch in modes may be due to the fast electrons from one peak catching up with the slow electrons of the next peak, creating an internal effect that switches the beam dynamics from coherent to non-coherent. Other possibilities, such as collisions with background gas or electrical noise on electrodes would explain such a stochastic behaviour; however, such external effects need to be further explored. Due to the higher ERS energy in this setup may cause more collisions with background gas that would provide such an external interaction discussed above (this is only a speculation at this point in the analysis). The dashed line in the figure is a fit to the points to the stochastic beam dynamic equation (equation 5.3), with $\Delta T = 15.33 \pm 0.07 \text{ ns}$.

5.2.7 Comparison: Asymmetric Pass Energies

The following table lists the conditions and analysis results of each asymmetric pass energy setup. The left column lists the pass energy values for each setup. The top row gives the key parameters for the experiment setup. The first and second columns give the lifetime of the spectrum and orbit time as found from the analysis (the lifetimes come from the change in area under each peak, which is the more accurate measurement of the exponential decay). The last four columns give the voltage ratios for the top and bottom lens stacks, respectively, where the primes have been omitted on the voltage ratios since the V_2 and V_3 voltages have left and right symmetry within figure 3.5.

	Lifetime (μ s)	Orbit Time (ns)	$V_2 / V_1(T)$	$V_2 / V_1(B)$	$V_3 / V_1(T)$	$V_3 / V_1(B)$
4/15	4.1	350.6	9.25	5.76	5.5	1.43
5/15	5.58	320.0	8.75	5.59	3.9	1.27
7/15	14.5	300.9	8.7	6.45	3.57	1.65
9/15	7.2	290.0	6.67	5.37	2.44	1.44
4/18	19.4	329.8	9.45	5.03	10.19	2.22
5/18	6.15	321.1	9.15	6.61	6.0	1.65
6/18	12.05	323.4	9.04	6.53	5.0	1.65
7/18	10.7	301.0	9.05	6.41	4.28	1.65
9/18	9.0	260.0	9.25	8.0	5.55	2.77

Table 5

The V_3 / V_1 and V_2 / V_1 ratios are a critical factor in storage (see Chapter 2). For simplicity, the V_3 / V_1 ratio (ERS energy / Pass energy) is fixed for a give setup. The V_2 elements are tuned to bring the ERS ring into a stability region for that given V_3 / V_1 arrangement. The asymmetric setup is further complicated by having four V ratios. Assuming the whole system has discrete stability regions, and then the overall efficiency of the ring may be determined by which stability region each V ratio lies in. For example, the top V_3 / V_1 may lie in a higher region of stability than the bottom V_3 / V_1 ratio, which may lead to a less overall efficiency of the ring, and thus the reason why there is no trend in the table.

5.3 HELIUM IONIZATION STUDIES

As already discussed, electrons that traverse the interaction region have an opportunity to interact with the gas target. These electronic interactions can produce excited metastable states or ionization. Due to the similarities in mass for the ions and metastables, the ions have similar time distributions to the metastable atoms. Long term storage within the ERS has been investigated by measuring helium ion time-of-flight (TOF) distributions with detector C (see figure 3.3), situated opposite the hypodermic needle (in the path of the gas beam). Ions detected at any given time must have originated from an electronic interaction. Therefore, detected ions at late times must have been produced by an electron beam still present in the ERS. The precise time spread for a single ionization peak is found by detecting ions for a single pass of the electron beam. A typical spectrum of the He^+ yield as a function of time after the electron injection pulse over a 300 μs time window is shown in figure 5.21 for a chamber gas pressure of 5×10^{-7} torr. The ion distribution in the non – recycling mode was also recorded for the same data acquisition time and is also displayed in figure 5.21. For these spectra, the HDA pass energies (top and bottom HDA) were arranged in the symmetric setup for a value of 18 eV and the orbit time was ~ 240 ns (measured at detector B, see figure 3.1). The non – recycling mode is achieved by pulsing the electron gun in an identical manner to the recycling mode, but with the HDA voltages not being switched after electron injection making it

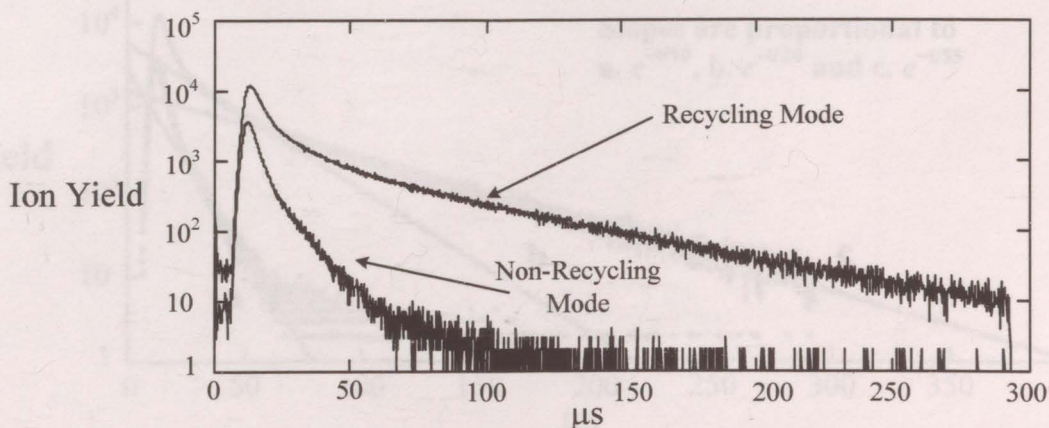


Figure 5.21: Logarithmic plot of helium ionization spectra taken within the ERS, for the symmetric pass energy setup of 18 eV.

physically impossible to recycle. In this mode, the observed signal corresponds to the inherent time of flight for helium ions created with a ~ 50 ns pulse of electrons (width W_0 from equation 5.1 of the initial injected electron beam).

More insight can be given for the ERS efficiency by analyzing the exponential decays as follows. The peak in the ion distribution occurs at ~ 13 μ s after the electron pulse reaches the detector, and the distribution has a characteristic decay time of $\tau_{NR} \approx 10$ μ s (NR \equiv non-recycling mode). The ion distribution in the recycling mode has a longer decay time $\tau_R \approx 55$ μ s, and there is still measurable ion yield at ~ 7 times that value, see figure 5.22 (the ion yield reduces by a factor of e every 55 μ s and are still observed at 300 μ s following the initial injected peak). Very few ions are detected after 60 and 340 μ s (extrapolated limit) in the non-recycling and recycling modes, respectively. Consequently, ions detected at $t = 340$ μ s originate from stored electrons in the ERS ring between $t = 280$ and 327 μ s (Ions require 13 μ s to reach the detector; thus, ions detected at 340 μ s would have been formed by an electron beam 13 μ s earlier, and the ions from the initial beam were formed 60 μ s after the initial electron beam reached detector B. Therefore, each electron beam will form an ion bunch that may have a width of ~ 60 μ s and traveled through the interaction region 13 μ s prior to ion detection). We conclude that at this operating pressure some electrons in the injected bunch were stored for ~ 5 ion lifetimes (and may

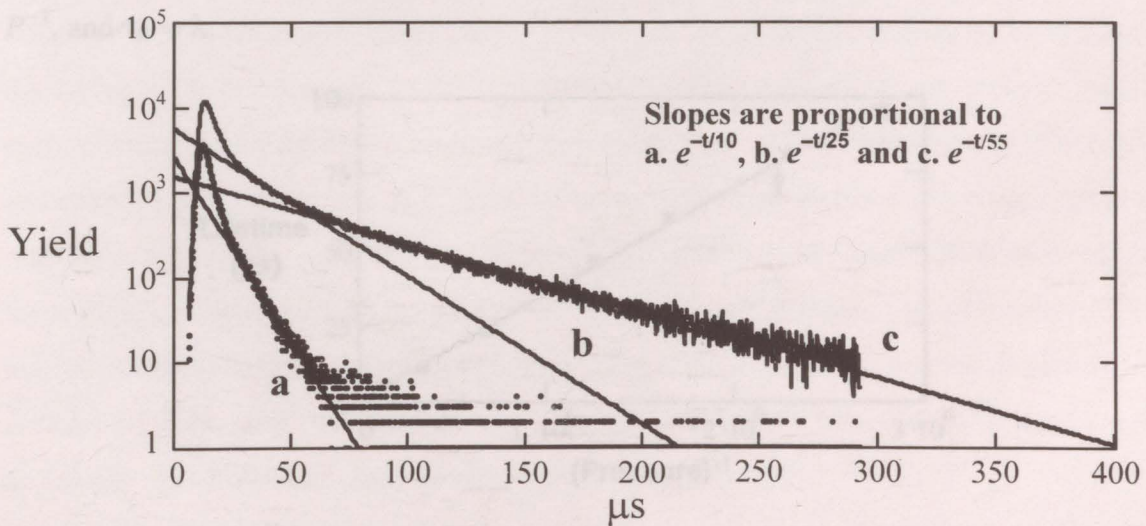


Figure 5.22: Helium ion time-of-flight distributions for non-recycling mode (a) and recycling mode (b) and (c). Exponential decay rates are $\tau_{NR} \approx 10$ μ s (a), and $\tau_R \approx 25$ μ s (b) and 55 μ s (c).

be as high as 6 lifetimes), equivalent to ~ 1000 orbits, corresponding to an electron of mean energy ~ 20 eV traveling over 650 m.

More insight can be given for the ERS efficiency by analyzing the exponential decays as a function of pressure. In Chapter 4 section 1.2, it was shown that an electron beam that travels through a gaseous medium will experience an exponential decay in current density. This loss mechanism is unavoidable and will always be seen within the analysis; therefore, the exponential decay will be a function of pressure, provided no other loss mechanisms are present. Helium ion TOF spectra were measured as a function of gas pressure, P , for identical ERS tuning and pulsing conditions. The analysis assumes that the gas pressure of the target region scales linearly with the background pressure of the chamber, which is acceptable provided there are no secondary collisions and where the pressure presented in figure 5.23 is the background pressure of the chamber [Johnson, Stair Jr. and Pritchard (1966)]. The HDA pass energies (top and bottom) were arranged in the symmetric setup for a value of 15 eV and ERS energy of 40 eV. The characteristic decay time, τ_R , determined at each pressure are displayed in Figure 5.23, plotted against P^{-1} and show a clear linear relationship. This demonstrates that the dominant loss mechanism is due to collisions with the target gas (as well as diffused background gas). These loss mechanisms are unavoidable in this experimental setup as mean free path $\lambda \propto P^{-1}$, and $\tau_R \propto \lambda$.

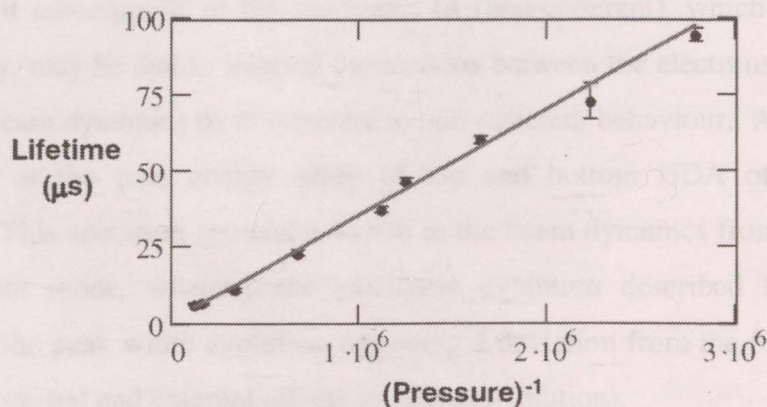


Figure 5.23: Decay lifetimes, τ_R , obtained from the asymptotic linear decay rates for 8 helium ion distributions each at a separate chamber gas pressures, P , spanning from 3.6×10^{-7} to 8.0×10^{-6} Torr.

5.4 SUMMARY

Following the theory on hemispherical deflector analyzers (HDAs) from Chapter 2, the pass energy eV_0 for the two HDAs can be identical or unequal while maintaining storage within the ERS. A data set is first presented for the identical or “symmetric” setup of top and bottom HDAs of 15 and 15 eV, respectively. The raw data is presented over a 30 μs storage cycle on logarithmic and linear graphs; also, peak width analysis, peak height and area variation as a function of orbit number n are presented. Following, is a discussion on the bunch analysis and beam dynamics within the ERS that are modeled after the linear electrostatic trap by Zajfman’s group.

Two spectra were recorded at a (4 | 18) and (4 | 15) asymmetric pass energy setup showing electron signal detected from 90° elastic and inelastic scattering at the interaction region. The first data set presented show a low exponential decay over a 50 μs storage cycle indicating optimum tuning conditions. Following, is a data set at a near double V_3 to V_1 ratio where storage has been maintained, albeit a less efficient operation. A spectrum was recorded at the pass energy setup of top and bottom HDA of 7 and 15 eV, respectively. The beam width evolution conforms to the coherent fit given by equation 5.1 for a portion of the peak spectrum, a deviation from equation 5.1 is then observed in a scatter of points about a fit to equation 5.3. The scatter in the points may be an artifact in the fitting or it corresponds to the stochastic fit (non-coherent), which despite the low current density, may be due to internal interactions between the electrons themselves that switches the beam dynamics from coherent to non-coherent behaviour. Another spectrum was recorded at the pass energy setup of top and bottom HDA of 9 and 18 eV, respectively. This spectrum showed a switch in the beam dynamics from a coherent to a non – coherent mode, whereby the stochastic evolution described by equation 5.3 conformed to the peak width evolution following a deviation from the fit to equation 5.1 as a result of internal and external effects (coherent evolution).

He^+ ions were collected at detector C of figure 3.3 to provide a representation of long term storage, giving an approximation of the total number of orbits executed by the

electron beam. Detection of ions at a given time indicates a propagating electron beam about the optic axis in the ERS at a time no greater than 60 μs prior to the ion signal. Thus, ions measured at the far right of the spectrum provide proof of electrons within the target region at long times after injection of the initial pulse without re-supplying electrons to the beam or use of active feedback components.

The ordinary performance of the ERS has been presented including beam width evolution as predicted in Section 1.3, and smooth exponential decay of the particle yield. The next Chapter will present more exotic features within the detected signal that involve a more complex beam dynamic and operation of the ERS.

Spectrum analysis

All of the analyses were performed on Mathcad 2001*i* through a Gaussian fitting method. The general function in the fit is:

$$y = b + A \left[-\frac{(E - E_o)^2}{w^2} \right], \quad (5.4)$$

where, b is average background or “noise” surrounding the given peak, A is the amplitude of the peak, E_o is the peak position, and w is the width, given by the following relation:

$$\text{FWHM} = 2\sqrt{\ln(2)}w. \quad (5.5)$$

The Gaussian is fitted using a complex algorithm developed by our collaborator Dr. Hammond (University of Western Australia) with the arguably dubious assumption that the electron signal does not lie on a background, which implies there are no metastables contributing to the observed yield. In principle, the observed merging of the sharp electron peaks may be a result of an underlining metastable continuum as shown in Fig 5.9; however, looking at figures 5.15 and 5.9 provides a comparison of the possible metastable contribution and the merging of the peaks. It is clear that the metastable is *not* the primary reason for why the peaks are merging in Fig 5.15, since there is no sign of metastable signal at $\sim 12\mu\text{s}$. An important caveat with this zero background assumption is that the analysis of the peak width variation and mode changes needs to be taken with

caution. Thus, the points of the peak can be used to calculate the FWHM as if they were not sitting above a background signal. Each spectrum contains an analysis section that contains the lifetimes, and orbit times. The magnitude of the lifetimes give an estimation of the efficiency of the system for the given pass energy setup. Whereby, the system may have been operating in a more stable mode for one set of pass energy values and (H, m) mode, which is not dependent on the pass energy setup. Electron storage rings are apt to respond more efficiently at certain resonances or modes, that depend on the external fields driving the beam [Dennison and Berlin (1946)].

- Journal of Statistical Physics, 37 (1966) 1551
- Khinchin A.I., *Foundations of Statistical Mechanics*, Dover Publications Inc. 1949
- Moos H.W. and Woodward K., *Phys. Rev. Lett.*, 30 (1973) 775
- Pedersen H.B., Strasser D., Ring S., Heber O., Rappaport M. L., Radtch Y., Sagi L. and Zajtman D., *Phys. Rev. Lett.*, vol. 87 (2001), 055001-1
- Pedersen H.B., Strasser D., Amarant B., Heber O., Rappaport M. L., and Zajtman D., *Phys. Rev. A*, vol. 65 (2002), 042704
- Phelps A.V., and Mohar J.P., *Phys. Rev.*, vol. 89 (1953) 1202
- Reif F., *Fundamentals of Statistical and Thermal Physics*, McGraw-Hill, Singapore, 1965
- Tessier D.R., Niu Y., Secomb D.P., Radtch Y.J., Alderman A. J., Birdsey B. G., Read F. H., and Hammond P., *Phys. Rev. Lett.*, 99 (2007) 233201
- Zajtman D., Strasser D., Heber O., Goldberg S., Diner A., and Rappaport M.L., *Nucl. Instrum. Methods A*, vol. 532 (2004) 195 - 202

REFERENCES

- Baldwin K.G.H., *Contemp. Phys.*, **46** (2005) 105
- Brunt J.N.H., King G.C., and Read F.H., *Jour. Phys. B*, **vol. 9** (1976) 2195
- Dennison D.M., and Berlin T.H., *Phys. Rev.*, **vol. 69** (1946) 542
- Drake G.W.F., *Phys. Rev. A.*, **3** (1971) 908
- Gopalan A., Bömmels J. B, Götte S., Landwehr A., Franz K., Ruf M.W., Hotop H., and Bartschat K., *Eur. Phys. J. D*, **22** (2003) 17
- Johnson J., Stair Jr. A.T., and Pritchard J.L., *J. Appl. Phys.*, **37** (1966) 1551
- Khinchin A.I., Foundations of Statistical Mechanics, Dover Publications Inc. 1949
- Moos H.W. and Woodworth R., *Phys. Rev. Lett.*, **30** (1973) 775
- Pedersen H.B., Strasser D., Ring S., Heber O., Rappaport M. L., Rudich Y., Sagi I., and Zajfman D., *Phys. Rev. Lett.*, **vol. 87** (2001), 055001-1
- Pedersen H.B., Strasser D., Amarant B., Heber O., Rappaport M. L., and Zajfman D., *Phys. Rev. A*, **vol. 65** (2002), 042704
- Phelps A.V., and Molnar J.P., *Phys. Rev.*, **vol. 89** (1953) 1202
- Reif F., Fundamentals of Statistical and Thermal Physics, McGraw-Hill, Singapore, 1965
- Tessier D.R., Niu Y., Seccombe D.P., Reddish T.J., Alderman A. J., Birdsey B. G., Read F. H., and Hammond P., *Phys. Rev. Lett.*, **99** (2007) 253201
- Zajfman D., Stasser D., Heber O., Goldberg S., Diner A., and Rappaport M.L., *Nucl. Instrum. Methods A*, **vol. 532** (2004) 196 – 202

CHAPTER 6: ANOMALOUS BEHAVIOR

6.1 NON - COHERENT EVALUATION	143
6.1.1 Preliminary Results	144
6.1.2 Peak Width Saturation for Symmetric Pass Energy	146
6.1.3 Peak Width Saturation for Asymmetric Pass Energy	148
6.1.4 Peak Width Saturation at Slightly Asymmetric Pass Energy	149
6.1.5 Summary	151
6.2 OSCILLATIONS ABOUT OPTIC AXIS	151
6.2.1 Symmetric Pass Energy	152
6.2.2 Asymmetric Pass Energy	153
6.2.3 Small Oscillations	155
6.3 SUMMARY	156
REFERENCES	158

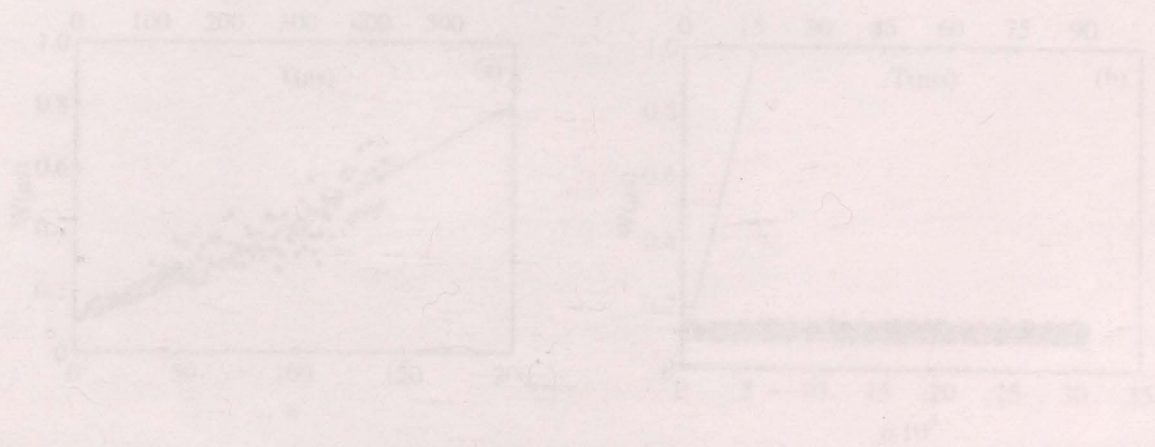


Figure 6.1: Peak width spectra [Pedersen et al. (2001)] (a) diffusion of the line within the FAS and (b) synchronization of the line oscillation, note: x - axis expanded by a factor of a 1000.

Oscillation of the ion between the two opposite "wells"

6.1 NON – COHERENT EVALUATION

In the linear electrostatic trap by Zajfman's group [Pedersen *et.al.* (2001), Pedersen *et.al.* (2002), and Zajfman *et.al.* (2004)] presented in Chapters 1 and 5, they have observed anomalies in the peak width evolution that have arisen in the ERS, which is the focal point of the Chapter. Equations 5.1 and 5.3 of Chapter 5 Section 1.3, describe the beam dynamics within the linear electrostatic trap and the ERS. Data was obtained with the linear electrostatic trap that was described by the conditions given in equation 5.1 (see figure 6.1 a) for "ordinary" behavior" within the trap. A separate data set (figure 6.1 b) revealed a deviation from the equation 5.1 fit (given as the solid line in the figures). In this case the beam width evolution takes on a different behaviour than that of figure 6.1 (a), whereby the beam width does not depend on time (or orbit number), and secondly has saturated to the most narrow value of figure 6.1 (a). The shift of modes of operation (figure 6.1 (a) to (b)) was theorized to be caused by internal interactions among the ions via the repulsive Coulomb force. Under these conditions the ion oscillations* become synchronized, which effectively "freezes" the peak width spreading, whereby the width evolution is no longer defined by either equation 5.1 or 5.3. Ultimately the synchronization must dominate over the diffusion that leads to beam width spreading described by equation 5.1 for the spectrum to take on the form of that in figure 6.1 (b).

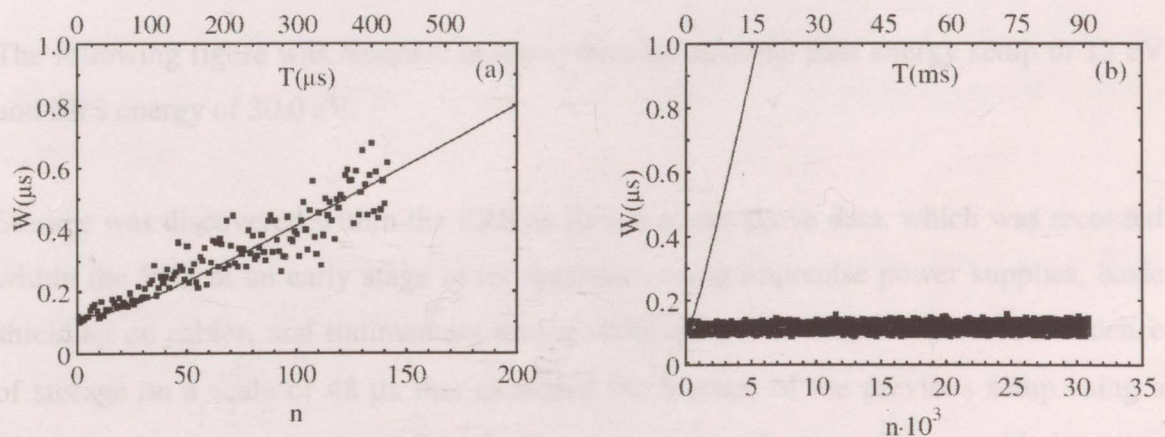


Figure 6.1: Peak width spectra [Pedersen *et.al.* (2001)] a) diffusion of the ions within the ERS and b) synchronization of the ion oscillation, note: x – axis expanded by a factor of a 1000.

* Oscillation of the ion between the electrostatic "mirrors"

Shown below in figure 6.2 is the total width evolution for the linear electrostatic trap. It is seen that a number of orbits must be executed for the synchronization to come into effect, i.e. the mass density of the ions must expand to a large enough value for the Coulomb collisions to be effective. Furthermore, the decrease in the peak widths between the $\sim 200^{\text{th}}$ and ~ 300 orbits, indicate a transition between the two modes of operation. The Coulomb force provides the non-linear coupling force that results in the synchronization of each electron oscillation (similar to a classical coupled pendulum).

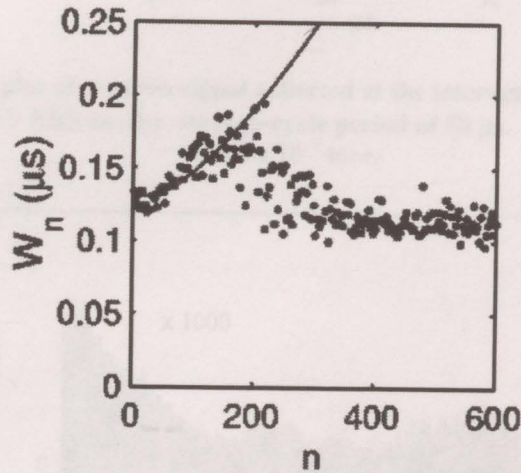


Figure 6.2: Peak width saturation within [Pedersen *et.al.* (2002)]; the solid line corresponds to a fit to equation 5.1.

6.1.1 Preliminary Results within the ERS

The following figure was recorded at the symmetric nominal pass energy setup of 12 eV and ERS energy of 30.0 eV.

Storage was discovered within the ERS as shown in the above data, which was recorded within the ERS at an early stage in its operation, using imprecise power supplies, basic shielding on cables, and rudimentary tuning techniques. This data set provides evidence of storage on a scale of 48 μs that exceeded the lifetime of the previous setup using a tungsten wire ring as the target for injection that gave motivation to pursue this injection method. Although the setup conditions are somewhat primitive, an anomalous behavior

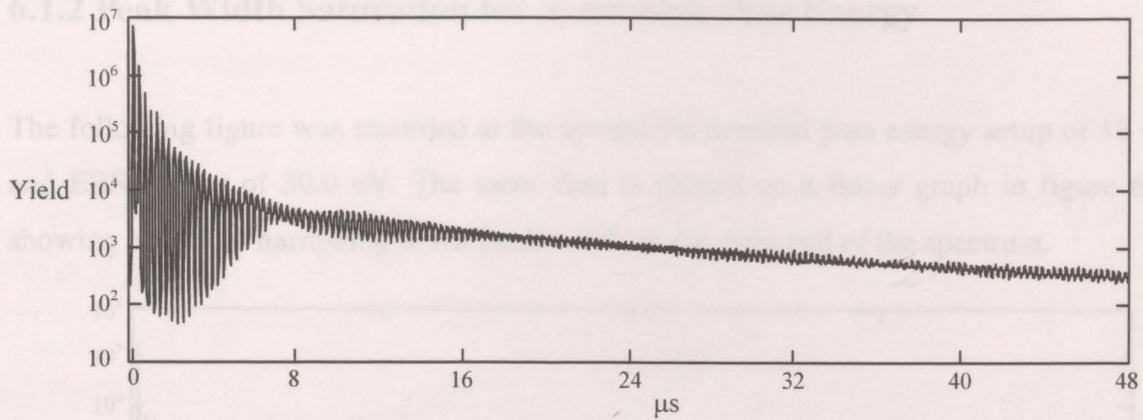


Figure 6.3: Logarithmic plot of electron signal collected at the interaction region for a setup of 12.0 eV pass energy and 30.0 eV ERS energy, storage-cycle period of 50 μs . Helium background pressure of 8.2×10^{-7} torr.

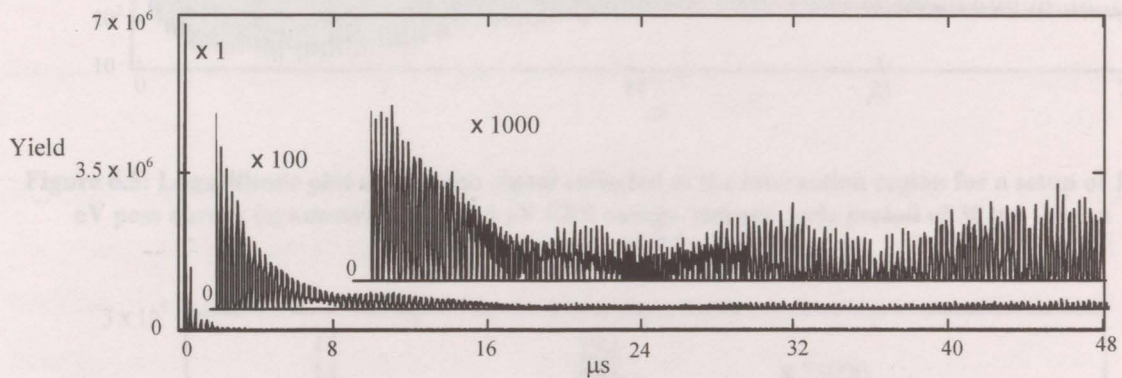


Figure 6.4: Displaying three linear plots of the data given in figure 6.3. The top graph is a cut-away section (between 10 and 48 μs) with a factor of a 1000 to bring out the peak features. Similarly, the graph between the x 1 and x 1000 has been expanded by a factor of 100 to make the peaks between 2 and 48 μs more visible.

was observed. As best seen in figure 6.4 there is a beating within the peak heights over a variable number of orbits (a thorough physical reasoning will be given in section 2 of this Chapter along with more data sets).

In line with the theory presented in the above introduction; similar behavior has been observed within the ERS, showing a “synchronization” effect of the peak width evolution. The following sections 1.2, 1.3, and 1.4 display the beam widths obtained from the ERS that have very similar trends to those seen in the linear electrostatic trap of figures 6.1 and 6.2.

6.1.2 Peak Width Saturation for Symmetric Pass Energy

The following figure was recorded at the symmetric nominal pass energy setup of 18 eV and ERS energy of 30.0 eV. The same data is plotted on a linear graph in figure 6.6, showing an abrupt narrowing in the peak width on the right end of the spectrum.

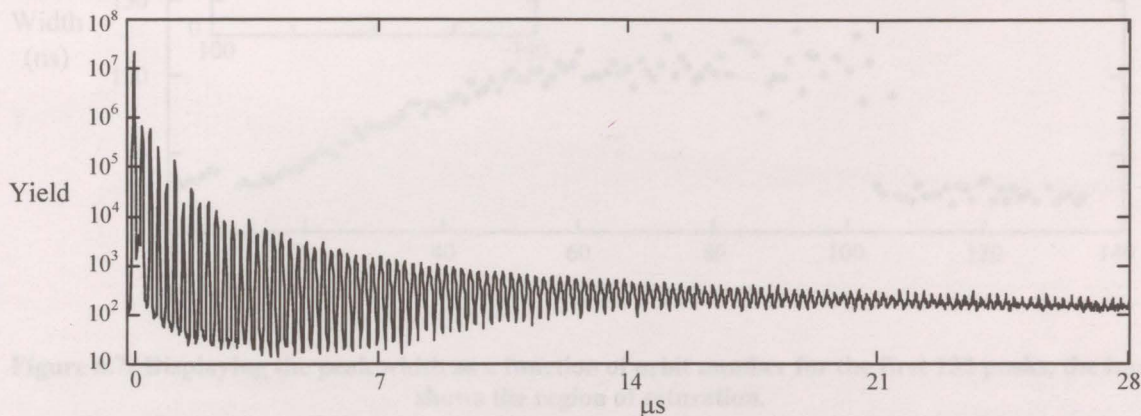


Figure 6.5: Logarithmic plot of electron signal collected at the interaction region for a setup of 18.0 eV pass energy (symmetric) and 30.0 eV ERS energy, storage cycle period of 30 μs . Argon background pressure of 9.5×10^{-7} torr.

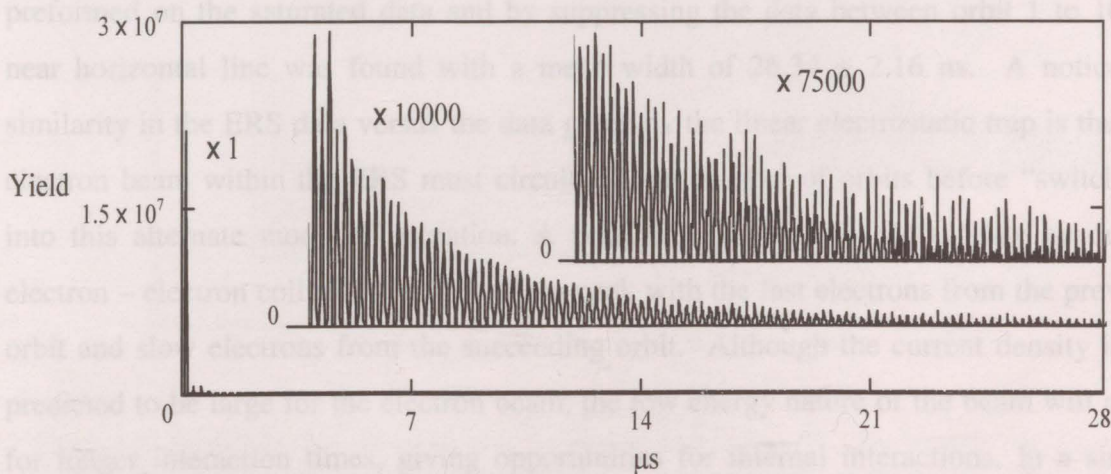


Figure 6.6: Displaying three linear plots of the data given in figure 6.5. The top plot is a cut-away section (between 12 and 28 μs) with a factor of a 75000 to bring out the peak features. Similarly, the graph between the x 1 and x 75000 has been expanded by a factor of 10000 to make the peaks between 4 and 28 μs more visible.

Analysis of the spectrum in figure 6.5 reveals that between the interval 6 to 24 μs (the range of peaks for the analysis has been truncated from 28 μs to 24 μs due to poor defined peaks in the last 4 μs of the spectrum) the electron peak heights have an exponential

decay of $\sim 5.3 \mu\text{s}$, and the area within each peak in that interval has a decay of $\sim 5.7 \mu\text{s}$. The analysis reveals an orbit time of $\sim 224.6 \text{ ns}$.

The following figure was recorded at the experiment's peak energy setup, top HDA peak energy 9 eV, bottom HDA peak energy 15 eV, and ERS energy of 22.8 eV.

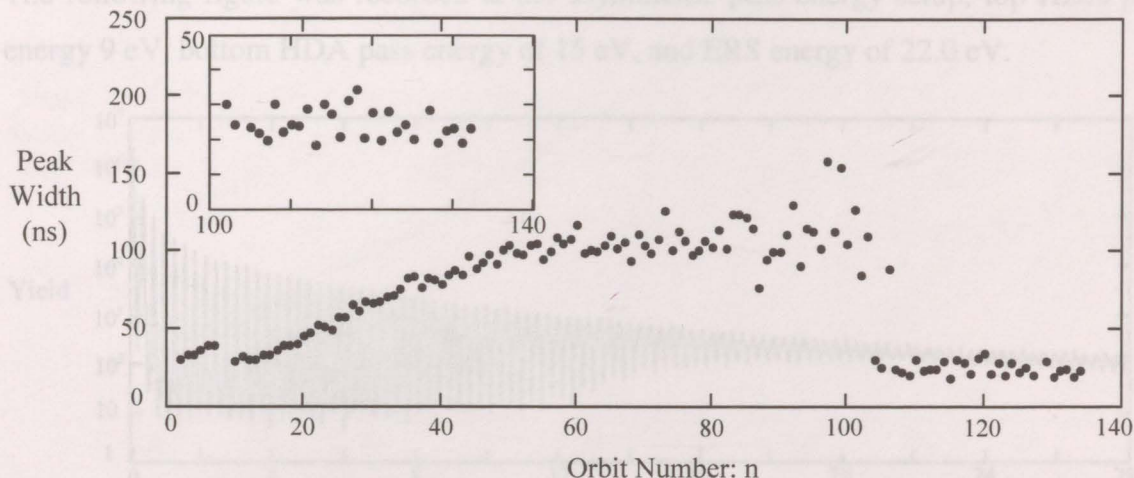


Figure 6.7: Displaying the peak width as a function of orbit number for the first 132 peaks, the insert shows the region of saturation.

In figure 6.7 the peak widths are presented as a function of orbit number. A saturation in the peak widths is observed beginning around orbit number 104. A least square fit was performed on the saturated data and by suppressing the data between orbit 1 to 103, a near horizontal line was found with a mean width of $26.34 \pm 2.16 \text{ ns}$. A noticeable similarity in the ERS data versus the data given by the linear electrostatic trap is that the electron beam within the ERS must circulate for a number of orbits before “switching” into this alternate mode of operation. A possible effect for the delay may be due to electron – electron collisions about a given peak with the fast electrons from the previous orbit and slow electrons from the succeeding orbit. Although the current density is not predicted to be large for the electron beam, the low energy nature of the beam will allow for longer interaction times, giving opportunities for internal interactions. In a similar fashion to the electrostatic trap, the switching of modes has occurred for a lower value of V_2 / V_1 ratio (typically ~ 9 for the previous modes, and ~ 6 for this “synchronization” mode), which reinforces the possibility of longer interaction times between peaks. The precise nature for the switching modes within the ERS is not fully understood, and is under investigation.

6.1.3 Peak Width Saturation Asymmetric Pass Energy

The following figure was recorded at the asymmetric pass energy setup; top HDA pass energy 9 eV, bottom HDA pass energy of 15 eV, and ERS energy of 22.0 eV.

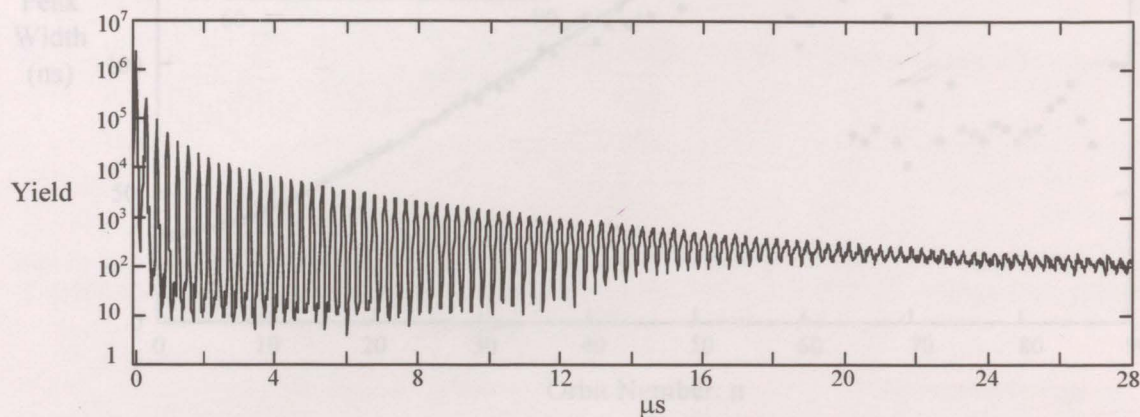


Figure 6.8 : Logarithmic plot of electron signal collected at the interaction region for a setup of 9 eV Top HDA and 15.0 eV bottom HDA pass energy, for an ERS energy of 22.0 eV, storage-cycle period of 30 μ s. Helium background pressure of 1.5×10^{-6} torr

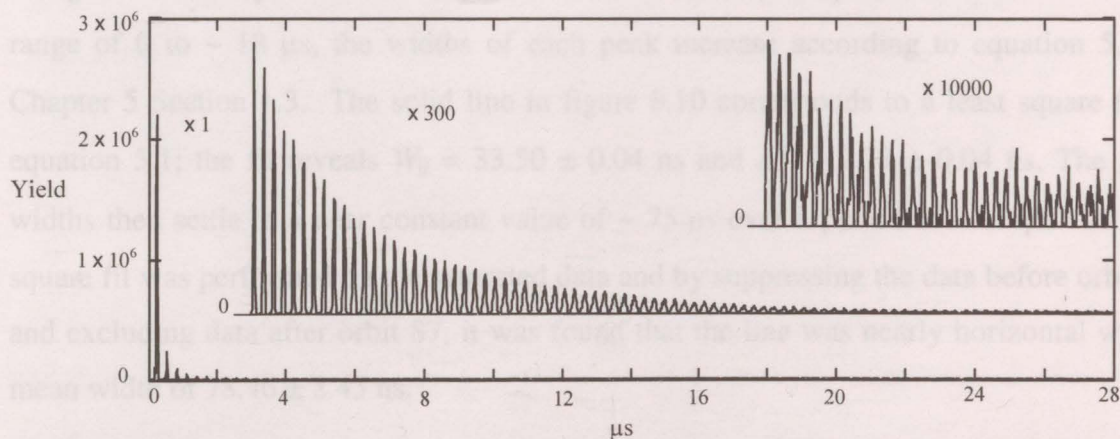


Figure 6.9: Displaying three linear plots of the data given in figure 6.8. The top plot is a cut-away section (between 18 and 28 μ s) with a factor of a 10000 to bring out the peak features. Similarly, the graph between the x 1 and x 10000 has been expanded by a factor of 300 to make the peaks between 3 and 28 μ s more visible.

Analysis of the spectrum in figure 6.8 reveals that between the interval 8 μ s to 28 μ s, the electron peak heights have an exponential decay of $\sim 6.37 \mu$ s, and the area within each peak in that interval has a decay of $\sim 7.2 \mu$ s. The analysis reveals an orbit time of ~ 290.8 ns.

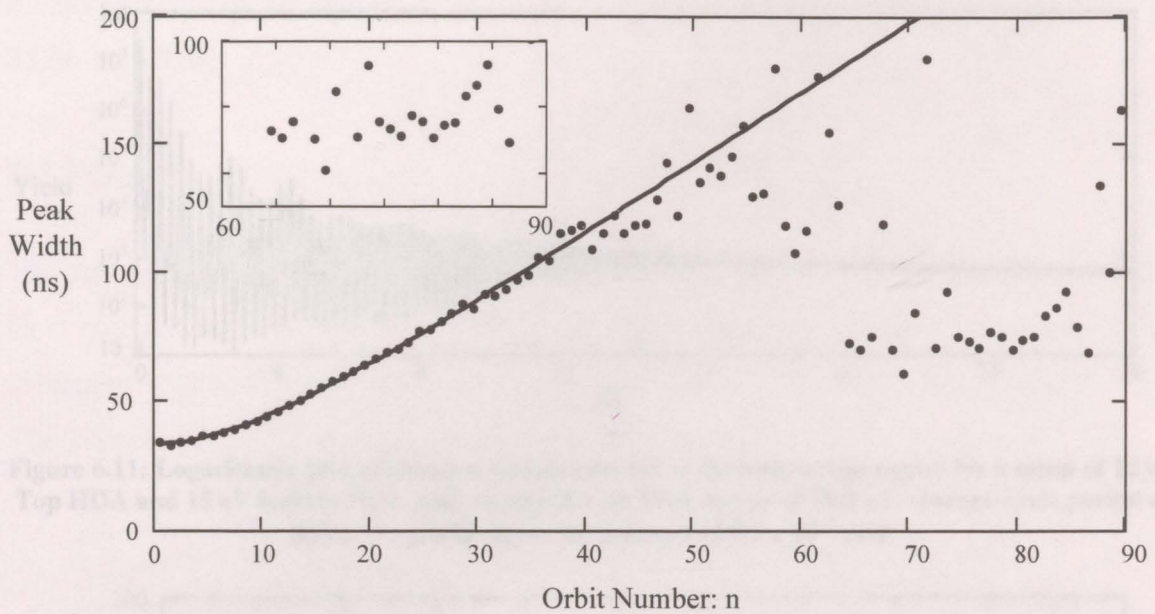


Figure 6.10 Displaying the peak width as a function of orbit number n , the insert shows the region of saturation

In figure 6.10 the peak widths are presented as a function of peak number n . Over the range of 0 to $\sim 18 \mu\text{s}$, the widths of each peak increase according to equation 5.1 of Chapter 5 Section 1.3. The solid line in figure 6.10 corresponds to a least square fit to equation 5.1; the fit reveals $W_0 = 33.50 \pm 0.04 \text{ ns}$ and $\Delta T = 2.78 \pm 0.04 \text{ ns}$. The peak widths then settle to a near constant value of $\sim 75 \text{ ns}$ over a period of $\sim 20 \mu\text{s}$. A least square fit was performed on the saturated data and by suppressing the data before orbit 65 and excluding data after orbit 87, it was found that the line was nearly horizontal with a mean width of $78.46 \pm 2.45 \text{ ns}$.

6.1.4 Peak Width Saturation at Slightly Asymmetric Pass Energy

The following figure (6.11) was recorded at the slight asymmetric pass energy setup of top HDA pass energy 12 eV, bottom HDA pass energy of 15 eV; with an ERS energy of 15.0 eV.

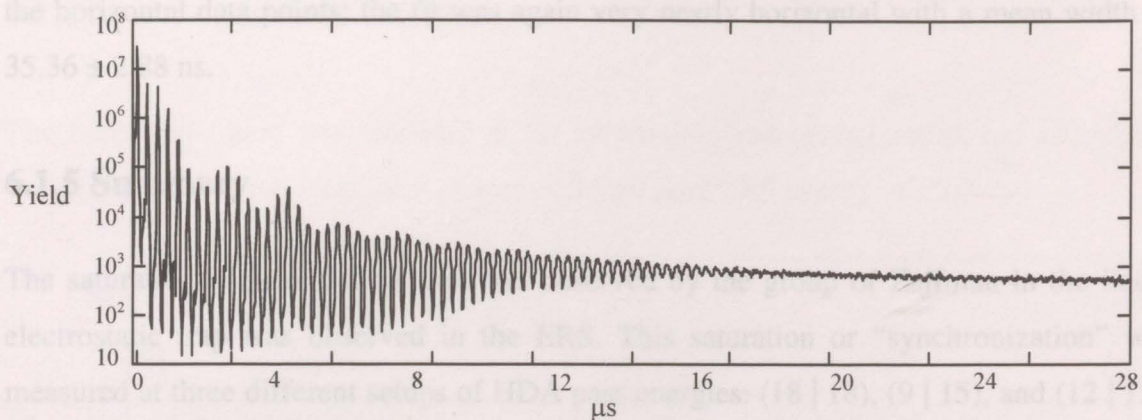


Figure 6.11: Logarithmic plot of electron signal collected at the interaction region for a setup of 12 eV Top HDA and 15 eV bottom HDA pass energy, for an ERS energy of 30.0 eV, storage-cycle period of 50 μs . Argon background pressure of 8.0×10^{-7} torr.

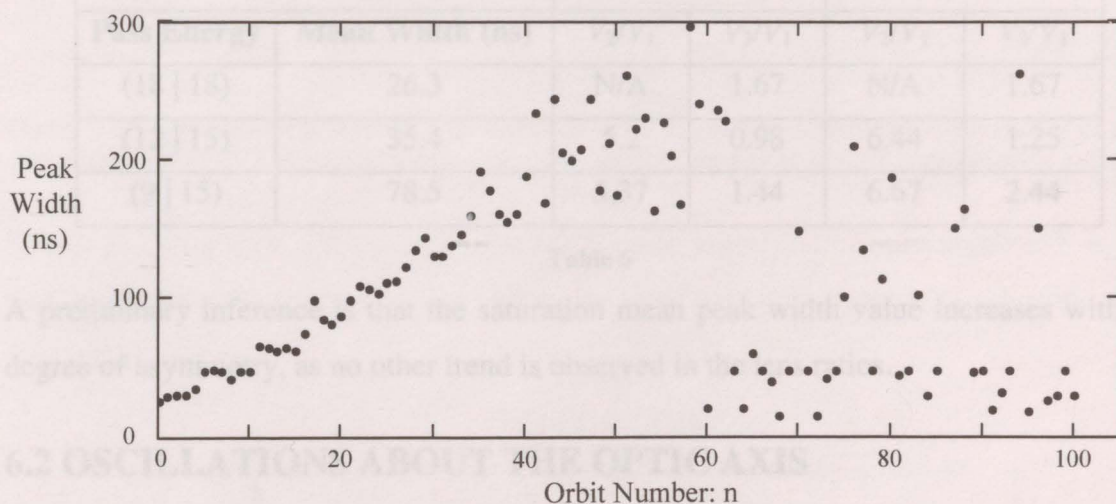


Figure 6.12: Displaying the peak width as a function of orbit number n .

In figure 6.12 the peak widths are presented as a function of peak number. It is seen that the widths increase consistently over the range of 0 to $\sim 18 \mu\text{s}$. In this mode of operation, the peak widths have saturated; however, some intermittent values lie far outside the constant value range. These anomalous data points may be an artifact of the fitting technique or may be sporadic shifting of the beam dynamics of the ERS. The conclusion for these skewed data points cannot be reached at this point as the theory and analysis is in progress. A least square fit of the saturated data was performed with suppressing the first 60 orbits; the fit was nearly horizontal with a y -intercept of 89.90 ± 17.85 ns. A second fit was performed that ignored the skewed data points, i.e. those lying far above

the horizontal data points; the fit was again very nearly horizontal with a mean width of 35.36 ± 2.88 ns.

6.1.5 Summary

The saturation in peak widths that was observed by the group of Zajfman in the linear electrostatic trap was observed in the ERS. This saturation or “synchronization” was measured at three different setups of HDA pass energies: (18 | 18), (9 | 15), and (12 | 15). The y-intercepts and lens ratios are shown in the table below:

Pass Energy	Mean Width (ns)	Bottom HDA		Top HDA	
		V_2/V_1	V_3/V_1	V_2/V_1	V_3/V_1
(18 18)	26.3	N/A	1.67	N/A	1.67
(12 15)	35.4	5.2	0.98	6.44	1.25
(9 15)	78.5	5.37	1.44	6.67	2.44

Table 6

A preliminary inference is that the saturation mean peak width value increases with the degree of asymmetry, as no other trend is observed in the lens ratios.

6.2 OSCILLATIONS ABOUT THE OPTIC AXIS

An extension to the behavior of the cases in Chapter 5 and those given above, where the observed beam heights decayed in succession with an overall exponential loss in beam density is a case where the peak heights display a “wavy” pattern. It is assumed that the cause of the “beating pattern” of the yield (or orbit amplitude) is due to an oscillation of the electron beam about the optic axis. Similar behavior exists within synchrotron rings, whereby the charged particle beam will propagate the ring in a stable fashion while oscillating. The modes of oscillation within the synchrotron are compared to those of a classical coupled pendulum[†] [Twiss and Frank (1949)].

[†] As well as the parameters: period and phase

6.2.1 Symmetric Pass Energy

The following figure was recorded at the symmetric pass energy setup; top HDA pass energy 15 eV, bottom HDA pass energy of 15 eV, and ERS energy of 15.0 eV.

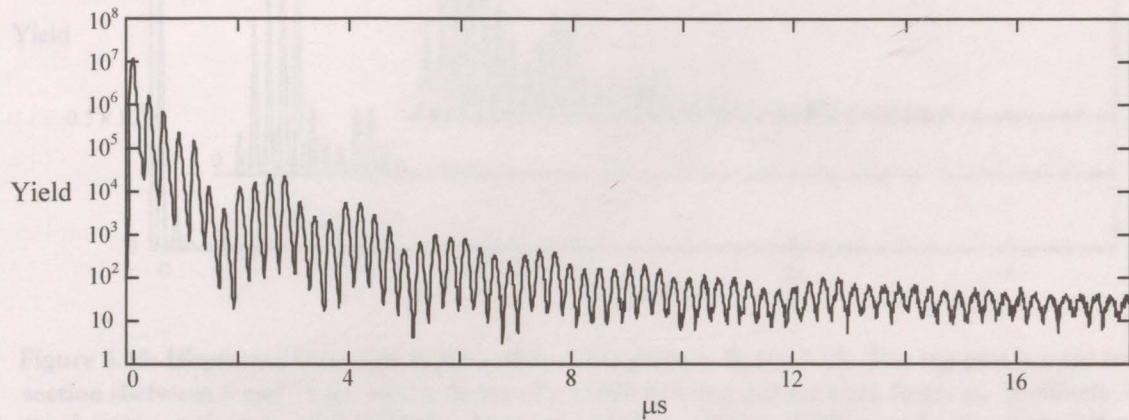


Figure 6.13: Logarithmic plot of electron signal collected at the interaction region for a setup of 15 eV Top HDA and 15 eV bottom HDA pass energy, for an ERS energy of 15.0 eV, storage-cycle period of 20 μs.

Shown in figure 6.14 is the peak height variation as a function of orbit number. It is seen that the electron trajectories oscillate about the optic axis with a period of ~ 6 orbits (or ~ 1.62 μs), in this case.

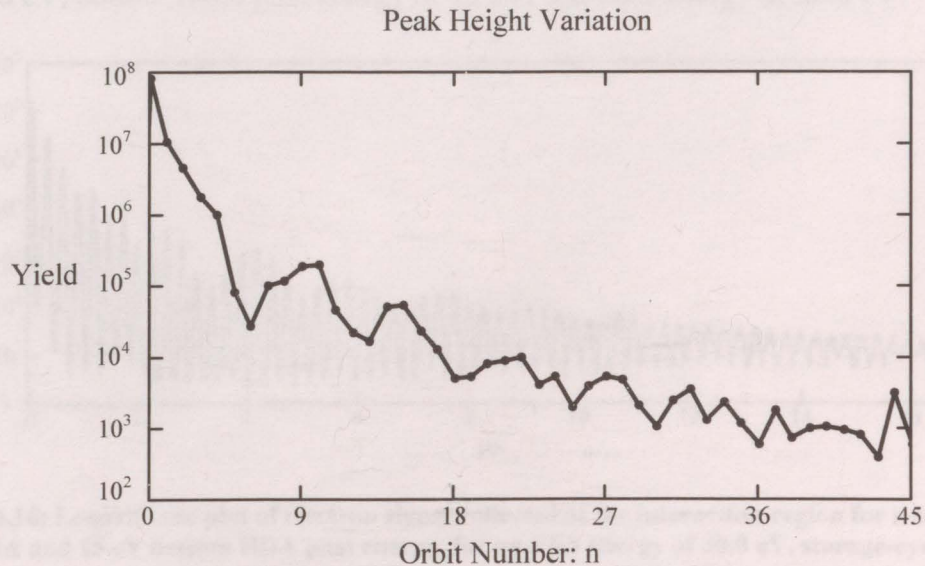


Figure 6.14: Displaying the variation in the peak height as a function of orbit number.

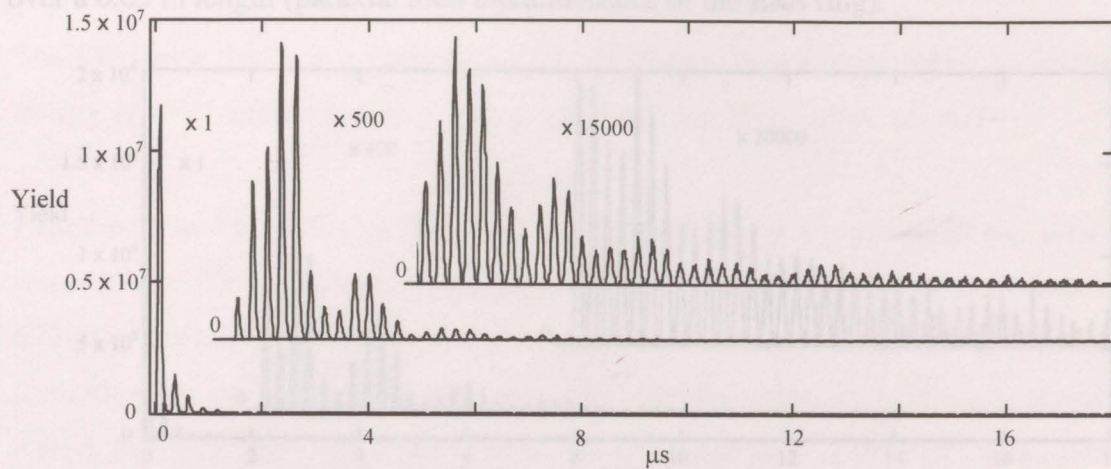


Figure 6.15: Displaying three linear plots of the data given in figure 6.13. The top plot is a cut-away section (between 5 and 18 μs) with a factor of a 15000 to bring out the peak features. Similarly, the graph between the x 1 and x 15000 has been expanded by a factor of 500 to make the peaks between 1.5 and 18 μs more visible.

6.2.2 Asymmetric Pass Energy

The following figure was recorded at the asymmetric pass energy setup; top HDA pass energy 8 eV, bottom HDA pass energy of 15 eV, and ERS energy of 30.0 eV.

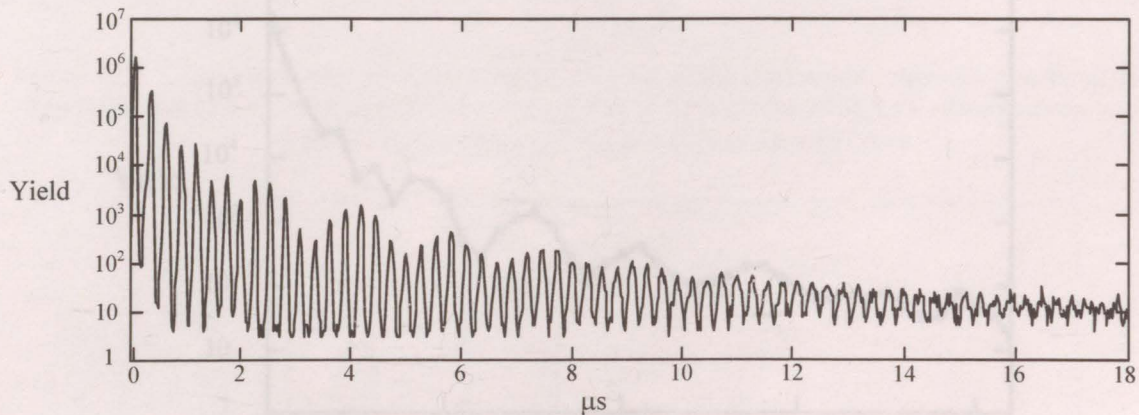


Figure 6.16: Logarithmic plot of electron signal collected at the interaction region for a setup of 8 eV Top HDA and 15 eV bottom HDA pass energy, for an ERS energy of 30.0 eV, storage-cycle period of 20 μs . Helium background pressure of 7.0×10^{-7} torr.

Analysis of the spectrum in figure 6.16 reveals that between the interval 4 to 18 μs the electron peak heights have an exponential decay of 3.39 μs , and the area within each peak

in that interval has a decay of 2.95 μs . The analysis reveals an orbit time of ~ 275.8 ns over a 0.65 m length (paraxial total circumference of the ERS ring).

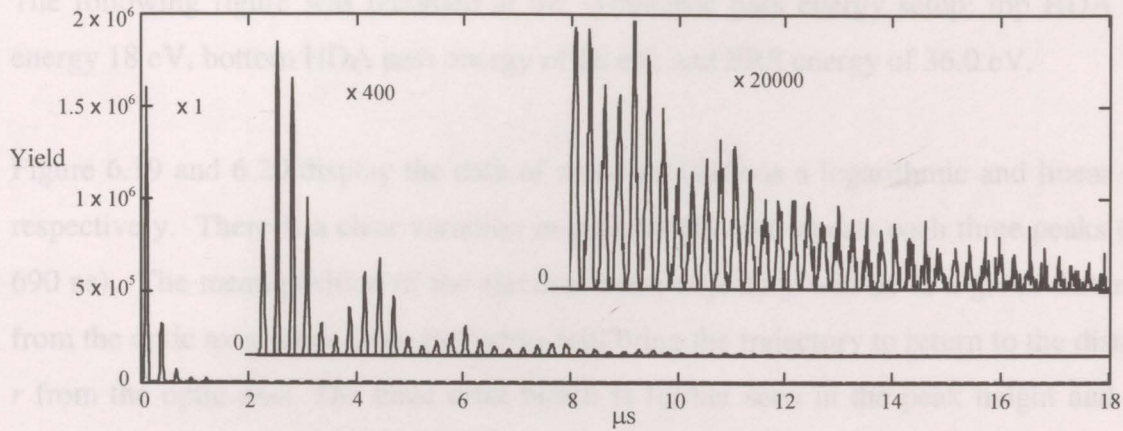


Figure 6.17: Displaying three linear plots of the data given in figure 6.16. The top plot is a cut-away section (between 8 and 18 μs) with a factor of a 20000 to bring out the peak features. Similarly, the graph between the x 1 and x 20000 has been expanded by a factor of 400 to make the peaks between 2 and 18 μs more visible.

Figure 6.17 displays the data from figure 6.16 on a linear plot. There is an evident oscillation in the beam axis with a period $\psi \sim 1.61$ μs , over a 6 orbit cycle (see figure 6.18).

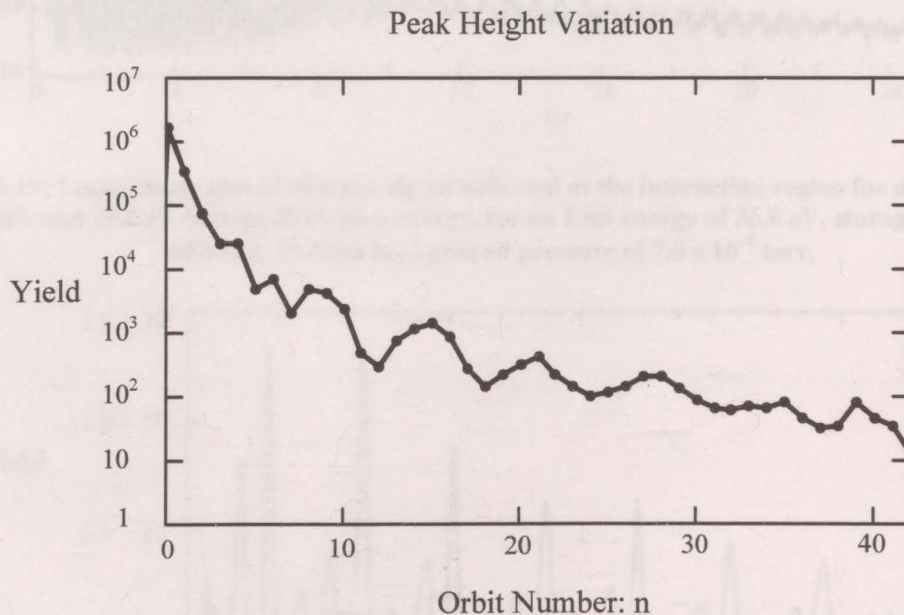


Figure 6.18: Displaying peak height variation as a function of orbit number.

6.2.3 Small Oscillations

The following figure was recorded at the symmetric pass energy setup; top HDA pass energy 18 eV, bottom HDA pass energy of 18 eV, and ERS energy of 36.0 eV.

Figure 6.19 and 6.20 display the data of small oscillations a logarithmic and linear plot, respectively. There is a clear variation in peak height that repeats each three peaks (or ~ 690 ns). The mean position of the electron beam trajectory will lie at a given distance r from the optic axis; three more full orbits will bring the trajectory to return to the distance r from the optic axis. The three orbit bunch is further seen in the peak height and area variations given in figures 6.21 and 6.22.

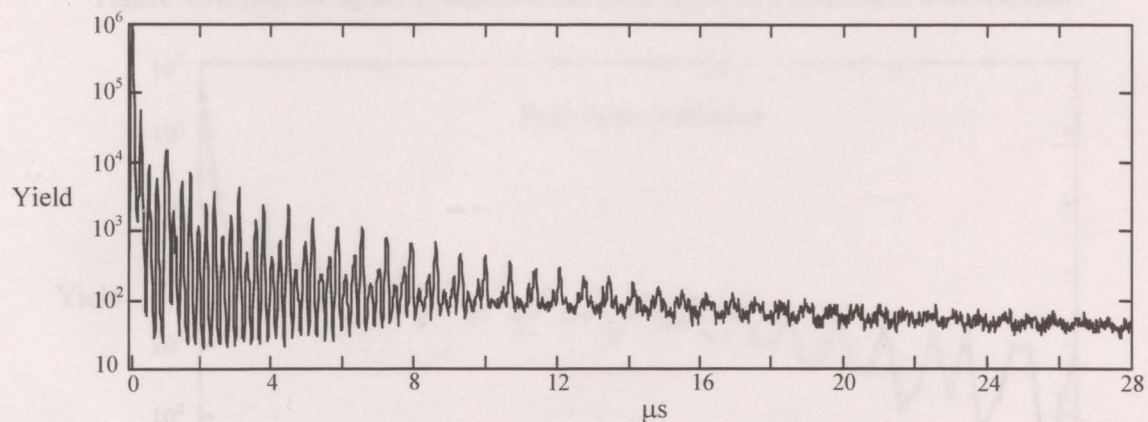


Figure 6.19: Logarithmic plot of electron signal collected at the interaction region for a setup of 18 eV Top HDA and 18.0 eV bottom HDA pass energy, for an ERS energy of 36.0 eV, storage-cycle period of 30 μs . Helium background pressure of 7.0×10^{-7} torr.

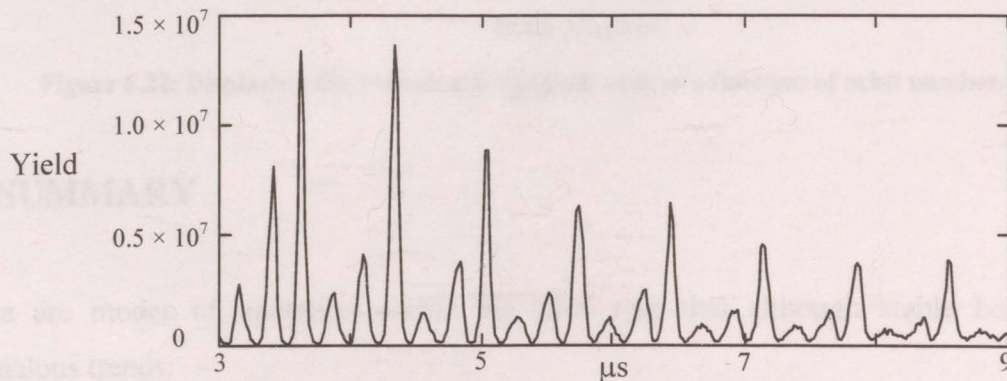


Figure 6.20: Displaying linear plot of the data given in figure 6.19. The Plot is a cutaway section between 3 and 9 μs .

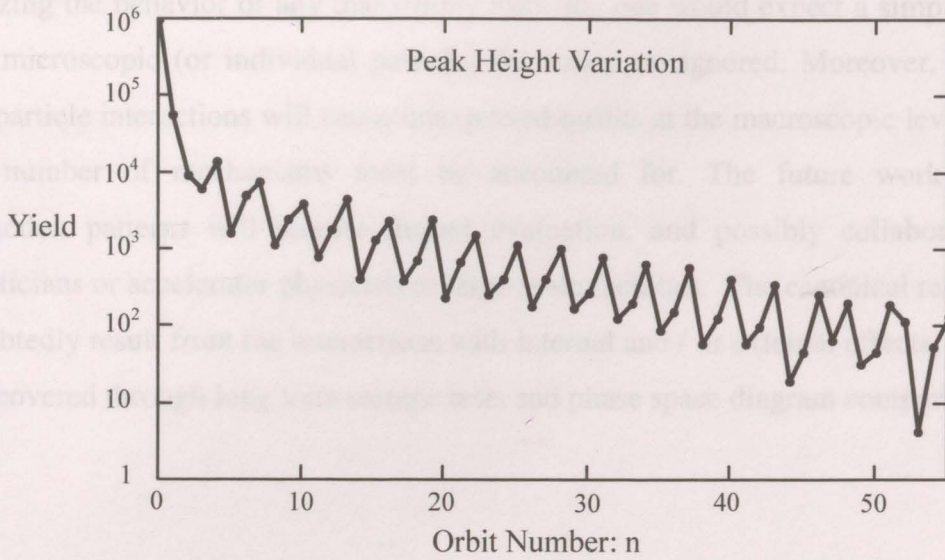


Figure 6.21: Displaying the variation in the peak height as a function of orbit number.

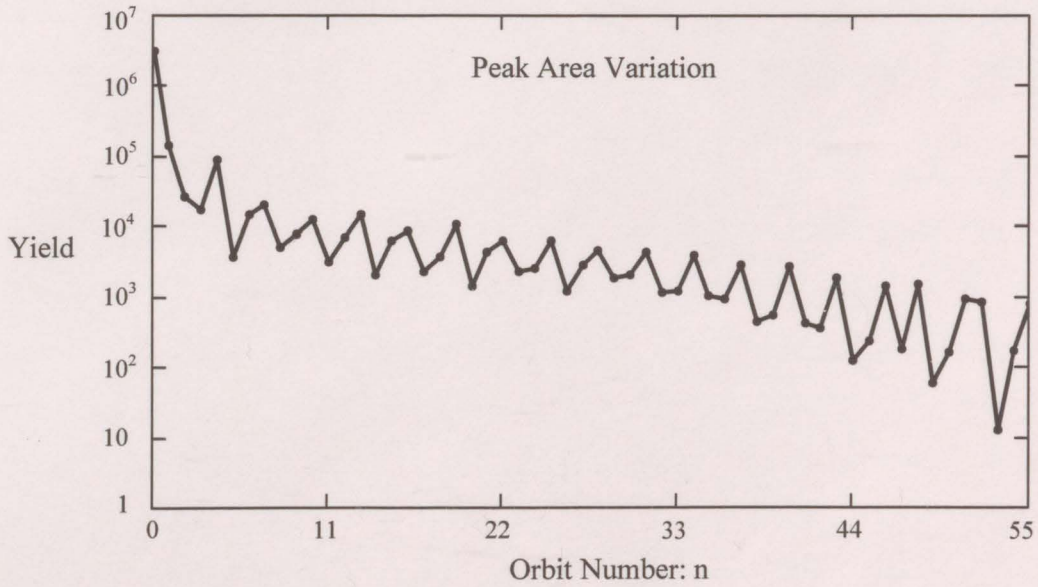


Figure 6.22: Displaying the variation in the peak area as a function of orbit number.

6.3 SUMMARY

There are modes of operation within the ERS ring that although stable behave in anomalous trends:

- Peak width saturation
- Oscillations about the optic axis

Analyzing the behavior of any many-body systems, one would expect a simple behavior when microscopic (or individual particle) dynamics are ignored. Moreover, substantial intra-particle interactions will cause unexpected results at the macroscopic level, where a large number of mechanisms must be accounted for. The future work for these unorthodox patterns will require further evaluation, and possibly collaboration with theoreticians or accelerator physicists at large scale facilities. The canonical relations will undoubtedly result from the interactions with internal and / or external effects, which will be discovered through long term storage tests and phase space diagram comparisons.

REFERENCES

Pedersen H.B., Strasser D., Ring S., Heber O., Rappaport M. L., Rudich Y., Sagi I., and Zafman D., *Phys. Rev. Lett.*, **vol. 87** (2001), 055001-1

Twiss R.Q., and N.H. Frank, *Rev. Sci. Instrum.*, **vol. 20** (1949) 1

Zafman D., Stasser D., Heber O., Goldberg S., Diner A., and Rappaport M.L., *Nucl. Instrum. Methods A*, **vol. 532** (2004) 196 – 202

CHAPTER 7: CONCLUSION

An instrument was conceived and constructed to store electrons within a desktop sized system consisting of two cylindrical lens straight sections and two hemispherical deflector analyzers (HDA). Low energy electrons were made to orbit the ERS about the optic axis from two separate injection techniques. Firstly, the electron beam was injected at 90° to the optic axis to impact on a tungsten wire ring; scattered electrons off the wire were directed along the optic axis by electric fields. A more efficient injection method was implemented whereby electrons were sent directly on axis through a pulsed electron gun in coincidence with a hemispherical deflector analyzer. The latter injection method was completely adopted and utilized for all storage and beam dynamic tests. Electrons of a few 10^1 's eV of energy traveled through a 0.65 m length containing eight 3 mm diameter apertures over a thousand times, corresponding to a group of electrons traveling nearly a kilometer.

Transfer matrices were employed to represent elements within the ring and electron beam propagation. A transfer matrix was generated for the source to the target portion of the ERS, namely M_{ST} . This matrix incorporates one 180° HDA and two focusing and collimating lenses. The second half of the ERS is geometrically symmetric to the top, therefore the target to source transfer matrix M_{TS} possesses many similarities in its components to that of the source to target transfer matrix. Thus, the transfer matrix for the whole ERS is the matrix product of M_{ST} and M_{TS} , tracing out the path from the source back to the source represented by M_{SS} . The constraints for stability within a closed ring can be evaluated using the M_{SS} transfer matrix. One of the determining parameters for stability is the lens ratios, in particular the ratio of V_2 / V_1 . A scan of the V_2 / V_1 ratio over the range negative 10 to positive 180 V has displayed a resonance type pattern of the stability within the ERS. The system is most stable when it takes on the inverse matrix ($-I$) oppose to a unity M_{SS} . In this mode each trajectory will experience a full inversion of its parameters upon each full orbit. Therefore, the ERS prefers an electron beam that inverts its parameters upon each orbit, rather than an exact retrace on every orbit.

Several electron orbit spectra were recorded for at a variety of setup conditions: pass energy values of HDAs (both equal and unequal), and lens voltage ratios. Initially presented was an equal arrangement of HDA pass energies at the value of 15 eV for an accelerating factor within the lenses of 1.0 (i.e. $V_1 / V_3 = 1$), giving an orbit time of ~ 271 ns and mean energy 16 eV. The HDA pass energy values were then set to unequal values with the notation: ($V_U | V_L$) corresponding to the voltage of the mean path of the gap of the upper HDA and that of the lower HDA, respectively. The first setup was (4 | 18) for an accelerating factor within the upper lenses of 10.0 and lower lenses of 2.2, with an average orbit time of ~ 330 ns and mean energy throughout the ring of ~ 10.8 eV. The next setup was (4 | 15) for an accelerating factor within the upper lenses of 5.5 and lower lenses of 1.2, with an average orbit time of ~ 350 ns and mean energy throughout the ring of ~ 9 eV. The next setup was (7 | 15) for an accelerating factor within the upper lenses of 3.57 and lower lenses of 1.67, with an average orbit time of ~ 301 ns. The next setup was (9 | 18) for an accelerating factor within the upper lenses of 5.56 and lower lenses of 2.8, with an average orbit time of ~ 260 ns.

Bunch dynamics were analyzed for the evolution of the beam width of the electron beam. The width of the electron peak in the time domain fits sufficiently well to a Gaussian curve. In the ordinary mode of operation the width of the Gaussian peak increases as a function of orbit according to a non – linear fit, which is primarily due to a velocity spread and a range of trajectories within the ERS. Deviations from the ordinary behavior were observed for different setups of the ERS parameters. The electrons within the beam can be randomized or coupled which destroys the simplistic behavior of the beam. In general, internal and external interactions will cause this “switch” from the ordinary mode to a more exotic mode of dispersion of the peak widths. Peak width saturation and less rapid dispersion are two of the anomalous forms of behavior observed within the ERS. A direct comparison was drawn between the ERS and the linear electrostatic trap produced by Zajfman’s group.

In the nominal operation of the ERS, the electron beam will travel paraxial. However, it was discovered that the electron beam can orbit the ERS about the optic axis and remain

stable. The beam will oscillate about the axis with a given frequency. This anomaly has also been found in other closed path storage rings, such as synchrotrons and betatrons; thus, is not unique to the ERS.

Future Prospective

A more efficient detection system is in progress in the laboratory that will involve differential pumping and a supersonic gas jet as the scatterer. In this setup the target gas within the interaction region will be a more collimated and focused beam. Thus, lowering the overall background pressure, and enabling gas phase studies for rotationally cool molecules.

An alternate source is being conceived that will inject an electron beam of high energy resolution. According to bunch analysis, the initial temporal width of the beam is crucial in defining the time width of the beam at a later point in the storage cycle, which is related to the energy resolution. A simple solution is to replace the simple electron gun with a stripped down spectrometer including an electron gun and a HDA with focusing and collimating lenses. A more sophisticated solution is a laser photoelectron source.

The precise energy of the orbiting electron beam can be ascertained by placing an energy analyzer at 90° to the interaction region. The accuracy of the detector is directly proportional to the type and style of detector. An optimal solution lies in attaching a separate chamber housing a 180° hemispherical energy analyzer of large dimensions and low pass energy (~ 0.1 to 0.25 eV).

Altering the lenses would improve the beam density and increase the efficiency of the stability of the system. As mentioned in Chapter 5, the pass energies of the top and bottom HDAs can be set asymmetric, however a lower limit of ~ 4 eV exists for either pass energy. Extending the lenses nearest the HDA of lower pass energy should give a more parallel beam at the entrance of the HDA, as the small range of acceptable angles given by the HDA combined with the range of angles of the beam for low energies as

dictated by the Helmholtz-Lagrange equation give a lower limit of the HDA pass energy. A five element lens of overall longer geometry will have a softer focus and allow for a paraxial beam of higher density.

An electron orbit spectrum has been obtained in the absence of a target gas within the interaction region. It must be concluded that in the absence of a gas that acts as a scatterer, that the apertures adjacent to both the source and interaction region are the cause of scattered electrons viewed in the channeltron detectors. Thus, the presence of 3 mm apertures is a loss mechanism of the beam. Expanding the aperture size in these regions will allow a larger percentage of the beam density to thread through these regions.

The peak width saturation mode needs further analysis. Specifically, this mode produces characteristics of the beam that cannot be obtained within a simple single pass spectrometer, such as ultra-high energy resolution. The stochastic mode (equation 5.3 of Chapter 5) may also contain “exotic” behaviours with the energy spread or momentum spread of beam.

The ERS could be redesigned to accommodate any type of charged particle beam. Such species of consideration are polarized electrons, positrons, or ions. In the case of polarized electrons and positrons that involve low currents for low energy beams, the ERS can best be utilized as a storage device that will enable the use of a greater fraction of the particles within the beam during collision experiments. Alternatively, the ERS can simply be used as an accumulator for these species. Electronic – atom collision studies can also be performed in areas of research that are limited by beam currents.

APPENDIX 1-A

M_{st} Matrix for Symmetric Setup

The form of M_{st} given as equation

$$M_{ST} = m_2 m_h m_1$$

$$= \left(-\frac{1}{f_1} \right) \left(-\frac{1}{f_2} \right) \begin{bmatrix} K_1 & K_1 K_2 - f_1 f_2 \\ 1 & K_2 \end{bmatrix} \begin{bmatrix} -1 & 0 \\ 0 & -1 \end{bmatrix} \begin{bmatrix} K_2 & K_1 K_2 - f_1 f_2 \\ 1 & K_1 \end{bmatrix}$$

Let $f = f_1 f_2$

And so

Then

$$= \left(-\frac{1}{f_1} \right) \left(-\frac{1}{f_2} \right) \begin{bmatrix} -1 & 0 \\ 0 & -1 \end{bmatrix} \begin{bmatrix} K_1 & K_1 K_2 - f_1 f_2 \\ 1 & K_2 \end{bmatrix} \begin{bmatrix} K_2 & K_1 K_2 - f_1 f_2 \\ 1 & K_1 \end{bmatrix}$$

$$= \left(-\frac{1}{f_1} \right) \left(-\frac{1}{f_2} \right) \begin{bmatrix} -1 & 0 \\ 0 & -1 \end{bmatrix} \begin{bmatrix} (K_1)(K_2) + K_1 K_2 - f_1 f_2 & (K_1)(K_1 K_2 - f_1 f_2) + (K_1 K_2 - f_1 f_2)(K_1) \\ K_2 + K_2 & K_1 K_2 - f_1 f_2 + (K_1)(K_2) \end{bmatrix}$$

$$= \frac{1}{f_1 f_2} \begin{bmatrix} f_1 f_2 - 2K_1 K_2 & 2K_1(f_1 f_2 - K_1 K_2) \\ -2K_2 & f_1 f_2 - 2K_1 K_2 \end{bmatrix}$$

Therefore,

$$\lambda = \frac{1}{2f_1 f_2} \left[(f_1 f_2 - 2K_1 K_2) \pm \sqrt{(f_1 f_2 - 2K_1 K_2)^2 - 4(-2K_2)(f_1 f_2 - 2K_1 K_2)} \right]$$

$$\lambda_1 = \frac{1}{2f_1 f_2} \left[(f_1 f_2 - 2K_1 K_2) + 2\sqrt{K_1 K_2 - (K_1 K_2)} \right]$$

$$\lambda_2 = \frac{1}{2f_1 f_2} \left[(f_1 f_2 - 2K_1 K_2) - 2\sqrt{K_1 K_2 - (K_1 K_2)} \right]$$

Therefore,

$$M_{ST} = \begin{bmatrix} \lambda_1 & 0 \\ 0 & \lambda_2 \end{bmatrix} = \begin{bmatrix} -1 & 0 \\ 0 & -1 \end{bmatrix}$$

Set $\lambda = -1$

APPENDIX 1-B

Eigenvalues of M_{st}

The form of M_{st} given as equation 2.19 above is:

$$M_{st} = \frac{1}{f_1 f_2} \begin{bmatrix} f_1 f_2 - 2K_1 K_2 & 2K_1 (f_1 f_2 - K_1 K_2) \\ -2K_2 & f_1 f_2 - 2K_1 K_2 \end{bmatrix}$$

Let $f = f_1 f_2$

And solve for the eigenvalues

Then

$$\begin{aligned} \det \left(\frac{1}{f_1 f_2} \begin{bmatrix} f_1 f_2 - 2K_1 K_2 & 2K_1 (f_1 f_2 - K_1 K_2) \\ -2K_2 & f_1 f_2 - 2K_1 K_2 \end{bmatrix} - \begin{bmatrix} \lambda & 0 \\ 0 & \lambda \end{bmatrix} \right) \\ = \left(1 - \frac{2K_1 K_2}{f} - \lambda \right) \left(1 - \frac{2K_1 K_2}{f} - \lambda \right) - \left(2K_1 \left(1 - \frac{K_1 K_2}{f} \right) \right) \left(-\frac{2K_2}{f} \right) \\ = \lambda^2 - 2\lambda - 4K_1 \frac{K_2}{f} + 4\lambda K_1 \frac{K_2}{f} + 4K_1^2 \frac{K_2^2}{f^2} + 1 + 4K_1 \frac{K_2}{f} - 4K_1^2 \frac{K_2^2}{f^2} = 0 \\ \rightarrow f^2 \lambda^2 - 2f^2 \lambda - 4fK_1 K_2 + 4\lambda fK_1 K_2 + 4K_1^2 K_2^2 + f^2 + 4fK_1 K_2 - 4K_1^2 K_2^2 = 0 \\ f^2 \lambda^2 + \lambda(4fK_1 K_2 - 2f^2) + f^2 = 0 \end{aligned}$$

Therefore,

$$\lambda = \frac{1}{2f^2} \left[2(f^2 - 2fK_1 K_2) \pm \sqrt{16f^2 K_1^2 K_2^2 - 16f^3 K_1 K_2 + 4f^4 - 4f^2 f^2} \right]$$

$$\lambda_1 = \frac{1}{f} \left[(f - 2K_1 K_2) + 2\sqrt{K_1^2 K_2^2 - fK_1 K_2} \right]$$

$$\lambda_2 = \frac{1}{f} \left[(f - 2K_1 K_2) - 2\sqrt{K_1^2 K_2^2 - fK_1 K_2} \right]$$

Therefore,

$$M_{st} = \begin{bmatrix} \lambda_1 & 0 \\ 0 & \lambda_2 \end{bmatrix} = \begin{bmatrix} -1 & 0 \\ 0 & -1 \end{bmatrix}$$

Set $\lambda = -1$

$$f - 2K_1K_2 + 2\sqrt{K_1^2K_2^2 - fK_1K_2} = -f$$

$$-2f + 2K_1K_2 = 2\sqrt{K_1^2K_2^2 - fK_1K_2}$$

Square both sides:

$$f^2 - 2fK_1K_2 + K_1^2K_2^2 = K_1^2K_2^2 - fK_1K_2$$

$$f^2 - 2fK_1K_2 = -fK_1K_2$$

$$f - 2K_1K_2 = -K_1K_2$$

$$f = K_1K_2, f = 0$$

Note: that $f = 0$ is not an physically acceptable solution.

Now, by setting $\lambda_2 = -1$ and solving, gives the identical result.

Now put $f \rightarrow f_1f_2$ gives $f_1f_2 = K_1K_2$.

APPENDIX 1-C

Comp Solving M_{ST} for $M_{SS} = -I$ (case)

$$M_{ST} = \begin{bmatrix} 0 & u \\ -\frac{1}{u} & 0 \end{bmatrix}$$

$$M_{ST} = \frac{1}{f_1 f_2} \begin{bmatrix} f_1 f_2 - 2K_1 K_2 & 2K_1 (f_1 f_2 - K_1 K_2) \\ -2K_2 & f_1 f_2 - 2K_1 K_2 \end{bmatrix}$$

Let $f_1 f_2 = 2K_1 K_2$

$$M_{ST} = \frac{1}{2K_1 K_2} \begin{bmatrix} 0 & 2K_1 (2K_1 K_2 - K_1 K_2) \\ -2K_2 & 0 \end{bmatrix}$$

$$= \frac{1}{2K_1 K_2} \begin{bmatrix} 0 & 2K_1 (K_1 K_2) \\ -2K_2 & 0 \end{bmatrix}$$

$$= \begin{bmatrix} 0 & K_1 \\ -K_1^{-1} & 0 \end{bmatrix}$$

$$\therefore u = K_1$$

So that

APPENDIX 1-D

Components of M_{SS} (non – unity case)

$$M_{SS} = M_{ST}M_{ST}$$

$$M_{ST} = \frac{1}{f_1 f_2} \begin{bmatrix} f_1 f_2 - 2K_1 K_2 & 2K_1 (f_1 f_2 - K_1 K_2) \\ -2K_2 & f_1 f_2 - 2K_1 K_2 \end{bmatrix}$$

$$M_{SS} = \begin{bmatrix} -4K_1 K_2 (-K_1 K_2 + f_1 f_2) + (-2K_1 K_2 + f_1 f_2)^2 & 4K_1 (-K_1 K_2 + f_1 f_2) (-2K_1 K_2 + f_1 f_2) \\ -4K_2 (-2K_1 K_2 + f_1 f_2) & -4K_1 K_2 (-K_1 K_2 + f_1 f_2) + (-2K_1 K_2 + f_1 f_2)^2 \end{bmatrix}$$

Matrix 1

Now,

$$\begin{aligned} M_{SS} &= \cos \theta \begin{bmatrix} 1 & 0 \\ 0 & 1 \end{bmatrix} + \sin \theta \begin{bmatrix} b_{11} & b_{12} \\ b_{21} & -b_{11} \end{bmatrix} \\ &= \begin{bmatrix} \cos \theta + b_{11} \sin \theta & b_{12} \sin \theta \\ b_{21} \sin \theta & \cos \theta - b_{11} \sin \theta \end{bmatrix} \end{aligned}$$

Matrix 2

From **Matrix 1** above, let $x = -4K_1 K_2 (-K_1 K_2 + f_1 f_2) + (-2K_1 K_2 + f_1 f_2)^2$ the diagonal component. Comparing with **Matrix 2** gives:

$$x = \cos \theta + b_{11} \sin \theta$$

$$x = \cos \theta - b_{11} \sin \theta$$

$$\Rightarrow b_{11} = (\sin \theta)^{-1} (x - \cos \theta) = -(\sin \theta)^{-1} (x - \cos \theta)$$

$$\therefore b_{11} = 0$$

Now reduce the two variable expression to a single variable form and recall “Helmholtz – Lagrange equation demands conservation of phase space, i.e. the determinant of the transfer matrix must equal unity”:

$$\det M_{SS} = 1 = \cos^2 \theta - b_{12} b_{21} \sin^2 \theta$$

Impose the constraint:

$$b_{12} b_{21} = -1$$

So that

$$\det M_{SS} = \cos^2 \theta - (-1)\sin^2 \theta$$

$$= \cos^2 \theta + \sin^2 \theta = 1$$

$$\therefore b_{21} = -\frac{1}{b_{12}}$$

APPENDIX 1-E

Solving M_{st} (Asymmetric Setup)

Compare the right and left sides of $(M_{st})_{21}$

$$-u^{-1} = -\frac{K_2 + K'_1}{f_2 f'_2}$$

$$\therefore K_1 = K'_2$$

$$\therefore u = \frac{f_2 f'_2}{2K_2}$$

Now compare the two $(M_{st})_{12}$ components

$$ru = \frac{1}{f_2 f'_2} [K_1 K_2 K'_2 - K_1 (K'_1 K'_2 - f'_1 f'_2)]$$

$$\therefore f'_1 f'_2 = 2K'_1 K'_2$$

$$\therefore ru = \frac{1}{f_2 f'_2} 2K_1 K_2 K'_2$$

$$= \frac{1}{f_2 f'_2} 2K_1 K_2 K'_2 \times 1$$

$$= \frac{1}{f_2 f'_2} 2K_1 K_2 K'_2 \times \frac{(f'_1)^2}{(f'_1)^2}$$

$$= \frac{(f'_1)^2}{f_2 f'_2} \frac{2K_1 K_2 K'_2}{(f'_1)^2}$$

Now make the substitution $f'_1 = \left(\frac{1}{f'_2}\right) 2K'_1 K'_2 = \left(\frac{1}{f'_2}\right) 2K_1 K_2$ (where, $K_1 = K'_2$ and $K_2 = K'_1$), which gives:

$$ru = \frac{(f'_1)^2}{f_2 f'_2} \frac{2K_1 K_2 K'_2}{4K_1^2 K_2^2} (f'_2)^2$$

$$= \frac{(f'_1)^2}{f_2} \frac{K'_2}{2K_1 K_2} f'_2$$

$$\because K_1 = K'_2$$

$$ru = \frac{(f'_1)^2 f'_2}{f_2 2K_2}$$

$$= \frac{(f'_1)^2 f'_2}{f_2 2K_2} \times \left(\frac{f_2}{f_2} \right)$$

$$\boxed{= \left(\frac{f'_1}{f_2} \right)^2 \frac{f_2 f'_2}{2K_2}}$$

i.e. the product $ru \rightarrow \left[r = \left(\frac{f'_1}{f_2} \right)^2 \right] \times \left[u = \frac{f_2 f'_2}{2K_2} \right]$.

APPENDIX 2

Photographs

Inner hemisphere

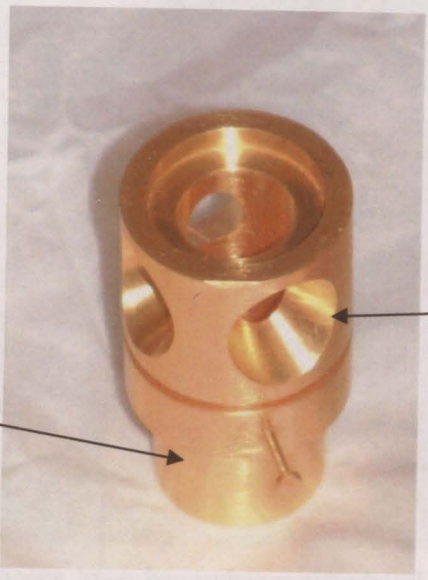
Inner Surface of the outer hemisphere

Three layers of hemispheres

Cylindrical electrodes

V_1 Element

Source or Interaction Cylinder



Photograph 1: Source or Interaction element

Inner Hemisphere

Inner Hole

Aperture Diameter / Exit of hemisphere

Outer Hole

Aperture Diameter

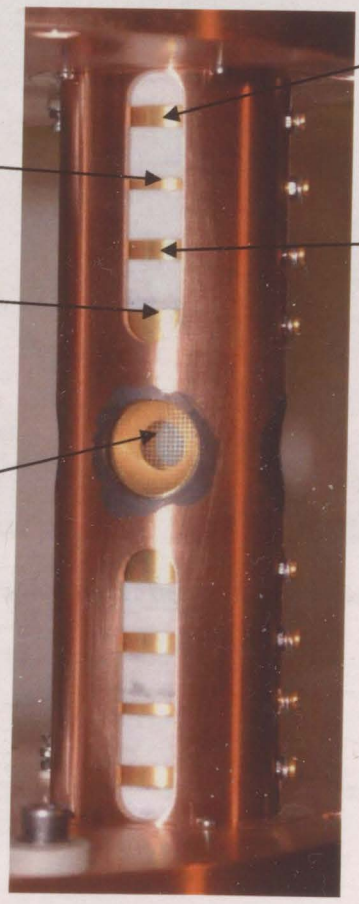
V_3

V_1

V_2

V_4

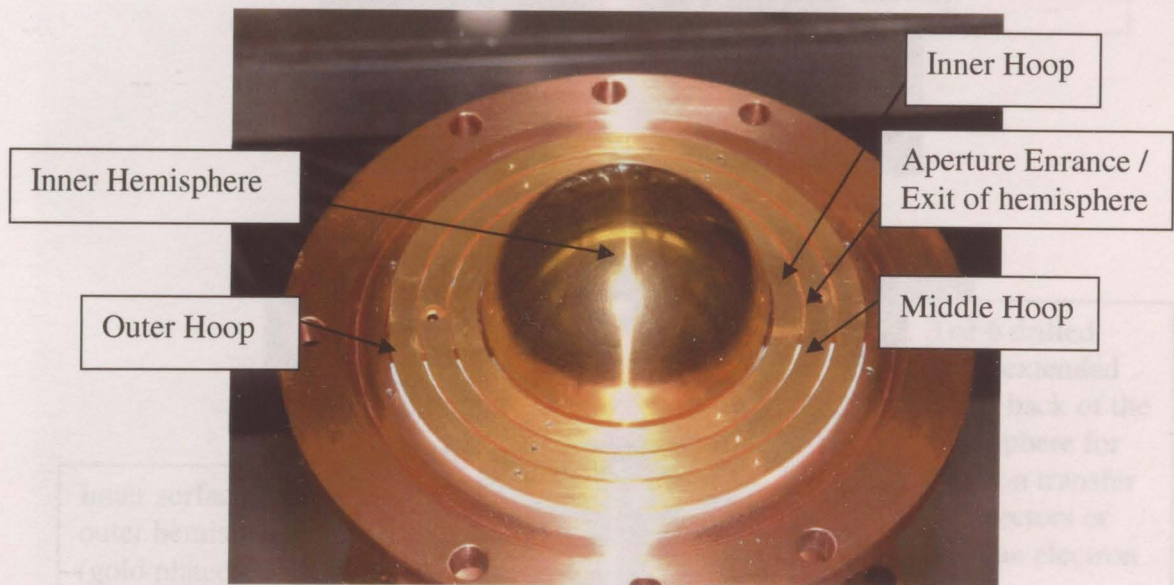
Source Region



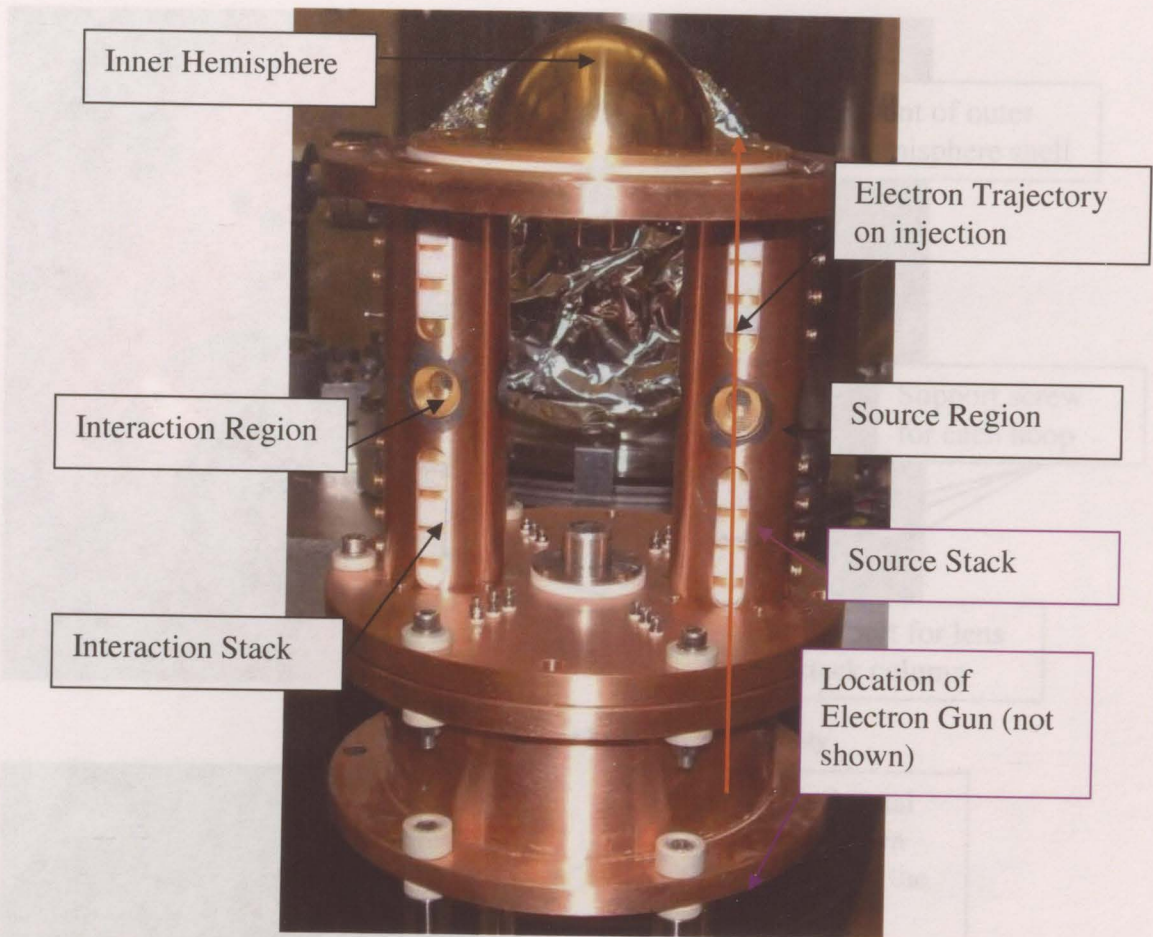
Photograph 2: Lens Stack



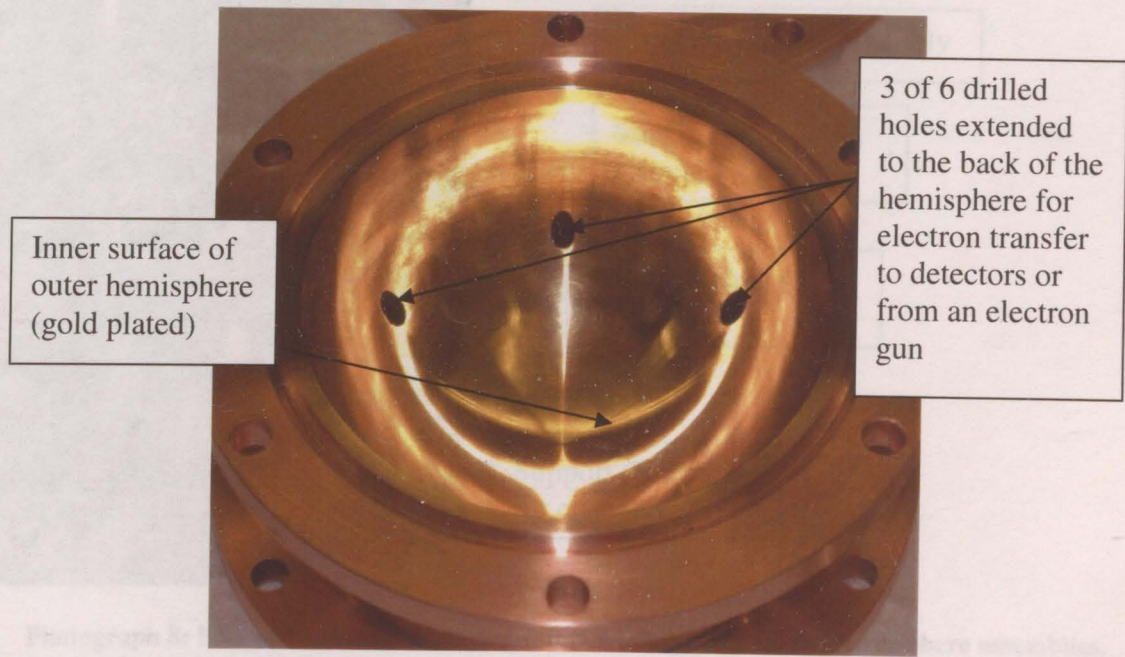
Photograph 3: Assortment of hoops, inner hemispheres, cylindrical lenses, and outer hemisphere



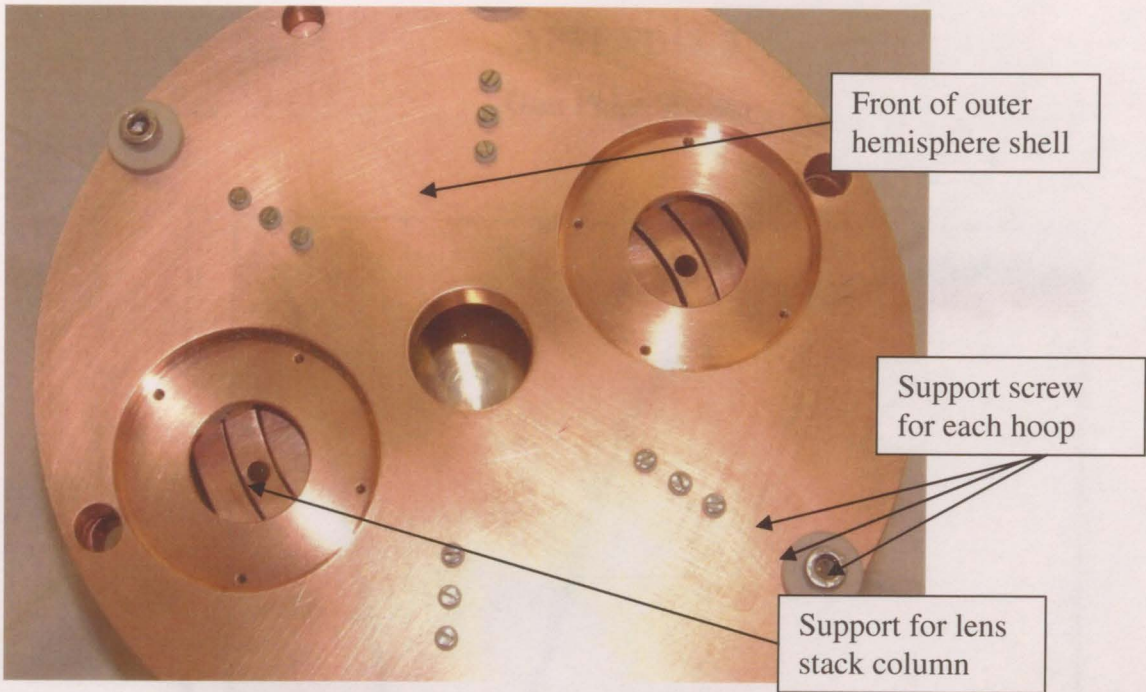
Photograph 4: Inner hemisphere and hoop base



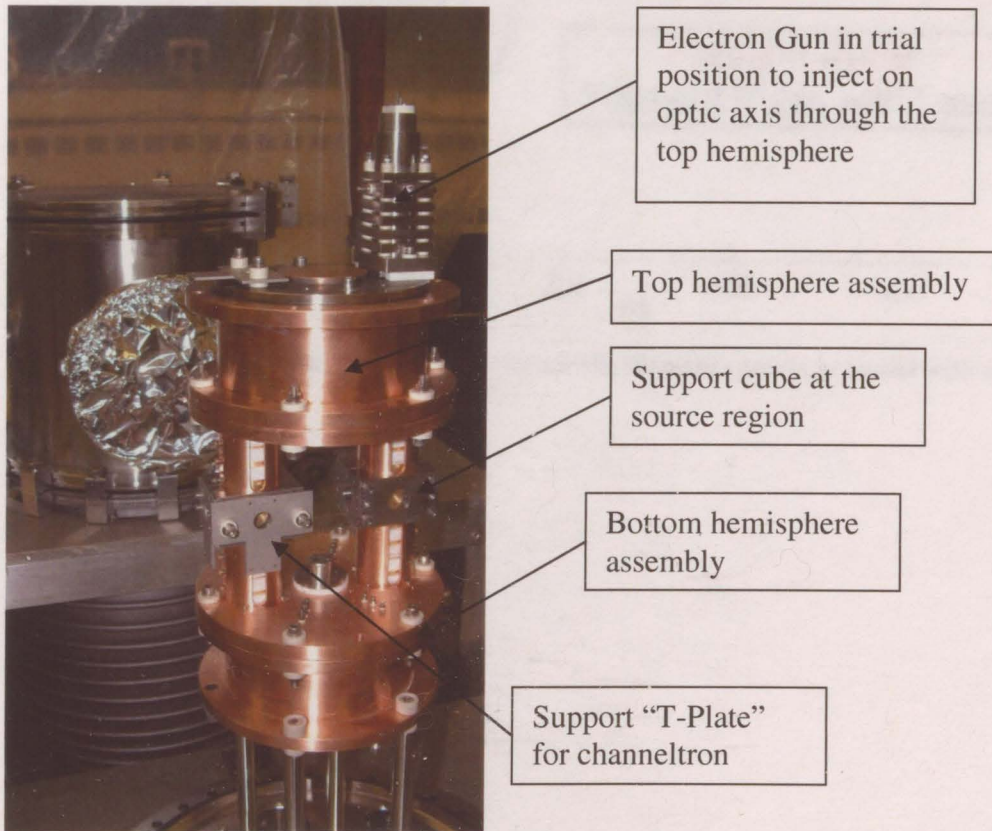
Photograph 5: ERS storage ring



Photograph 6: Inner surface of outer hemisphere



Photograph 7: Outer hemisphere assembly



Photograph 8: ERS storage ring displaying full ring, electron gun, and hemisphere assemblies. Background contains additional vacuum chamber and oil diffusion pump for supersonic gas jet as an accessory to the ERS system.

APPENDIX 3

Gun Pulse Shapes

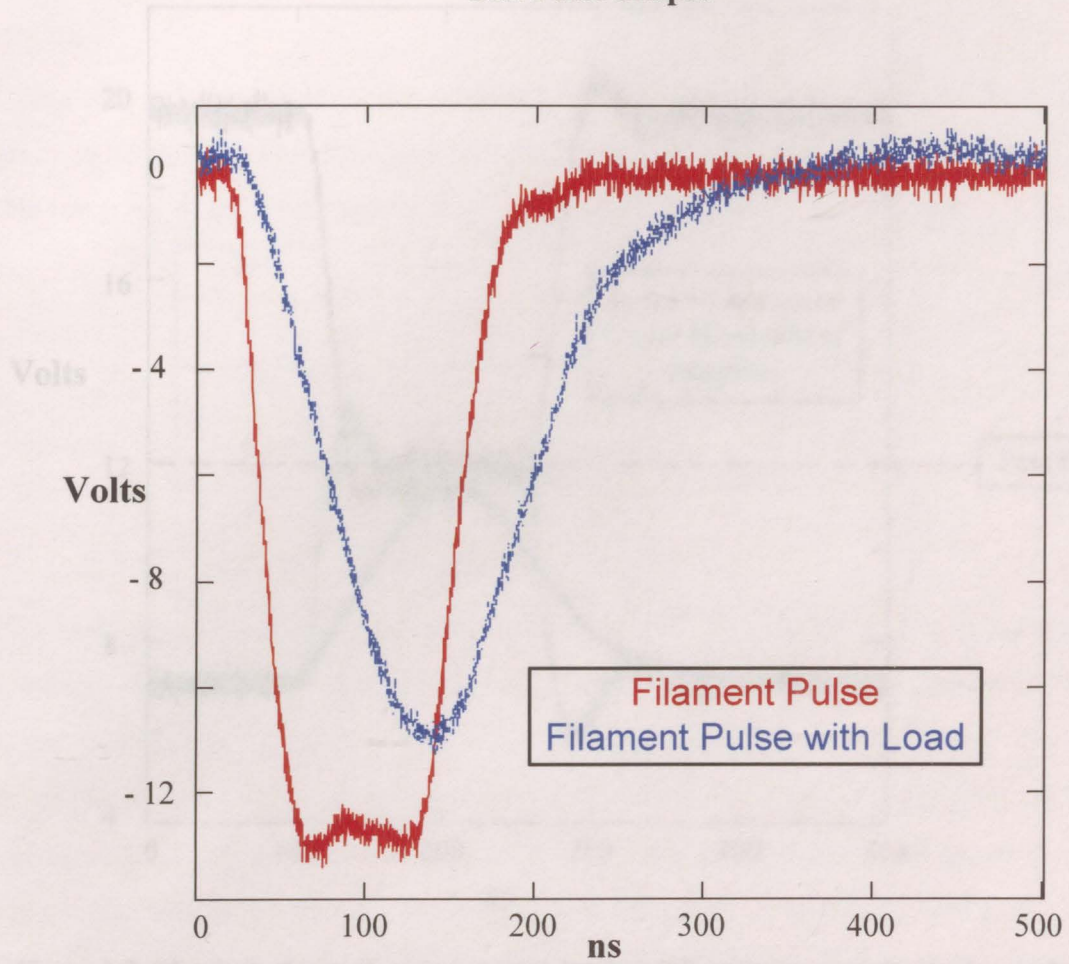


Figure A.1 : Displaying the driving pulse for the filament contact potential with and with a load

APPENDIX 4

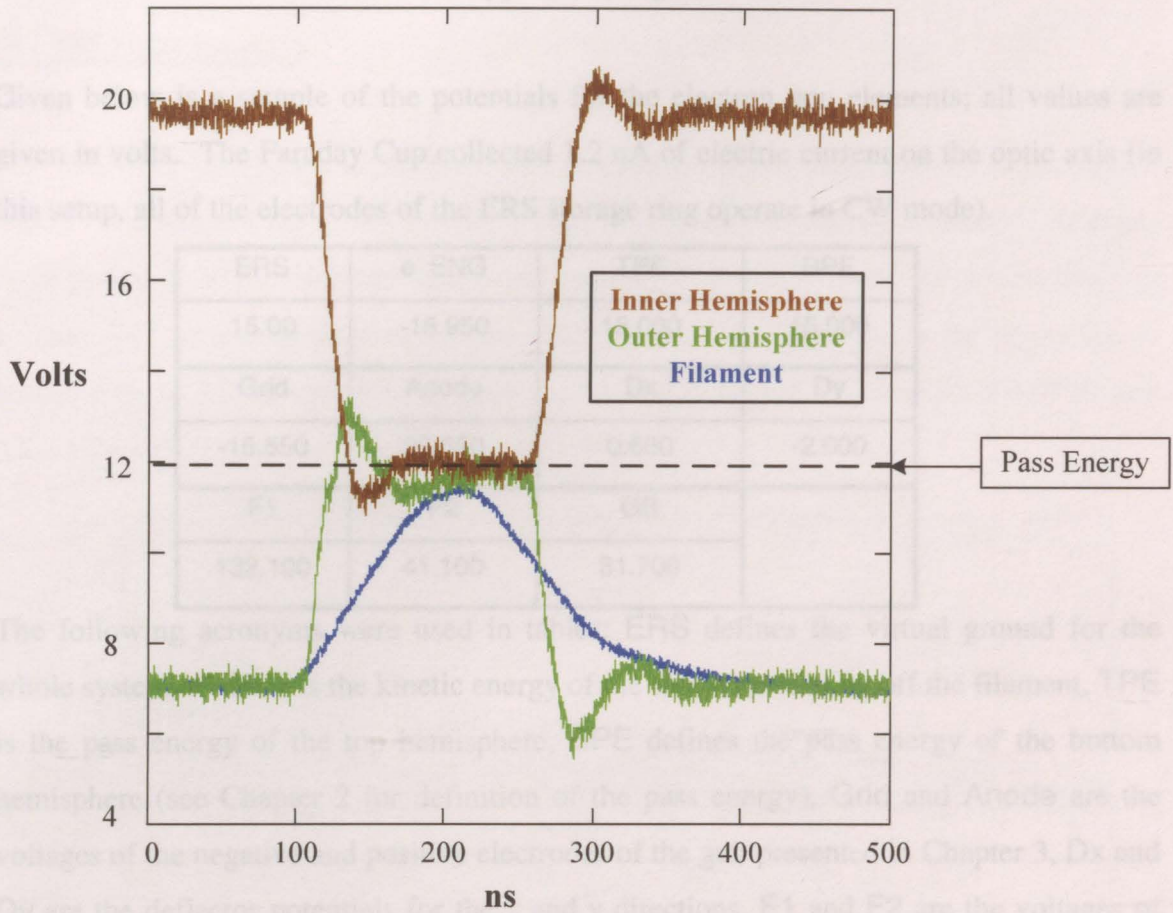


Figure A.3: The above figure give the output pulse that defines the inner and outer hemisphere, and filament. The input (or driving pulse for the circuit) is a TTL pulse

ERS	a-ENG	YFE	SPE
15.00	-15.950	15.000	15.000
Grid	Angle	Dx	Dy
-14.450	31.100	0.750	-1.250
F1	F2	GS	
100.000	39.200	92.400	

APPENDIX 5

Typical Voltages

Given below is a sample of the potentials for the electron gun elements; all values are given in volts. The Faraday Cup collected 1.2 nA of electric current on the optic axis (in this setup, all of the electrodes of the ERS storage ring operate in CW mode).

ERS	e ⁻ ENG	TPE	BPE
15.00	-15.950	15.000	15.000
Grid	Anode	Dx	Dy
-15.550	28.650	0.660	-2.600
F1	F2	GB	
132.100	41.100	31.700	

The following acronyms were used in tables: **ERS** defines the virtual ground for the whole system, **e⁻ ENG** is the kinetic energy of the electrons coming off the filament, **TPE** is the pass energy of the top hemisphere, **BPE** defines the pass energy of the bottom hemisphere (see Chapter 2 for definition of the pass energy), **Grid** and **Anode** are the voltages of the negative and positive electrodes of the gun presented in Chapter 3, **Dx** and **Dy** are the deflector potentials for the *x* and *y* directions, **F1** and **F2** are the voltages of the focusing aperture lenses, and **GB** is the voltage on the base of the gun (end of the gun, opposite the filament).

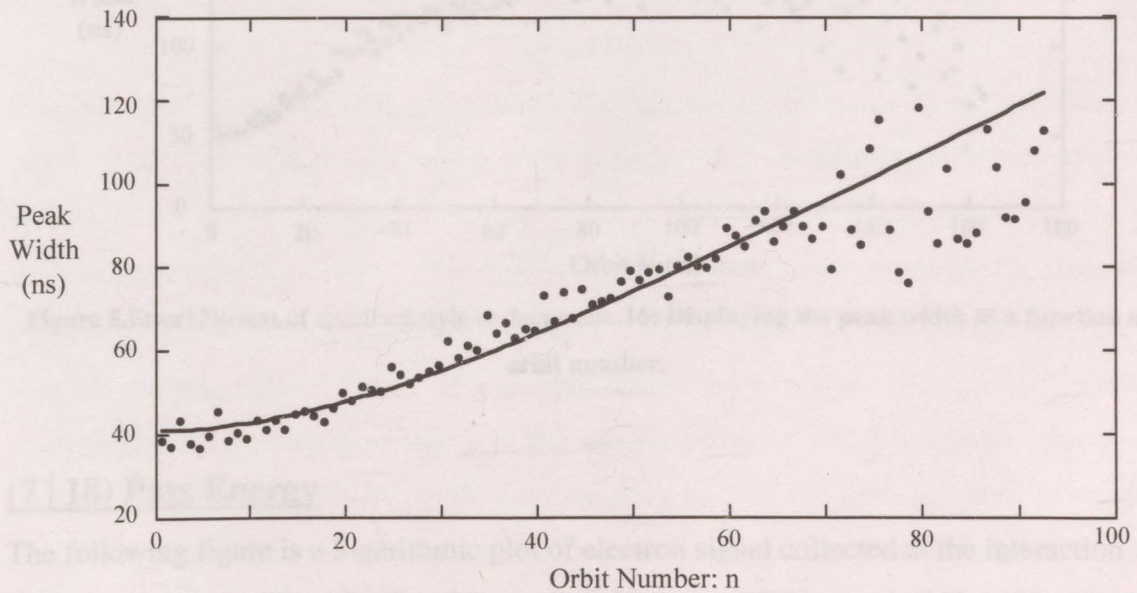
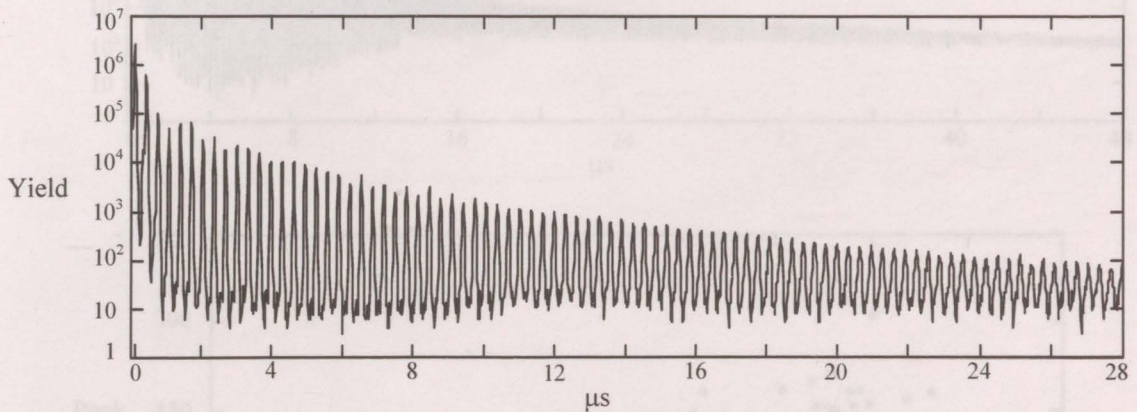
The table below give the gun potentials, where 1 nA of the current is detected at the top of the interaction stack after being deflected by the top hemisphere.

ERS	e ⁻ ENG	TPE	BPE
15.00	-15.580	15.000	15.000
Grid	Anode	Dx	Dy
-14.490	31.100	0.750	-1.250
F1	F2	GB	
136.000	39.200	32.400	

Additional Spectra

(5 | 18) Pass Energy

The following figure is a logarithmic plot of electron signal collected at the interaction region for a setup of $E_U = 5$ eV and $E_L = 18.0$ eV, for an ERS energy of 30.0 eV, storage-cycle period of 30 μ s. Helium background pressure of 7.0×10^{-7} torr. The widths begin at a value ~ 41 ns and increase to a value of ~ 120 ns. The solid line in the below figure corresponds to a least square fit to equation 5.1; the fit reveals $W_0 = 40.98 \pm 0.07$ ns and $\Delta T = 1.24 \pm 0.07$ ns.



(6 | 18) Pass Energy

The following figure is a logarithmic plot of electron signal collected at the interaction region for a setup of $E_U = 6$ eV and $E_L = 18.0$ eV, for an ERS energy of 30.0 eV, storage-cycle period of 50 μ s. Helium background pressure of 7.0×10^{-7} torr. The widths begin at a value ~ 41 ns and increase to a value of ~ 120 ns.

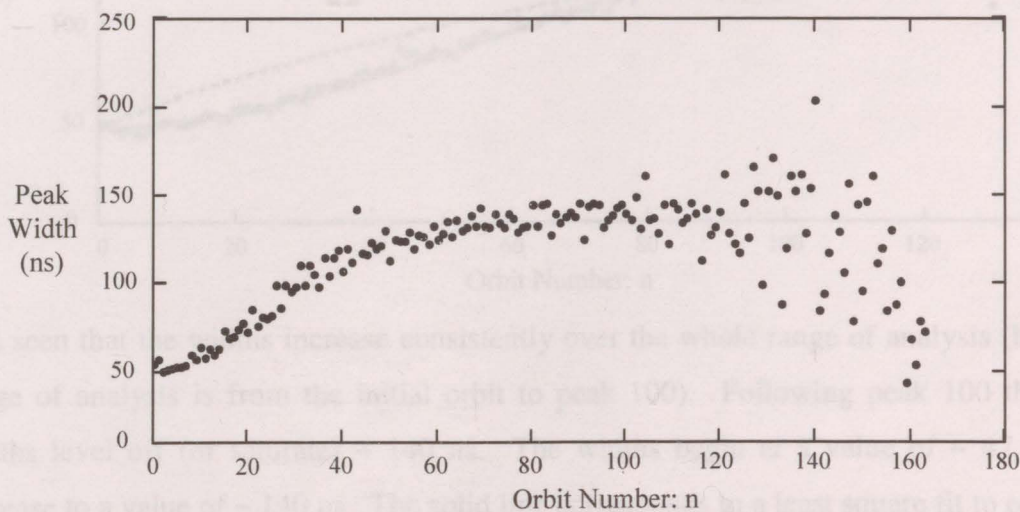
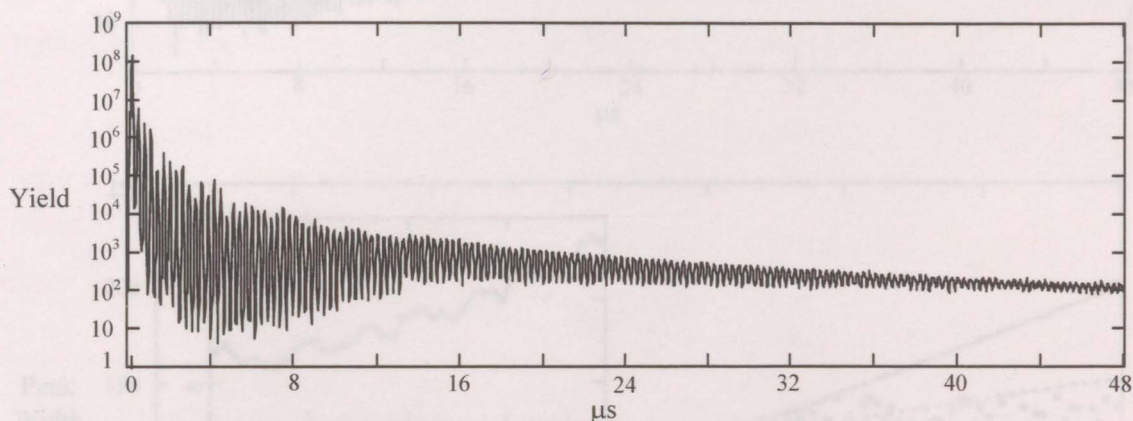
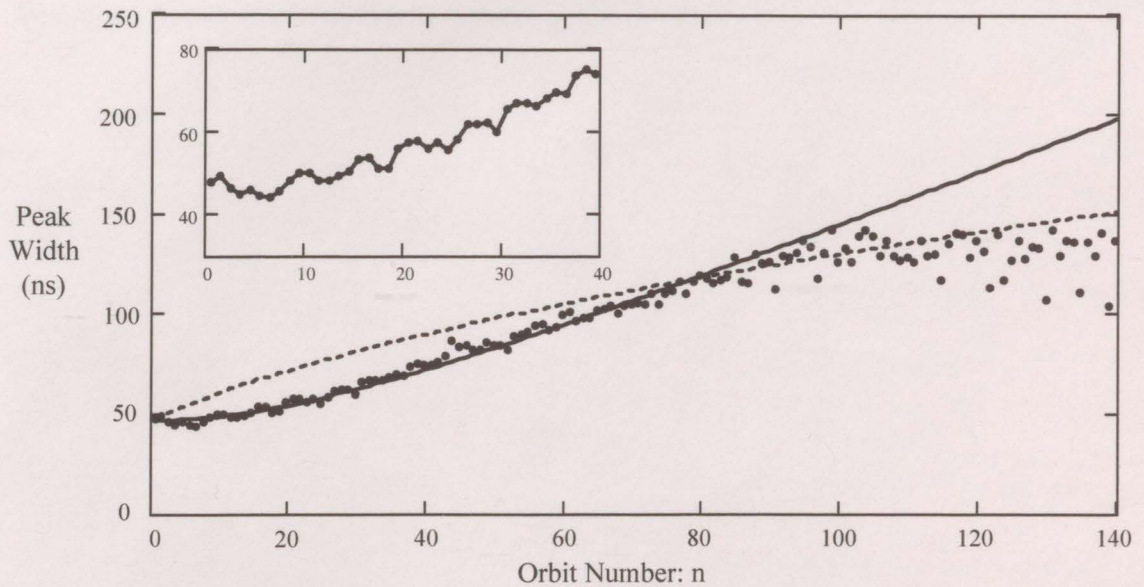
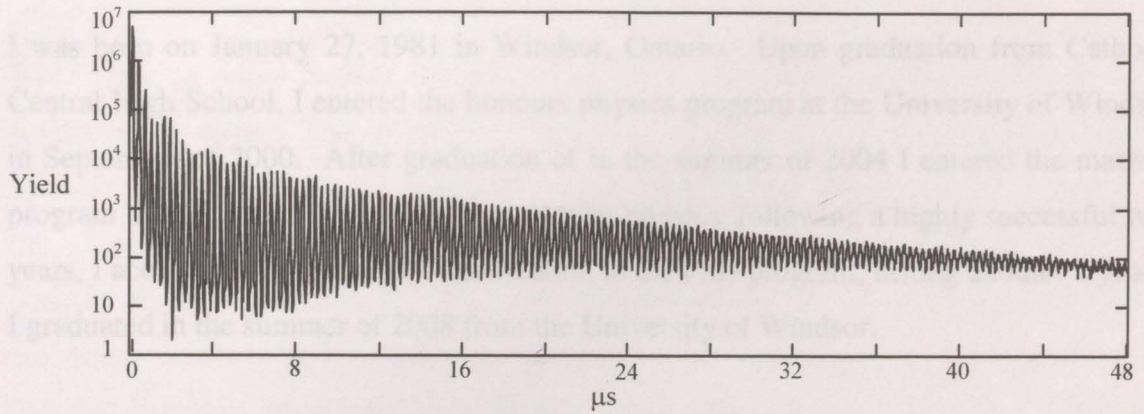


Figure 5.Error! No text of specified style in document..16: Displaying the peak width as a function of orbit number.

(7 | 18) Pass Energy

The following figure is a logarithmic plot of electron signal collected at the interaction region for a setup of $E_U = 7$ eV and $E_L = 18.0$ eV, for an ERS energy of 30.0 eV, storage-cycle period of 50 μ s. Helium background pressure of 7.0×10^{-7} torr.



It is seen that the widths increase consistently over the whole range of analysis (here the range of analysis is from the initial orbit to peak 100). Following peak 100 the peak widths level off (or saturate) ~ 140 ns. The widths begin at a value of ~ 47 ns and increase to a value of ~ 140 ns. The solid line corresponds to a least square fit to equation 5.1; the fit reveals $W_0 = 46.97 \pm 0.05$ ns and $\Delta T = 1.38 \pm 0.05$ ns. The scatter in the points may be an artifact in the fitting or it corresponds to the stochastic fit or non-coherent fit from Zajfman modeling (equation 3 in the above section on bunch analysis), which may be due to the fast electrons from one peak catching up with the slow electrons of the next peak, creating an internal effect that switches the beam dynamics from coherent to non-coherent. The dashed line in the figure is a fit to the points to the stochastic beam dynamic equation (equation 3), with $\Delta T = 12.16 \pm 0.12$ ns.

PER VITA AUCTORIS

I was born on January 27, 1981 in Windsor, Ontario. Upon graduation from Catholic Central High School, I entered the honours physics program at the University of Windsor in September of 2000. After graduation of in the summer of 2004 I entered the masters program in experimental atomic and molecular physics, following a highly successful two years, I accepted the offer of re-classification to the PhD program, lasting another 2 years, I graduated in the summer of 2008 from the University of Windsor.

D.R. Tessier^a, Y. Niu^a, D.P. Seecombe^b, T.J. Reddish^c, A.J. Alderman^a, B. Birdsey^a, P. Hammond^a and F.H. Read^a

PERMISSION FOR REPRINT

^a Department of Physics, University of Western Australia, Perth, Western Australia

^b School of Physics, University of Western Australia, Crawley WA 6009, Australia

^c School of Physics and Astronomy, University of Manchester, Manchester M13 9PL, UK

The following pages include the two articles that were published during the graduate studies of the author. The article titled “Passive Electrostatic Recycling Spectrometer of Desk-Top Size for Charged Particles of Low Kinetic Energy” is a reprint with permission from Tessier D.R., Niu Y., Seecombe D.P., Reddish T.J., Alderman A. J., Birdsey B. G., Read F. H., and Hammond P., *Phys. Rev. Lett.*, **99** (2007) 253201, Copyright (2007) by the American Physical Society. The article titled “The Development of an Electrostatic Charged-Particle Orbit Recycling System” has been granted permission from the Australian Institute of Physics to include in this dissertation.

Abstract

The present system is a passive electrostatic recycling system for charged particles of low kinetic energy. It consists of a source of positive & negative ions, an electrostatic lens, a hemispherical deflector and a hemispherical collector. The ions are accelerated and focused by an electrostatic lens into the entrance of a hemispherical deflector. The electric field between the hemispheres bends the ions through the interaction region, and they are then collected by a hemispherical collector. The ions are recycled and pass through the interaction region many times, increasing the probability of interaction with the target.

Keywords: storage ring, electrostatic trap, spectrometer, electron, positron, ions

Introduction

The trapping of charged particles in laboratory scale instruments has been generally achieved in accelerating systems deflected through magnetic fields, such as the free beam tube now used in teaching laboratories for the measurement of m_e for electrons, through to cyclotron-type storage rings introduced by Lawrence in the late 1920's (Lawrence 1949). Storage rings based on electrostatic trapping have been far less explored. A recent development of such a ring is the ion storage ring ELISA (Wolter 1997). Linear electrostatic traps, in which charged particles oscillate back and forth along the same path, have also been successfully introduced (Paul 1990, Dahan *et al* 1998).

The present system was originally intended as an electron storage ring of desktop size based on passive electrostatic orbit definition, but the design is applicable to any type of charged particle. The Electron Recycling System (ERS) was conceived as a high energy resolution electron source spectrometer that was meant to overcome the delicate nature and low current yield of previous high energy resolution electron sources (Gopalan 2003). In typical scattering experiments, each electron in the source beam has a very low probability of scattering from the target of interest, meaning that a very small fraction of the low current in such sources has an opportunity to excite the process of interest. In the ERS, generated electrons are collected, passed around the ERS ring, and re-focused through the interaction region for more collision opportunities – they are literally recycled so that each electron stored in the ERS may pass through the interaction region many times and have many opportunities to scatter from the target.

For example, a single electron in a recycling orbit with an orbit time of ~ 300 ns and retained in the system for 1 μ s would be equivalent to a “beam current” in the interaction region of ~ 0.5 pA. Hence 1000 recycling electrons stored in the ERS would be equivalent to ~ 0.5 nA – a typical current in a single pass electron spectrometer passing 5×10^6 electrons s^{-1} . The ratio of source strengths required for a recycling system in comparison to a single pass system is proportional to the number of recycling orbits that can be achieved, and hence the achievement of long storage times is crucial.

The first successfully stored beam in the prototype Electron Recycling System is reported in this article with a preliminary analysis of its performance.

Materials and Methods

The passive electrostatic orbit recycling system for electrons is shown schematically in figure 1. Consider electrons leaving the source towards the right in the figure. They are accelerated and focused by an electrostatic lens into the entrance of a hemispherical deflector. The electric field between the hemispheres bends the electrons through the interaction region, and they are then collected by a hemispherical collector. The electrons are recycled and pass through the interaction region many times, increasing the probability of interaction with the target.

THE DEVELOPMENT OF AN ELECTROSTATIC CHARGED-PARTICLE ORBIT RECYCLING SYSTEM

D.R. Tessier^A, Y. Niu^A, D.P. Seccombe^A, T.J. Reddish^A, A.J. Alderman^B, B. Birdsey^B, P. Hammond^B and F.H. Read^C

^A Department of Physics, University of Windsor, Windsor, Ontario N9B 3P4, Canada

^B School of Physics, University of Western Australia, Crawley WA 6009, Australia

^C School of Physics and Astronomy, University of Manchester, Manchester M13 9PL, UK

Abstract

The progress in the development of a completely new type of electron spectrometer, an Electron Recycling System (ERS) is described, in which low energy electrons are passively stored in a desktop sized ring. The design of the system is likely to enable the storage of any type of charged particles, including positrons, polarized electrons, and positive & negative ions. Preliminary results will be presented which demonstrate electron storage with lifetimes $\sim 9.3 \mu\text{s}$ corresponding to ~ 30 orbits. The orbital path for the electrons is 0.65 m long and defined through the application of design voltages to two series of cylindrical lenses inserted between two identical hemispherical deflector analysers. The ERS design concept exploits the very low scattering cross sections in electron-molecule collisions, where the majority of electrons do not interact with the target. Unscattered electrons are collected and passed back through the ERS for another collision opportunity in the interaction region - i.e. they are "recycled" so that each electron generated in the electron source may undertake multiple passes through the interaction region.

Keywords: storage ring, electrostatic trap, spectrometer, electron, positron, ions

Introduction

The trapping of charged particles in laboratory scale instruments has been primarily achieved in recirculating systems defined through magnetic fields, such as the fine beam tube now used in teaching laboratories for the measurement of e/m for electrons, through to cyclotron-type storage rings introduced by Lawrence in the late 1920's (Lawrence 1939). Storage rings based on electrostatic trapping have been far less explored. A recent development of such a ring is the ion storage ring ELISA (Møller 1997). Linear electrostatic traps, in which charged particles oscillate back and forth along the same path, have also been successfully introduced (Paul 1990, Dahan *et al* 1998).

The present system was originally intended as an electron storage ring of desktop size based on passive electrostatic orbit definition, but the design is applicable to any type of charged particle. The Electron Recycling System (ERS) was conceived as a high energy resolution electron source/spectrometer that was meant to overcome the delicate nature and low current yield of previous high energy resolution electron sources (Gopalan 2003). In typical scattering experiments, each electron in the source beam has a very low probability of scattering from the target of interest, meaning that a very small fraction of the low current in such sources has an opportunity to excite the process of interest. In the ERS, unscattered electrons are collected, passed around the ERS ring, and re-routed through the interaction region for more collision opportunities - they are literally recycled so that each electron stored in the ERS may pass through the interaction region many times and have many opportunities to scatter from the target.

For example, a single electron in a recycling orbit with an orbit time of ~ 300 ns and retained in the system for 1 s, would be equivalent to a "beam current" in the interaction region of ~ 0.5 pA. Hence 1000 recycling electrons stored in the ERS would be equivalent to ~ 0.5 nA - a typical current in a single pass electron spectrometer passing 3×10^9 electrons s^{-1} . The ratio of source strengths required for a recycling system in comparison to a single pass system is proportional to the number of recycling orbits that can be achieved, and hence the achievement of long storage times is crucial.

The first successfully stored beam in the prototype Electron Recycling System is reported in this article with a preliminary analysis of its performance.

Materials and Methods

The passive electrostatic orbit recycling system for electrons is shown schematically in figure 1. Consider electrons leaving the source towards the right in the figure. They are accelerated and focused by an electrostatic lens onto the entrance of a hemispherical deflector analyser. Here the electric field between the hemispheres bends

the trajectories of electrons with kinetic energy similar to the pass energy of the analyser around to the exit plane. Electrons leaving the analyser pass through a second electrostatic lens and are focused into the interaction region. For the initial tests no gas jet is present in the interaction region, and electrons pass through a third lens which focuses onto the entrance of the second hemispherical deflector analyser where again electron trajectories are bent onto the exit plane. A fourth lens refocuses the electrons back into the source region, from where the whole orbiting process is repeated. Although the geometrical configuration is “race-track” in shape, the potentials around the ERS vary such that it is better described as a “rollercoaster” from the perspective of electron energy. The apparatus is housed in an UHV vacuum system currently operating at a base pressure of 10^{-7} mbar. Magnetic fields are minimised using mu-metal shielding and Helmholtz coils to < 2 mGauss.

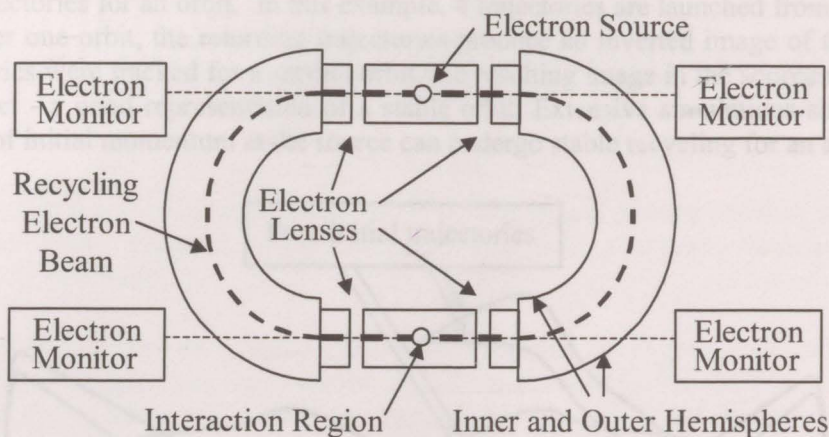


Figure 1. Schematic of the charged particle recycling system for electrons.

At present, electrons are injected into the ERS by scattering a high current, pulsed electron gun of temporal width ~ 150 ns from a 4 mm diameter wire loop in the source region as shown in figure 2. Low energy secondary electrons are produced on the wire loop and extracted by pulsing the voltage applied to both the wire loop and the surrounding cylinder synchronously with the pulsing of the incident electron beam. Following this pulse, all electrode elements in the source return to their normal voltages, producing a nominally field-free region in the source. If the source region was not modified in this way during the flight-time of the initial electron pulse, electrons on re-entrant trajectories would be forced to impact the ring on their return.

Scattered electron signal from the interaction region is detected using a particle counting channel electron multiplier (CEM). Timing spectra are recorded using a Time to Amplitude Converter (TAC) with start and stop signals provided by the CEM and the electron gun driving pulse.

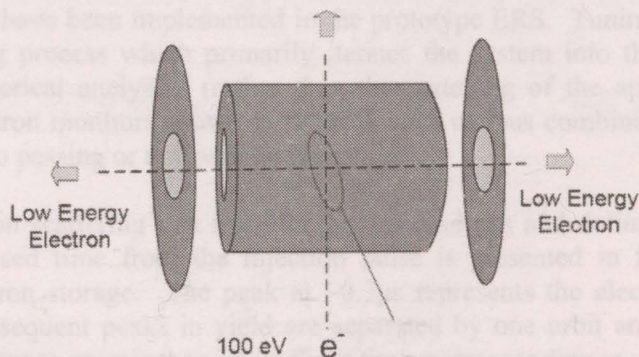


Figure 2. The pulsed, low-energy secondary electron source produced from ~ 100 eV electron impact on the tungsten wire loop.

The design of the charged particle optics has been achieved through the combined use of formal matrix representations of electron beam transport through the optical system and a three dimensional model of the ERS in the CPO3D simulation program (CPO3D). This software solves Laplace’s equation using a charge density representation for electrodes from which trajectory integrations are performed. A number of advantages are achieved through this process. The matrix representation of the optics is rather “ideal” and for trajectories that may explore the voltage space many thousands of times this may not necessarily model “reality”, due to the existence of higher order aberrations. Predictions from this matrix model were tested in the numerical model, which intrinsically includes aberrations in the optical performance of lenses and hemispherical deflector analysers. However the

tracing of many orbits in a numerical model is very time consuming and may also suffer from the build up of numerical calculation inaccuracies. It was for these reasons that both the matrix and numerical approaches were used in an interlinked manner, with the expectation that consistency between the approaches would accurately describe the prototype "real" ERS constructed to excellent mechanical tolerances.

Results and Discussion

The matrix approach to the design of the charged particle optics suggests passive stability can be achieved with a number of different voltage sets applied to the lenses. A simple example of this is shown in figure 3 where a voltage set for the optics to produce a particular charged particle storage mode are used in the CPO-3D numerical model to trace the trajectories for an orbit. In this example, 4 trajectories are launched from the source and tracked around the ERS. After one orbit, the returning trajectories produce an inverted image of the object in the source region. If the trajectories were tracked for a second orbit, the resulting image in the source region would map back onto the original object - a good representation of a stable orbit. Extensive simulations show that electrons with well specified ranges of initial momentum at the source can undergo stable recycling for an arbitrary length of time.

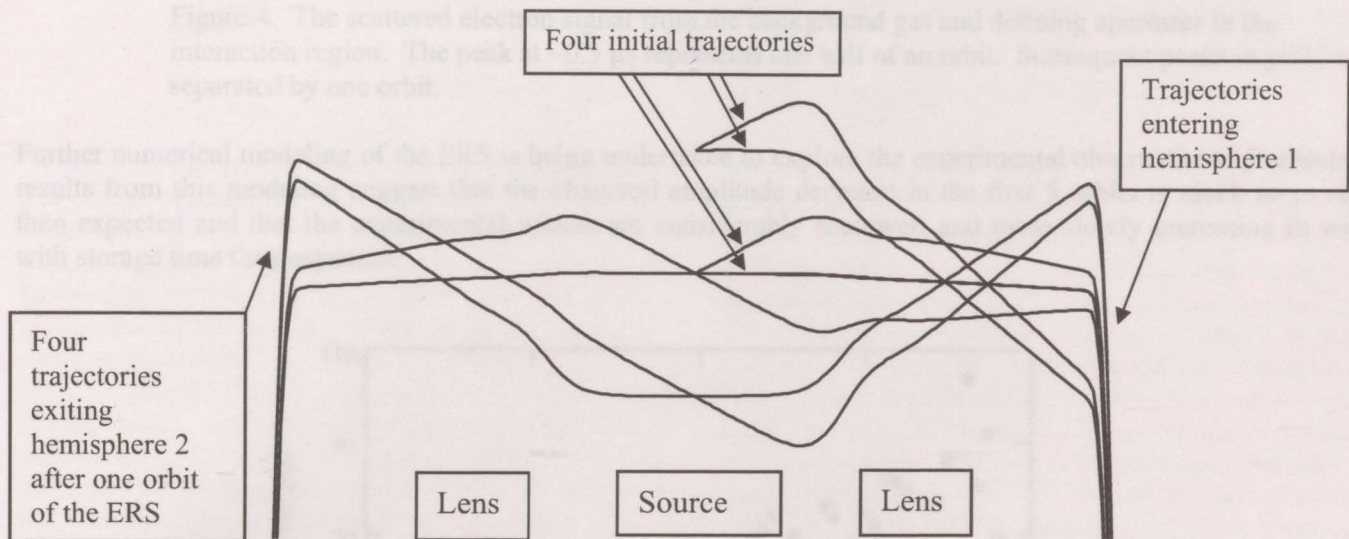


Figure 3. The focusing properties of the ERS for 4 paraxial trajectories in the source lens stack tracked over 1.3 orbits and showing an inverted image of the initial object after one orbit. The scale is magnified in the vertical direction.

The design optics for storage have been implemented in the prototype ERS. Tuning the spectrometer into storage is a complex and challenging process which primarily iterates the system into the matching of the actual pass energies of the two hemispherical analysers (rather than the matching of the applied voltages). This process requires the use of the 4 electron monitors shown in figure 1 with various combinations of the two hemispherical deflector analysers being set to passing or not-passing electrons.

A measurement of the electron scattering rate from the background gas and defining apertures in the interaction region as a function of elapsed time from the injection pulse is presented in figure 4 and demonstrates the achievement of passive electron storage. The peak at $\sim 0.3\mu\text{s}$ represents the electron pulse from the wire loop traversing half an orbit. Subsequent peaks in yield are separated by one orbit and the recycling passage of the electron pulse can be tracked out to greater than $18\mu\text{s}$ flight time, corresponding to $\sim 38\text{m}$ flight distance.

Preliminary analysis of the signal profile shown in figure 4 indicates an orbit time of $\sim 310\text{ ns}$ around the orbit of length 0.65 m . The source and interaction region voltages are $\sim 10\text{ V}$ and the nominal pass energy of the two hemispherical deflection analysers was 10 eV . Two lifetime components can be discerned in the decrease of the peak amplitude as a function storage time. In approximately the first 5 orbits the storage lifetime is $\sim 190\text{ ns}$ whereas longer term storage has a lifetime of $\sim 9.3\mu\text{s}$. The experimental results also show a distinct variation in the full width at half maximum of the peaks as a function of orbit time as shown in figure 5. There is a decrease in the width of the peaks over approximately the first five orbits with the minimum width reached being $\sim 37\text{ ns}$. Following this the peak widths increase in an approximately linear manner.

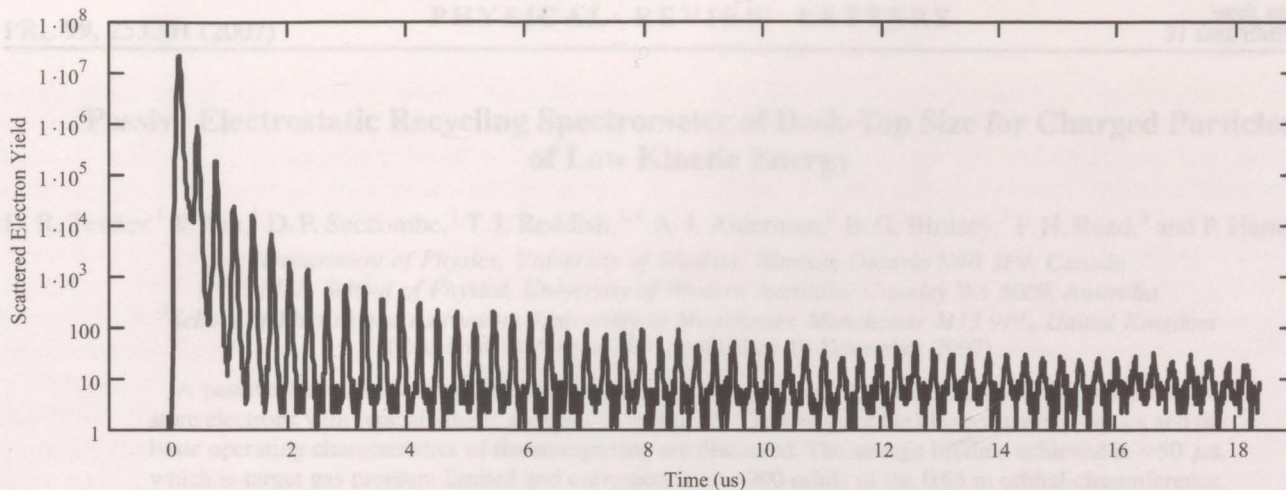


Figure 4. The scattered electron signal from the background gas and defining apertures in the interaction region. The peak at $\sim 0.3 \mu\text{s}$ represents one half of an orbit. Subsequent peaks in yield are separated by one orbit.

Further numerical modeling of the ERS is being undertaken to explore the experimental observations. Preliminary results from this modeling suggest that the observed amplitude decrease in the first 5 orbits is much more rapid than expected and that the experimental widths are considerably narrower, and more slowly increasing in width with storage time than expected.

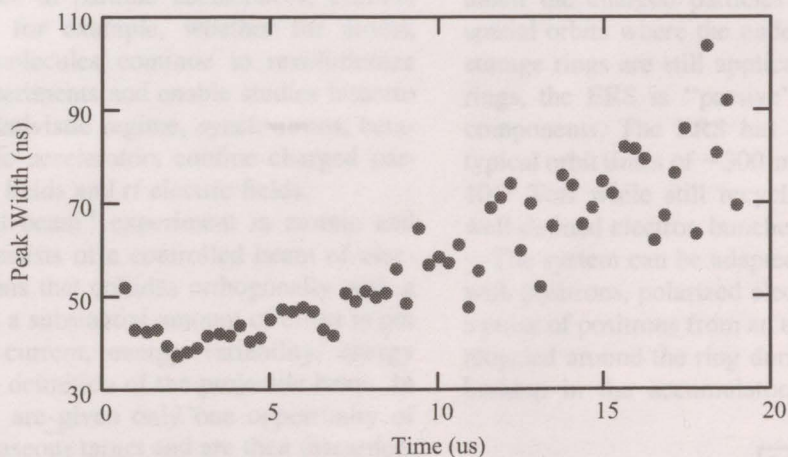


Figure 5. The widths (FWHM) of the stored electron signal as a function of storage time.

Conclusion

The storage of electrons in a passive electrostatic desk top sized ring has been demonstrated with a storage lifetime of $\sim 9.3 \mu\text{s}$.

Acknowledgements

Financial support from The Paul Instrument Fund of the UK Royal Society, the Australian Research Council Linkage Infrastructure Fund (LE0238631) and the Canadian funding agencies CFI, OIT and NSERC.

References

- CPO3D programs, available from www.electronoptics.com
- Dahren M. *et al* (1998) *Rev. Sci. Instrum.* **69**, 76-83
- Gopalan A. *et al* (2003) *Eur.Phys.J.D* **22**, 17-29
- Paul W. (1990), *Reviews of Modern Physics* **62**, 3
- Lawrence E.O. (1939) *Nobel Prize Lectures*, <http://nobelprize.org/physics/laureates/1939/index.html>
- Møller S.P.(1997), *Nucl. Inst. Meth. A* **394**, 281

Passive Electrostatic Recycling Spectrometer of Desk-Top Size for Charged Particles of Low Kinetic Energy

D. R. Tessier,¹ Y. Niu,¹ D. P. Seccombe,¹ T. J. Reddish,^{1,*} A. J. Alderman,² B. G. Birdsey,² F. H. Read,³ and P. Hammond^{2,†}

¹Department of Physics, University of Windsor, Windsor, Ontario N9B 3P4, Canada

²CAMSP, School of Physics, University of Western Australia, Crawley WA 6009, Australia

³School of Physics and Astronomy, University of Manchester, Manchester M13 9PL, United Kingdom

(Received 14 August 2007; published 18 December 2007)

A passive electrostatic recycling spectrometer for charged particles is described and demonstrated to store electrons with typical kinetic energies of tens of eV. The design of the charged particle optics and the basic operating characteristics of the storage ring are discussed. The storage lifetime achieved is $\sim 50 \mu\text{s}$, which is target gas pressure limited and corresponds to ~ 200 orbits of the 0.65 m orbital circumference. The storage ring also has controllable energy dispersive elements enabling it to operate as a spectroscopic device.

DOI: 10.1103/PhysRevLett.99.253201

PACS numbers: 39.10.+j, 29.20.Dh, 34.85.+x, 41.75.-i

There has been sustained interest in the manipulation and control of electrons, and other charged particles since the pioneering days of J. J. Thomson. New areas of physics have emerged over the last century that rely on such knowledge, resulting in a myriad of applications from semiconductor devices to particle accelerators. Particle trapping techniques, for example, whether for atoms, ions, or polarized molecules continue to revolutionize certain classes of experiments and enable studies hitherto impossible. In the relativistic regime, synchrotrons, betatrons and other cyclic accelerators confine charged particles using magnetic fields and rf electric fields.

A typical “crossed beam” experiment in atomic and molecular physics consists of a controlled beam of electrons, positrons, or ions that collides orthogonally with a gas beam. In general, a substantial amount of effort is put into optimizing the current, energy variability, energy resolution and spatial definition of the projectile beam. In such beams particles are given only one opportunity of interacting with the gaseous target and are then discarded. This is inefficient because the vast majority of the charged particles do not interact with the target gas due to the small collisional cross sections. In some applications this is severely limiting, as the particle source flux can be inherently low (e.g., [1–3]) or challenging to generate.

Here we introduce an innovative electrostatic apparatus for the storage of low energy charged particles (<150 eV) orbiting in a desktop sized ring with a view to enabling a new class of high precision measurements. For the present apparatus, called an electron recycling spectrometer (ERS) and shown schematically in Fig. 1, the experiments described here explore only the storage capability and characteristics of the racetrack shaped ring coupled with a simple external pulsed electron source. Imagine a spherical capacitor; electrons of appropriate energies and suitable (r , θ , φ) values undergo Kepler orbits indefinitely in the $1/r^2$ electric field between the two spherical electrodes. The ERS makes this “thought experiment” practicable by

splitting the capacitor in half, separating the two hemispheres, and filling the intervening space with electrostatic lenses. Electrons unscattered in the target gas beam are collected and returned for multiple crossings through the gas beam. This “recycling” concept is analogous to a trap; albeit the charged particles here are confined in stable spatial orbits where the underlying stability conditions of storage rings are still applicable [4]. Unlike most storage rings, the ERS is “passive”; it has no active feedback components. The ERS has a circumference of 0.65 m, typical orbit times of ~ 300 ns, and can operate up to $\sim 1 \times 10^{-5}$ Torr while still recycling spatially and temporally well-defined electron bunches of controllable energy.

The system can be adapted in a variety of ways for use with positrons, polarized electrons and ions. For example, a pulse of positrons from an external accumulator could be recycled around the ring during the next period of charge buildup in the accumulator. An alternate configuration

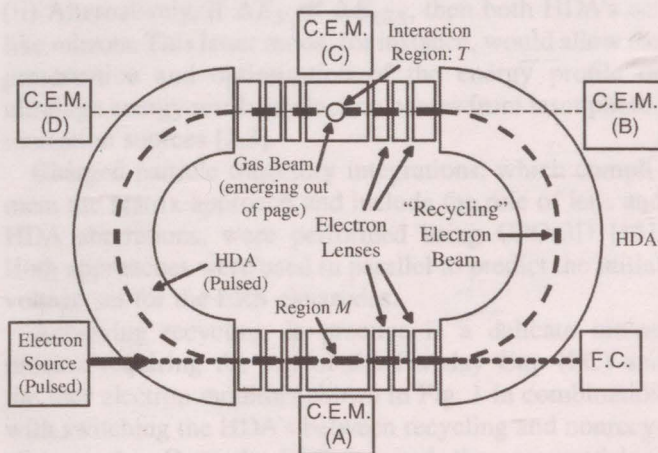


FIG. 1. Schematic of the electrostatic charged particle recycling system for electrons. Particle detection is achieved via channel electron multiplier's located in key positions around the spectrometer.

would place the charged particle source, such as a laser photoionization electron source, internal to the ring to allow accumulation of photoelectrons of well-defined kinetic energy. If on average each photoelectron makes N orbits of the ring, then a photoelectron source generating a flux a factor N less than a single pass apparatus would yield the same overall photoelectron flux, but with an improved energy resolution, due to the reduced source photoion space charge of a less intense source [2].

Over the last decade electrostatic storage rings for non-relativistic ion beams have been developed for use in atomic and molecular physics [5–10]. These devices typically have circumferences of 7–35 m, operating energies of ~ 20 –50 keV with vacuum base pressures of 10^{-11} – 10^{-13} Torr. They are complimented by the compact “fast” ion trap developed by Zajfman and co-workers [11,12]. The ERS has features analogous to both electrostatic ion storage rings and Zajfman’s linear ion beam “resonator.” The change of mass scale from ions to electrons is very significant because of the much shorter orbital time scales. The ERS allows, for the first time, the orbital confinement of low energy electrons.

In the ERS (Fig. 1), electrons emitted from a hot tungsten filament are collimated into a beam in a short electron gun. This beam is injected in a pulse ~ 50 ns wide through an aperture in the outer hemisphere of a hemispherical deflector analyzer (HDA) in which, for the duration of the pulse, the inner and outer hemisphere voltages are temporarily set to the voltage equivalent of the pass energy, E_L , of the deflector. Following the electron injection pulse the hemisphere voltages are set to normal operating voltages, a process which takes tens of nanoseconds to reach stable, quiescent voltage levels. The injected electron bunch is transported by a four element cylinder lens (FECL) into region M (electron energy E_M), viewed by a channel electron multiplier (CEM) labeled A (see Fig. 1). A subsequent FECL transports the electron bunch from region M onto the entrance of a second HDA operating with pass energy E_U . Electrons passed by this analyzer are then focused by another FECL into region T , where electrons of energy E_T are crossed with an effusive gas target beam. This interaction region is viewed by two CEM’s, C in Fig. 1, and E placed inline with the gas beam (not shown in Fig. 1). Unscattered electrons are refocused by a fourth FECL to reenter the first HDA now operating in the normal voltage regime and passing electrons of energy E_L . Electrons exiting this HDA, having completed an orbit of the ERS, then retrace similar orbital paths. In this way the electrons are recycled.

The ERS is housed in an ultrahigh vacuum chamber with a typical base pressure of 5×10^{-8} Torr. The chamber is internally double lined with mu metal and externally surrounded by orthogonal pairs of Helmholtz coils to magnetically shield the ERS to < 2 mG.

Passive recycling performance is critically dependent upon minimizing mechanisms for electron loss from the recycling low energy beam. These loss mechanisms can be

divided into two categories: (i) those that can be addressed by careful design and (ii) those that are inherent. Precision mechanical construction and alignment was ensured, together with the minimization of magnetic fields and electrode voltage instabilities. Oxygen-free copper ERS components were all gold plated to reduce localized surface property variations that could give rise to time varying distortions in electric fields [13]. Note that, in comparison to ion storage rings, fluctuations in electric (and magnetic) fields are particularly damaging to the passive recycling of electrons or positrons due to their much smaller mass. Inevitable loss mechanisms, namely, electron optical aberrations and collisions with residual background gas, are controlled through detailed electron optical design and suitable choice of operating pressure, respectively. Other losses, such as radiation and space charge limitations can be shown to be negligible in this case.

The design of the charged particle optics has been partly achieved using a formal matrix representation of the idealized lenses and HDA’s. The general condition for stable orbits is given by:

$$\frac{1}{2} |\text{Tr}(M_{ss})| \leq 1, \quad (1)$$

where M_{ss} is the overall transfer matrix for one complete orbit [4]. While there can be no overall acceleration in one orbit, one can achieve the stability condition in a variety of ways, so it is not necessary to have $E_L = E_U$ or $E_T = E_M$ [14]. Consequently, the racetrack configuration of Fig. 1 is more like a roller coaster in electron energy. Since HDA’s are energy dispersive, only electrons within a specific energy range, ΔE_{ERS} , will be recycled. Utilizing the well-known properties of HDA’s enables useful flexibility in the ERS operation. (i) When $E_U \ll E_L$, ΔE_{ERS} is largely determined by E_U and the HDA with E_L acts more like a mirror than a prism. Moreover, if ΔE_{ERS} is less than the inherent energy spread from the electron gun, ΔE_S , (as in this study), then the ERS also acts as an energy filter. (ii) Alternatively, if $\Delta E_S \ll \Delta E_{ERS}$, then both HDA’s act like mirrors. This latter mode, for instance, would allow the preservation and optimisation of the energy profile of ultrahigh energy resolved electron beams from laser photoionization sources [2,3].

Charged particle trajectory integrations, which compliment the matrix approach and include the role of lens and HDA aberrations, were performed using CPO-3D [15]. Both approaches were used in parallel to predict the initial voltage set for the ERS electrodes.

Achieving recycling in practice is a delicate tuning process requiring the use of the Faraday Cup (FC) and the four electron monitors shown in Fig. 1 in combination with switching the HDA’s between recycling and nonrecycling modes. Once the ERS is tuned, the measured lens voltages compare favorably with those predicted by the analytical models.

Data demonstrating storage of electrons in the ERS following electron injection are shown in Fig. 2. This timing spectrum was obtained with CEM (C), orthogonal

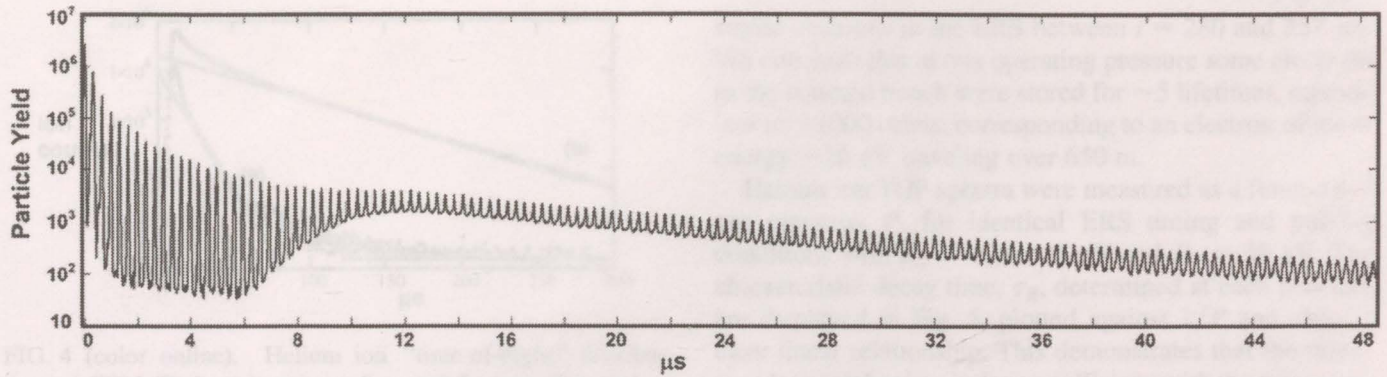


FIG. 2. A logarithmic plot of the signal yield in CEM (C) from 30 eV (E_T) electron collisions with helium at a chamber pressure of 7×10^{-7} Torr as a function of time after the initial electron injection. The spectrum shows ~ 150 sharp peaks due to scattered electrons whose time structure corresponds to that of the recycling electron beam and a broad underlying continuum due to metastable helium atoms.

to both the electron and gas beams, with $E_L = 18$ eV and $E_U = 4$ eV. The recorded signal consists of two components, one arising from 30 eV electrons elastically scattered from helium at 90° and a second from excited helium atoms in metastable states [2,16]. Electrons appear as repetitive peaks spaced at 330 ns intervals corresponding to sequential orbits of the electrons stored in the ERS. The metastable atom signal is broad in time, with an onset at $\sim 6 \mu\text{s}$ after electron injection, and underlies the sharp electron peaks. The delayed onset corresponds to the time-of-flight of thermal atoms with their velocity spread causing atoms excited by sequential orbits of the electron bunch to have overlapping times of flight. Analysis of the spectrum in Fig. 2 reveals that after $\sim 15 \mu\text{s}$ the electron peak heights have an exponential decay characterized by $\tau_H \approx 13.6 \mu\text{s}$. However, the area within each peak is a better comparative measure and its decay rate is slower with $\tau_A \approx 19.4 \mu\text{s}$.

The spectrum in Fig. 2 shows that electrons recycling in the ERS performed over 150 orbits traveling ~ 100 m in a chamber pressure of 7×10^{-7} Torr. The full-width half maximum (FWHM) bunch width variation as a function of orbit number is shown in Fig. 3. The bunch width reduces from 51 to 45 ns in the first few orbits because $\Delta E_S > \Delta E_{ERS}$ and consequently the HDA's and apertures eliminate trajectories with inappropriate energy, radial distance and angle for sustained recycling. After the first ≈ 5 orbits, the bunch width increases with orbit number. In the linear electrostatic ion trap, Pedersen *et al.* [17] observe very similar behavior despite the differences in physical geometry and the ~ 1000 factor in time scale. They show the recycling pulse width, W_n , increases with orbit number n as

$$W_n = \sqrt{W_0^2 + n^2 \Delta T^2}, \quad (2)$$

where W_0 is the initial temporal width. For the ERS, W_0 is largely determined by the duration of the electron injection pulse. The time spread per orbit, ΔT , consists of two components: (i) ΔT_{ERS} , the time spread within the ERS

for an electron of given energy due to the possible ranges of positions and angles, (r, θ) , giving rise to a range of orbit times. These different trajectories depend on the geometrical configuration and operating potentials of the ERS; (ii) ΔT_S is due to the inherent spread in the electron energies at $t = 0$ and is usually solely a property of the source. In the present experiment, where $\Delta E_S > \Delta E_{ERS}$, we define this "initial" time spread as that after the post-injection "clean up" of the first ~ 5 orbits. Taking ΔT_{ERS} and ΔT_S to be independent, the total time spread for each orbit bunch in the ERS is given by

$$\Delta T^2 = \Delta T_{ERS}^2 + \Delta T_S^2. \quad (3)$$

This assumes no coupling between these processes from internal mechanisms within the beam, such as Coulomb interactions (space charge effects), or from external perturbors, such as residual gas scattering and electrical noise on the electrodes. Under these conditions, ΔT will remain a constant for all orbits as each electron moves independently of the others, preserving its initial orbital period. There is clearly excellent agreement with the form of Eq. (2) with least squares fit values of $W_0 = 46.5 \pm 0.1$ ns and $\Delta T = 0.74 \pm 0.05$ ns (see solid line, Fig. 3).

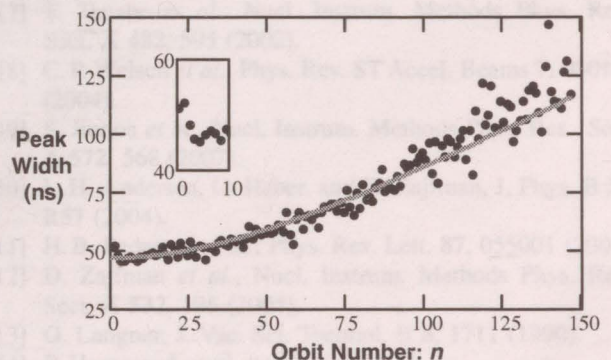


FIG. 3 (color online). Time width of the stored electron bunch as a function of orbit number n for the peaks in Fig. 2. The solid line is a fit to Eq. (2), as discussed in the text.

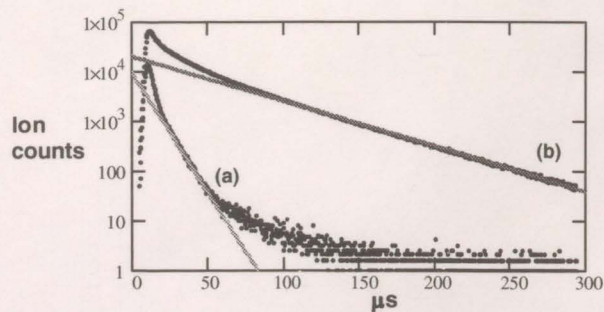


FIG. 4 (color online). Helium ion “time-of-flight” distributions at CEM (E) for (a) nonrecycling and (b) recycling modes. The asymptotic linear decay rates are (a) $\tau_{NR} \approx 9 \mu\text{s}$ and (b) $\tau_{NR} \approx 48 \mu\text{s}$; see text for discussion.

Consequently, the underlying assumptions of this diffusion process describe the electron dynamics of the ERS under the present operating conditions.

Long term storage within the ERS has been investigated by measuring helium ion time-of-flight (TOF) distributions with CEM (E), situated opposite the effusive gas beam. A typical spectrum of the He^+ yield as a function of time after the electron injection pulse over a 300 μs time window is shown in Fig. 4 for a chamber gas pressure of 5×10^{-7} Torr. The ion distribution in the nonrecycling mode was also recorded for the same data acquisition time and is also displayed in Fig. 4. For these spectra, $E_L = E_U = 18$ eV and the orbit time was 240 ns [measured at CEM (A)]. The nonrecycling mode is achieved by pulsing the electron gun in an identical manner to the recycling mode, but with the HDA voltages not being switched after electron injection making it physically impossible to recycle. In this mode, the observed signal corresponds to the inherent time of flight for helium ions created with a ~ 50 ns pulse of electrons. The peak in the ion distribution occurs at $\approx 13 \mu\text{s}$ after the electron pulse and the distribution has a characteristic decay time of $\tau_{NR} \approx 9 \mu\text{s}$. The ion distribution in the recycling mode has a longer decay time $\tau_R \approx 48 \mu\text{s}$, although there is measurable ion yield at ~ 7 times that value. Very few ions are detected after 60 and 340 μs in the nonrecycling and recycling modes, respectively. Consequently, ions detected at $t = 340 \mu\text{s}$ originate from

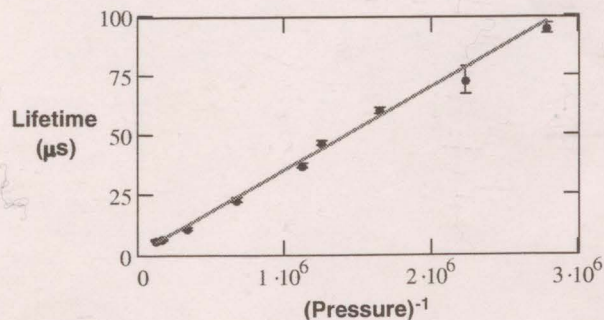


FIG. 5. Decay lifetimes, τ_R , obtained from the asymptotic linear decay rates in helium ion (see Fig. 4) for a range of chamber gas pressures, P , spanning from 3.6×10^{-7} to 8.0×10^{-6} Torr.

stored electrons in the ERS between $t = 280$ and $327 \mu\text{s}$. We conclude that at this operating pressure some electrons in the injected bunch were stored for ~ 5 lifetimes, equivalent to ~ 1000 orbits, corresponding to an electron of mean energy ~ 20 eV traveling over 650 m.

Helium ion TOF spectra were measured as a function of gas pressure, P , for identical ERS tuning and pulsing conditions with $E_L = E_U = 15$ eV and $E_T = 40$ eV. The characteristic decay time, τ_R , determined at each pressure are displayed in Fig. 5, plotted against $1/P$ and show a clear linear relationship. This demonstrates that the dominant loss mechanism is due to collisions with the target gas, as mean free path, $\lambda \propto 1/P$ and $\tau_R \propto \lambda$.

This experimental study shows the ERS to be sufficiently stable to the potential loss mechanisms and to have enough stored current to perform gas phase collision experiments that are target pressure limited. Measurements are currently underway to quantify the stored current and determine the energy resolution of the recycling beam as a function of storage time, in order to compare it with theory [14]. The ability to scan E_T to perform energy and time dependent studies will also be explored.

The authors wish to acknowledge John Corner and Alan Bott (University of Newcastle upon Tyne, UK) for precision engineering. Financial support for this work was provided by the Paul Instrument Fund (UK); ARC (Australia); CFI, OIT, NSERC, and the University of Windsor (Canada).

*reddish@uwindsor.ca

†phammond@physics.uwa.edu.au

- [1] S. J. Gilbert *et al.*, Nucl. Instrum. Methods Phys. Res., Sect. B **171**, 81 (2000).
- [2] A. Gopalan *et al.*, Eur. Phys. J. D **22**, 17 (2003).
- [3] J. Bömmels *et al.*, Phys. Rev. A **71**, 012704 (2005).
- [4] E. D. Courant and H. S. Snyder, Ann. Phys. (Leipzig) **3**, 1 (1958).
- [5] S. P. Møller, Nucl. Instrum. Methods Phys. Res., Sect. A **394**, 281 (1997).
- [6] S. P. Møller and U. V. Pedersen, Phys. Scr. **T92**, 105 (2001).
- [7] T. Tanabe *et al.*, Nucl. Instrum. Methods Phys. Res., Sect. A **482**, 595 (2002).
- [8] C. P. Welsch *et al.*, Phys. Rev. ST Accel. Beams **7**, 080101 (2004).
- [9] S. Jinno *et al.*, Nucl. Instrum. Methods Phys. Res., Sect. A **572**, 568 (2007).
- [10] L. H. Andersen, O. Heber, and D. Zajfman, J. Phys. B **37**, R57 (2004).
- [11] H. B. Pedersen *et al.*, Phys. Rev. Lett. **87**, 055001 (2001).
- [12] D. Zajfman *et al.*, Nucl. Instrum. Methods Phys. Res., Sect. A **532**, 196 (2004).
- [13] G. Langner, J. Vac. Sci. Technol. B **8**, 1711 (1990).
- [14] P. Hammond *et al.* (to be published).
- [15] CPO Programs: <http://www.electronoptics.com/>.
- [16] S. J. Buckman *et al.*, J. Phys. B **16**, 4039 (1983).
- [17] H. B. Pedersen *et al.*, Phys. Rev. A **65**, 042704 (2002).

stored electrons in the ERS between $t = 280$ and 327 ns. We conclude that at this operating pressure some electrons in the injected bunch were stored for ~ 2 lifetimes, equivalent to ~ 1000 orbits, corresponding to an electron of mean energy ~ 50 eV traveling over 630 m.

Helium ion TOP spectra were measured as a function of gas pressure P , for identical ERS timing and pulsing conditions with $E_0 = 50$ eV and $E_1 = 40$ eV. The characteristic decay time, τ_d , determined at each pressure and displayed in Fig. 2, plotted against $1/P$ and show a clear linear relationship. This demonstrates that the dominant loss mechanism is due to collisions with the target gas, as shown for both $\lambda \propto 1/P$ and $\tau_d \propto \lambda$.

This experimental study shows the ERS to be suitably stable to the potential loss mechanisms and to have enough stored current to perform gas phase collision experiments that are target pressure limited. Measurements are currently underway to quantify the stored current and determine the energy resolution of the receiving beam as a function of storage time, in order to compare it with theory [14]. The ability to scan E_1 to perform energy and time dependent studies will also be explored.

The authors wish to acknowledge John Cornish and Alan Ross (the variety of the words) for their support for this work and also acknowledge financial support from STFC (UK), AEC (Australia), CNR (Italy), NSERC (Canada) and the University of Windsor (Canada).

1. J. G. Kirkwood, *Phys. Rev. Lett.* **95**, 015001 (2005).
 2. A. J. G. Cook, *Phys. Rev. Lett.* **95**, 015002 (2005).
 3. J. G. Kirkwood, *Phys. Rev. Lett.* **95**, 015003 (2005).
 4. J. G. Kirkwood, *Phys. Rev. Lett.* **95**, 015004 (2005).
 5. J. G. Kirkwood, *Phys. Rev. Lett.* **95**, 015005 (2005).
 6. J. G. Kirkwood, *Phys. Rev. Lett.* **95**, 015006 (2005).
 7. J. G. Kirkwood, *Phys. Rev. Lett.* **95**, 015007 (2005).
 8. J. G. Kirkwood, *Phys. Rev. Lett.* **95**, 015008 (2005).
 9. J. G. Kirkwood, *Phys. Rev. Lett.* **95**, 015009 (2005).
 10. J. G. Kirkwood, *Phys. Rev. Lett.* **95**, 015010 (2005).
 11. J. G. Kirkwood, *Phys. Rev. Lett.* **95**, 015011 (2005).
 12. J. G. Kirkwood, *Phys. Rev. Lett.* **95**, 015012 (2005).
 13. J. G. Kirkwood, *Phys. Rev. Lett.* **95**, 015013 (2005).
 14. J. G. Kirkwood, *Phys. Rev. Lett.* **95**, 015014 (2005).
 15. J. G. Kirkwood, *Phys. Rev. Lett.* **95**, 015015 (2005).
 16. J. G. Kirkwood, *Phys. Rev. Lett.* **95**, 015016 (2005).
 17. J. G. Kirkwood, *Phys. Rev. Lett.* **95**, 015017 (2005).
 18. J. G. Kirkwood, *Phys. Rev. Lett.* **95**, 015018 (2005).
 19. J. G. Kirkwood, *Phys. Rev. Lett.* **95**, 015019 (2005).
 20. J. G. Kirkwood, *Phys. Rev. Lett.* **95**, 015020 (2005).

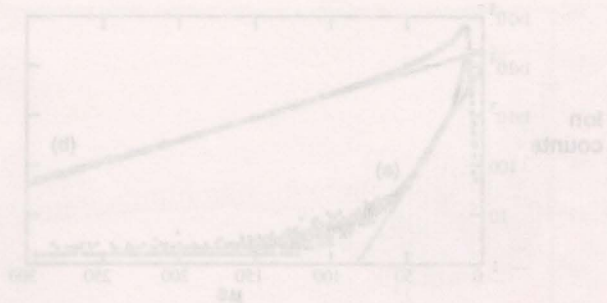


FIG. 4 (color online). Helium ion "time-of-flight" distribution at CEM (a) for (a) nonrecycling and (b) recycling mode. The asymptotic linear decay rates are (a) $\tau_{d0} = 9$ ns and (b) $\tau_{d0} = 48$ ns; see text for discussion.

Consequently, the underlying assumptions of this diffusion process describe the electron dynamics of the ERS under the present operating conditions.

Long term storage within the ERS has been investigated by measuring helium ion time-of-flight (TOP) distributions with CEM (5) situated opposite the electron gun beam. A typical spectrum of the He^+ yield as a function of time after the electron injection pulse over a 500 ns time window is shown in Fig. 4 for a chamber gas pressure of 2×10^{-7} Torr. The ion distribution in the nonrecycling mode was also recorded for the same data acquisition time and is also displayed in Fig. 4. For these spectra $E_1 = E_0 = 50$ eV and the orbit time was 240 ns (measured at CEM (A)). The nonrecycling mode is achieved by pulsing the electron gun in an identical manner to the recycling mode, but with the HDA voltages not being switched after the non injection making it physically impossible to recycle. In this mode, the observed signal corresponds to the parent time of flight for helium ions injected ~ 100 ns prior to the electron pulse in the ion distribution curve at $t = 13$ ns after the electron pulse and the distribution has a characteristic decay time of $\tau_{d0} = 9$ ns. The ion distribution in the recycling mode has a longer decay time of $\tau_{d0} = 48$ ns, although there is measurable ion yield at $t = 100$ ns after the pulse. Very low ions are detected after 60 and 100 ns in the nonrecycling and recycling modes, respectively. Consequently, ions detected at $t = 240$ ns originate from

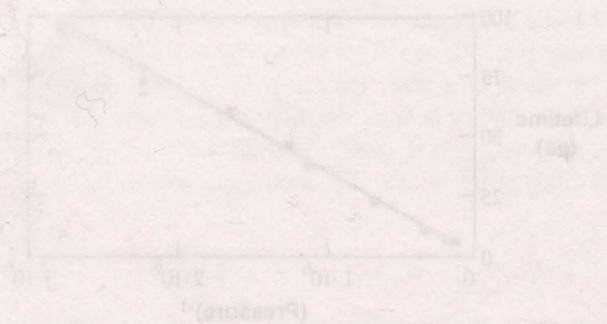


FIG. 2. Decay lifetime, τ_d , obtained from the asymptotic linear decay rates in helium (see Fig. 4) for a mass of 4 amu ions at pressure P , spanning from 5×10^{-8} to 8.0×10^{-6} Torr.

980063



3 1862 018 142 915
University of Windsor Libraries

University 
of Windsor

Date Due

JAN 16 2009

LEDL
THES
Thesis
2008
.T47